Mechanics Study and Application of Micro-engineered Smart Surface

D WANG

PhD

2019

Mechanics Study and Application of Micro-engineered Smart Surface

DING WANG

A thesis submitted in partial fulfilment of the requirements of the University of Northumbria at Newcastle for the degree of Doctor of Philosophy

Department of Mechanical and Construction Engineering

January 2019

Abstract

Naturally existing functional surfaces with micro-structure arose competing interests due to their potential application in engineering filed such as wetting control, optical control, micro-fluidic, tissue scaffolds, marine engineering, oil field, etc al. A patterned surface with stimuli responsive properties attracts considerable interest for its importance in advanced engineering, partly due to its reversibility, easy design and control, good compatibility and responsive behaviour to external stimuli. In this work, we have investigated various surface instabilities that enable a convenient strategy of micro-engineered structure impart reversible patterned feature to an elastic surface. We focus on the classic bi-layer system contains a stiff layer on a soft substrate that produces parallel harmonic wrinkles at uniaxial compression and ultimately develop into deep creases and fold. By introducing the micro-scale planar Bravais lattice holes, we guided these instabilities into various patterns to achieve an anisotropic manipulation of single liquid droplet by initialize localized surface morphologies. The Finite Element Analysis provided the fundamental theory on the surface instabilities evolution and development. The finding demonstrates considerable control over the threshold of a surface elastic instability and bi-axial switching of droplet shape that relevant to many novel applications including wearable electronic devices, bio-medical systems, micro-fluidics and optical devices.

Acknowledgement

First, I am very grateful to sending my regard to my supervisor Dr. Ben Bin Xu, whose intelligence in ideas and brilliant in mind. Without his untiring support I could not made this thesis possible. Before I started my post-graduate study, Dr. Xu took me as an internship student in his laboratory in Summer 2010 when I was still a junior student in Heriot-Watt University. He has not only taught me how to work as a qualified researcher, but also passed his valuable life experience, and how to become an outstanding individual in the society. I have benefited a lot from his diversity of research attitude and personality manner.

Second, a special gratitude to Prof. Glen McHale, Dr. Yifan Li for their encouragement and scientific guidance throughout out my research life.

Third, my thanks to Prof. David Wood and Dr. Michael Cooke from Durham University, Dr. John Simeon Biggins from University of Cambridge, Dr. Alex Laude from Newcastle University, Dr. James Martin and Dr Simone Stuart-Cole from Reece Innovation, Dr. Terence Liu, Dr. Gary Wells, Dr. Pietro Maiello, Miss Rebecca Payne and Mr. Gavin Warburton from Northumbria University for their advice and help throughout my postgraduate studies.

I would also like to thank everyone who has been working in the same lab and office with me, for their valuable advices and discussions on my research and study. Furthermore, I would like to express my thanks to the

staffs in the lab, workshop for their help. I appreciate the lab facilities and computing resources that are provided by Northumbria University.

I appreciate the contributions from the collaborated institutes and project partners, which are:

Most important, I would like to express my deepest gratitude to my family for their endless dedication throughout my existing time on earth. I wouldn't have achieved anything without their love and care.

Declaration

I declare that the work contained in this thesis has not been submitted for any other award and that it is all my own work. I also confirm that this work fully acknowledges opinions, ideas and contributions from the work of others. The work was done in collaboration with the Durham University, Newcastle University and is funded by Reece Innovation.

Any ethical clearance for the research presented in this thesis has been approved.

I declare that the word count of this thesis is currently 24602 words

Name: Ding Wang

Signature:

Date: 31/01/2019

Abbreviations

AFM	atom force microscopy
LSCM	laser scanning confocal microscopy
DSA	droplet shape analyser
OM	optical microscopy
SEM	scanning electron microscopy
MEMS	microelectron mechanical system
CA	contact angle
PDMS	polydimethylsiloxane
DI water	deionized water
CA	contact angle
FEA	finite element analysis

Contents

Achievement

Journal paper:

1. Ansu Sun, ***Ding Wang***, Honghao Zhou, Yifan Li, Chris Connor, Jie Kong, Jining Sun, Ben B. Xu, Spatially Engraving Topological Structure on Polymeric Surface by Ion Beam Milling, **Polymer,** 2019, 11, 1229

2. Peng Miao, Kaiyang Cheng, Hongqiang Li, Junwei Gu, Kaijie Chen, Steven Wang, ***Ding Wang***, Terence X. Liu, Ben B. Xu and Jie Kong, Poly(dimethylsilylene)diacetylenes-Guided ZIF-Basedf Heterostructures for Full Ku-Band Electromagnetic Wave Absorption, **ACS Applied Materials Interface,** 2019, 11, 17706-17713

3. Xingyi Dai, Yuzhang Du, Jiye Yang, ***Ding Wang,*** Junwei Gu, Yifan Li, Steven Wang, Ben B. Xu and Jie Kong, Recoverable and Self-healing Electromagnetic Wave Absorbing Nanocomposites, **Composites Science and Technology,** 2019, 174, 27-32 (**TOP 5% journal** in *MATERIALS SCIENCE, COMPOSITES*)

4. Nicolas Cabezudo, Jining Sun, Behnam Andi, Fei Ding, ***Ding Wang,*** Wenlong Chang, Xichun Luo and Ben B. Xu, Enhancement of Surface Wettability via Micro and Nanostructures by single point diamond turning, **Nanotechnology and Precision Engineering**, 2019, 2, 8-14

5. ***Ding Wang***, Nontawit Cheewaruangroj, Yifan Li, Glen McHale, Yinzhu Jiang, David Wood, John Simeon Biggins, Ben Bin Xu, Spatially Configuring Wrinkle Pattern and Multiscale Surface Evolution with Structural Confinement, **Advanced Functional Materials,** 2018, 28, 1704228. (**TOP 5% journal** in *MATERIALS SCIENCE,* **cover paper**)

6. Yifan Li, ***Ding Wang***, Jack Richardson and Ben B. Xu, Responsive Hydrogels Based Lens Structure with Configurable Focal Length for Intraocular Lens (IOLs) Application, **Macromolular Symposia,** 2017, 372, 127–131. (2016 Young Investigator Award paper from PNG for Dr Ben Xu)

7. A Flexible Tpop-Optical Sensing Technology with Ultra-high Contrast, *Nature Communications*, October 2019, **under review**.

Conference & Seminar:

1. *UK Fluid Networks (UKFN) – Multiscale Modelling of Wetting Phenomena*, 12 -13 SEP 2018, Durham, UK (**Poster**)

2. *The 25th Joint Annual Conference of CSCST-SCI*, 6 - 7 SEP 2018, University of Manchester, UK (**Poster**)

3. *UK Fluids Conference 2018*, 4 – 6 SEP 2018, University of Manchester, UK (**Oral Presentation**)

4. *EE PGR Conference 2018 – Research for a Better Tomorrow,* 21 June 2018, Northumbria University, Newcastle upon Tyne (**Oral Presentation**)

5. *UKFN SIG mini-symposium: Structural surfaces and liquid/surface interactions*, 20 April 2018, Heriot-Watt University, Edinburgh (**Video Presentation**)

6. *UK Fluids Networks (UKFN) – Early Career Researcher Event,* 21 March 2018, Northumbria University, Newcastle upon Tyne (**Poster**)

7. *2017 Materials Research Society Fall Meeting & exhibit*, 26 NOV – 01 DEC 2017, Boston, Massachusetts (**Poster**)

8. Cong Wang, ***Ding Wang***, Valery Kozhevnikov, Ben Bin Xu, Yifan Li, Elastic Instability Induced Mechano-Responsive Luminescence for Super-Flexible Strain Sensing, 2017 IEEE SENSORS, Glasgow, UK, DOI: 10.1109. ICSENS. 2017.8234210 (**Conference Paper**)

9. *Bruker SPM Conference & Users Meeting,* 10-11 October 2017, Leeds

10. *The 24th Joint Annual Conference of UKFN SIG and CSCST-SCI*, 23 – 24 June 2017, Newcastle upon Tyne (**Oral Presentation**)

11. *EE PGR Conference 2017 – Research Connects,* 15 June 2017, Northumbria University, Newcastle upon Tyne (**Oral Presentation**)

12. *15th European Mechanics of Materials Conference*, 07-09 September 2016, Brussels (**Oral Presentation**)

13. *The 23rd Joint Annual Conference of CSCST and SCI,* 03 September 2016, Nottingham (**Oral Presentation**)

14. *EE PGR Conference 2016,* 20 June 2016, Northumbria University, Newcastle upon Tyne (**Oral Presentation**)

15. *The 22nd Joint Annual Conference of CSCST and SCI*, 19 September 2015, Birmingham (**Poster**)

16. *Northumbria Research Conference – Showcasing Research,* 20 May 2015, Northumbria University, Newcastle upon Tyne (**Poster**)

Award and certificated workshop:

1. **First Prize** in Poster Presentation, The 25th Joint Annual Conference of CSCST-SCI, 6-7 SEP 2018, University of Manchester

2. **Third Prize** in Oral Presentation, The 24th Joint Annual Conference of UKFN SIG and CSCST-SCI, 23-24 June 2017, Newcastle upon Tyne

3. **Third Prize** in Eureka & Discovery category, EPSRC National Photography Competition 2017, media presses in *EPSRC*, *Guardian*, *NECONNECTED*,*THE GLOBAL AND MAIL*.

4. Advanced Biomedical Modeling Workshop – From Image to Simulation, SYNOPSYS, 20 October 2016, Reading

Chapter 1

Introduction

The aim of work presented in this thesis was to investigate the properties of micro-engineered elastic topographical surface and hence to manipulate micro-droplets anisotropically on these smart surfaces. The main objective is to design and fabricate the functional smart surfaces with micro/nano-structures, to create hierarchical structure, and hence to understand the mechanism on how it achieves the anisotropic droplet shaping with the effects of micro/nano-structures with corresponding physical, mechanical and chemical properties.

1.1 Background of Functional Surfaces and Hierarchical Structure

Functional surfaces with micro-structures are naturally existed, such as butterfly wings, lotus leaves and claw skin of gecko, with multi-scale and hierarchical patterns that enable enhancement on specific function, i.e. structural colour [1], wettability [2], or dry adhesion [3]. These bio-inspired smart properties have arisen a growing interest for their potential engineering applications, including wetting control [2], optical control [4], micro-fluidic [5], tissue scaffolds [6], marine engineering [7], oil field [8]. Recently, researchers have attempted various approaches to bring these applications to advance

engineering level by emulating different hierarchical structures, especially, on cross-disciplinary area with developing responsive structure on soft matter under various external stimuli such as light [9], temperature [10], electric field [11], magnetic field [12], etc. This project will focus on developing responsive structure that is capable to deliver fundamental surface physical and chemical transitions such as mechanic-geometrically surface re-shaping (wrinkling, creasing), swollen/shrank, hydrophilic/hydrophobic, etc.

Up to date, micro-topographical responsive surfaces are becoming more commonly used in industrial and commercial areas. Bio-mimetics can be defined as the investigation of structures and designs of biological materials which are found in nature, these materials inspire the possible designs of new materials which could be used in industry. Examples of micro-topographical surfaces can be found in many different areas of nature with varying purposes such as a Mosquito's eye which provides antifogging capabilities or a lotus leaf which has super hydrophobicity properties.

1.2 Objectives

The overall aim of the project is to design and fabricate the micro-engineered smart structure capable of behaving fundamental surface physical/chemical transition/switches, which meet the requirements for potential application in geometrically surface re-shaping (wrinkling, creasing), swollen/shrank, hydrophilic/hydrophobic, etc, and understand the

mechanism on how it responses to external stimuli. The project involves a range of advanced chemical, physical and mechanical testing techniques, since the related structure fabrication through chemical/physical reactions and the characterizations demand extensive physical structure-properties knowledge.

The approach was to use self-designed commercial mask as a template, and then to fabricate micro-structure systematically using appropriate lithographic method and in-lab chemical synthesis of polydimethylsiloxane (PDMS). Specific consideration was given to the control of structure thickness, especially on the surface chemical property for multi-level structure generation. The fabricated micro-structures were characterised at microscopic scales and their overall performance were assessed.

Mechanical property was evaluated using a self-designed mechanical device which gives the strain value related to corresponding physical properties. Physical properties were characterized using a combination of optical microscopy, atom force microscopy (AFM) and laser scanning confocal microscopy (LSCM). Optical microscopy gives the first visual site of micro-structure and how it changes with corresponding strain value, whereas AFM offered a range of in-plane properties allowing measurement down to nano-level. LSCM was used to provide further information for structure out-of-plane property. Other tests, such as droplet shape analyser (DSA) was used to provide surface wetting information directly to support the development of surface structure. Droplet shape manipulate demonstration were carried out to define the micro-structure anisotropic wetting effect. Finally, simulation

method was also used to provide micro-structure information for the specific materials.

The primary aim of this project is to fabricate the micro-structural materials and investigate the responsive behaviour to the external stimuli with different hierarchically patterning. It was anticipated that a novel micro-structure would be identified in this work, alongside the establishment of a dynamic method for property evaluation. Analysis of the experiment data was expected to result in the understanding of functional structure surfaces.

The objectives of this report are listed as follows:

a. Design and develop the micro-fabrication techniques for structures on different length-scale based on the existing techniques (photo-lithography, electro-spinning, 3D-printing, etc).

b. Experimentally investigate the mechanics of surface micro-structure and the evolution process with the defined boundary conditions.

c. Analys the anisotropic droplet shape manipulation based on nano/micro-structure.

c. Understand and theoretically model the mechanism of the surface micro-structure and the evolution of morphology with the defined boundary conditions.

1.3 Outline of Thesis

Chapter 1: Introduction. A description of how the present project was inspired and its contributions to the novel structure materials.

Chapter 2: Literature review. The origins of the micro-structure phenomenon and the history are introduced. Classifications of micro-structure are explained in detail. The smart material concept is provided, with a brief introduction on the theoretical simulation methods.

Chapter 3: Experimental methods. The in-lab techniques that put effect in sample fabrication with surface instabilities and demanded characterization methods including Optical Microscopy (OM), Atom Force Microscopy (AFM), Laser Scanning Confocal Microscopy (LSCM), Scanning Electron Microscopy (SEM), etc. In addition, the mathematical simulation method to helped us in specific surface morphology understanding.

Chapter 4: Spatially configuring wrinkle pattern and multiscale surface evolution with structural confinement. Primary finding on novel surface instabilities shape with designed spatial lattice hole pattern in elastic surface with famous bi-layer system.

Chapter 5: Bi-axially Switching Droplet Shape by Initiating Localized Wrinkle Pattern Transformation upon Elastic Surface. In-lab investigation on droplet

shape manipulation based on the wrinkle pattern that induced the surface morphology change and roughness variation.

Chapter 6: Theoretical understanding on configuring the elastic instability on soft surface. Finite element analysis on surface pattern deformation simulation and wrinkle phenomenon investigation on three-dimensional thin film plane.

Chapter 7: Conclusion and future prospective. Overall summary on current research work based on primary findings of lattice hole guided surface instabilities and corresponding surface wetting phenomenon of single droplet. In addition to the Finite Element Analysis conclusion, future work is outlined here as well.

Chapter 2

Literature Review

This chapter presents a general overview of the typical concept of smart micro-engineered structure: surface mechanical instability. This review will begin with a summary of nature-existing bio-inspired surfaces. It will then describe the basic concept of mechanical instability, including the mechanism which drives instability formation, historic development on theoretical prediction, experimental observation and possible applications, followed by fundamental theory for surface wettability on structure surface, and also the simulation concept understanding on material selection.

2.1 Bio-inspired Surfaces

Generally, biological responsive system is a complicated system to be imitated. It is a hybrid composite material which presents organic or inorganic properties and responds to external stimuli [13]. However, some less complex special features of surface in biology have received intense attention. Many examples can be found in nature to represent the micro-topographical surface such as hydrophobic leaf (**Figure 2.1a**) [14], antifogging Mosquito's eye (**Figure 2.1b**) [15], highly adhesive gecko's feet (**Figure 2.1c**) [16] and periodic micro-structure of beetle wing cases (**Figure 2.1d**) [17].

One particular feature of smart surfaces is to react to special environmental stimuli and have the ability to drive mechanical reversible instabilities [18]. It is attractive to have buckling instabilities designed for stimuli responsive material system where the deformation remains elastic. Examples of instability deformation of stimuli-responsive smart materials include wrinkling, tuneable optics, stretchable electronics, microfluidics, controlled wetting, adjustable adhesives, and creasing. Furthermore, elastic instabilities of smart surfaces may provide new approaches for large-scale surface pattern fabrication [18].

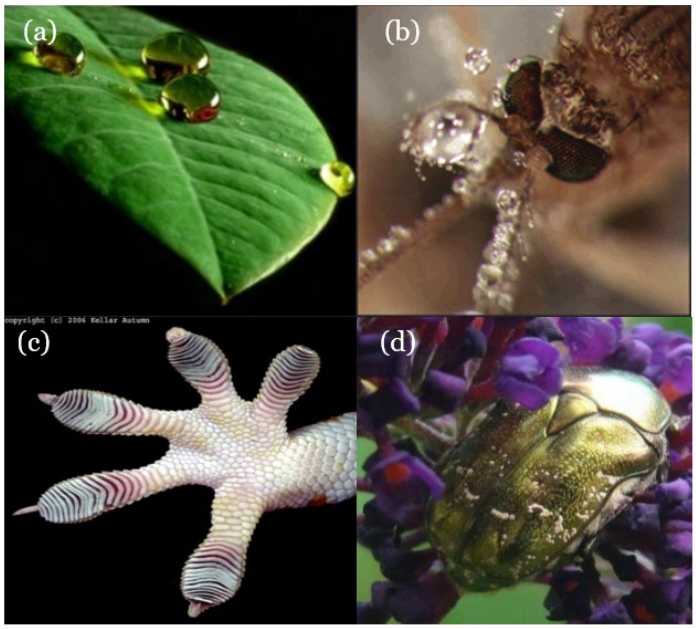

Figure 2.1 (a) Hydrophobic leaf [14] (b) Antifogging Mosquito's eye [15] (c) Gecko's highly adhesive feet [16] (d) Beetle wing cases [17]

2.2 Surface Instabilities

Surface morphologies such as wrinkles, creases, folds, ridges, crinkles, and crumples on solid surfaces are commonly referred to as surface instabilities. Surface instabilities are ubiquitous in everyday life and nature [19]–[22] (**Figure 2.2**). Work on surface instabilities are important to a range of applications including flexible electric devices [23], hydrophobic materials [24], adhesion devices [25], self-assembled patterns [26], brain subject [27]–[29]. Surface instabilities on elastic material are triggered with specific external conditions and reflect themselves by various surface morphologies changes. Here the elastic material system was defined by their surface pattern formation process, two types can be considered, one is deformation surface instabilities, and another is growth induced surface instabilities [30]. The formation of instabilities is due to various external forces, such as mechanical excitation. The material surface remains unaltered if the external force is small, but it will lose stability if a critical value is reached. Growth induced instabilities exhibit surface pattern mainly caused by material deposition procedure and it is usually observed in plants morphology [31]–[38] and bio-system [39]–[44], for example the morphogenesis in brain system [28],[45],[46], formation on fingerprint [47], folding of mucus [48]–[51] and development of gut [52]–[55].

(a) (b) (c)

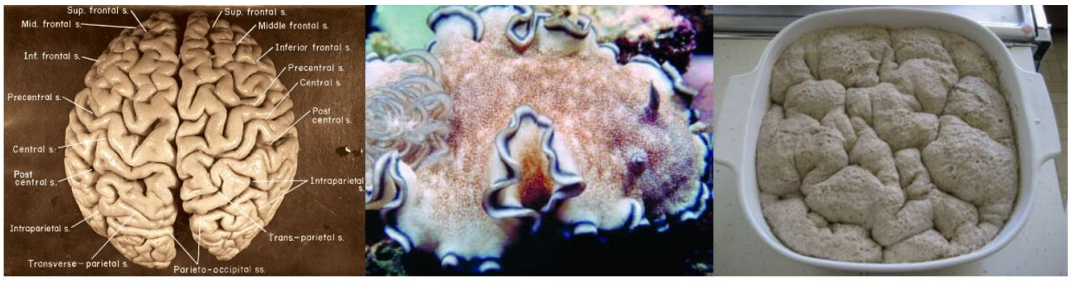

Figure 2.2: (a) The cortex structure of Einstein's brain (discover magazine) [56]; (b) Wavy edges in nature (Sticta limbate) [19] (c) Creases of rising dough [57]

In structure engineering, mechanical instabilities were considered as a mode of failure as they can cause structure fracture, such as buckling of pipes [58], crack in Microelectron Mechanical System (MEMS) [59] and composite materials [60]. However, scientists have been transforming these unwanted phenomena into useful technologies and have achieved significant progresses by advancing the understandings on the mechanics of mechanical instabilities [18],[61]–[65]; especially the elastic property on soft materials that enable the state-switch between smooth and instability in a repeated cycle. The instabilities were used to measure material properties [66]–[71], fabricate stretchable electronics [71]–[76], align cells [77],[78], and work on applications for surface chemistry [79], reversibly adhesion [80]–[82], wettability [83]–[86] and microfluidics devices [87]–[89].

Different types of mechanical instability in soft materials are studied in this thesis: wrinkles [90], crease [91] and folds [92]. It is highly possible to access to new model of instabilities because soft material is usually more stretchable

than stiff material, and they have also highly nonlinear properties which are identified in the past several years [93]–[95].The following sections describe the different types of instabilities.

2.2.1 Wrinkle

When an applied in-plane compressive stress is beyond a critical value on a stiff thin layer, strain change leads to the occurrence of an elastic instability and causes out-of-plane buckling film [18]. However, the stiff layer would form a periodic pattern of buckles if this stiff thin plate is coupled on a thick soft elastic substrate. This phenomenon is referred to as wrinkles (**Figure 2.3**) while its critical condition can be determined by a classical linear perturbation analysis [92],[96],[97]. A critical wavelength [98] of

$$\lambda = 2\pi h \left(\frac{\bar{E}_f}{3\bar{E}_s}\right)^{1/3} \tag{2.1}$$

would occur to balance the buckling energy of the film and the stretching energy of the substrate. $\bar{E} = E/(1-v^2)$, is the plane strain modulus [98], with E being the Young's modulus and v being the Poisson's ratio. Thus, $\bar{E}_f$ represents the plane strain modulus of film and $\bar{E}_s$ represents the plane strain modulus of substrate. Critical strain raised with the energy comparison between flat state and wrinkled state [99],

$$\varepsilon_c = \frac{1}{4}\left(\frac{3\bar{E}_s}{\bar{E}_f}\right)^{2/3} \tag{2.2}$$

here the critical wavelength and critical strain of wrinkle has been steadily and extensively investigated by mechanics research, along with the dependence of material property, and the loading conditions including pre-stretch and finite deformation [100],[101]. Wrinkle also has the primary feature of weak imperfection sensitivity and stable amplitude growth, while the characterization has been undertaken in experimental measurement on the film property relative to that of the substrate [66],[102].

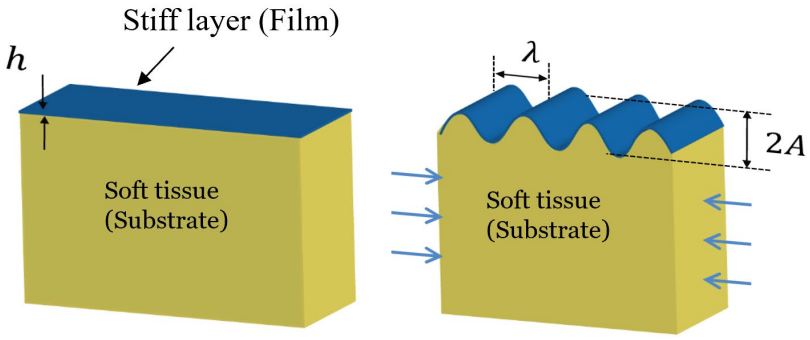

Figure 2.3 Schematic illustrating wrinkle developing in a bilayer system. A stiff film of thickness of h, on top of a soft substrate under compression force. The wrinkle have a wavelength λ and amplitude A.

Short wavelength of wrinkles is favoured by the substrate deformation, whereas the long wavelength is favoured by the bending of the thin plate [93],[103]–[105]. Parallel wrinkles form vertically to the compression direction if the loading is uniaxial [106], however, it can produce complex pattern of wrinkles if the loading is biaxial [61],[97],[107]–[110]. The formation of wrinkles phenomenon was also studied under tensile [111]–[114], shearing [115],[116] and bending [117],[118].

With the flat state as a reference, an incremental boundary value problem is formulated by linear perturbation analysis, and it is corresponded to the onset of wrinkles which brought an eigenvalue problem. The surface instability of a hyper-elastic half space [119] and interfacial instability of two hyper-elastic half spaces were studied by Biot [120] with linear perturbation analysis method. The film and substrate are both considered as linear elastic materials in modelling. The thin film was also assumed to have a thickness much smaller than wrinkles wavelength. Biot predicted the free surface of an elastomeric half-space would be unstable for sinusoidal waves formation when a critical compression strain parallel to the surface reaches 0.46 [119]. However, Biot's wrinkling instability has never been observed. Scientists further developed nonlinear theories of wrinkles that predict the initiation of wrinkles and the growth of wrinkles under small strains [99],[121]–[123].

2.2.2 Crease

As schematic shown in **Figure 2.4**, a creasing instability is a phenomenon when the free surfaces create a sharp self-contacting area when soft elastic materials is under compression beyond a critical value [63],[124]. Different from wrinkle instabilities, crease is a localised deformation and the buckling procedure occurs instantly with irreversibility property.

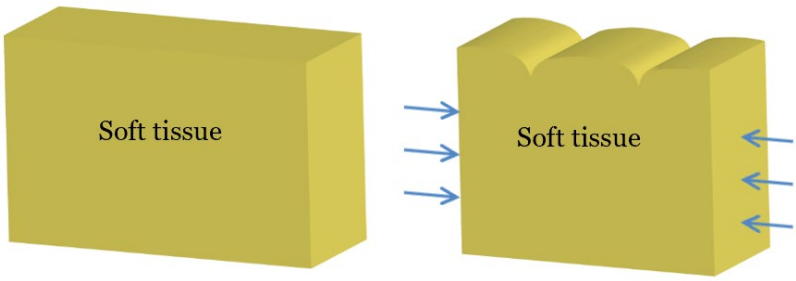

Figure 2.4 Schematic illustrating crease formed in soft elastic materials under compression.

Creasing instability was found with a Neo-Hookean material at a compression strain about 0.35 ±0.07, when Gent and Cho bent a rubber block in experimental test [125]. Later it was proven by the numerical simulations contributed by Hohlfeld and Mahadevan [63], a theoretical understanding of creasing. They introduced a skin layer with finite bending stiffness to provide an energy barrier and break the symmetry balance and create a discontinuous transition between flat state and crease. They found that a Neo-Hookean solid free surface will become unstable at $\varepsilon_c = 0.35$ in plane strain and thus form creases nonlinearly. A pre-pinching method was also used to show the critical strain for creasing *via* a finite element simulation [126].

Biot's solution and creases are two distinct instabilities, shown by Hohlfeld and Mahadevan. Biot's solution corresponds to a smooth, wavy surface at lower strain value and linearized the boundary condition at a state of finite homogeneous. However, crease is a localized self-contact phenomenon at large strain value relative to the homogeneous state (**Figure 2.5**). Crease instability has sharp tips and the cross-section has a very different

shape from wrinkle. It has been observed continually on compressed elastic material achieved by various method, like mechanical stimuli [96],[125],[127]–[130], restrictive swelling [124],[131]–[143], temperature variation [79], electric field [144]–[149], and light excitation [150].

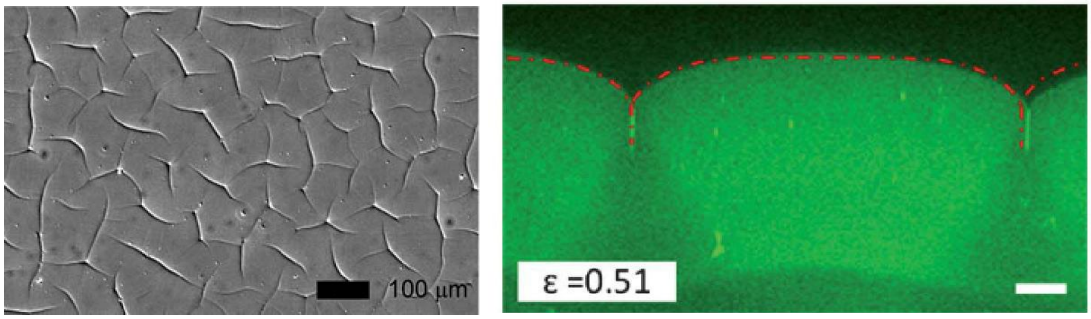

Figure 2.5 Crease instability observed in experiment (a) Crease of a swelling gel due to the constraint of the substrate [124]. (b) Cross-section view of crease [96].

Diab *et al.* found that the crease localization is a form of instability from wrinkle state or fundamental state [151],[152]. A barrier is added to the nucleation of crease by surface energy, which makes the nucleation sensitive to defect [119, 138]. Thus, a consequence of bifurcation was revealed by the snap buckling of crease which is a state-switching between subcritical and supercritical [63],[126],[153]–[155]. This can be explained by the hysteresis of crease that appeared and disappeared, corresponding with the applied compressive strain increases and decreases, when crease on top of a surface free from traction and have finite thickness [154]. For another aspect, despite the reversibility of local deformation is elastic, the hysteresis is still exhibited by the global irreversibility during loading and unloading [63],[152]. However, if the external loading is an electric field, the formation of crease, or wrinkle, is dependent on

the elasto-capillary number [146]. Soft tissue is one of the subjects that could take advantage of crease [43],[46],[48], and the crease has been connected with the appearance of Schallamach waves on a rubber against a solid surface during the frictional sliding [156]. Crease can be put into a range of applications, such as the control of chemical pattern[79],[150], biofouling [157], adhesion [158] and the behaviour analysis of cellular organism [159].

2.2.3 Fold and Ridge

Wrinkle is formed with the compressive force reached to a critical value at a bilayer system that contains a stiff thin film set on top of a soft thick substrate. A secondary bifurcation, which varies depending on the substrate property, can occur if the compressive force keeps increasing. Once the bilayer system is compressed far beyond the critical value of wrinkle, then localized fold formed because there is no mismatch stress between the film and substrate at this point (**Figure 2.6a**) [62],[64],[91],[160]–[163]. In other words, the fold is formed from wrinkle at higher amplitude aspect ratio for self-contact if the amplitude of wrinkle keeps growing. Here the higher amplitude aspect ratio means the wrinkle amplitude is in a much large value compared to the wrinkle wavelength.

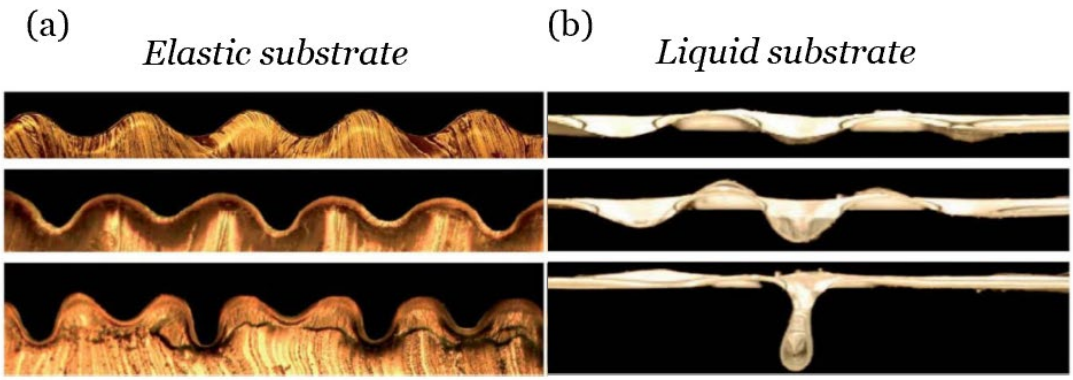

Figure 2.6 Fold instability. (a) Progression of the folds with increase of strain from top to bottom when the substrate is an elastic solid [162] (b) Progression of the folds with increase of strain from top to bottom when the substrate is a viscous liquid [91].

The fold can be set periodically by the period multiplication of wrinkle and then leads to the localization of fold subsequently. That is when wrinkle up against the appearance of sub-harmonic modes due to the nonlinearity of elastic response and since loses its initial periodicity [64],[164]. Normally, a period-doubled state is developed first from wrinkle state, followed by a period-quadrupled state, and finally the formation of self-contacting folds [64],[160],[162]. When the wrinkle surface starts the self-contact progression for folding, a few selected fold tips initiate the advancing into substrate with several of unfolding surround the folds, causing the localization of fold. Localized folds can be manipulated by the patterns of the substrate [165], even when the substrate is in liquid format (**Figure 2.6b**) [91],[166],[167] or elastic foam [168]. Folding is relevant for the fabrication of nano-structured surfaces, several research groups have investigated a variety of characterisation methods for folding process, such as wrinkle period multiplication on bilayer system [64] and water floated elastic film [91]. Sun, *et al.* has revealed the nonlinearity of

substrate during the winkle post-buckling evolution with a numerical method for fold[160], and followed by further investigation by Zhao, *et al* [169] and Hutchinson [94]. But the critical conditions for large amplitude wrinkle evolution is still un-clear.

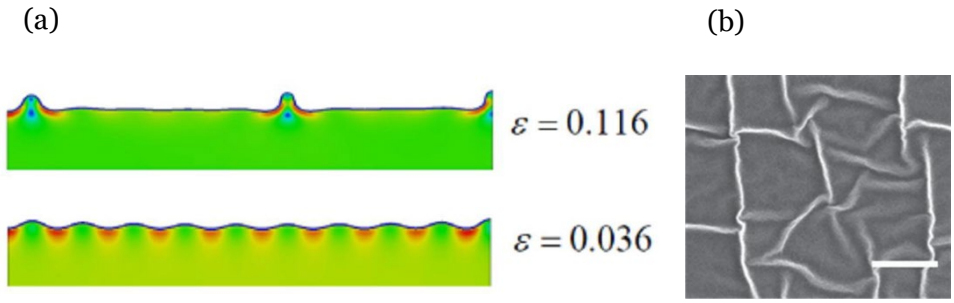

Figure 2.7 Ridge instability. (a) Simulation result showing the cross-section view of a secondary bifurcation from wrinkles to ridges [92]. (b) Experimental results showing the top view of ridges [170].

Similar to crease of a localised and irreversible hysteresis behaviour, ridge instability is normally formed as the secondary bifurcation on a compressed surface layer by releasing a highly pre-stretched substrate (**Figure 2.7a**) [92],[97],[170]–[172]. The morphology of ridge and fold is very different although they are both localised structures. Ridge buckles outward and bring the surface upward, while the fold developed inwards and collapse the surface inside (**Figure 2.7b**). The structural evolution of ridge is generally irreversible with a snap buckling process, and ridge is easy to develop into a ridge-folds state at large strain of a compressed surface [169]–[173]. However, fold occurs as a secondary bifurcation from wrinkles if the substrate has no pre-stretched tension [64]. Ridge instability can be explained by the nonlinearity of

elastic substrate and it was first predicted in a numerical simulation [92], and then was found in experiments [97],[170]–[172].

Table 2.1 Summary of surface instabilities between wrinkle, crease, fold and ridge.

	Description	Schematic
Wrinkle	Periodic waves formed from the top stiff layer in a bi-layer system when it encountered a compression force above critical value.	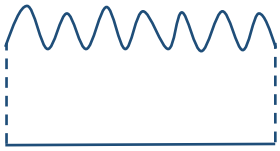
Crease	Localised deformation of a sharp self-contacting area when soft materials under compression force above critical value.	
Fold	Formed from wrinkle at much higher amplitude wavelength where no modulus mismatch between two layers because compression force far beyond the critical value.	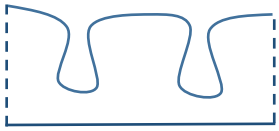
Ridge	Different from fold, ridge buckled outward and bring the surface upward when it under compression force.	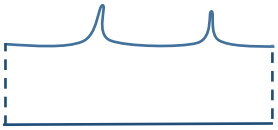

2.3 Studies on Switchable Surface Wettability

2.3.1 Contact Angle

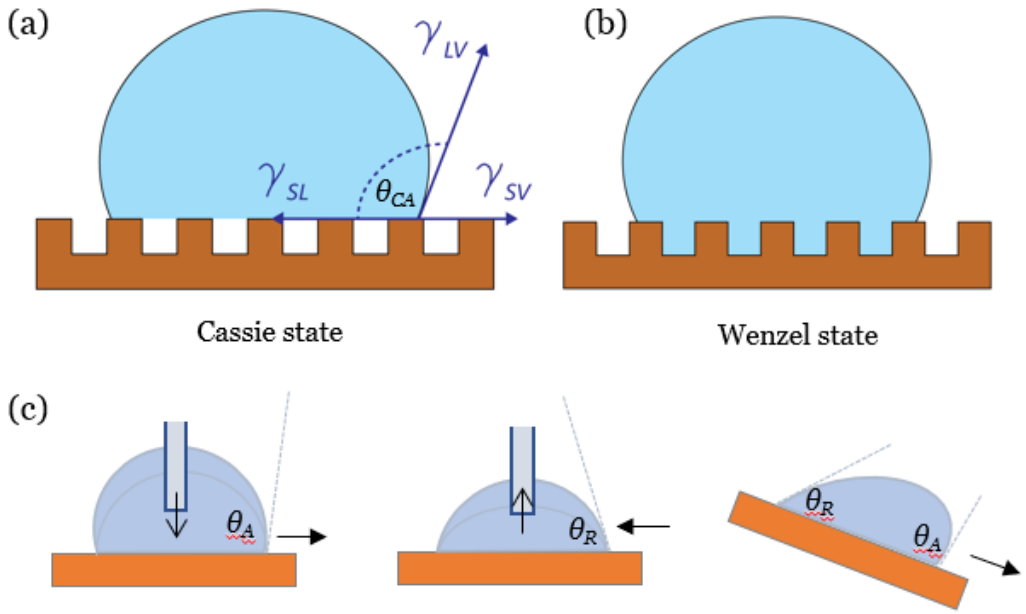

Figure 2.8 (a) Illustrations of surface wettability defined by contact angle, and a "Cassie" state (b) A droplet in a "Wenzel" state (c) Advancing and receding contact angle measurement

When a liquid droplet is placed on a solid surface, there is a balance between the three interfacial phases, liquid (L), solid (S), and vapour (V), where the interfacial energy of γ_{SV} (solid-vapour), γ_{SL}(solid-liquid), γ_{LV}(liquid-vapour) determines the droplet state whether it should spread out into a film or remain as a droplet. If it remains as a droplet, there exists a contact angle (θ_{CA}) at the edge of the droplet, where it is measured between the liquid-vapour (LV) and solid-liquid (SL) interfaces at the three phase contact-line (**Figure**

2.8a). The equilibrium contact angle θ_{CA} can be determined by Young's Equation [174]:

$$cos\theta_{CA} = \frac{\gamma_{SV}-\gamma_{SL}}{\gamma_{LV}}, \quad (2.3)$$

If the droplet contact angle is smaller than 90°, the surface is considered as hydrophilic. If the contact angle is larger than 90°, the surface is hydrophobic. Highly hydrophobic surfaces made of low surface energy materials may have water contact angles around 120°.

2.3.2 Contact Angle Hysteresis

Inspired by the lotus leaf, hydrophobic surface with a bio-mimic self-cleaning function, where combination of low-surface energy and surface roughness leads to the hydrophobic property [175]. Surface wetting behaviour can be greatly influenced by surface roughness [176]. If the surface is hydrophobic, adding roughness makes it more hydrophobic. On the contrary, if the surface is hydrophilic, it masks it more hydrophilic. It is important to understand the behaviour of liquid on different topographic surface because the surface roughness plays a key role in surface wetting property. Typical wetting states of hydrophobic surface include "Cassie-Baxter" state [174] and "Wenzel" state [177]. "Cassie-Baxter" state is when a droplet places on the top of surface roughness and leaving an interface of solid-liquid and liquid-vapour below it (**Figure 2.8a**). "Wenzel" state is where a liquid stick to the surface and maintains contact with the entire surface roughness (**Figure 2.8b**). It is

not easy to describe the local contact angle in either “Wenzel” state or “Cassie-Baxter” state as the surface is no longer flat. Therefore, with these two-ideal descriptions of liquid behaviour on rough surfaces, wettability of a roughness surface can also be described in terms of contact angle hysteresis.

If a droplet is placed on a surface with certain roughness feature, and same droplet liquid is added slowly inside, the water droplet volume starts to expand. As the volume increases, the contact angle also increases and reaches a critical value (θ_A) where the three-phase contact line experiences a sudden outward motion. This threshold value θ_A is referred as advancing contact angle (**Figure 2.8c**). Reversely, decreasing the water droplet volume will make the contact line recede suddenly at some point, the contact angle before the movement is called the receding contact angle (θ_R). The difference between advancing and receding contact angle is known as the contact angle hysteresis [178]. In Wenzel state the liquid penetrates surface asperities resulting in a high contact angle hysteresis. In Cassie state the liquid only contacts the top surface of asperities therefore it has a low contact angle hysteresis. On the other side, it is common to have different contact angles at the front and rear edge of a water droplet sitting on a tilted surface (**Figure 2.8c**).

To achieve topographical surface with desired wettability performance, composite methodology has been explored such as lithography, plasma techniques, electrochemical method, electrospinning techniques, low-surface energy coating, etc [179]. It was found that geometric morphology, surface

microstructure and molecular properties characteristics contribute mainly to the control of smart surface wettability [85],[180],[181].

2.3.3 Anisotropic Droplet Shaping

The non-uniform distribution of surface energy is an expression of anisotropic wetting of droplet deformation, where the wettability directional dependence acts as the asymmetric chemical or physical chemical patterns on a material's surface [182]. Different from isotropic wetting where wetting properties are identical in all directions, the anisotropic wetting may need additional information for wetting characterisation [183]. In this case, different contact angle measurement along perpendicular and parallel direction to the surface features can be exhibited from an anisotropic surface droplet with chemical or topographic features (**Figure 2.9a**) [89].

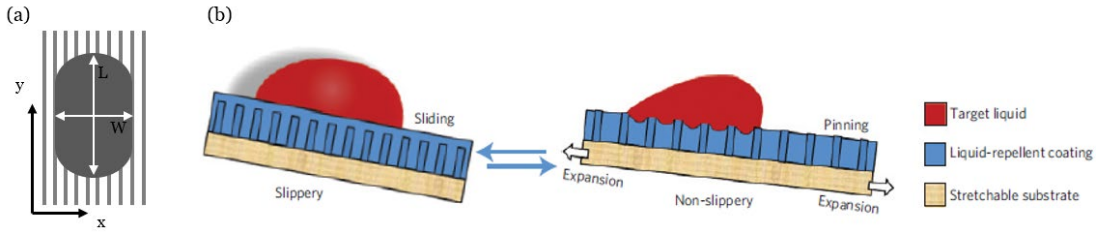

Figure 2.9 (a) Anisotropic droplet on grooved surface [89]. (b) Droplet sliding on un-stretched surface and pinned by stretched surface with patterned features uncovered [184].

Droplet motion control on solid surfaces has become an indispensable technology in various industrial areas include hydrophobic coating, electromechanical system and micro-chip architectures [185],[186]. It is well

known that micro patterned surfaces with different wettability can provide wetting anisotropy which is depended on surface topography and chemical composition. Surface topography is a reliable parameter to control a wide range of smart surface functions such as wettability, adhesion, cell patterning and optical reflection. Aizenberg Group [184] in Harvard University have approached a method to manipulate the mobility of droplet dynamically by using a liquid infused system. The stretched film with liquid-repellent coating forms a wavy surface morphology by uncovering the solid pattern features which will stop the droplet from sliding (**Figure 2.9b**) [184].

2.4 Theoretical Understanding on Analytical Method

Over the past decade, researchers have revealed various characterisation on one dimensional (1D) surface instability structures with analytical method on solid-surface deformation under in-plane compression [64],[125],[160],[173],[187]. The characterization of morphology of the surface instabilities also found useful for a series of technological applications [23]–[25],[188]. A bi-layer system of a thin film on an elastic substrate under compression, a variety of surface instabilities developed if the mismatch modulus existed between the film and the substrate. Bi-layer system produces comparative simple surface instabilities phases, which include single- or multi-mode wrinkles, creases, folds and ridges. Investigations of instabilities phase transitions enable us to understand the formation process of biological and geological structure [189],[190]. Accurate control of self-organizing instabilities

phase could help us to create unprecedented properties material by folding 2D material structures [191].

Here, the basic bi-layer system, among variable combinations of film/substrate geometries and soft elastic properties, was considered as neo-Hookean material model. To simulate soft material, hyper-elastic model was aimed to use. If the material is assumed to follow incompressible neo-Hookean material model, the strain energy expression represented here as:

$$W = C_1(\bar{I}_1 - 3), \tag{2.4}$$

where C_1 ($C_1 = \mu/2$) is the material parameter which contains shear modulus (μ) of the material, and $\bar{I}_1$ represents the first deviatoric of strain invariant.

However, when a bi-layer is gradually compressed, the film on the top buckled to form a periodic wrinkle, depending on stiffness ratio between film and substrate. A phase diagram is represented by collecting the instabilities phase on a plane of elastic stiffness ratio (or instability wavenumber) versus the compressive strain [151][152][127], similar to the *material phase diagram* that phenomenological descripted its minimum free energy for various equilibrium phase [192].

In general, stiffness ratio and the film property decide the instability wavenumber when normalized by the film thickness. But the normalized wavenumber of bi-layer is conducted by the modulus ratio. In particular, the

dependence of the normalized wavenumber on the stiffness ratio is converted to [92],[94],[160],

$$\bar{k} = \frac{2\pi h}{\lambda} = \left(\frac{3\mu_s}{\mu_f}\right)^{1/3}, \tag{2.5}$$

for $\frac{\mu_s}{\mu_f} \ll 1$, where λ is the wavelength, μ_s and $\mu_f$is the shear modulus of the substrate and film. The above equation not only represents the stiff-film bi-layer wavenumber, but also a convenient modulus-ratio index. All bi-layer instabilities phases can be plot in a bound plane of ($\varepsilon, \bar{k}$), where ε represents the applied compressive stain on bi-layer. By employing finite element analysis, bi-layer instabilities phase diagram can be built with instability evolution under compression, while the instabilities localizations, irreversible transition and substrate mismatch strain effect on the bi-layer could be observed with the phase diagram.

Finite element analysis is used to perform the simulation of surface instabilities phase development by linking the strain deformation in bi-layer system under lateral system. If the material considered as compressible neo-Hookean constitutive model, both the film and substrate will be adopted with same shear modulus. With this setting, the strain energy expression is expended as [193]:

$$\mathrm{W} = C_1(\bar{I_1} - 3) + D_1(J-1)^2, \tag{2.6}$$

where *D1* is the incompressibility parameter, and *J* is elastic volume ratio.

2.5 Summary

This chapter has introduced the background of surface instabilities as an aspect of functional smart surface that behave topography phenomenon, and surface wetting concept that is possible induced by the geometrical surface structure or surface chemical treatment. Moreover, the basic theoretical understanding on analytical method based on a bi-layer system was reviewed. Possible material selection was also presented with general FEA package requirement. More specific background is included in the following chapters.

Chapter 3

Experimental Methods

This chapter summarises the general experimental methodologies used throughout the project, including fabrication process for functional micro-structure surface and the characterization method used for investigation.

3.1 Fabrication Method

Micro-engineering and surface treatment of pattern template: Structural patterned template of SU-8 micro-cylinders on silicon wafer was obtained through standard photo-lithographic fabrication technique in cleanroom at Durham University. The masks were manufactured from external company. Templates with different lattice arrays (square and centered square) and various aspect ratios were prepared. A small portion (≈1ml) of Trichloro(1H,1H,2H,2H-perfluorooctyl) silane (Sigma-Aldrich), was applied from vapour phase at 20 °C for 30 min to facilitate subsequent release of the PDMS film.

Fabrication of Structural Confined Elastic Bilayer: The mounting layer was made from a commercially available elastomer product (Elite Double 22, Shear modulus ≈ 0.35 MPa) from Zhermack Ltd. After mixing the vinylpolysiloxane base with curing agent with a weight ratio of 1:1 for 1 minute,

the mixture was cured in the petri dish at 20 °C for 30 minutes. The cured elastomeric film was ≈ 2 mm in thickness, and a stripe of ≈ 10×30 mm was cut and pre-stretched to 600% of its original length on a uniaxial mechanical strain stage. The soft PDMS layer with thickness of 125 μm (Sylgard 184, Dow Corning, 30:1 for elastomer base : crosslinker) was prepared by spin-coating the degassed mixture on a SU-8 patterned silicon wafer (≈ 1 cm^2) at 1000 rpm for 120 s, followed by curing at 70 °C for 1 h. An adhesive PDMS layer with the same composition of 30:1 was spin-coated on this cured layer at 3000 rpm for 120 s, to bond to the mounting layer. After transferring the adhesive coated soft PDMS layer to the mounting layer, the assembly was baked at 70 °C for 8 h to cure the adhesive layer. Prior to characterization, the bilayer was treated with oxygen plasma (HPT-100, Henniker) under a working power of 100 watt, with a mixed gas atmosphere of oxygen/nitrogen ratio ≈ 0.2.

3.2 Characterization Method

Two characterization methods were introduced here for Chapter 4 and Chapter 5. The strain was applied by releasing the pre-stretched mounting layer with mechanical strain stage.

Characterization 1: The bilayer was progressed to measurement as soon as the oxygen plasma treatment is completed. Incremental deformations in nominal strain of ≈ 0.004 were applied to the sample by releasing the mounting layer pre-stretched by a fixed amount at regular intervals and

situated for 15 min in room temperature. Sample surfaces were observed in situ using an upright optical microscope (Nikon LV-100) in brightfield reflection mode. For the laser scanning confocal microscopic imaging (Nikon A1R), the top layer was labelled by adding a small amount of fluorescent monomer (0.1 mg fluorescein-o-acrylate per 1 g PDMS). Scanning electron microscopy (MIRA3, TESCAN) was used to observe the surface structure. The surface topographic features were assessed with an atom force microscopy (D3100, Veeco). Thickness of the plasma treated PDMS was measure with surface roughness profiler (BRUKER DektakXT). And the out-of-plane measurement was carried out with laser scanning confocal microscopy (Nikon A1R)

Characterization 2: The experiment was carried out immediately after the oxygen plasma treatment. A 2 μl deionized (DI) water droplet (dyed with red food colour gel, Dr. Oetker, at a weight ratio of 10:1) was deposited on the sample surface using a micropipette. Incremental deformation in nominal strain of ≈ 0.04 were applied to the sample by releasing the pre-stretched mounting layer (Elite Double 22, Zhermack Ltd) by a fixed amount at regular intervals. 2D profiles of the droplet was recorded in situ using both an upright optical microscope (Nikon LV-100) in brightfield reflection mode and a digital camera (model D3200, Nikon) with a macro lens (model 105mm 1:2.8, SIGMA). Static contact angle (CA), advenceing CA and receding CA value of droplet was measured using a Droplet Shape Analyzer (DSA30S, Kruss). The surface topographic features were assessed with an atom force microscopy

(D3100, Veeco). Laser scanning confocal fluorescence microscopy (Nikon A1R) was used to observe the droplet shape in 3D by dyed it with Fluorescein isothiocyanate-dextran (SIGMA) at a weight ratio of 1000:1.

3.3 Numerical Simulations

The numerical analysis used a finite element package in Mathematica to solve the 2D plain-strain linear elasticity problem for the deformation in the patterned soft substrate. A repeatable 2D unit cell was first defined with the geometry corresponding to the experiment and, as seen in **Figure 3.1**, the domain by a fine mesh consisting of around 4000 triangles was described.

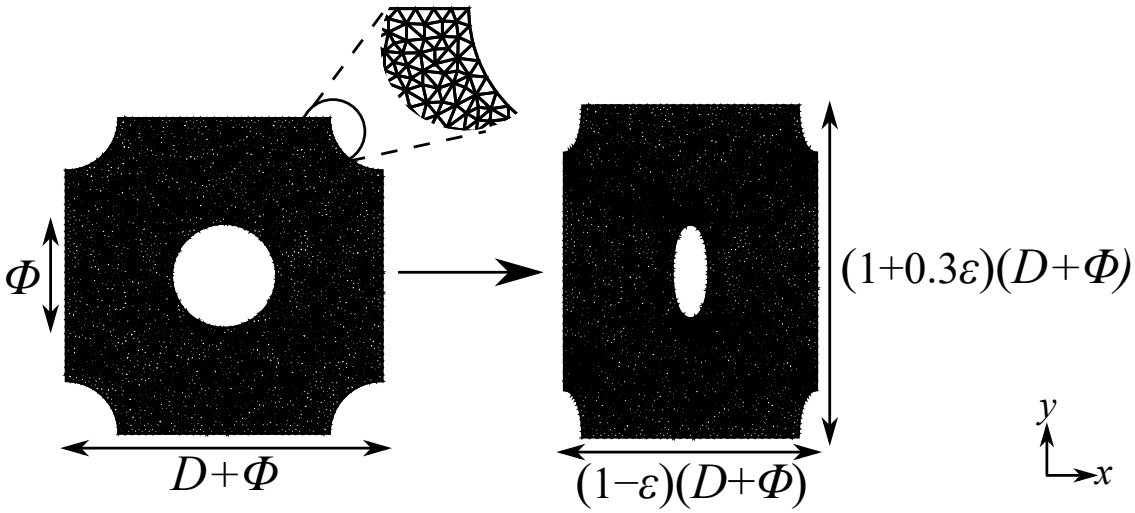

Figure 3.1. Discretized mesh elements for the numerical analysis of a unit cell: (left) non-deformed unit cell, (right) deformed unit cell with a macroscopic strain ε=0.2.

A plain-strain deformation was then assumed, described by the 2D displacement field $(u(x,y)\,\hat{\boldsymbol{x}} + v(x,y)\,\hat{\boldsymbol{y}})$ so the plain-strain stress tensor is

$$\sigma = \frac{E}{(1+\nu)}\begin{pmatrix} \frac{(1-\nu)u_{,x}+\nu v_{,y}}{(1-2\nu)} & \frac{u_{,y}+v_{,x}}{2} \\ \frac{u_{,y}+v_{,x}}{2} & \frac{\nu u_{,x}+(1-\nu)v_{,y}}{(1-2\nu)} \end{pmatrix}, \tag{3.1}$$

where E is the Young's modulus, ν is the Poisson's ratio, and the comma-notation denotes partial derivatives. The Mathematica finite element package was then used to solve $\boldsymbol{\nabla} \cdot \sigma = \mathbf{0}$ in the meshed domain, subject to the boundary conditions that $\sigma.\hat{\boldsymbol{n}} = \mathbf{0}$ on the hole edges, and that the straight edges of the cell move with the macroscopic strain of the underlying substrate (-ε in the x-direction and 0.3ε in the y-direction) as seen in **Figure 3.1**.

After solving the displacement fields, the stress on the film can be evaluated from the stress tensor above. To determine whether the region is unstable towards wrinkling, we diagonalized the stress tensor to find its maximum compressive stress. By comparing this compressive stress with the theoretical critical value, we can identify the wrinkling region, while the wrinkle direction is perpendicular to the principal direction of the maximum compressive stress.

For 3D numerical analysis, simulation package of ANSYS Workbench was used. On soft elastic surface material, both wrinkles and creases can be described as a state of homogeneous deformation undergoes terms of field variables of specified points called nodal points or nodes. A mathematical description of strain at any point in the element with nodal displacement is

$$\{\varepsilon\} = [B]_e\{\delta\}_e \tag{3.2}$$

where $\{\varepsilon\}$ is strain at any point in the element, $[B]_e$ is strain displacement matrix and $\{\delta\}_e$ is displacement vector of nodal values of the element [194]. Once the element properties and boundary conditions are imposed to assemble global properties to get system equation. The solution of these system equations gives the nodal values which can be combined with additional calculations to describe and predict the elastic surface pattern transitions under the compressions.

The material selection was decided on the linear and non-linear procedure that include a compressive neo-Hookean model for non-linear progress, as shown blow:

$$\mathrm{W} = C_1(\bar{I}_1 - 3) + D_1(J-1)^2, \qquad (3.3)$$

where *C1* is the material parameter, $\bar{I}_1$ represents the first deviatoric of strain invariant, *D1* is the incompressibility parameter, and *J* is elastic volume ratio.

Chapter 4

Spatially Configuring Wrinkle Pattern and Multiscale Surface Evolution with Structural Confinement

4.1 Introduction

Elastic instabilities such as wrinkles, creases and folds, are usually considered as unwanted when they appear in engineering structures, as they can precipitate fracture and failure. Recently, scientists have significantly advanced our understanding of the mechanics of elastic instabilities [18],[29],[61]–[65],opening the possibility of transforming these unwanted phenomena into tools for producing useful shape changes in response to a range of external stimuli [148],[195]–[199]. The latter perspective has enabled engineering opportunities containing conceptual self-adaptive/autonomous structures in low dimensions and has implications in many different contexts such as micro-/nano-fluidics [200]–[202],flexible electronics [130][23], adhesion [80][81], organic solar cells [76], tunable optics [203]–[205], wettability [89][86][206], and promising methods for surface patterning [61],[79],[207]–[209]. While our scientific/technical understanding has advanced, there remains much to be explored about the

control of instability morphology, and in particular how to configure the instabilities, such as wrinkling and creasing, to desired patterns with selective distribution covering the surface and bespoken thresholds for the formation and evolution of instabilities.

When compressing a bilayer elastomer system with a stiff skin layer, the formation of surface wrinkles releases in-plane compression of the stiff layer, as bending is energetically more favourable than compression. With further compression, the wrinkles experience further bifurcations, including period-doubling and quadrupling [64][210], and turn into deep folds/creases [151],[169],[211]. These wrinkling and post-winkling behaviours have been well understood by considering the intrinsic material properties of a bilayer (module mismatch, Poisson's ratio, etc), structural variables (thickness) and the pre-strains imposed on the system. However, thus far, such compressive instabilities have been studied in non-patterned surface systems, where both wrinkling and further bifurcations occur as global events, spanning the entire surface at once. Notably, Huck and co-workers investigated the spontaneous formation of patterns of aligned buckles on a flat gold/PDMS bilayer with placed confinement [212]. Kim and co-workers studied the morphological transitions on the surface of a bilayer under a biaxial compressive stress and revealed a mechanism to controllably generate a 2D wrinkle/fold pattern on the entire film surface [62]. Wang and Zhao have summarised the instability bifurcations on flat surfaces and generated a phase diagram by considering the geometrical variations and module mismatches [213][214]. Recent work has also studied

bilayer instabilities on surfaces with curvature [108],[215]–[217], where wrinkling is still a global event, but where the pattern and threshold are influenced by the curvature. In this chapter, the investigation focuses on whether the wrinkling and further bifurcation in patterned sub-regions of a bilayer can be induced by explicitly patterning the surface, thus paving the way for bespoke instability morphologies at bespoke thresholds.

Such controllable formation and development of instabilities in targeted regions are highly desirable for engineering applications such as a strain sensing structures, actuating units in wearable devices, healthcare devices, bio-fluidic devices, etc. In this chapter, a simple strategy is demonstrated to initiate 2D harmonic surface wrinkle patterns and targeted morphological transitions on the surface of an elastic bilayer under uniaxial compressive stress, by employing structural confinement (Bravais lattice holes) to regulate the in-plane stress map on a surface. The regions adjoining the Bravais lattice holes nucleate harmonic wrinkle networks at small compressive strains due to the confinement. At higher compression, the wrinkle-crease transition is initialized at selected areas with strain energy localization guided by the curved geometrical boundary from the edge of Bravais lattice holes, which then finally leading to a global creasing. The dynamics of the formation of planar wrinkle patterns and localised wrinkle-creasing transition are studied, and a distinct kind of stepwise instability pattern evolution is illustrated towards a hierarchical surface. The numerical simulation is also

combined with experiments to track the in-plane stress state and study the generation of harmonic morphology under the confinement.

4.2 Results and Discussion

4.2.1 Formation of Surface Instabilities with Confinement

The Bravais lattice (named after Auguste Bravais, a set of discrete arrays with certain distance) template was prepared by lithographically fabricating SU-8 pillars on a Silicon wafer (**Figure 4.1a**). The Bravais pattern was then transferred to a soft substrate by coating the template with a thin (125 μm) layer of softer PDMS (shear modulus ≈ 0.1 MPa), which was then cured on a substantially pre-stretched elastic 'mounting' base layer (thickness ≈ 3 mm, Shear modulus ≈ 0.35 MPa). After curing, the PDMS structure was released from the template, aided by a salinization treatment applied to the template to reduce surface adhesion. Under compression, patterned surfaces composed of polygonal shape, i.e., triangles, squares, etc., can yield strain energy concentrations and localised bulk deformations around the corners, making it difficult to reach the energy threshold to trigger the surface instability. Therefore, patterned surface with circular (hole) shape was used to avoid the strain energy localization and also expected that the curvatures can be used to regulate the formation of instability. Two different Bravais lattices (**Figure 4.1b–e**), square and centered square, were employed with various geometries, hole diameter (Φ), hole distance (D), hole depth (h), to establish a range of

patterned soft surfaces, where the ratio between distance and diameter represents the aspect ratio (D/Φ). Finally, oxygen plasma treatment was used to create a thin stiff layer on the patterned soft substrate (**Figure 4.1f**) prior to the compression.

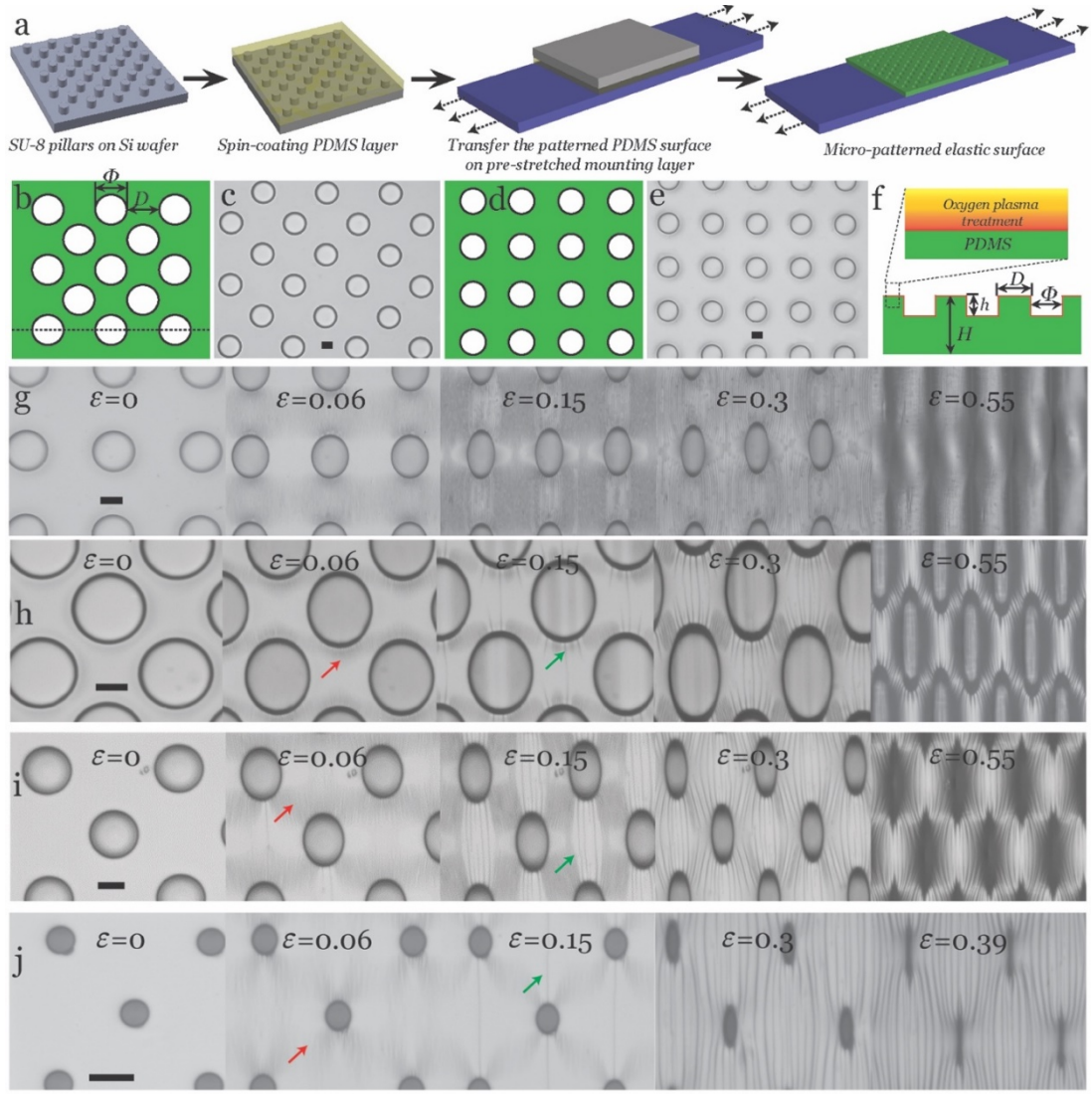

Figure 4.1. Illustration of design and fabrication process of structural confinements and guided formation of surface morphologies under compression. (a) The structural surface was fabricated by spin-coating a thin PDMS precursor layer on lithographically made template (SU-8 pillars array on a silicon wafer), then transferring and curing the thin PDMS layer (≈ 125 μm) on the top of a

pre-stretched mounting elastomer layer with thickness ≈ 3 mm. Two in-plane arrays with varied aspect ratios are designed, (b) illustration and (c) optical microscopy for centered square lattice array, (d) illustration and (e) optical microscopy for square lattice array. (f) The micro-fabricated surface was treated with oxygen plasma to achieve a stiff skin layer (≈ 50 nm). (g) The observation of surface morphology changes on square lattice array patterned surface at different compression level. (h-j) The observation of surface morphology changes on centered lattice array patterned surface at the same compression sequences in (g) with different aspect ratios. The wrinkle patterns are marked with red arrows and creases are marked with green arrows. All images in this figure have been formatted with same scale bar of 20 μm.

Upon subsequent release of the mounting layer from a pre-stretched length L_0 to a length L, the patterned PDMS layer is under compression, which the nominal (far-field) uniaxial compressive strain $\varepsilon = L_0/L - 1$ is characterized. The oxygen plasma effect was examined on a surface with pattern features of D =160 μm, Φ = 80 μm, h =20 μm. For surfaces without plasma treatment, the holes slowly closed as the compressive strain increased, but no surface wrinkling was observed. In contrast, on the plasma treated surface, a series of patterned surface instabilities was observed as compression increases, starting with winkles formed at $\varepsilon \approx 0.04$, then in-plane wrinkling bifurcation (period doubling) occurs at $\varepsilon \approx 0.08$, followed by the nucleation of creasing (wrinkling-creasing transition) at $\varepsilon \approx 0.1$, and global creasing at $\varepsilon \approx 0.3$, and finally the closure of lattice hole at $\varepsilon \approx 0.55$.

The morphological development of the surface was characterized under reflected light optical microscopy to study the dynamic surface evolution with different lattice arrays. A series of observations were made at the same strain

sequence to reveal surface states at the same deformation level. For the pattern with a square lattice (**Figure 4.1g**), the in-plane wrinkle pattern appears to be lateral straight stripes and does not changing much with different aspect ratios (D/Φ) (**Figure 4.2**). For the pattern with centered square lattice, the case is more interesting, and three types of in-plane wrinkling patterns are formed at small compressive stress with a high sensitivity to the aspect ratios of lattice that applied. For $D/\Phi = 1$, an in-plane curved stripes pattern is developed with a strong dependency on the local curvature determined by the lattice hole and aspect ratio of lattice array (**Figure 4.1h**). Straight wrinkle stripes pattern is evident when the $D/\Phi = 2$ (**Figure 4.1i**), which is similar to the surface patterned with square lattice. However, an in-plane 'star' wrinkle pattern is generated for $D/\Phi = 4$ (**Figure 4.1j**), the wrinkle morphology shows a 2D periodic distribution around each hole with a 'star' shape, implying a diagonal strain energy localization.

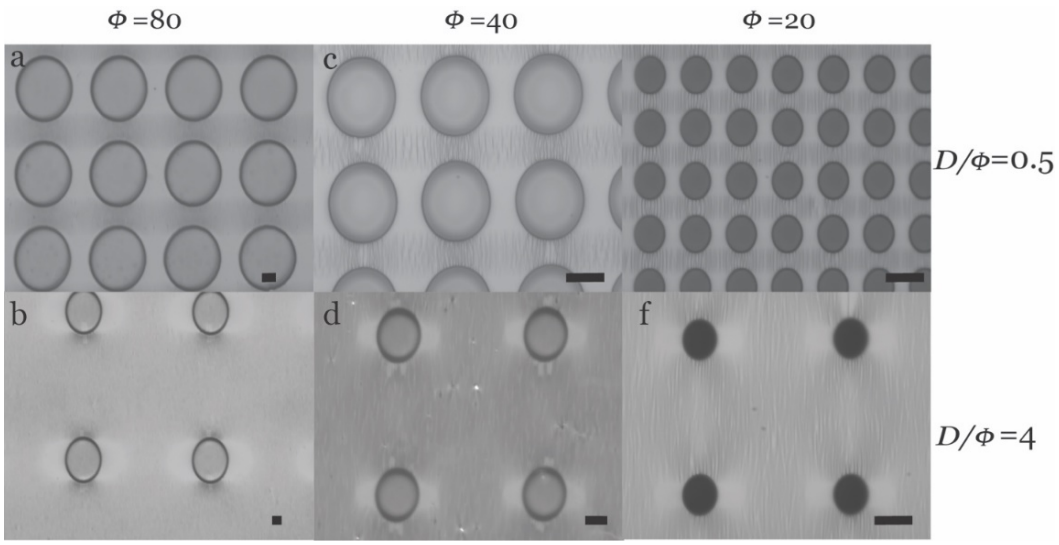

Figure 4.2. The formation of the lateral wrinkle pattern for the square lattice patterned surface with different geometrical aspect ratio.

At higher compression, all patterned surfaces develop morphological evolutions showing a wrinkle-crease transition, the surface creases nucleate at the edge of lattice hole perpendicular to the compression direction at $\varepsilon \approx 0.06$ - 0.013. The creases progress as the compression increases, then fully cover the surface at $\varepsilon \approx 0.3$. Among these morphological transitions, an interesting phenomenon is discovered that a single crease can be generated on the surface with centered square lattice holes (D =80μm, Φ = 20 μm, h =20 μm). This has great potential to enable new types of surface actuator with targeted compression effects within the scale of a few micrometres. It should also be noted that the critical strains for initializing the transition ($\varepsilon \approx 0.06$ - 0.013) are much lower than the typical critical strain value of $\varepsilon_{crease} \approx 0.35$-0.55 [18][65]. The reason is that the nominal strain level used as a control parameter does not well reflect the strain localization on the structural confined surface. The strain energy localization at a curved boundary near a hole edge for a patterned surface could be several folds of that on a non-patterned surface.

4.2.2 Numerical Analysis of Surface Instabilities

To understand the instability patterns (**Figure 4.3a-4.3c**) and thresholds observed above, a numerical analysis was conducted by calculating the pattern of deformation under the imposed global compressive strain for lattice patterned surfaces (**Figure 4.3d**). Deformation around a single hole and square/centered square arrays of holes has been previously studied within linear elasticity [92],[218], and generally produce stress concentrations near the holes. To generalize these results to the lattices, the patterned substrate was

modelled as a linear-elastic 2D plane-strain system consisting of an infinite incompressible elastic material containing the appropriate infinite lattice of holes. As seen in **Figure 4.3e**, a square unit cell of the resulting system (centered square patterned surface) is considered, and Mathematica finite elements was used to solve the plane strain field in response to an imposed compressive strain, ε_{plain}, in the x direction and, as measured in experiments, a sympathetic extension of 0.3 ε_{plain} in the y direction, and with stress free boundary conditions at the edges of the holes.

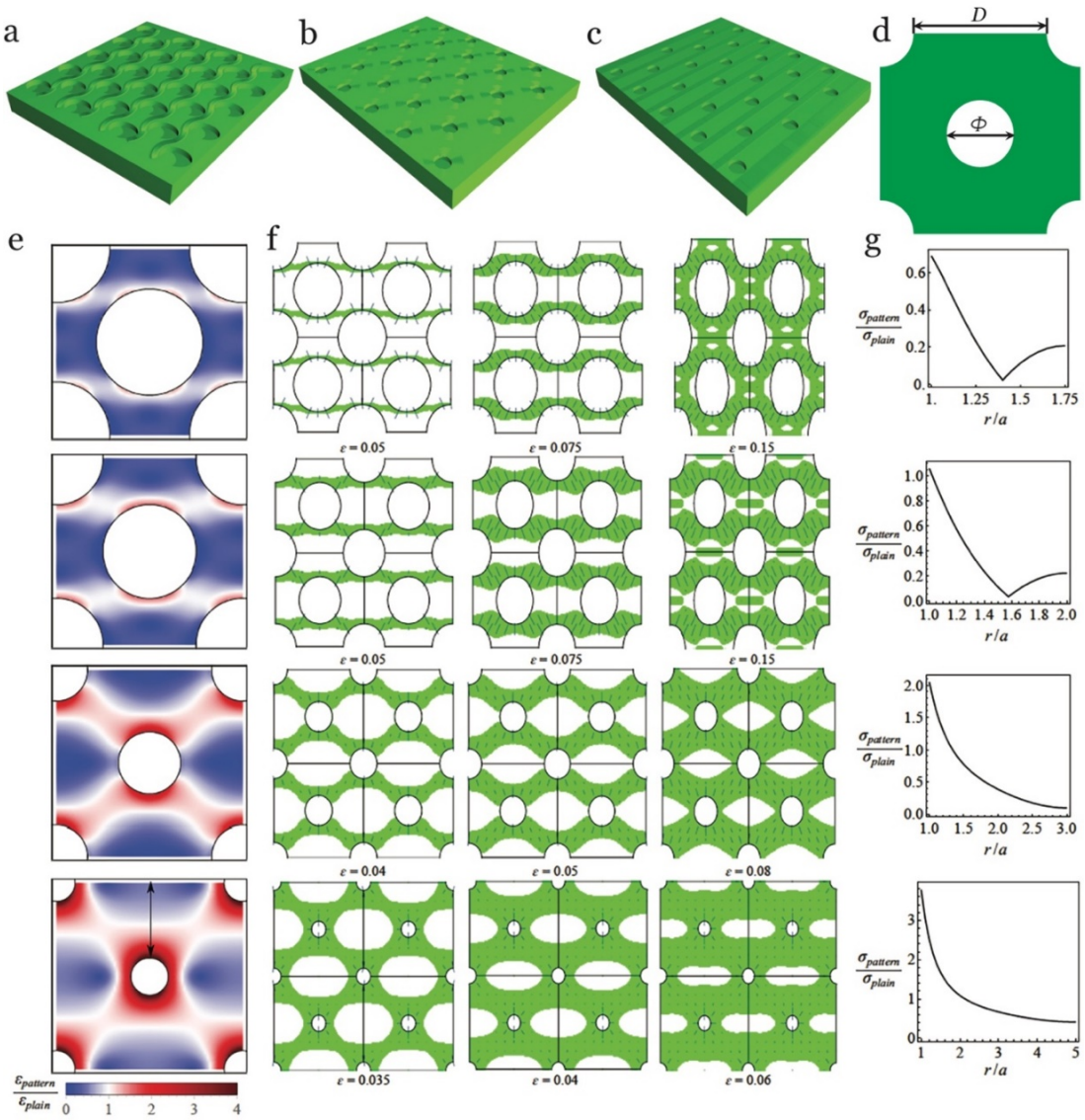

Figure 4.3. Analytical approach of the generated harmonic winkle patterns. Three harmonic patterns are generated as (a) curved ribbon, (b) star shape, (c) straight belt. (d) A representative unit area is chosen for numerical analysis. (e) Compression of the patterned substrate relative to the compression of the non-patterned substrate. Blue and red indicate the less and more compressive areas. (f) Evolution of wrinkling region as a function of applied strain in the deformed bilayer system with patterned holes. Green areas are the wrinkling regions. Lines indicate the direction along which the wrinkles will grow while their lengths are the relative distance from the wrinkling threshold. (g) Compressive stress in the stiff layer in the patterned bilayer system relative to the non-patterned system values at different position from the rim of the hole of radius a (maximum stress) to the edge of the unit cell (see arrow in (e) bottom). All plotted with D/Φ=0.75, 1, 2 and 4.

In **Figure 4.3f**, the local maximum compressive strain is plotted, $\varepsilon_{pattern}$, as a fraction of ε_{plain}, for several different aspect ratios of lattice. The compressive strain is strongly localized around the holes. In centered square lattices with smaller holes, there are also clearly star-shaped patterns of increased compression running between the holes. Same plots for a simple square lattice in **Figure 4.4,** showing compression concentration in lateral straight stripes through the holes at all aspect ratios of pattern.

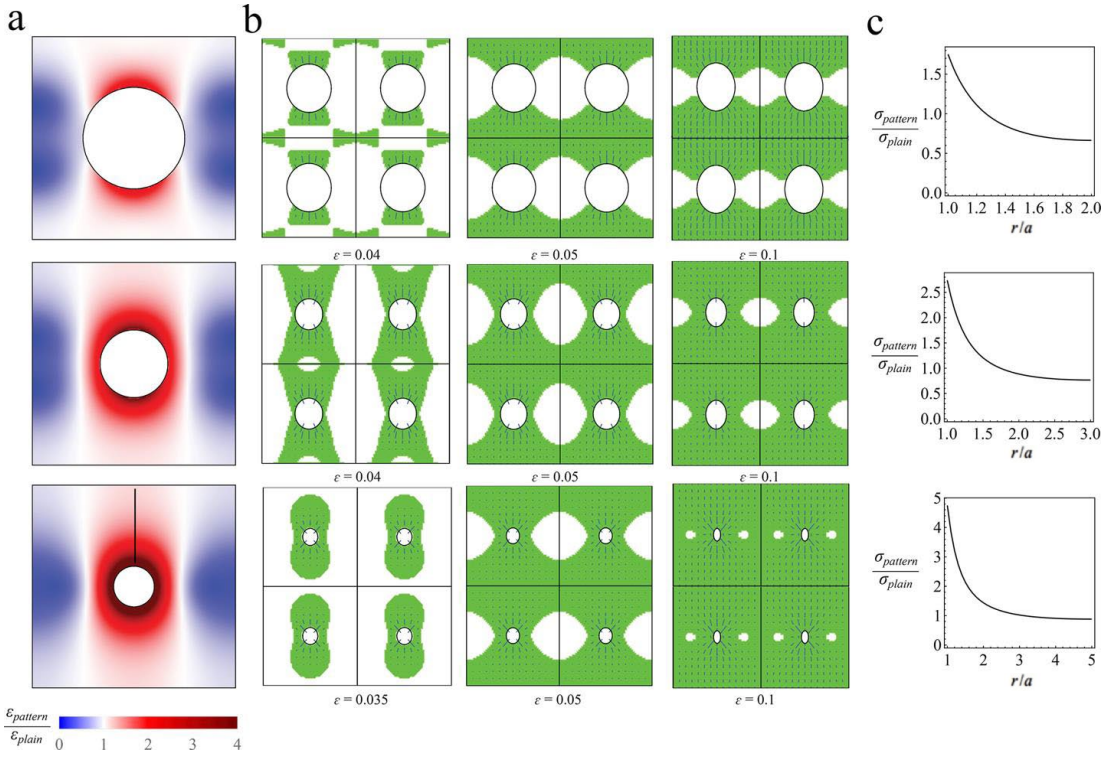

Figure 4.4. Numerical simulation of the wrinkle pattern generation on square lattice patterned surfaces. (a) Compression of the patterned substrate relative to the compression of the non-patterned substrate. Blue and red indicate the less and more compressive areas. (b) Evolution of wrinkling region as a function of a bilayer system with patterned holes. Green areas are the wrinkling regions. Lines indicate the direction along which the wrinkles will grow while their lengths are the relative distance from the wrinkling threshold. (c) Compressive stress in the stiff layer in the patterned bilayer system relative to the non-patterned system values at different

position from the rim of the hole of radius α (maximum stress) to the edge of the unit cell (see arrow in (c) bottom). All plotted with D/Φ= 1, 2 and 4.

The wrinkling pattern on the stiff plasma-treated skin that decorates this base-state deformation was calculated next. To achieve that, the compressive stress σ_c in the thin film was calculated first, assuming it has a Poisson ratio of ν_f=0.3 (silicon like thin film) directly follows the deformation in the soft substrate. The value of this compressive stress, as a fraction of the compressive stress that would be observed in an unpatented system, is plotted for each lattice in **Figure 4.3g**, as a function of distance from the centre of the central hole, along the line shown in the bottom figure of **Figure 4.3e**. For centered square lattice patterned surface, the compressive stress is severely enhanced at the edge of hole, particularly in lattices with small holes, explaining why wrinkling occurs earlier in patterned systems. To predict wrinkling patterns, the standard result for wrinkling on a substrate was applied, which is that wrinkling occurs if $\sigma_c > \frac{1}{4}\left(3\frac{\bar{E}_s}{\bar{E}_f}\right)^{2/3}\bar{E}_f$, where $\bar{E}_f$ and $\bar{E}_s$ refer to the plane-strain elastic modulus for the oxidized stiff layer and PDMS substrate, respectively, which are related to the Young's moduli, E, by $\bar{E} = E/(1-\nu^2)$, where ν is the Poisson ratio. Taking the physically reasonable modulus ratio $\bar{E}_f/\bar{E}_s$ =100, plotted in **Figure 4.3f**, how the predicted wrinkle regions grow as the global compression is increased. In accordance with experiment, that moving from large holes to small holes does indeed change the wrinkling pattern from wavy lines, to straight lines, to stars, and that the

patterns with smaller holes wrinkle at smaller global compressions, because the compressive stress is more concentrated around the hole.

4.2.3 Surface Modulus Measurement with AFM

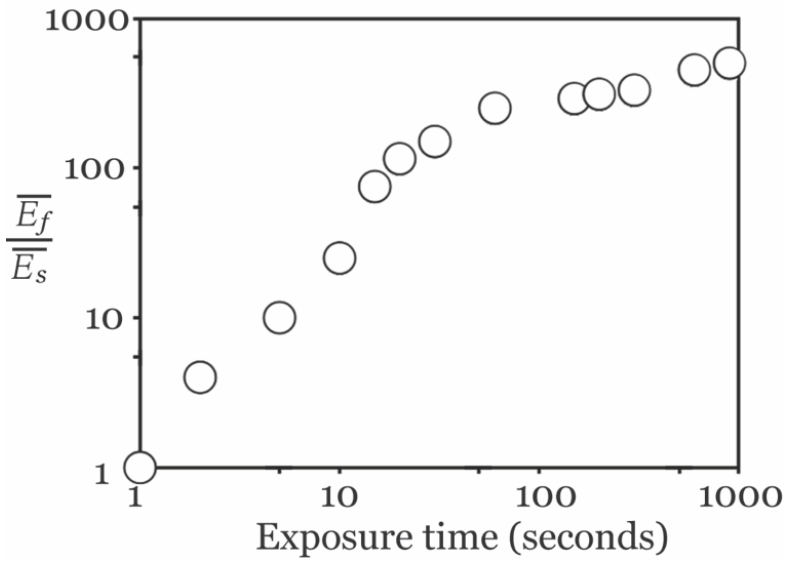

Figure 4.5. The modulus mismatch as function of plasma treating duration.

After the plasma treatment for 10 seconds, the surface modulus measurement (**Figure 4.5**) obtained by AFM indentation suggests the plane-strain elastic modulus mismatch between the film and the substrate is about $\bar{E}_f/\bar{E}_s \approx 25$. Accordingly, the critical wrinkling strain for wrinkling from linear stability analysis [98],[121],[219],[220] is $\varepsilon_w = \frac{1}{4}\left(3\frac{\bar{E}_s}{\bar{E}_f}\right)^{2/3}$ from the critical strain for wrinkle formation would be expected at a small strain of $\varepsilon_W = 0.061$, which agrees well with in-lab result of $\varepsilon \approx 0.068 \pm 0.008$ for a non-patterned surface (**Figure 4.6**). However, it does not agree with the case of a lattice patterned

surface, in which wrinkle patterns are already present at $\varepsilon = 0.06$, indicating that wrinkling occurs at a lower threshold strain as a result of strain energy localization near the lattice holes. Furthermore, according to the report from Kim and co-workers [62], as compression is increased in system with $\bar{E}_f/\bar{E}_s \approx 25$, wrinkles are expected to period double then evolve into crease. It is expected that patterning to also reduce the thresholds for these further bifurcations, but they cannot be effectively identified under reflected optical microscopy.

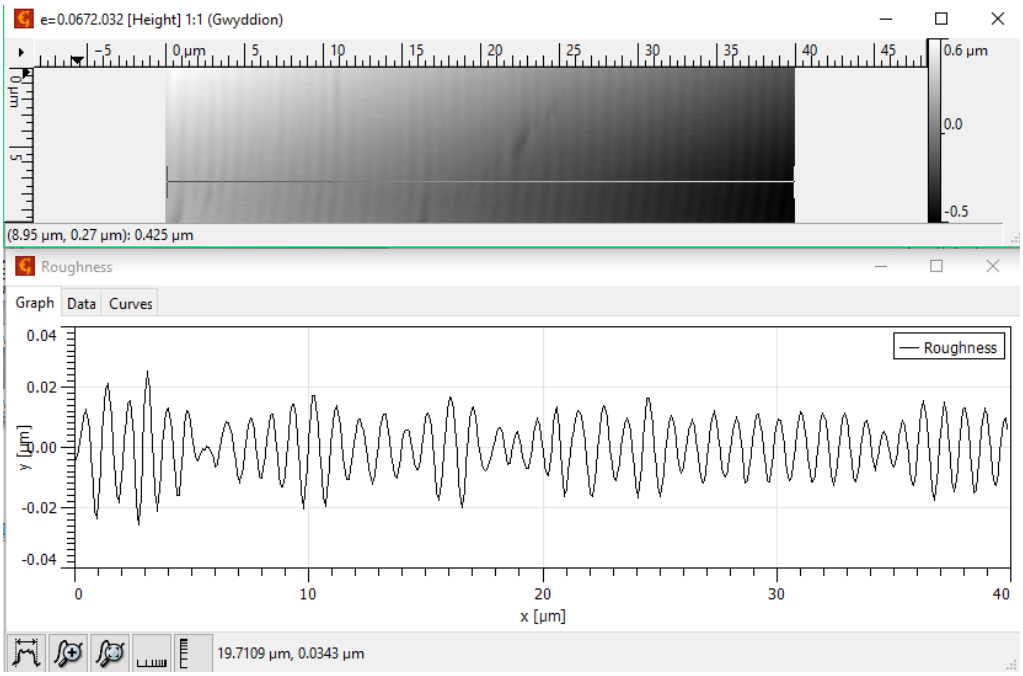

Figure 4.6. The onset of wrinkle at a critical strain of 0.0672 for non-patterned PDMS surface under plasma treatment for 10 seconds.

4.2.4 Analysis of Surface Morphology Development

To unveil more details, AFM was used to track the morphology changes as the compressive strain was gradually increased, focusing on the region of stress concentration "above" a hole as indicated by the dashed box in **Figure**

4.7a. For the centered square patterned surface with aspect ratio of D =80 μm, Φ = 40 μm, h =43 μm, the onset of wrinkling starts at a small compressive strain of ε = 0.02 (**Figure 4.7b-c**) and proceeds to cover the region by ε = 0.11. The initial wavelength (λ_o) is predicted to be $\lambda_0 = (2\pi h_f)(\bar{E}_f/3\bar{E}_s)^{1/3}$, or 700 nm for an oxidized layer thickness of h_f = 55 nm (measured by surface roughness profiler - BRUKER DektakXT), which is in reasonable agreement with the measured value of ≈ 850 nm. The progressive wrinkling over this range of strain presumably reflects the influence of the energy boundaries resulted from the local curvature. It to be noticed that the creases start to nucleate at ε = 0.11, and start to grow at ε = 0.15, then fully cover the region at ε = 0.25. A hierarchical surface is formed at ε = 0.55, where the periodic surface can be seen under the reflective optical microscopy in **Figure 4.7d**.

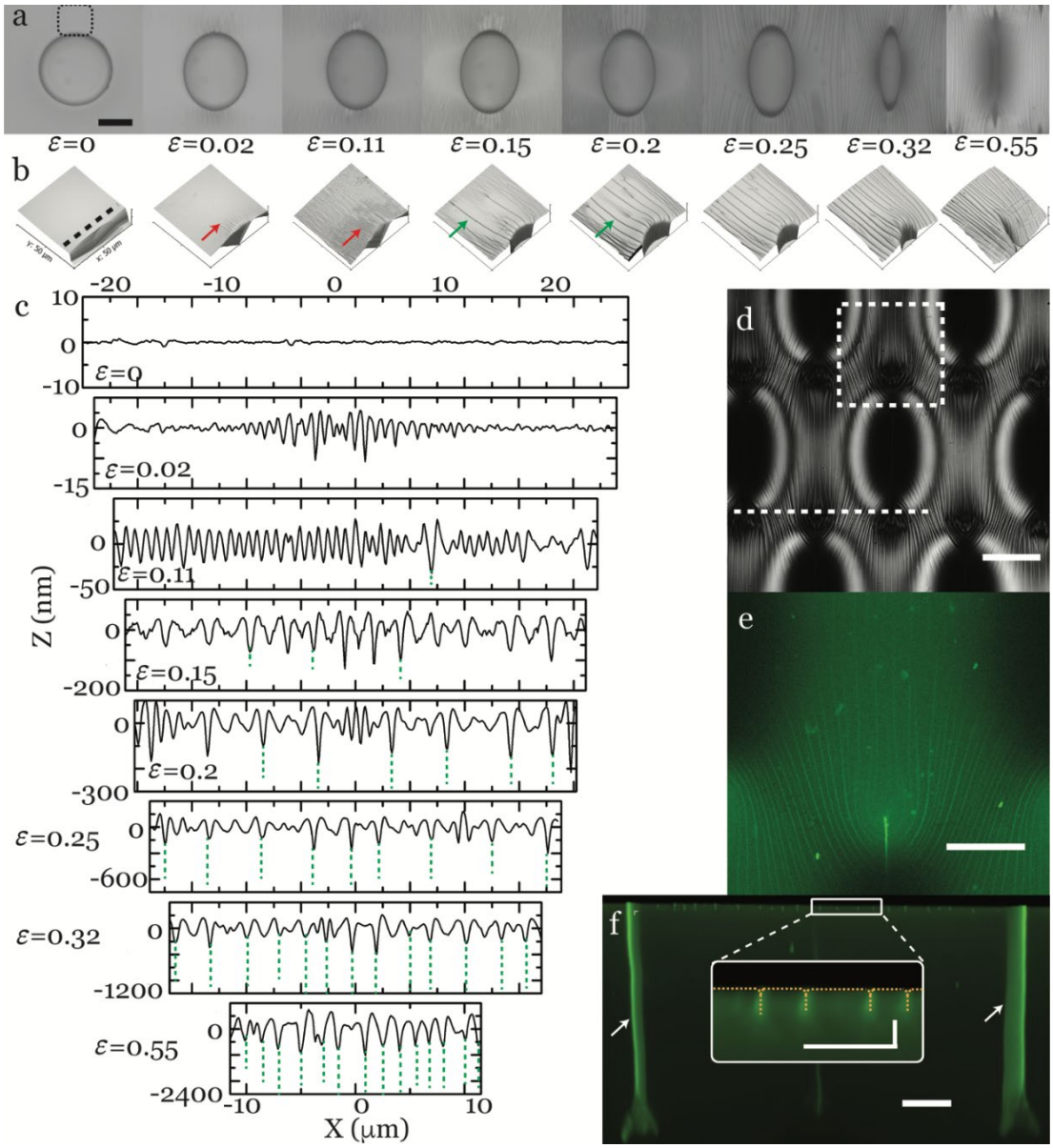

Figure 4.7. Characterization of the instabilities on the single hole and their evolutions under the uniaxial compression. (a) Top view observations and (b) AFM profiling of the selected area in (a) for surface morphology changes under the uniaxial compression for a unit area (centered square lattice array) with in-plane aspect ratio of D =80 μm, Φ = 40 μm, h =43 μm. (c) The surface morphology development is plotted with the dependency on compression strain, the surface starts to initialize localized wrinkles on ε = 0.02, then develop into periodic doubling at ε = 0.15, the surface start to form creases locally on ε = 0.2, where the sharp self-contacts within the PDMS (green dash lines) are detected by LCSM, the creasing develops

globally at last. (d) The reflective image shows a surface hierarchy formed when the hole reached the 'off' state at a compression deformation of 0.55. Laser confocal scanning results in (e) the in-plane distribution of creases and (f) the out of plane morphology developed into the PDMS substrate for the selected area in (d), the arrows show the high intensity fluorescence signal due to the closure of neighbouring holes. The scale bar for the inset figure in (f) is 3 μm. The other scale bars are 40 μm.

There is clearly a curvature guided formation of wrinkle at $\varepsilon = 0.02$ with non-uniform amplitude distribution which reveals the state of energy concentration, where the hole edge perpendicular to the compression axis scores the highest (**Figure 4.7c**). The period doubling pattern can be observed at $\varepsilon = 0.15$ with every second wrinkle grows in amplitude while its neighbours shrink. The strain value for this bifurcation is also smaller than the reported strain value ≈ 0.17 [64]. From $\varepsilon = 0.15$, further compression does not noticeably influence the in-plane morphology, since the AFM result cannot reflect the out of plane deformation towards the substrate, *i.e.* self-contact area of the crease. Therefore, the cross-sectional scanning data of the film was added from laser-scanning confocal fluorescence microscopy (LSCM, **Figure 4.7e**) to reveal the out of plane morphological development for the selected area (**Figure 4.7f**). At strain of $\varepsilon = 0.15$ (**Figure 4.7c**), the LCSM data shows a shallow crease depth (self-contact area) within 100 nm, where it is considered as the onset of the crease. Similar with the wrinkling, this second bifurcation is found to be highly sensitive to the presence of local planar curvature (**Figure 4.8**). At higher compressive strains, the crease depth develops under higher compressive strains and extends to all scanned areas.

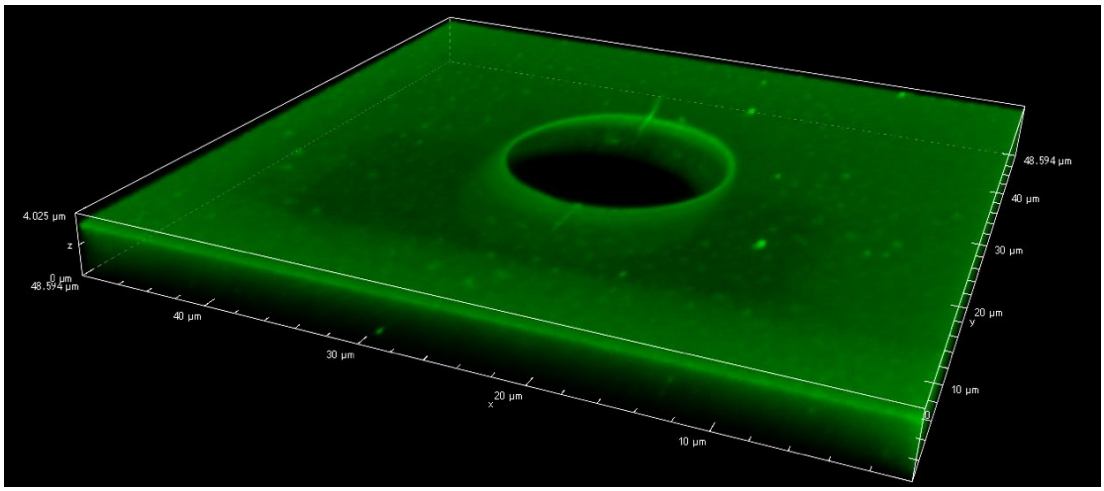

Figure 4.8. The LCSM scanning to review the initialising of the creasing on the targeted area for the centered square lattice patterned surface with aspect ratio of Φ=20µm, h=43µm, D/Φ =4.

4.2.5 Lattice Pattern Effects on Instabilities Development

The lattice pattern effects on post wrinkling bifurcations occurring at a higher strain level was considered. It should be noted that the crease nucleates but it does not grow across the region adjoining the lattice holes (**Figure 4.10**) for $D/\Phi \leq 1$. It is expected this may arise due to the viscoelastic nature of the substrate, and/or the influence of large curvature. A brief classification of the transitions based on the number of initiated crease is summarized in **Figure 4.9a-c** for the lattice patterned surface with aspect ratio $D/\Phi > 1$. There are two transition types (single crease and multiple creases) for the stripe pattern, and the formation of creasing is revealed in **Figure 4.9d** as the white arrows indicated, where the sample was tilted to enable scanning on the wall of hole. The "star" type wrinkle pattern seems more likely to generate a single crease when being further compressed.

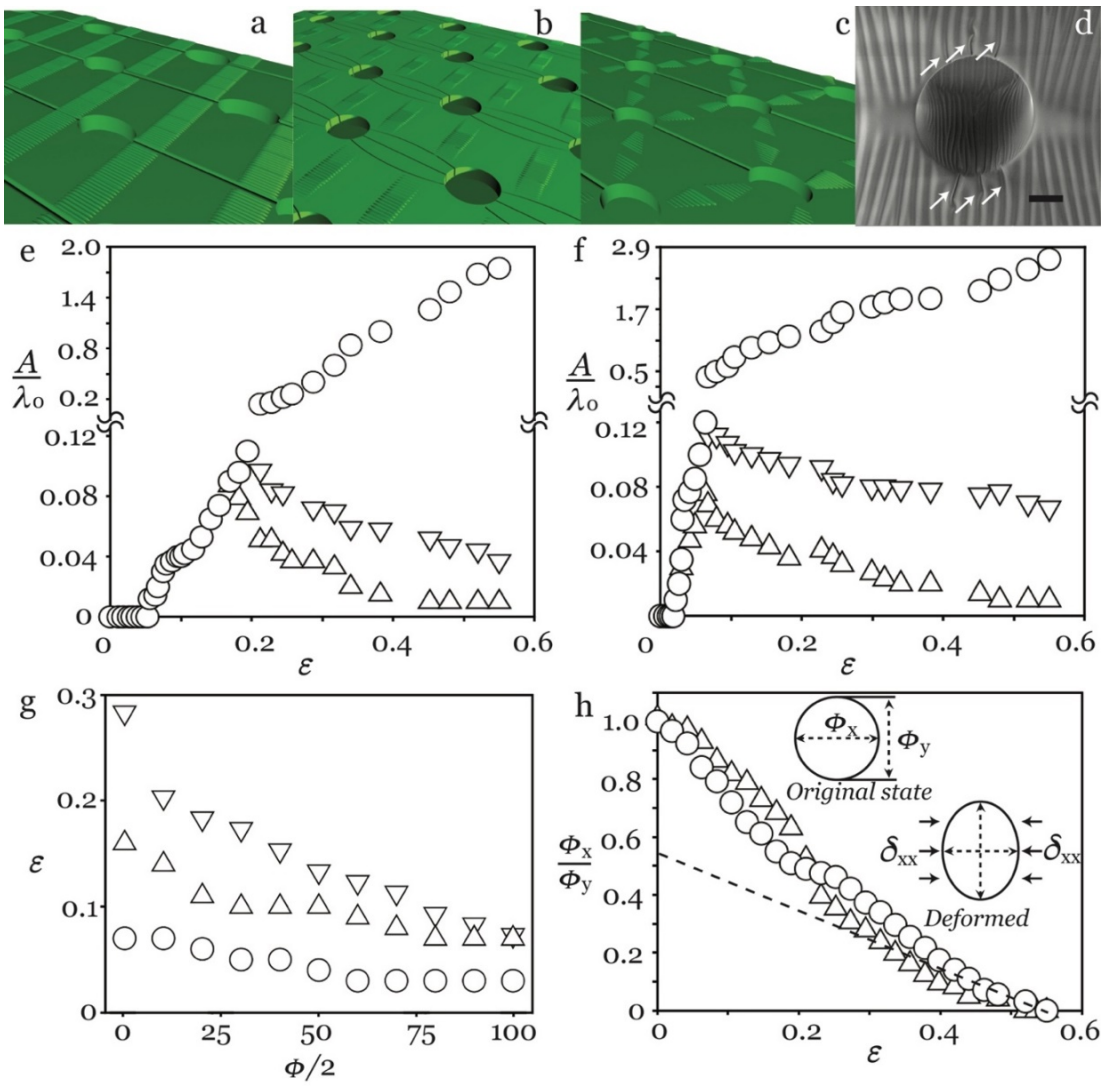

Figure 4.9. The evolution of surface morphology at higher compression, from wrinkling to creasing. Schematic illustrations of the transition from wrinkling to creasing for different harmonic patterns, (a) straight belt, (b) star shape, (c) curved ribbon. (d) SEM image reveals the transition moment from wrinkling to creasing with the captured initialization of creases. The normalized amplitudes of surface features A/λ_0 reveal two post-wrinkling bifurcations with increasing strain for (e) homogeneous PDMS surface and (f) patterned PDMS surface (centered lattice) with in-plane aspect ratio of D =80 μm, Φ = 40 μm, h =43 μm. Normalised amplitudes change along with two bifurcations and represented with first order (○), second

order(△), and third order (▽). (g) The critical strains for initiating wrinkle (○), periodic doubling (△), creasing(▽) for the centered square array with different diameter. (h) The compression (△) and recovery (○) curves show the hysteresis and non-linearity on the deformation of single hole under uniaxial compression.

Next, the normalized wrinkle amplitude (A/λ_o, where λ_o indicates the initial amplitude and A represents the measured amplitude) was plotted as a function of the nominal applied strain on a non-patterned surface (**Figure 4.9e**) and a Bravais lattice patterned surface (**Figure 4.9f,** D =80 μm, Φ = 40 μm, h =43 μm). In each case, beyond wrinkling onset, two additional instabilities/bifurcations are seen, corresponding to period doubling and then crease formation. However, both the onset of wrinkling and the further bifurcations occur at considerably lower global strains in the patterned system: the critical wrinkle strain for the patterned surface of ≈ 0.02 is less than one third of that in flat surface ($\varepsilon \approx 0.068$), the critical strain for periodic doubling in a patterned surface is ≈ 0.06, whereas it is ≈ 0.18 in flat surface, and for the final bifurcation, the wrinkle-crease transition, the critical strain needed is ≈ 0.08 in patterned surface, which is less than half of that for flat surface ($\varepsilon \approx$ 0.22). This threshold reduction effect by considering the stress concentration in the analytic calculations for systems with D/Φ=2, (seen in **Figure 4.3g**), which exhibit a two-fold stress concentration at the edge of the hole relative to the non-patterned system, and hence predicts two-fold reduction in the various thresholds. The discrepancy between this calculation and the observed three-fold reduction is probably due to the analytic plane-strain

approximation not capturing the full 3-D structure of the actual deformation field.

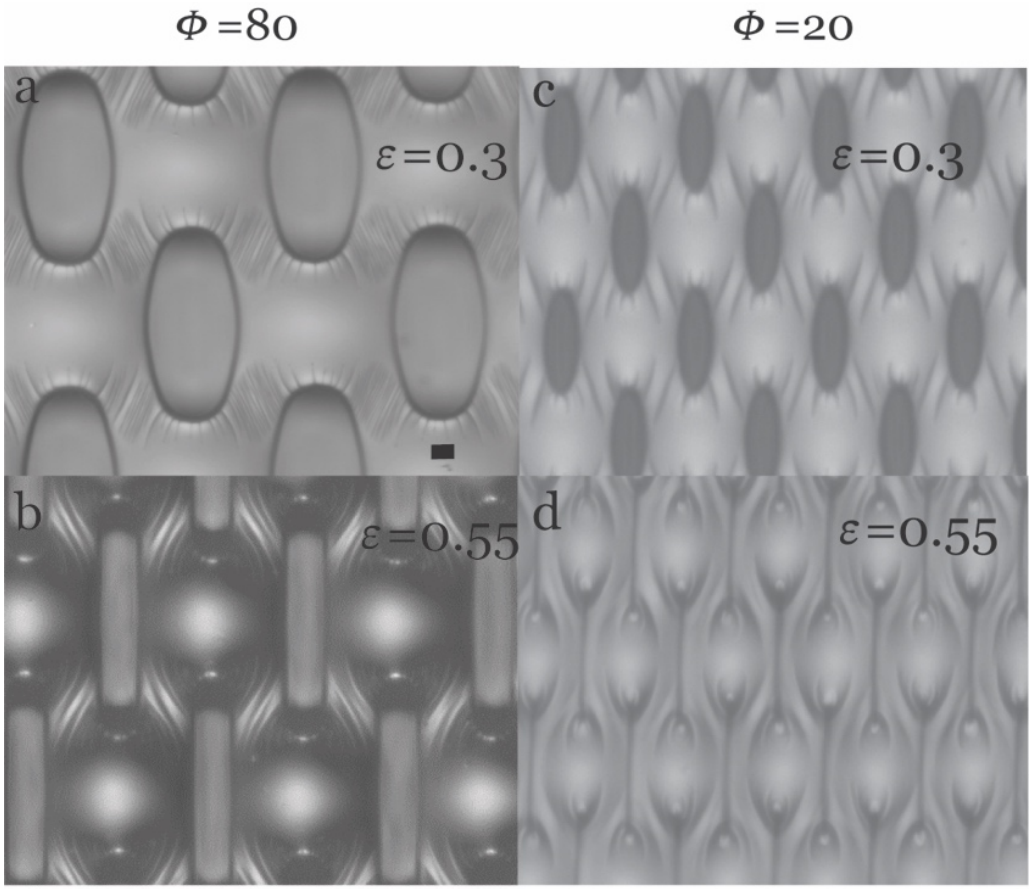

Figure 4.10. The deformation of patterned surface under high compression with different hole diameter.

It is important to understand quantitatively how these instabilities develop in the presence of the curved boundary from the edge of lattice hole. Thus, the normalized strain (the ratio between critical strain and reference strain) was plotted for the onset of each instability as a function of the radius of lattice hole for D/Φ =2. As seen in **Figure 4.9g**, the critical strains are clearly separated in different ranges, while the planar curvature decided by the

radius of the holes influence the strains significantly. The overall strains are reduced as a result of the strain localization guided by the curved boundary, and it seems the strains for each instability likely to collapse, which agreed well with the reported value by Kim that the doubling bifurcations are likely to be mixed with creasing with the $\bar{E}_f/\bar{E}_s$ value in the range of 14–47 [151],[169]. A key advantage of the elastic instability enabled technology is that, as an elastic process, it should yield a low degree of hysteresis. Then the hysteresis of the lattice patterned surface was investigated with labelling the lateral dimension change in the hole (**Figure 4.9f**), the results suggest a robust transformation, which indicates that the viscoelastic relaxation of the soft PDMS layer used here is less important.

4.3 Summary

In this chapter, an approach was presented to generate periodic planar wrinkle 2D pattern and controllable instability evolution towards a hierarchical surface by pre-placing Bravais lattice patterns on the surface as in-plane structural confinements. The bilayer system shows kinetic bi-stabilities at certain well-defined strain values of initializing the wrinkles and further elastic bifurcations at the designated areas/locations which are closely related to the geometries of the confinements. The formation of lateral wrinkle patterns has been studied with the dependencies on the geometrical variables of in-plane confinements and in good agreement with the predictions from numerical analysis. At higher compression, a targeted formation of wrinkle-to-

crease transition was revealed as result of the reorganization of surface strain field. This localized formation of surface instabilities is anticipated, and the demonstration of bi-stability over a substantial range of strains will open new opportunities for applications of elastic instabilities on responsive surfaces for future lab on chip device, by enabling delicate responses to mechanical inputs as selectively sensing or actuating structures.

Chapter 5

Bi-axially Switching Droplet Shape by Initiating Localized Wrinkle Pattern Transformation upon Elastic Surface

5.1 Introduction

Surfaces with controllable wetting property have been seen of particular importance in downstream applications such as water harvesting [221],[222], self-cleaning [223]–[225], surface coating [226],[227], adhesion [228]–[230] and microfluids devices[231]–[234]. One simple strategy to realize the controllability on surface wetting is to develop topographical surface structures [235],[236], thereby enabling a desired liquid/solid interaction [237]–[240]. Recent advances brought diverse approaches to create surface with specific wetting performance by using chemical treatment [241]–[243], delicate pattern designs [244]–[246], and functional materials [247],[248]. Notably, Quere and co-workers[235] reported the droplet shape manipulation on an elastic surface with soft pillars. Park et al. studied a structured shape memory polymer and revealed a mechanism to manipulate droplet with adjustable surface morphology [249].

In addition to above exercises, researchers developed strategies to manipulate surface capillary by creating wrinkled surface [250]–[252], where sinusoidal wrinkle can be generated on the stiff surface by relieving the strain of pre-strained soft elastomeric foundation layer [103],[253],[254]. The periodicity, amplitude, and orientation of wrinkle pattern can be designed and the morphological transitions under mechanical stimuli will yield changes on the local liquid/solid interaction, even a reorganization of the capillary map over the surface [81],[255],[256]. Extensive studies have been performed to investigate the geometrical effects on surface energy barriers and the associated pinning effects on contact line. Stafford [83] studied the wetting behavior upon a tunable single-period micro-wrinkled surfaces, as a result of the differences in energetic barriers. Yang and co-workers [89] have investigated the influences of groove geometry on the anisotropic wetting and fluidic transport with a combining force balanced model. Feng *et al* [257] reported anisotropic wetting on hierarchical wrinkling surface that induced by elastic bilayers curvature and free energy change. Previous report indicated that to generate wrinkle-cracking bi-axial morphology spontaneously on the gold/shape memory polymer bilayer [258], could further explored to use this mechano-responsive morphology to initialise the anisotropic wetting state autonomously. However, all above studies focused on shaping droplet in one direction, understandings on shaping droplet bi-axially in a continuous, dynamic and reversible manner is yet to be explored.

In this work, a surface with switchable capillary landscape that constructed allows us to continuously and reversibly manipulate droplet shape to extreme stages in biaxial. By initiating and transforming localized wrinkle pattern under uniaxial mechanical stimuli, hierarchical surface structure can be driven to change and hence create a continuous transition of surface roughness at selected region, leading to an enhanced local pinning effect and a dynamical and reversible organization of capillary map. As a result, a dynamic and reversible shaping of droplet to extreme oval shape in biaxial can be achieved. The concept of reversible and robust shaping of droplet bi-axially with a configurable capillary map can lead to significant applications in soft robotics, oil-gas engineering, water treatment, healthcare, micro-fluidics, etc.

5.2 Results and Discussion

5.2.1 Droplet Shaping by Localized Wrinkle Pattern

The structural elastic surface with centered square Bravais lattice pattern was prepared using the method in previous report [259]. The geometrical parameters for the centered square Bravais lattice hole, *e.g.* diameter (Φ), distance (d) and depth (h) are defined in **Figure 5.1a**. Oxygen plasma treatment was used to create a thin stiff layer on the patterned soft substrate (**Figure 5.1b**) prior to the compression. Upon subsequent release of the mounting layer from a pre-stretched length L_i to a length L, the patterned PDMS player is under compression, which the strain can be calculated by $\varepsilon_{comp} = 1 - L/L_i$. The occurrence of morphology is observed under upright optical

microscopy at ε_{comp} = 0.21 (**Figure 5.1b**), where wrinkling is only developed on the surfaces after plasma treatment. Apart from the one-dimensional (1D) wrinkles for flat surface, regionally distributed two-dimensional (2D) wrinkles are obtained for elastic surface patterned with centered square Bravais lattice holes.

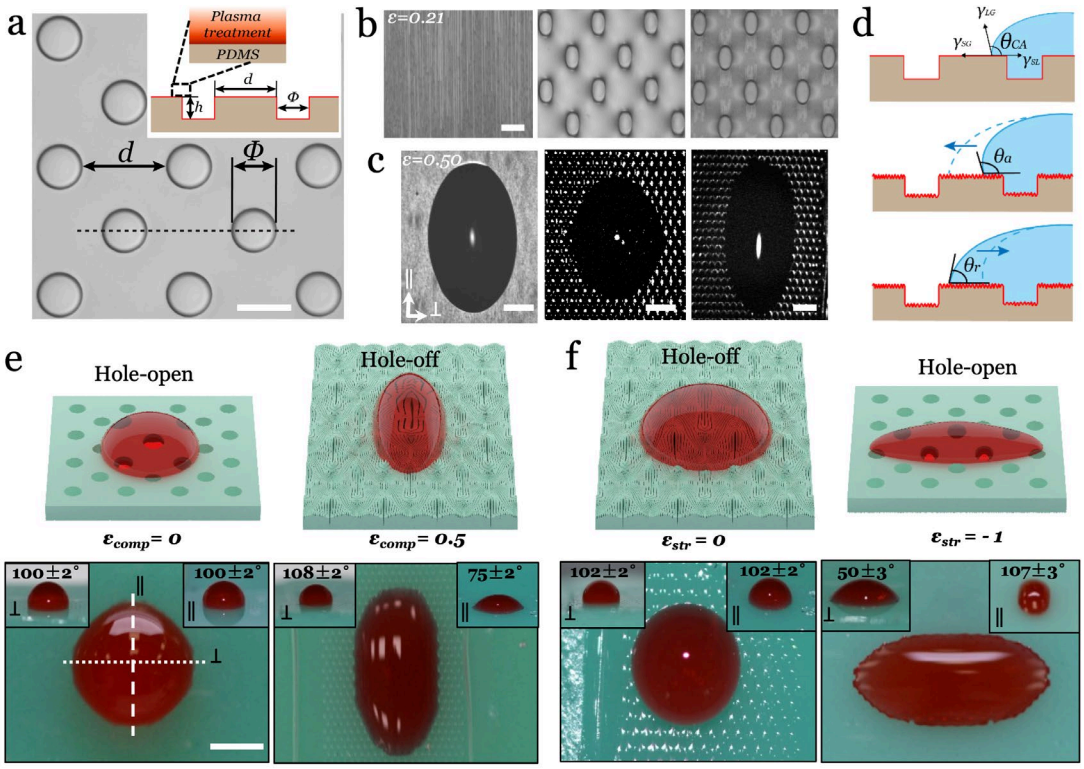

Figure 5.1. Structural surface design and realization of droplet shaping by initiating the elastic instability morphologies. a) Optical microscopy image of the centre square lattice hole on PDMS surface. b) Observations of surface morphologies at a compressive strain of 0.21 on plane surface after oxygen plasma treatment (left), patterned surface without oxygen plasma treatment (middle) and patterned surface with oxygen plasma treatment (right), c) observation of droplet shape at a compressive strain of 0.5 for the corresponding surfaces in b). d) The illustrations of locally pinning effect on static contact angle, advancing contact angle and receding contact angle on instability surface. e) Schematic and illustration of

shaping droplet under compression and i) stretching on patterned surface (D = 160 μm, Φ = 80 μm, h = 40 μm. The scale bar is 1 mm.). The other scale bars are 100 μm.

In demonstration, the droplet is shaped to extreme state on the mechano-responsive surface (**Figure 5.1c**). After depositing a droplet on the pre-strained elastic surface, a compressive strain was subsequently applied to the surface. A typical anisotropic wetting was achieved on wrinkled surfaces (plane and patterned with lattice holes) with water droplet spreading along grooved patterns as previously reported by other researchers [260],[261]. The directions perpendicular (⊥) and parallel (∥) to the wrinkle/groove direction are defined to describe surface topography and droplet shape (wetting anisotropy). As a dynamic wetting process (**Figure 5.1d**), the contact angle perpendicular to the grooves is much larger because of the pinning of the three-phase contact line, also known as the contact angle hysteresis caused by the advancing angle (θ_a) and receding angle (θ_r).

The concepts of controlling surface anisotropy under uniaxial mechanical stimuli are exercised with a single loop of compression (**Figure 5.1e**) and stretching (**Figure 5.1f**). Under compression, surface instabilities occurred and developed to form energy barrier to stop liquid from propagating in perpendicular (⊥) direction (inset **Figure 5.1e**, ε = 0.50). Meanwhile, the shape of droplet extends along the parallel (∥) direction due to the absence of such barrier, allowing the droplet to infuse surface groove (inset **Figure 5.1e**, ε = 0.50). Consequently, an oval shape of droplet is formed with an aspect ratio ($D_{\parallel}/D_{\perp}$) of 1.87, where $D_{\parallel}$ and $D_{\perp}$represents the diameter of droplet in pararral

direction and perpendicular direction, respectively. The programable stretching of droplet is demonstrated by depositing droplet on the fully compressed substrate, then gradually releasing the compressive strain till the hole-open (initial) state. The stretching strain ε_{str} is calculated by $\varepsilon_{str} = 1 - L/L_i'$, where L_i' is the length for initial state. In **Figure 5.1f**, the droplet reaches $D_{\parallel}/D_{\perp} \sim 0.45$, due to the pinning of contact line pinned by local roughness.

5.2.2 Anisotropic Wetting on Developed Topographical Surface

To reveal the detailed surface topographical changes, AFM was used to trace the development of surface morphology at the cross area between voids (the dash box in **Figure 5.2a**). For patterned surface with aspect ratio $d/\Phi = 4$ (**Figure 5.2b**, △), the measured roughness ($R_{\perp}$) is ≈ 50 nm at $\varepsilon_{comp} = 0.13$, follow by an increase to ≈ 170 mm at $\varepsilon_{comp} = 0.21$, then a gentle decrease till $\varepsilon = 0.46$. The amplitude is predicted to be $A = h\,[\varepsilon/\varepsilon_c - 1]^{1/2}$, or 58.49 nm at $\varepsilon_{comp} = 0.13$ for an oxidized layer thickness of 55 nm at cross area, which is in reasonable agreement with the measured value of ≈ 50 nm [259]. Interestingly, an in-plane directional shifting of the nucleated wrinkle/grooves was observed, where the shifting angle ($\varphi_{\parallel}$, **Figure 5.2a**) is defined between the groove and the horizontal compressive stress direction. The wrinkle pattern nucleates with a higher angle degree (≈ 85°) at the beginning (**Figure 5.2c**), then reduced to ≈ 40° for the surface with lattice aspect ratio of 1 (**Figure 5.2c**, ○). It should be noted that the in-plane angle change dependents on lattice aspect ratio, the angle barely changed at an aspect ratio of 4 (**Figure 5.2c**, ▽), which means

the re-orientation of wrinkle/groove pattern is significantly affected by the distribution of lattice hole. The combining effects from increment on $R_{\perp}$ and shifting of $\varphi_{\parallel}$ facilitate the re-organization of the in-plane capillary map, thus lead to an enhanced localized pinning effect to restrain contact line movements.

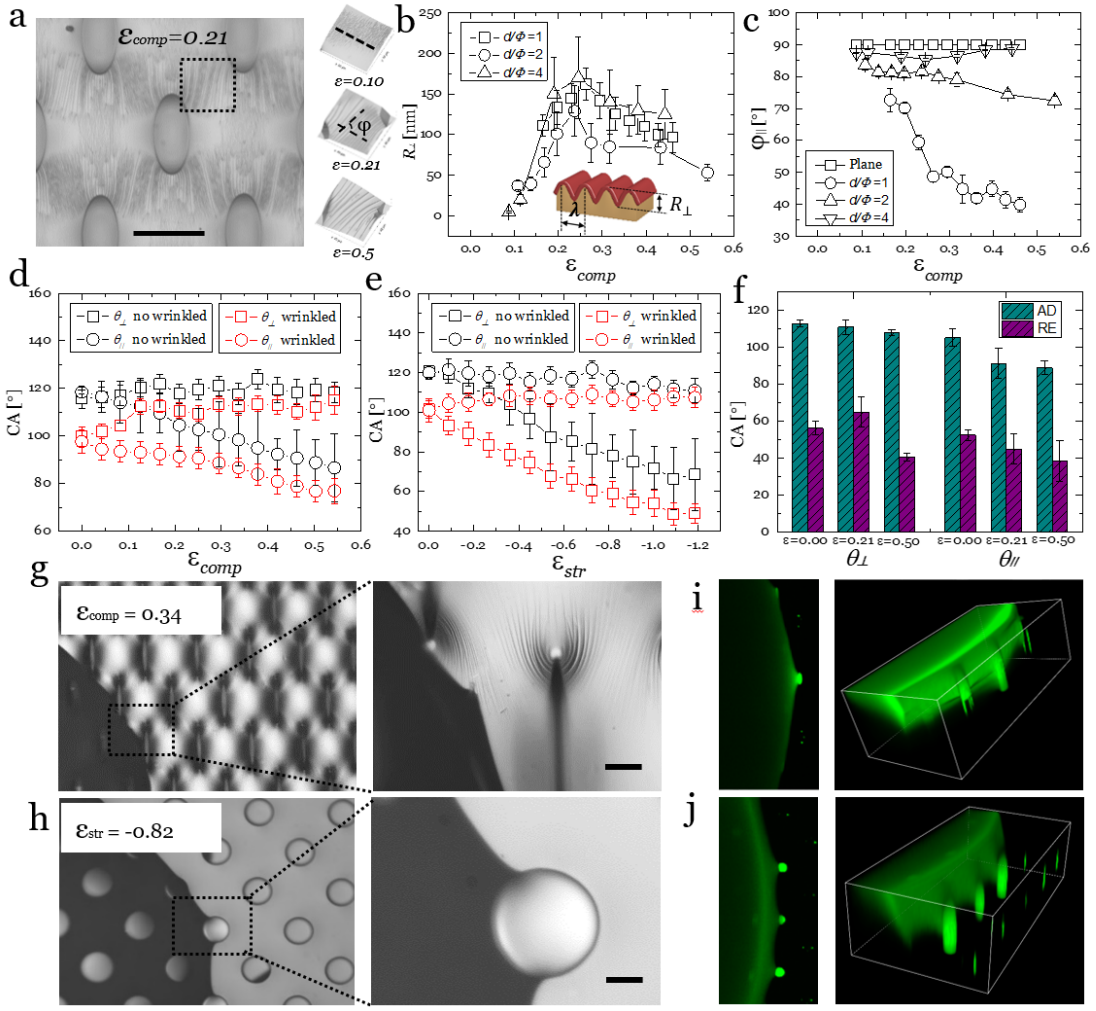

Figure 5.2. Characterization of the mechano-responsive morphology transformation and its induced anisotropic wetting. a) Observation and AFM profiles of morphology changes for lattice patterned surface (d = 80 μm, Φ = 40 μm, h = 20 μm) under the compression. b) Roughness ($R_{\perp}$), c) directional angle ($\varphi_{\parallel}$), static CA under d) compression and e) stretching deformation. f) Contact angle hysteresis for the complex surface in a) at different compressive strains. Observations of contact line pinning by g) wrinkle instability and h) lattice patterned hole. Laser scanning

confocal records for i) the pinning of contact line by single hole, and j) the residual liquid in the hole after the withdraw of contact line.

The effect of morphology transition on surface anisotropic wetting was assessed by measuring the contact angle (CA) statically and dynamically. The static CA measurement was performed by depositing droplets on the deformed surface at each strain, where the CAs for both directions stably kept around 120° (**Figure 5.3**). For dynamical measurement, the contact angle change was traced for a single droplet on the surface undergo a continuous loop of compression/stretching with a strain rate of 0.004^{-1}. For lattice patterned surface without wrinkle, the perpendicular static CA ($\theta_{\perp}$, □) shows a value around 120° with a slow increasing trend (**Figure 5.2d**) under compression, similar to the static results. However, the value of parallel static CA ($\theta_{\parallel}$, ○) shows a decline trend due to the Poisson's ratio effect induced physical stretching in the parallel direction. For lattice patterned surface with wrinkle, the contact angle value has been reduced from 120° to 100° due to the plasma treatment. The amplitude of the wrinkles and thus the curvature of the topography lead to a higher deformation of a circularly shaped liquid droplet to oval shape to minimize its surface energy. At stretching mode, the perpendicular static CA performed a reducing trend (**Figure 5.2e**) while the parallel static CA keep at constant angle degree of ≈ 120°, when the surface transited from hole-off to hole-open state. For both compression and stretching processes, a large bifurcation of the CA values between the $\theta_{\perp}$ and $\theta_{\parallel}$ is obtained for lattice patterned surface with wrinkles, indicating a better droplet shaping effect.

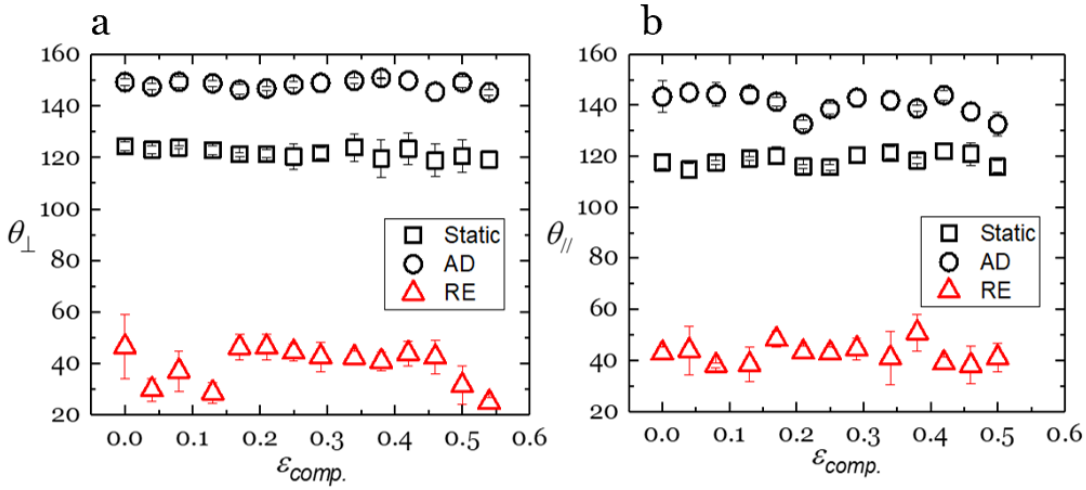

Figure 5.3 Static contact angle and dynamic contact angle measurement on deformed surface at each strain a) Perpendicular CA b) Parallel CA

The contact angle hysteresis results were summarized on lattice patterned surface with wrinkles (**Figure 5.2f**), where the results show a good maintenance of perpendicular advancing angle with a change less than 6° and a significant drop on parallel advancing angle with a reduction of 26° between initial state ($\varepsilon_{comp} = 0$) and a fully compressed state ($\varepsilon_{comp} = 0.5$). For the lattice patterned surface without wrinkles, the changes on advancing angle on both axes are less than 5°, representing a low efficiency on droplet shaping. An increasing on perpendicular advancing angle up to 15° is also observed due to the significant development of wrinkles and a decree on parallel advancing angle of 8° as a result of the extension of droplet along the wrinkle direction for plane wrinkled surface.

To further understand how the surface morphology influences droplet sharping effect, an mismatch of in-plane contact angle ($\Delta\theta$) is defined by $\Delta\theta = |\theta_{\perp} - \theta_{\parallel}|$, where $\theta_{\perp}$ and $\theta_{\parallel}$ are the dynamic contact angle hysterisis (advancing

angle or receding angle) from two axies. It is expected that the in-plane advancing angle mismatch ($\Delta\theta_a$) and the in-plane receding angle mismatch ($\Delta\theta_r$) will be critical to determine the droplet aspect ratio under compression and stretching, respectively. For the lattice patterned surface with wrinkles (**Figure 5.2f**), a $\Delta\theta_{adv}$ of less than 3° for initial state (ε_{comp} = 0) was found, then increase to 23 ± 6° at max wrinkled roughness state (ε_{comp} = 0.21), finally reach to 27 ± 3° at fully compressed (ε_{comp} = 0.5). However, the $\Delta\theta_a$ for wrinkled flat surface reaches a value of 21 ± 4° when the substrate was fully compressed. Interestingly, an ignorable $\Delta\theta_{adv}$ vaule of 7 ± 3° is shown for the lattice patterned surface without wrinkles (**Figure 5.4**) at ε_{comp} = 0.5. This in-plane advancing angle difference clearly prove that a preferred surface energy barrier is generated on the elastic surface with lattice patterns and regional wrinkles, which help to shape the droplet to extreme state under compression.

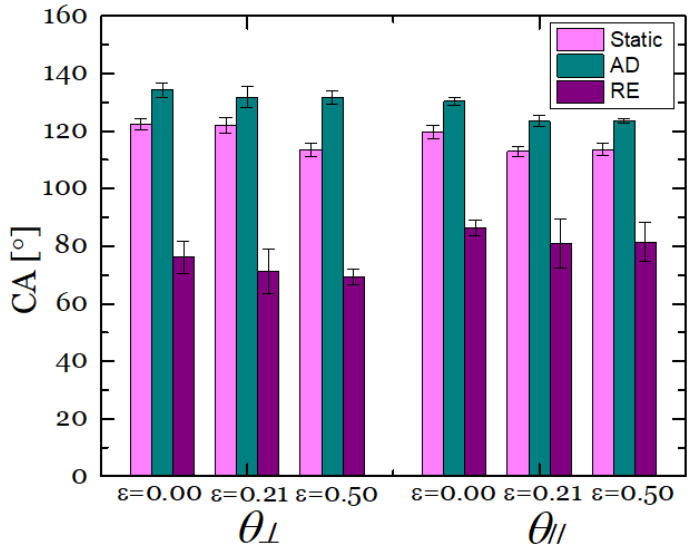

Figure 5.4 Contact angle hysteresis for the complex no wrinkled surface at different compressive strains.

Since the droplet stretching is examined by depositing droplet on the fully compressed surface, then reversibly restore the substrate to pre-strain state, the in-plane receding angle mismatch ($\Delta\theta_r$) in compression loop therefore can be also used to unveil the effect of surface topology on the droplet stretching in a reversal order. It is found that the $\Delta\theta_{rec}$ increases from 0± 5° at starting point of stretching (ε_{comp} = 0.5), then jump to 18 ± 4° at max wrinkled roughness state (ε_{comp} = 0.21) and reduce to 4 ± 3° when the substrate recovered at initial pre-strain state (ε_{comp} = 0), for the lattice patterned surface with wrinkles, whereas the $\Delta\theta_r$ changes less than 8° during the stretching for both plane wrinkled surface and the lattice patterned surface without wrinkles.

The initial contact between droplet and surface is Cassie-Baxter[43] state where the hole was not filled with liquid (**Figure 5.5**), the hypothesis is that the surface morphological development plays a critical role in changing liquid/solid interaction by translating the contact mode from Cassie/Baxter model to Wenzel model. Under compression, the localised wrinkles around the hole (**Figure 5.2g**) produce a strong pining effect on the perpendicular direction by generating the roughness and directional angle shifting. During the stretching, a combining effect between the wrinkle and lattice pattern influence the droplet shape to offer a strong pinning state (**Figure 5.2h-i**), where we even can see the contact line is pined at the edge of hole. Further information from Laser confocal scanning results shows there is even a residual liquid in the hole after the contact line move away from the region

(LSCM, **Figure 5.2i-j**), as the hole become more favourable for liquid after plasma treatment.

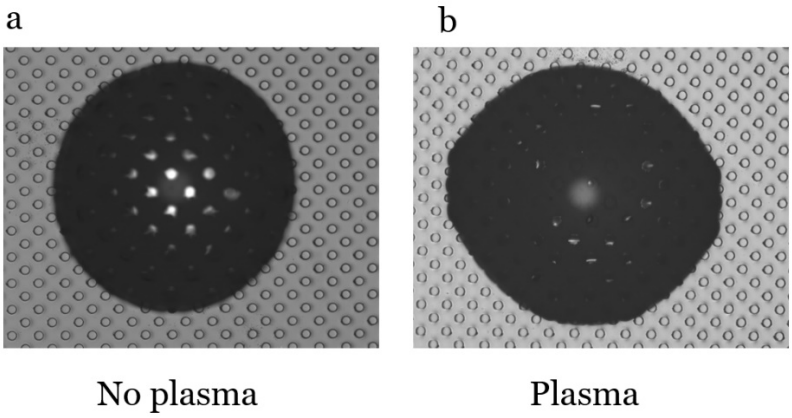

Figure 5.5: Optical image of droplet on pattern surface at static state. a) Droplet is in Cassis-Baxter state as the liquid not filling the patterned hole which proved by the white reflected beam. b) Droplet is in Wenzel state as the liquid filling the patterned hole.

5.2.3 Droplet Shape Control on Different Surface Pattern

The droplet shaping efficiency was evaluated as a function of the geometrical factor of lattice pattern (hole size), by plotting the droplet anisotropy value ($D_{\parallel}/D_{\perp}$) under compression (positive strain) and stretching (negative strain) (**Figure 5.6a**). Under compression, wetting anisotropy on the plane surface (non-patterned and no wrinkles) gives a value of $D_{\parallel}/D_{\perp}$ = 1.3 for the droplet, whereas the plane surface with wrinkles achieve an improved performance with $D_{\parallel}/D_{\perp}$ = 1.6, due to the increased hydrophilicity (more hydroxyl group) and surface wrinkles (stiffen thin top layer) induced by plasma treatment. The quantitative results indicate that the lattice patterned

surfaces with wrinkles reach significant increase on wet anisotropy with the value of $D_{\parallel}/D_{\perp}$ high than 1.8, it also show a preference on the pattern specification as the one with hole size of 60 μm achieves the highest value of $D_{\parallel}/D_{\perp}$ = 2.4. Under stretching, all lattice patterned surfaces (wrinkled and non-wrinkled) achieve low $D_{\parallel}/D_{\perp}$ values of around 0.45, indicating a better shaping effect than plane surface (non-patterned and no wrinkles) which has a $D_{\parallel}/D_{\perp}$ of 0.55.

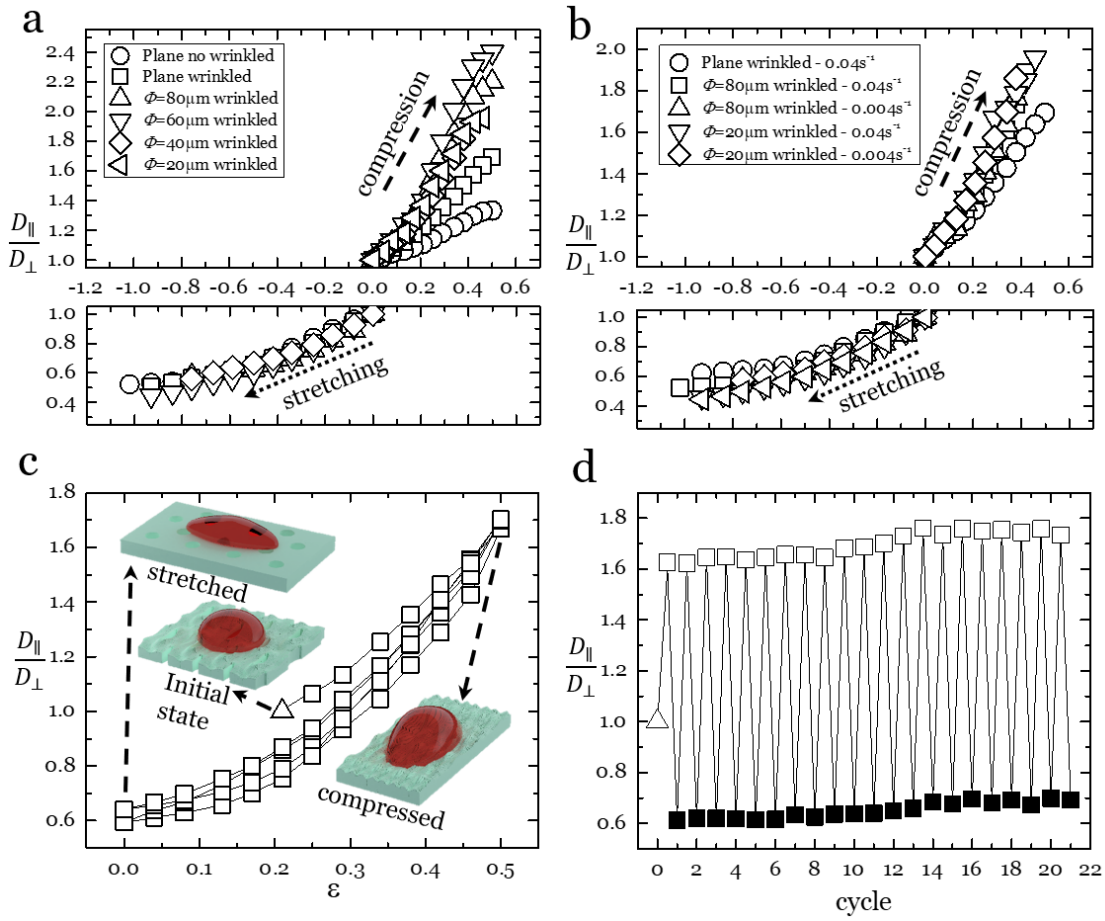

Figure 5.6 Evaluation of droplet shaping efficiency and reproducibility. a) The impact of surface geometrical factors on droplet shaping under compression and stretching. b) The effect of deforming speed on droplet shaping under compression and stretching. c) the hysteresis assessment for the biaxial droplet shaping. d) The

cyclic droplet shaping result for lattice patterned surface (d = 80 μm, Φ = 40 μm, h = 20 μm).

The key advantage of using this elastic process to switch anisotropic wetting, is the high degree of repeatability. The importance of loading/unloading rate were further characterized on the different surfaces (**Figure 5.6b**). With increasing average strain rates over the range of 0.004 – 0.04 s^{-1}, there is no obvious difference for the surface with same lattice pattern at compression and stretching. The biaxial shaping of droplet starts by depositing the droplet on the substrate with partially relieving the pre-strain of substrate to 0.2 (**Figure 5.6c**). From the multi-cycle biaxial shaping result in **Figure 5.6c**, a hysteresis of less than 0.1 is found between the first compression and the second cycle. From the second cycle, the hysteresis become ignorable. Good repeatability in cyclic testing the robust bi-axial droplet shaping upon the structural elastic surface is obtained (**Figure 5.6d**), with high $D_{\parallel}/D_{\perp}$ values between 1.65 to 1.7 and low $D_{\parallel}/D_{\perp}$ values from 0.65 to 0.77 over a number of cycles. A small increase was noticed on both values, this may arise due to the deformation relaxation of substrate, the viscoelastic nature of the interaction between the substrate and droplet, and/or the influence of surface conditions (hydroxyl groups), also the surface tension, but a detailed investigation of this point is defered to future studies.

5.3 Summary

In this chapter, bi-axial droplet shaping was demonstrated that can control the anisotropy by using the multi-level hierarchical structures based on wrinkle/crease in the presence of in-plane structural confinement. Compression and stretching was applied to the plasma-treated PDMS bi-layer with lattice hole pattern to generate localized wrinkle/creases bifurcation in the direction perpendicular to the compressive stress direction. The shape of droplet liquid can be bi-axially manipulated on the patterned surface by simply tuning the roughness of surface and orientation of the wrinkle/crease. The surface roughness has been studied with the dependencies on the geometrical layout of lattice hole, corresponding with the measurement of contact angle and contact angle hysteresis. Moreover, the combined effects of the surface instability, lattice hole confinement and compressive/stretching deformation enabled control of anisotropy of water droplets in a single platform. It is promised this concept of mechanical-responsive bi-axial droplet wetting will open new opportunities for various anisotropic wetting such as microfluidic, self-clean and propose a new way to develop dynamic bi-axial wetting surface.

Chapter 6

Theoretical Investigation on Configuring the Elastic Instability in Soft Surface

6.1 Introduction

The theoretical approach in this chapter is carried out by finite element analysis (FEA) using software ANSYS Workbench. FEA is a computerized method for predicting how a product reacts to real-world physical effects, such as forces, vibrations, heat and fluid flow. An object is broken down into a large number of finite elements and the behaviour of each element is predicted by equilibrium equations with boundary conditions, then the individuals are summed up to predict the behaviour of the actual object with specific boundary conditions.

A flow chart for carrying out the FEA is presented below.

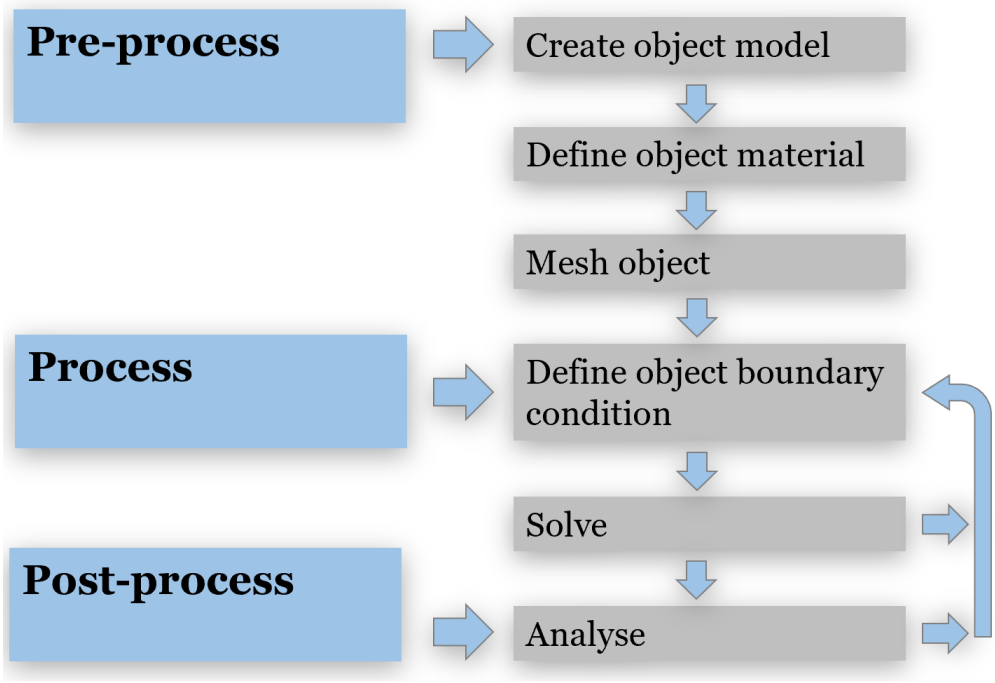

Figure 6.1 Flow chart for Finite Element Analysis

In this case, the object is Polydimethylsiloxane (PDMS) which is a silicone elastomer that behave highly non-linearly. It has properties including thermal stability, high gas permeability, low surface energy, and it is simple to manipulate which makes it is attractive for developing microfluidics and microstructure components [262]–[267]. The system consists of a thin PDMS film with bi-layer structure where the top layer was treated with plasma to achieve increased modulus, while the bottom layer was untreated and kept the original property of PDMS. The concept of non-linearity in this case refers to the non-linear properties of the PDMS material and non-linear geometry variation due

to large deformation in thin film structure. There is a clear need to utilise the viscoelasticity of PDMS material on structural changes with the applied force that justify potential applications and robust designs [268], where the hyper-elasticity of PDMS is able to demonstrate non-linear properties of elasticity.

Hyper-elastic material is the model used here to simulate the soft material. There are several hyper-elastic models[269] based on empirical values to describe it.

- The neo-Hookean model: which uses the material's characteristics to describe the PDMS behaviour. It is adapted to low deformations.

- The Mooney Rilvin model: which is more precise than the Neo-Hookean model for low deformations. Calculation methods are based on empirical values, obtained by realizing experiences.

- Arruda Boyce model: which uses the microscopic and mechanical properties of the material. It is precise and adapted to low and high deformations. The Gent model is a simplified version of the Arruda Boyce model

- The Odgen model: which use empirical values and it has the most accurate property of hyper-elastic . Like the Moonley Rilvin model, calculation methods area based on empirical values

- Yeoh model: used for biological tissues.

All of these models are able to describe the behaviour of PDMS. Here, the neo-Hookean model was used because only low deformation is studied, and it allows for shorter calculation time. The model was proposed in 1948 by Ronald Rivlin [270]. The Neo-Hookean model is used to translate the non-linear behaviour of a hyper-elastic material on large deformation which similar to the Hooke's law. Hyper-elastic material is initially linear and then transformed to be non-linear. Assume the material follows neo-Hookean representation, which has the strain energy expression of:

$$W = C_1(\overline{I_1} - 3), \tag{6.1}$$

Where C_1 is the material parameter which contain shear modulus of material. $\overline{I_1}$ is the first deviatoric strain invariant and W is the strain energy density

This chapter begins with a single block linear analysis to find the proper settings of block model and best software performance for comparison with non-linear analysis. Non-linear setting of block model is designed to match the experimental result. At later stage, the analysis is simplified from single block into thin film to reduce the convergence time.

6.2 Single Block Linear and Non-linear Simulation

6.2.1 Linear Specification

To understand the chemical and physical transition phenomenon on surface of complex systems of soft matters, the concept starts from a simple simulation of hole deformation on a rubber-like material under a compression pressure. This study is realise in microscopic scale and aims to understand how the hole becomes distorted according to its diameter and depth. A specific model was used to simulate the process at the beginning with standard setup. This model is in a basic cuboid shape with a square base and a hole with two variable parameters: diameter (Φ) and depth (H). Seven diameters (160µm, 120µm, 80µm, 50µm, 30µm, 20µm, 10µm) were used, along with different depths (38µm, 27µm, 21µm, 17µm, 14µm) for each diameter.

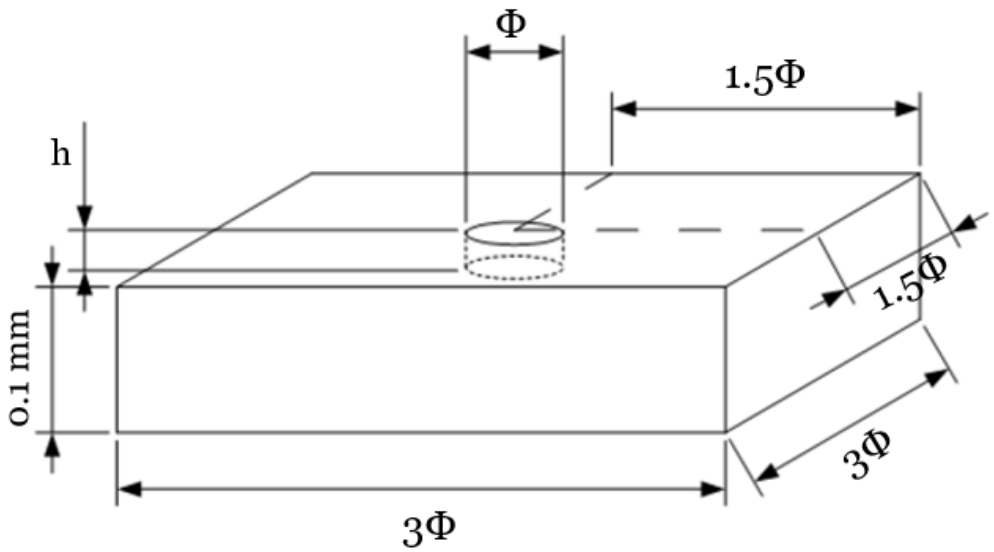

Figure 6.2 Specific dimensions of the single block model.

Hooke's law expresses a relation between stress (σ) and strain (ε) which fundamentally describes the behaviour of linear elastic material, represented as:

$$\sigma = E\varepsilon, \tag{6.2}$$

where 'E' is the material Young's modulus. However, non-linear elastic material has different behaviours in loading and unloading of the stress and strain relation. Therefore, the Hooke's law which describes the stress on a solid is proportional to the strain provided the stress is less than elastic limit which is unavailable in non-linear elastic material. Rubber material was used because of its hyper-elasticity and polymerizability [271]. It can withstand large strains (more than 500%) and this material is more or less incompressible, which means it has a Poisson ratio close to 0.5. The rubber material applied in this section has a density of approximately 990 kg/m^3, estimated Poisson's ratio (ν) of 0.49 (nearly incompressible) and Young's modulus, E, of 670kPa [272].

The geometry of the model was built in SolidWork with designed dimensions. **Table 6.1** summaries the desired elements mesh sizes and hole diameters. Diameter/Elements Size ratio were kept constant (6666.667) for simulation accuracy. A refinement of the elements near the edge of hole was applied to increase the accuracy in this area.

Table 6.1 Mesh element size of block with different diameters of hole

Diameter (μm)	160	120	80	50	30	20	10
Element Size (mm)	0.024	0.018	0.012	0.0075	0.0045	0.003	0.0015

A frictionless support (**Figure 6.3a**) was applied it permits movement in X-axis and Y-axis, rather than the fixed support (**Figure 6.3b**).

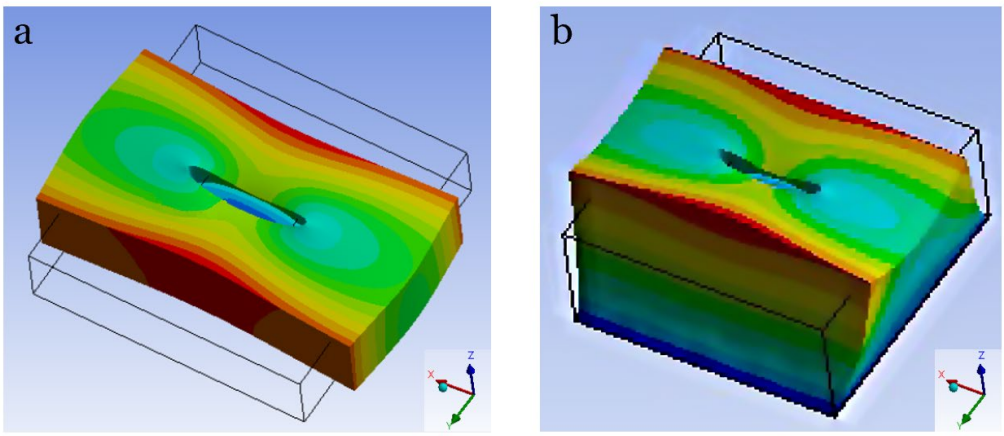

Figure 6.3 Graphic pictures showing the pressure responding of the model under a) frictionless support, and b) fixed support.

A compression pressure was applied on the two opposite sides of the block. To be able to compare the results, the same pressure value was applied for all parameter regimes. Total deformation was set as the 'solution' for diameter ratio calculation.

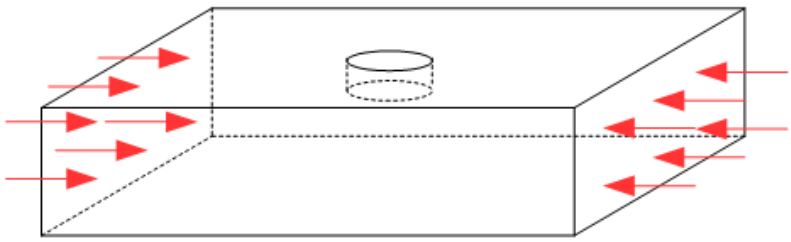

Figure 6.4 Illustration of compression pressure on block model (Red arrows indicate the applied pressure on sides of the block).

6.2.2 Results – Linear Setting

The deformation along the X axis, $\Delta\Phi_X$, and along the Y axis, $\Delta\Phi_Y$ were recorded for different strain values. A constant interval strain of 0.3 was applied.

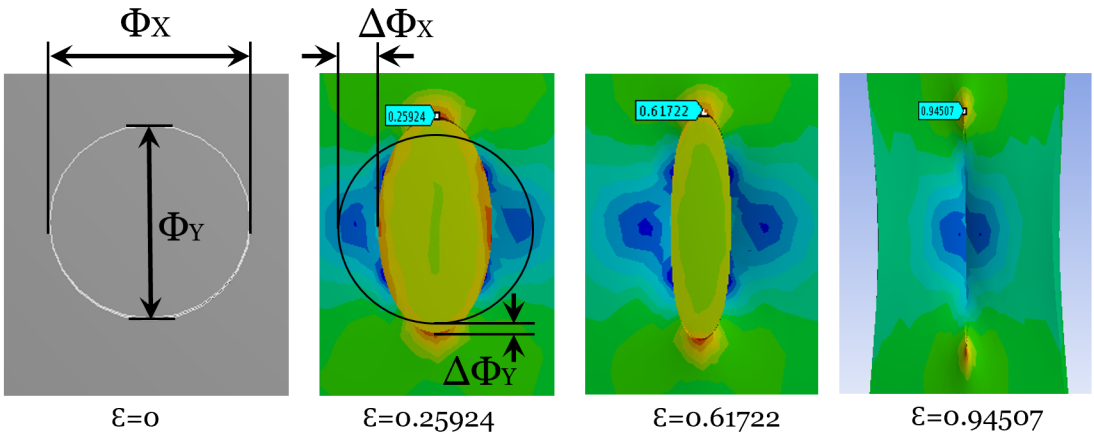

Figure 6.5 Illustration of diameter deformation on block model

The ratio of Φ_X/Φ_Y was recorded along with compression strain. Results was plotted together for seven different diameters. As shown in **Figure 6.6a**, the diameter has a significant impact on the deformation of the block. For all hole diameters, the ratio of Φ_X/Φ_Y decrease linearly with compression strain.

The smaller the diameter, the smaller the strain is needed for closing the hole. On the other hand, larger strains are required to switch off the large diameter holes. Only the case wherein Φ = 30 μm was simulated because it was found that the hole depth does not affect the deformation ratio (**Figure 6.6b**). All curves for five different hole depths collapsed onto each other. However, all these results were generated with linear setting which is based on the theoretical property, which could not reflect reality.

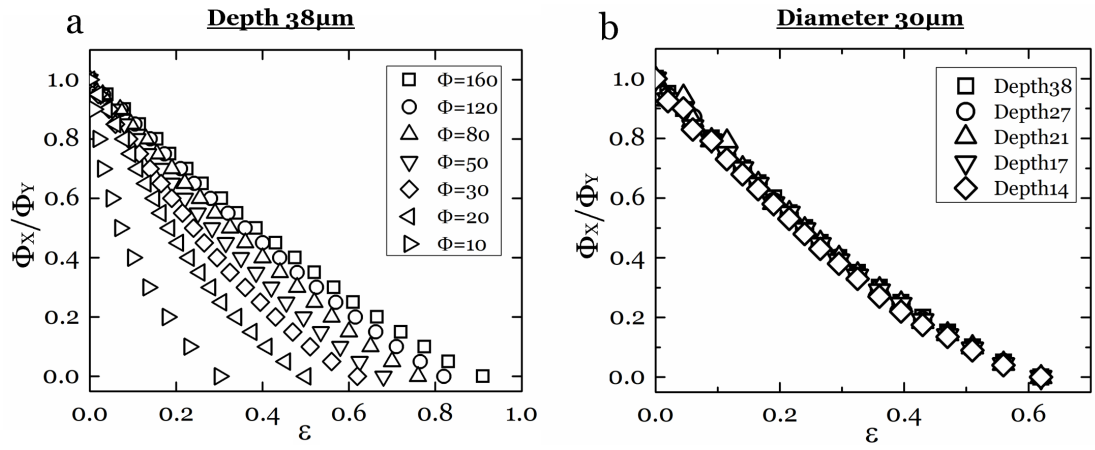

Figure 6.6 a) The development of diameter ratio with increasing strain for different hole diameters. b) The development of diameter ratio with increaing strain for different hole depths.

6.2.3 Non-linear Specification

As it is said above, to reach a maximal approach of the reality the neo-Hookean model was applied. For a compressible neo-Hookean material, the strain energy density is defined by [193]:

$$W = C_1(\bar{I_1} - 3) + D_1(J - 1)^2, \tag{6.3}$$

where C1 is the material constants, $\bar{I_1}$ is the first deviatoric strain invariant, $D1$ is the incompressibility parameter and W is strain energy density.

By integrating the neo-Hookean model it is expected to see perturbations on the surface. In fact, when rubber is distorted, a modification of the surface finishing can be observed, hence appearance of the waves and cracks. Two parameters, the initial shear modulus μ and the incompressibility parameter $D1$, need to be determined in order to apply neo-Hookean model. Shear modulus is the modulus of rigidity, it is the coefficient of elasticity for a shearing or torsion force. Initial shear modulus is defined by:

$$\mu_o = \frac{E}{2(1+v)}, \tag{6.4}$$

where E is Young's modulus of the material and v is Poisson's ratio, hence:

$$\mu_o = \frac{670000}{2(1+0.49)} = 224830 \text{ Pa} \tag{6.5}$$

Incompressibility parameter D1 is defined as:

$$D_1 = \frac{2}{K_o}, \tag{6.6}$$

where K_o is the initial bulk modulus.

Relative compressibility of a material can be assessed by the ratio of its initial bulk modulus, K_o, to its initial shear modulus, μ_o. Table below provides the representative values.

Table 6.2 Representative value between initial bulk modulus and initial shear modulus [273].

K_0/μ_0	Poisson's ratio
10	0.452
20	0.475
50	0.490
100	0.495
1,000	0.4995
10,000	0.49995

Hence the initial bulk modulus is calculated at Poisson's ratio of 0.49:

$$K_o = \mu_o \times 50 = 11241500\, Pa, \tag{6.7}$$

and the incompressibility parameter D_1 is:

$$D_1 = \frac{2}{K} = \frac{2}{11241500} = 177 \times 10^{-9}\,, \tag{6.8}$$

The same geometry model, mesh setting, and boundary condition were applied to new material. However, the solver was unable to converge the solution for previous boundary setting, therefore more frictionless supports were inserted. The pressure load was replaced by a displacement as it acts like

pressure on the model and the hole deformation will be the same with both loads.

Unfortunately, the analysis based on this Neo-Hookean model was extremely time consuming. At the end, the simulation failed to converge. At this point, another approach was generated to reduce the simulation process, by decreasing the elements. Instead of using a whole block of 3D model, a thin film geometry was generated to help reduce the analysis time.

6.3 Thin Film Non-linear Simulation

6.3.1 Non-linear Specification

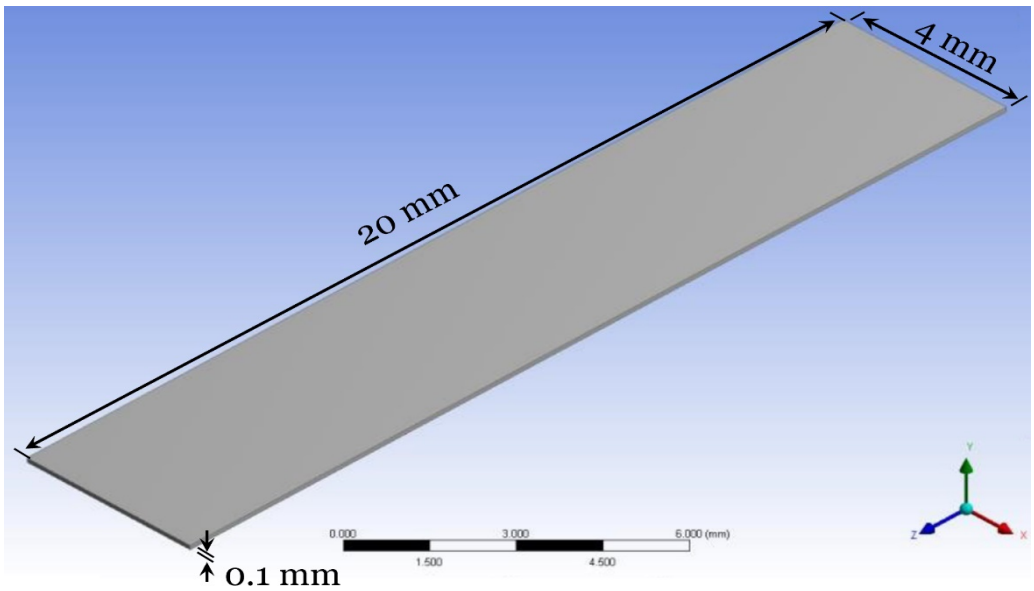

Figure 6.7 Geometry model of the thin film (20×4×0.1 mm).

A film was created with dimensions of 20 mm × 4 mm × 0.1 mm (**Figure 6.7**). Properties of PDMS were obtained from an in-lab stress-strain tensile test and were inserted into ANSYS.

For each strain-stress data point, Young's modulus was calculated by:

$$\sigma = E\varepsilon, \tag{6.9}$$

then an averaged value of Young's modulus was calculated: 299600 Pa. The same Poisson's ratio of 0.49 of PDMS was applied. Initial shear modulus, μ_0, and incompressibility parameter, D_1, was calculated again with the new Young's modulus.

$$\mu_o = \frac{E}{2(1+v)} = 100536 \text{ Pa}, \tag{6.10}$$

$$D_1 = \frac{2}{K} = 397 \times 10^{-9} \ , \tag{6.11}$$

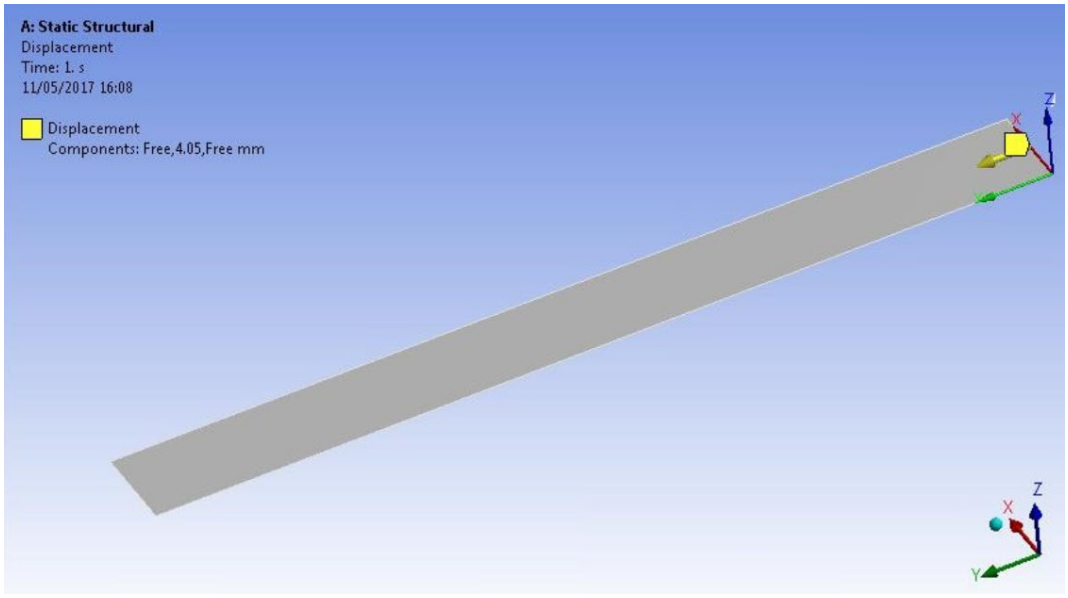

Figure 6.8 Geometry model of the thin film (20×4×0.1 mm) with one side fixed and another side under an imposed displacement.

As shown in **Figure 6.8**, a displacement was applied on one side of the thin film (along the Y-axis) to represent the force applied on the film, while the other side was fixed. The input value of the displacement was 4.05 mm. Initially, a meshing size of 0.001 mm was used which exceeded the limitation of the solving process, a large meshing size of 0.1 mm was subsequently used. To speed up the solving process, the length of the model was reduced, however the width of the model was chosen as the primary parameter and thus fixed.

6.3.2 Results

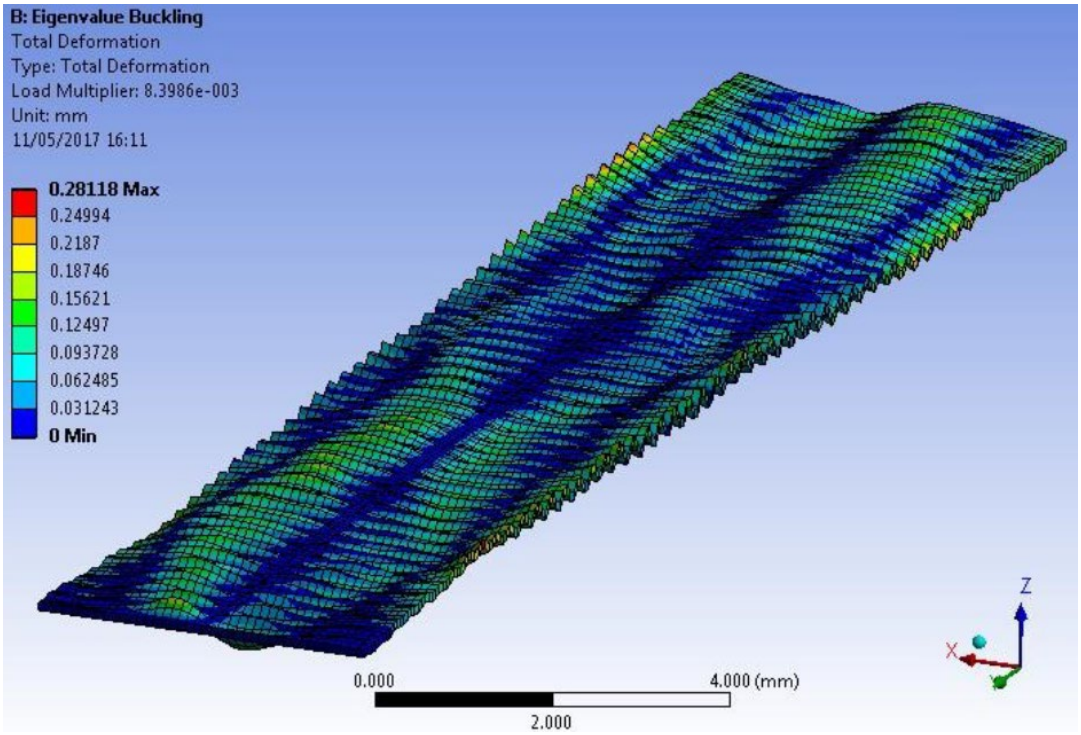

Figure 6.9 First approach of neo-Hookean simulation with film width of 4 mm.

The simulation result from the first approaching is shown below in **Figure 6.9**, continuous waves in Y-axis were observed in this 3D structure that represents the wrinkling phenomenon under compression force. However, the model shaping also went in X-axis that is not according with the real case

which is single direction wrinkle shape. This might be due to less-restrict boundary condition of the film.

Increasing the width of the film, it was found that the wider film is the large the load is needed to maintain the same strain change. To keep the displacement of 4.05 mm and to seek reasonable structure development, the width of the film was reduced. After several attempts, a film width of 2 mm was selected because wrinkle phenomenon was perfectly observed on the structure at this film width (**Figure 6.10**).

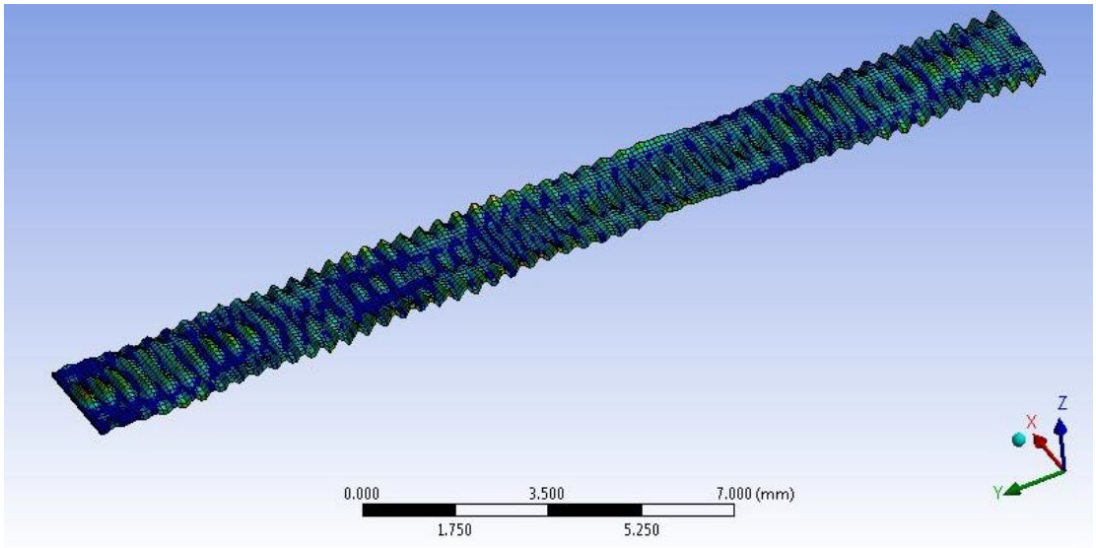

Figure 6.10 neo-Hookean simulation result with film width of 2 mm.

In previous setting, only one-layer thin film was presented. However, wrinkle is formed when a critical compressive load is applied on a bi-layer system where top stiff thin film has larger modulus than the bottom soft substrate. To mimic the soft substrate, an elastic support boundary condition

under the thin film was applied to represent the lower modulus. The software requires an input of material stiffness (k_o), it was calculated by:

$$k_o = \frac{AE}{L} = \frac{(0.2\times10^{-6})\times299600}{0.02} = 2.996, \qquad (6.12)$$

where A is the cross-sectional area, E is the Young's modulus and L is the length of thin film. The modulus mismatch was set from 1 to 50 in order to find the influence of modulus.

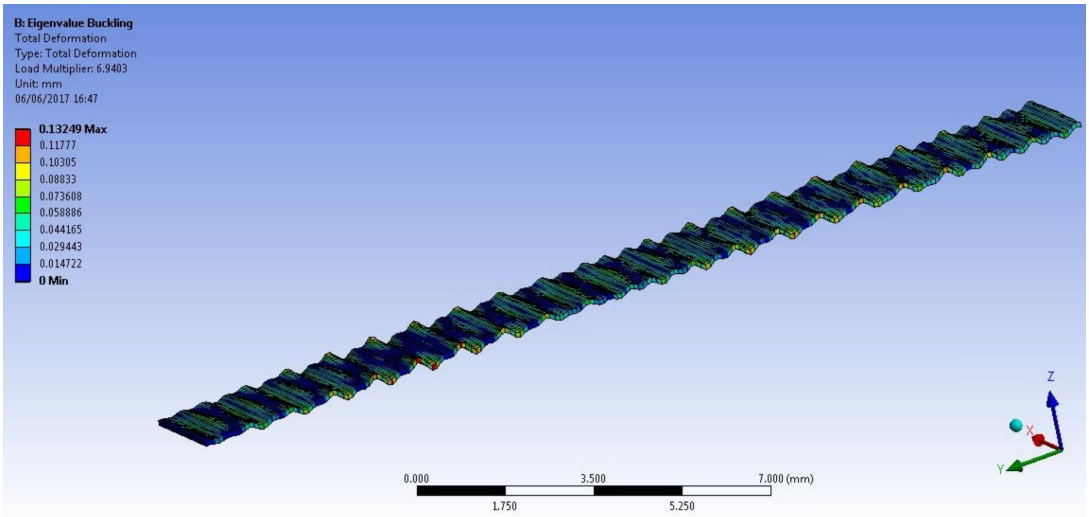

Figure 6.11 Neo-Hookean simulation result with higher modulus mismatch.

An interesting phenomenon was found during these simulations. With large modulus mismatch, which means the elastic support have lower modulus, the simulation result shows a uniform and regular wave that represent the wrinkle phenomenon (**Figure 6.11**). However, if the substrate has higher modulus that give lower modulus mismatch in bi-layers system, the simulation result is not as uniform as large-modulus-mismatch one. As shown in **Figure**

6.12, the wrinkle phenomenon was generated, but a mild disorder was also created under lower modulus mismatch condition.

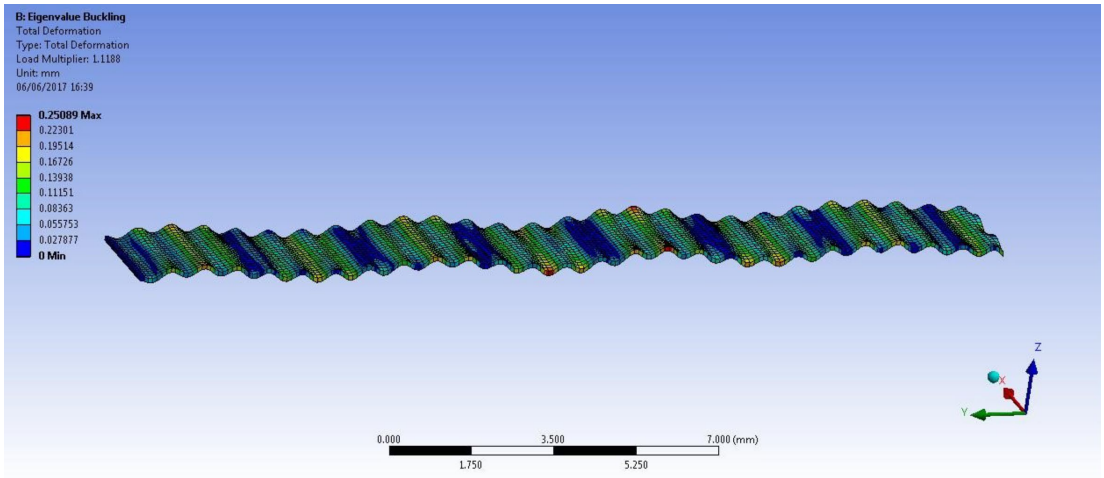

Figure 6.12 neo-Hookean simulation result with lower modulus mismatch.

The difference between these two cases suggests that the modulus mismatch has a significant influence on the thin film instability in a bi-layer system. To compare with experiment result, a modulus ratio of 100 was set in the elastic support boundary condition, and a new geometry model with holes on thin film was built to represent the experimental conditions. This simulation work is left for further act.

6.4 Summary

In this chapter, several approaches were used to investigate the linearity of rubber-like material, non-linearity of the hyper-elastic material, PDMS with properties input from literature and in-lab test. A linearity of material was investigated first to catch a glimpse of pattern transformation with the dependencies on geometrical variable of hole diameter. The result suggests diameter size indeed has influence on the switch-off strain of hole, but the model design was extremely for non-linear analysis. For non-linearity, related parameters were calculated to satisfy the simulation requirement on neo-Hookean model in ANSYS Workbench. With simple film design, it can create the periodic planar wrinkle to control instability evolution in certain conditions. The film model was significantly reducing the simulation process time. In addition, the bilayer system, where the film encountered an elastic support, shows the possibility to produce wrinkle phenomena with a further simplified approach. Although the specific controllable instability evolution towards a spatial lattice hole patterned surface has not yet come to a success with a 3D modelling design, the current result gives us a clearer 3D view on planar wrinkle over the mathematic simulation presented in chapter 3, and provides a possible solution for hyper-elasticity material simulation.

Chapter 7

Conclusion and Future Possibilities

7.1 Overall Conclusion

Various surface instabilities enable a convenient strategy of micro-engineered structure impart reversible patterned topography to a surface. Chapter 2 is focus on the classic system of a tiff layer on a soft substrate, which famously produces parallel harmonic wrinkles at modest uniaxial compression that period-double repeatedly at higher compressions and ultimately evolve into deep folds and creases. By introducing micron-scale planar Bravais lattice holes to spatially pattern the substrate, these instabilities were guided into a wide variety of different patterns, including wrinkling in parallel bands and star shape bands, and radically reduce the threshold compression. The experimental patterns and thresholds were understood by considering a simple plane-strain model for the patterned substrate-deformation, decorated by wrinkling on the stiff surface layer. The experiments also show localized wrinkle-crease transitions at modest compression, yielding a hierarchical surface with different generations of instability mixed together. By varying the geometrical inputs, the control over the stepwise evolution of surface morphologies was demonstrated. These results demonstrate considerable

control over both the pattern and threshold of a surface elastic instability and have relevance to many emerging applications of morphing surfaces, including in wearable/flexible electronics, bio-medical systems and optical devices.

In chapter 3, the wetting phenomena of liquid reshaping at micro and macro scale on a sinusoidal wrinkle and crease patterned surface was investigated. Non-uniform distributions of surface energy caused the anisotropic wetting and droplet deformation, while asymmetric physical patterns on a material surface induced the directional wetting. On an elastic wrinkled groove surface, it is noticed that a droplet can start imbibing into the grooves leading to an eventual filling of entire grooves as certain compressive strain is approached, hence, to change the droplet shape. To achieve highly controllable instabilities and a bi-axial switching droplet shape, a patterned elastic surface was created able to initialize localized surface instabilities and induce reversible surface morphology changes. At equilibrium, the topographic surface consists of a set of circular voids distribute an equilibrium manner. By using plasma treatment and mechanical stimuli, the evolution of the nano/micro-structure on surface was investigated, which form under mechanical stimuli and redistribute the surface energy. A droplet placed on our surface is pinned by the topographic features and deforms as the circular shapes elongate to elliptical shapes. The static, advancing and receding contact angles were measured before and after plasma treatment, showing the enhancement of the surface wettability due to changes in the surface chemistry, morphology and roughness.

In chapter 4, a theoretical approach of Finite Element Analysis was presented to understand the non-linearity of hyper-elasticity material and the possible morphology evolution under certain compressive load or displacement. Simulation was proceeded with different structure model design at variable stage. Both literature and in-lab test property of soft material were considered to find the appropriate parameters for neo-Hookean model analysis on the material non-linearity. The experimental patterned surface was simplified into single block and thin film structure to reduce the computer working process. The morphology transformation was analysed with simple plane-strain model and achieved a reasonable structure variation. However, patterned structure is still needed for further analysis to corresponding the experimental result to show localized wrinkle-crease transitions at compressive load and yield different a hierarchical surface by vary the geometrical input.

7.2 Future Possibilities

In this thesis, the bilayer system was investigated by focusing mechanism study of spatial patterned surface with external mechanical loading. Following with investigation on anisotropic droplet shape manipulation based on the soft material system. Though out our research work, various soft material on bilayer surface properties were presented such as topographic roughness evolution, surface morphology development, out-of-plane physical self-contact depth, patterned surface wettability and macro-

level droplet shaping. Although we have covered many aspects in soft material bilayer system, there are still limitations of our work. For example, the theoretical assumption on droplet shaping and material non-linearity simulation on bilayer system.

To follow up what we have investigated and uncovered in the previous chapters, three categories of potential aspects are classified here for future work.

- Hierarchical wrinkle and crease of multi-layered materials is expected to have many applications such surface coating, adhesion control, wetting control with hydrophobic/hydrophilic surfaces. More systematic study of morphology evolution of the multi-scale wrinkles and the reaction mechanism is needed. Regarding to different hierarchical morphologies, it is essential to have a guide of multi-layer structure durability design for surface pattern control.

- There has been some progress in studying surface instability induced droplet shape manipulation in our work. Surface wettability was investigated thought out the surface roughness analysis, morphology directional development, and capillary mechanism that induced droplet pinning. However, there still exists issues on accurately control the droplet shape in an area expanding manner with the bi-axially compression/stretch of substrate, and the experimental control of droplet motion transferability over an appreciable area. From experimental aspect,

droplet motion manipulated mechanics under viscoelasticity, dynamic loading, combined with anisotropic structure is still waiting to be explored.

- Much of recent progress in theoretical mechanics research was thanks to the advancement of computational mechanism, especially finite element method for multi-scale analysis. However, more efforts are still needed to develop reliable numerical methods to solving 3D surface instability calculations, droplet shaping analysis and the concept of non-linear pattern transformation.

Bibliography

[1] Zhang, X., Shi, F., Niu, J., Jiang, Y. & Wang, Z. Superhydrophobic surfaces: from structural control to functional application. *J. Mater. Chem.* **18**, 621–633 (2008).

[2] Shirtcliffe, N. J., McHale, G., Atherton, S. & Newton, M. I. An introduction to superhydrophobicity. *Adv. Colloid Interface Sci.* **161**, 124–138 (2010).

[3] Roach, P., Parker, T., Gadegaard, N. & Alexander, M. R. Surface strategies for control of neuronal cell adhesion: A review. *Surf. Sci. Rep.* **65**, 145–173 (2010).

[4] Debreczeny, M. P., Svec, W. A. & Wasielewski, M. R. Optical control of photogenerated ion pair lifetimes: An approach to a molecular switch. *Science (80-.).* **274**, 584–587 (1996).

[5] Duffy, D. C., McDonald, J. C., Schueller, O. J. A. & Whitesides, G. M. Rapid prototyping of microfluidic systems in poly(dimethylsiloxane). *Anal. Chem.* **70**, 4974–4984 (1998).

[6] Norman, J. J. & Desai, T. A. Control of Cellular Organization in Three Dimensions Using a Microfabricated Polydimethylsiloxane–Collagen Composite Tissue Scaffold. *Tissue Eng.* **11**, 378–386 (2005).

[7] Yu, J. Biodegradation-based polymer surface erosion and surface renewal for foul-release at low ship speeds. *Biofouling* **19**, 83–90 (2003).

[8] Kjellerup, B. V. *et al.* Monitoring of microbial souring in chemically treated, produced-water biofilm systems using molecular techniques. *J. Ind. Microbiol. Biotechnol.* **32**, 163–170 (2005).

[9] Colwill, R. M. & Rescorla, R. A. Evidence for the hierarchical structure of instrumental learning. *Anim. Learn. Behav.* **18**, 71–82 (1990).

[10] Nam, P. H. *et al.* A hierarchical structure and properties of intercalated polypropylene/clay nanocomposites. *Polymer (Guildf).* **42**, 9633–9640 (2001).

[11] Morariu, M. D. *et al.* Hierarchical structure formation and pattern replication induced by an electric field. *Nat. Mater.* **2**, 48—52 (2003).

[12] Ruckerl, B. & Jung, C. Hierarchical structure in the chaotic scattering off a magnetic dipole. *J. Phys. A. Math. Gen.* **27**, 6741–6758 (1994).

[13] Xia, F. & Jiang, L. Bio-inspired, smart, multiscale interfacial materials. *Adv. Mater.* **20**, 2842–2858 (2008).

[14] L.E. THE LOTUS EFFECT. (2010).

[15] Gao, X. *et al.* The Dry-Style Antifogging Properties of Mosquito Compound Eyes and Artificial Analogues Prepared by Soft Lithography. *Adv. Mater.* **19**, 2213–2217 (2007).

[16] Fearing, R. Smart Gecko Tape.

[17] Zawischa, D. Multiple-beam interference: structural colours, iridescence.

[18] Chen, D., Yoon, J., Chandra, D., Crosby, A. J. & Hayward, R. C. Stimuli-responsive buckling mechanics of polymer films. *J. Polym. Sci. Part B Polym. Phys.* **52**, 1441–1461 (2014).

[19] Eran, S., Marder, M. & Swinney, H. L. Leaves, Flowers and Garbage Bags: Making Waves. *Am. Sci.* **92**, 254–261 (2004).

[20] Vandeparre, H. *et al.* Wrinkling hierarchy in constrained thin sheets from suspended graphene to curtains. *Phys. Rev. Lett.* **106**, (2011).

[21] Li, B., Cao, Y.-P., Feng, X.-Q. & Gao, H. Mechanics of morphological instabilities and surface wrinkling in soft materials: a review. *Soft Matter* **8**, 5728–5745 (2012).

[22] Vandeparre, H. *et al.* Hierarchical wrinkling patterns. *Soft Matter* **6**, 5751–5756 (2010).

[23] Rogers, J. A., Someya, T. & Huang, Y. Materials and Mechanics for Stretchable Electronics. *Science (80-.).* **327**, 1603 LP-1607 (2010).

[24] Zhang, Z., Kim, K.-S. & Gao, H. An accordion model integrating self-cleaning, strong attachment and easy detachment functionalities of gecko adhesion AU - Zhang, Teng. *J. Adhes. Sci. Technol.* **28**, 226–239 (2014).

[25] Zhang, Z., Zhang, T., Zhang, Y. W., Kim, K.-S. & Gao, H. Strain-Controlled Switching of Hierarchically Wrinkled Surfaces between Superhydrophobicity and Superhydrophilicity. *Langmuir* **28**, 2753–2760 (2012).

[26] Cao, G., Chen, X., Li, C., Ji, A. & Cao, Z. Self-Assembled Triangular and Labyrinth Buckling Patterns of Thin Films on Spherical Substrates. *Phys. Rev. Lett.* **100**, 36102 (2008).

[27] Cullen, D. K. *et al.* Blast-induced color change in photonic crystals corresponds with brain pathology. *J. Neurotrauma* **28**, 2307—2318 (2011).

[28] Budday, S., Raybaud, C. & Kuhl, E. A mechanical model predicts morphological abnormalities in the developing human brain. *Sci. Rep.* **4**, 5644 (2014).

[29] Tallinen, T., Chung, J. Y., Biggins, J. S. & Mahadevan, L. Gyrification from constrained cortical expansion. *Proc. Natl. Acad. Sci.* **111**, 12667 LP-12672 (2014).

[30] Ahmed, S. F., Rho, G.-H., Lee, K.-R., Vaziri, A. & Moon, M.-W. High aspect ratio wrinkles on a soft polymer. *Soft Matter* **6**, 5709–5714 (2010).

[31] Dumais, J. & Steele, C. R. New Evidence for the Role of Mechanical Forces in the Shoot Apical Meristem. *J. Plant Growth Regul.* **19**, 7—18 (2000).

[32] Liang, H. & Mahadevan, L. The shape of a long leaf. *Proc. Natl. Acad. Sci.* **106**, 22049 LP-22054 (2009).

[33] Liang, H. & Mahadevan, L. Growth, geometry, and mechanics of a blooming lily. *Proc. Natl. Acad. Sci.* **108**, 5516 LP-5521 (2011).

[34] Armon, S., Efrati, E., Kupferman, R. & Sharon, E. Geometry and Mechanics in the Opening of Chiral Seed Pods. *Science (80-.).* **333**, 1726 LP-1730 (2011).

[35] Shipman, P. D. & Newell, A. C. Phyllotactic Patterns on Plants. *Phys. Rev. Lett.* **92**, 168102 (2004).

[36] Dervaux, J. & Ben Amar, M. Morphogenesis of Growing Soft Tissues. *Phys. Rev. Lett.* **101**, 68101 (2008).

[37] Katifori, E., Alben, S., Cerda, E., Nelson, D. R. & Dumais, J. Foldable structures and the natural design of pollen grains. *Proc. Natl. Acad. Sci.* **107**, 7635 LP-

7639 (2010).

[38] Yin, J., Cao, Z., Li, C., Sheinman, I. & Chen, X. Stress-driven buckling patterns in spheroidal core/shell structures. *Proc. Natl. Acad. Sci.* **105**, 19132 LP-19135 (2008).

[39] Basan, M., Joanny, J.-F., Prost, J. & Risler, T. Undulation Instability of Epithelial Tissues. *Phys. Rev. Lett.* **106**, 158101 (2011).

[40] Li, B., Jia, F., Cao, Y.-P., Feng, X.-Q. & Gao, H. Surface Wrinkling Patterns on a Core-Shell Soft Sphere. *Phys. Rev. Lett.* **106**, 234301 (2011).

[41] Goriely, A. & Vandiver, R. On the mechanical stability of growing arteries. *IMA J. Appl. Math.* **75**, 549–570 (2010).

[42] Forterre, Y., Skotheim, J. M., Dumais, J. & Mahadevan, L. How the Venus flytrap snaps. *Nature* **433**, 421 (2005).

[43] Suo, L. J. and S. C. and Z. Creases in soft tissues generated by growth. *EPL (Europhysics Lett.* **95**, 64002 (2011).

[44] Wyczalkowski, M. A., Chen, Z., Filas, B. A., Varner, V. D. & Taber, L. A. Computational models for mechanics of morphogenesis. *Birth Defects Res. C. Embryo Today* **96**, 132—152 (2012).

[45] Caviness, V. S. Mechanical model of brain convolutional development. *Science (80-.).* **189**, 18 LP-21 (1975).

[46] Bayly, P. V, Taber, L. A. & Kroenke, C. D. Mechanical forces in cerebral cortical folding: a review of measurements and models. *J. Mech. Behav. Biomed. Mater.* **29**, 568—581 (2014).

[47] Kücken, M. & Newell, A. C. A model for fingerprint formation. *Eur. Lett.* **68**, 141–146 (2004).

[48] Yang, W., Fung, T. C., Chian, K. S. & Chong, C. K. Instability of the two-layered thick-walled esophageal model under the external pressure and circular outer boundary condition. *J. Biomech.* **40**, 481—490 (2007).

[49] Li, B., Cao, Y.-P., Feng, X.-Q. & Yu, S.-W. Mucosal wrinkling in animal antra induced by volumetric growth. *Appl. Phys. Lett.* **98**, 153701 (2011).

[50] Li, B., Cao, Y., Feng, X.-Q. & Gao, H. *Surface wrinkling of mucosa induced by volumetric growth: Theory, simulation and experiment. Journal of the Mechanics and Physics of Solids* **59**, (2011).

[51] Moulton, D. E. & Goriely, A. Possible role of differential growth in airway wall remodeling in asthma. VO - 110 RT - Journal Article. *Journal of applied physiology (Bethesda, Md. : 1985) OP - 1003-1012*

[52] Savin, T. *et al.* On the growth and form of the gut. *Nature* **476**, 57 (2011).

[53] Hannezo, E., Prost, J. & Joanny, J.-F. Instabilities of Monolayered Epithelia: Shape and Structure of Villi and Crypts. *Phys. Rev. Lett.* **107**, 78104 (2011).

[54] Shyer, A. E. *et al.* Villification: How the Gut Gets Its Villi. *Science (80-.).* **342**, 212 LP-218 (2013).

[55] Ben Amar, M. & Jia, F. Anisotropic growth shapes intestinal tissues during embryogenesis. *Proc. Natl. Acad. Sci.* **110**, 10525 LP-10530 (2013).

[56] Blair, J. Probing Einstein's Brain for Clues to His Genius. (2015).

[57] Cai, S., Bertoldi, K. & Suo, Z. Osmotic collapse of a void in an elastomer : breathing , buckling and creasing †‡. 5770–5777 (2010). doi:10.1039/c0sm00451k

[58] Chater, E. & Hutchinson, J. W. On the Propagation of Bulges and Buckles. *J. Appl. Mech.* **51**, 269–277 (1984).

[59] Craighead, S. K. and B. R. I. and D. S. and S. S. and H. The pull-in behavior of electrostatically actuated bistable microstructures. *J. Micromechanics Microengineering* **18**, 55026 (2008).

[60] Hu, Y., Hiltner, A. & Baer, E. *Buckling in elastomer/plastic/elastomer 3-layer films*. *Polymer Composites - POLYM COMPOSITE* **25**, (2004).

[61] Bowden, N., Brittain, S., Evans, A. G., Hutchinson, J. W. & Whitesides, G. M. Spontaneous formation of ordered structures in thin films of metals supported on an elastomeric polymer. *Nature* **393**, 146 (1998).

[62] Kim, P., Abkarian, M. & Stone, H. A. Hierarchical folding of elastic membranes under biaxial compressive stress. *Nat. Mater.* **10**, 952 (2011).

[63] Hohlfeld, E. & Mahadevan, L. Unfolding the Sulcus. *Phys. Rev. Lett.* **106**, 105702 (2011).

[64] Brau, F. *et al.* Multiple-length-scale elastic instability mimics parametric resonance of nonlinear oscillators. *Nat. Phys.* **7**, 56 (2010).

[65] Chen, D., Cai, S., Suo, Z. & Hayward, R. C. Surface energy as a barrier to creasing of elastomer films: An elastic analogy to classical nucleation. *Phys. Rev. Lett.* **109**, 1–5 (2012).

[66] Stafford, C. M. *et al.* A buckling-based metrology for measuring the elastic moduli of polymeric thin films. *Nat. Mater.* **3**, 545 (2004).

[67] Chung, J. Y., Nolte, A. J. & Stafford, C. M. Surface Wrinkling: A Versatile Platform for Measuring Thin-Film Properties. *Adv. Mater.* **23**, 349–368 (2011).

[68] Metrology, B. *et al.* Measuring the Modulus of Soft Polymer Networks via a Buckling-Based Metrology. 4138–4143 (2006). doi:10.1021/ma060266b

[69] Huang, J. *et al.* Capillary Wrinkling of Floating Thin Polymer Films. *Science (80-.).* **317**, 650 LP-653 (2007).

[70] Howarter, J. A. & Stafford, C. M. Instabilities as a measurement tool for soft materials. *Soft Matter* **6**, 5661–5666 (2010).

[71] Khang, B. D., Rogers, J. A. & Lee, H. H. Mechanical Buckling : Mechanics , Metrology , and Stretchable Electronics. 1526–1536 (2009). doi:10.1002/adfm.200801065

[72] Khang, D.-Y., Jiang, H., Huang, Y. & Rogers, J. A. A Stretchable Form of Single-Crystal Silicon for High-Performance Electronics on Rubber Substrates. *Science (80-.).* **311**, 208 LP-212 (2006).

[73] Lee, S. *et al.* Reversibly Stretchable and Tunable Terahertz Metamaterials with Wrinkled Layouts. *Adv. Mater.* **24**, 3491–3497 (2012).

[74] Lipomi, D. J., Tee, B. C.-K., Vosgueritchian, M. & Bao, Z. Stretchable Organic Solar Cells. *Adv. Mater.* **23**, 1771–1775 (2011).

[75] White, M. S. *et al.* Ultrathin, highly flexible and stretchable PLEDs. *Nat.*

Photonics **7**, 811 (2013).

[76] Kim, J. B. *et al.* Wrinkles and deep folds as photonic structures in photovoltaics. *Nat. Photonics* **6**, 327 (2012).

[77] Chen, A. *et al.* Shrink-Film Configurable Multiscale Wrinkles for Functional Alignment of Human Embryonic Stem Cells and their Cardiac Derivatives. *Adv. Mater.* **23**, 5785–5791 (2011).

[78] Guvendiren, M. & Burdick, J. A. Stem Cell Response to Spatially and Temporally Displayed and Reversible Surface Topography. *Adv. Healthc. Mater.* **2**, 155–164 (2013).

[79] Kim, J., Yoon, J. & Hayward, R. C. Dynamic display of biomolecular patterns through an elastic creasing instability of stimuli-responsive hydrogels. *Nat. Mater.* **9**, 159 (2009).

[80] Lin, P.-C., Vajpayee, S., Jagota, A., Hui, C.-Y. & Yang, S. Mechanically tunable dry adhesive from wrinkled elastomers. *Soft Matter* **4**, 1830–1835 (2008).

[81] Chan, E. P., Smith, E. J., Hayward, R. C. & Crosby, A. J. Surface Wrinkles for Smart Adhesion. *Adv. Mater.* **20**, 711–716 (2008).

[82] Rahmawan, Y., Chen, C.-M. & Yang, S. Recent advances in wrinkle-based dry adhesion. *Soft Matter* **10**, 5028–5039 (2014).

[83] Chung, J. Y., Youngblood, J. P. & Stafford, C. M. Anisotropic wetting on tunable micro-wrinkled surfaces. *Soft Matter* **3**, 1163–1169 (2007).

[84] Lin, P. & Yang, S. Mechanically switchable wetting on wrinkled elastomers with dual-scale roughness. 1011–1018 (2009). doi:10.1039/b814145b

[85] Xia, D., Johnson, L. M. & Lõpez, G. P. Anisotropic wetting surfaces with one-dimesional and directional structures: Fabrication approaches, wetting properties and potential applications. *Adv. Mater.* **24**, 1287–1302 (2012).

[86] Lee, S. G. *et al.* Switchable Transparency and Wetting of Elastomeric Smart Windows. *Adv. Mater.* **22**, 5013–5017 (2010).

[87] Mei, Y., Thurmer, D. J., Cavallo, F., Kiravittaya, S. & Schmidt, O. G. Semiconductor Sub-Micro-/ Nanochannel Networks by Deterministic Layer Wrinkling. *Adv. Mater.* **19**, 2124–2128 (2007).

[88] Chung, S., Lee, J. H., Moon, M.-W., Han, J. & Kamm, R. D. Non-Lithographic Wrinkle Nanochannels for Protein Preconcentration. *Adv. Mater.* **20**, 3011–3016 (2008).

[89] Khare, K., Zhou, J. & Yang, S. Tunable Open-Channel Microfluidics on Soft Poly(dimethylsiloxane) (PDMS) Substrates with Sinusoidal Grooves. *Langmuir* **25**, 12794–12799 (2009).

[90] E. Hohlfeld. Creasing, post-bifurcations and the spontaneous breakdown of scale invariance. (Harvard University, 2008).

[91] Pocivavsek, L. *et al.* Stress and Fold Localization in Thin Elastic Membranes. *Science (80-.).* **320**, 912 LP-916 (2008).

[92] Cao, Y. & Hutchinson, J. W. Wrinkling Phenomena in Neo-Hookean Film/Substrate Bilayers. *J. Appl. Mech.* **79**, 31019 (2012).

[93] Huang, Z. Y., Hong, W. & Suo, Z. Ã. Nonlinear analyses of wrinkles in a film

bonded to a compliant substrate. **53**, 2101–2118 (2005).

[94] W., H. J. The role of nonlinear substrate elasticity in the wrinkling of thin films. *Philos. Trans. R. Soc. A Math. Phys. Eng. Sci.* **371**, 20120422 (2013).

[95] Kohn, R. V & Nguyen, H.-M. Analysis of a Compressed Thin Film Bonded to a Compliant Substrate: The Energy Scaling Law. *J. Nonlinear Sci.* **23**, 343–362 (2013).

[96] Cai, S., Chen, D., Suo, Z. & Hayward, R. C. Creasing instability of elastomer films. *Soft Matter* **8**, 1301–1304 (2012).

[97] Audoly, B. & Boudaoud, A. Buckling of a stiff film bound to a compliant substrate—Part I:: Formulation, linear stability of cylindrical patterns, secondary bifurcations. *J. Mech. Phys. Solids* **56**, 2401–2421 (2008).

[98] Genzer, J. & Groenewold, J. Soft matter with hard skin: From skin wrinkles to templating and material characterization. *Soft Matter* **2**, 310–323 (2006).

[99] Groenewold, J. Wrinkling of plates coupled with soft elastic media. **298**, 32–45 (2001).

[100] Cai, K. L. and D. G. and S. Gravity-induced wrinkling of thin films on soft substrates. *EPL (Europhysics Lett.* **100**, 54004 (2012).

[101] Biot, M. A. Instability of a continuously inhomogeneous viscoelastic half-space under initial stress. *J. Franklin Inst.* **270**, 190–201 (1960).

[102] Choi, H.-J. *et al.* Wrinkle-Based Measurement of Elastic Modulus of Nano-Scale Thin Pt Film Deposited on Polymeric Substrate: Verification and Uncertainty Analysis. *Exp. Mech.* **50**, 635–641 (2010).

[103] Cerda, E. & Mahadevan, L. Geometry and Physics of Wrinkling. *Phys. Rev. Lett.* **90**, 74302 (2003).

[104] Chen, X. & Hutchinson, J. W. Herringbone Buckling Patterns of Compressed Thin Films on Compliant Substrates. *J. Appl. Mech.* **71**, 597–603 (2004).

[105] Danov, K. D., Kralchevsky, P. A. & Stoyanov, S. D. Elastic Langmuir Layers and Membranes Subjected to Unidirectional Compression: Wrinkling and Collapse. *Langmuir* **26**, 143–155 (2010).

[106] Efimenko, K. *et al.* Nested self-similar wrinkling patterns in skins. *Nat. Mater.* **4**, 293 (2005).

[107] Cai, S., Breid, D., Crosby, A. J., Suo, Z. & Hutchinson, J. W. Periodic patterns and energy states of buckled films on compliant substrates. *J. Mech. Phys. Solids* **59**, 1094–1114 (2011).

[108] Breid, D. & Crosby, A. J. Effect of stress state on wrinkle morphology. *Soft Matter* **7**, 4490–4496 (2011).

[109] Yin, J., Yagüe, J. L., Eggenspieler, D., Gleason, K. K. & Boyce, M. C. Deterministic Order in Surface Micro-Topologies through Sequential Wrinkling. *Adv. Mater.* **24**, 5441–5446 (2012).

[110] Lin, P.-C. & Yang, S. Spontaneous formation of one-dimensional ripples in transit to highly ordered two-dimensional herringbone structures through sequential and unequal biaxial mechanical stretching. *Appl. Phys. Lett.* **90**, 241903 (2007).

[111] Cerda, E., Ravi-Chandar, K. & Mahadevan, L. Wrinkling of an elastic sheet under tension. *Nature* **419**, 579 (2002).

[112] Bico, A. T. and F. B. and B. R. and J. Stretch-induced wrinkles in reinforced membranes: From out-of-plane to in-plane structures. *EPL (Europhysics Lett.* **96**, 64001 (2011).

[113] Nayyar, V., Ravi-Chandar, K. & Huang, R. Stretch-induced stress patterns and wrinkles in hyperelastic thin sheets. *Int. J. Solids Struct.* **48**, 3471–3483 (2011).

[114] Volynskii, A. L., Bazhenov, S., Lebedeva, O. V & Bakeev, N. F. Mechanical buckling instability of thin coatings deposited on soft polymer substrates. *J. Mater. Sci.* **35**, 547–554 (2000).

[115] Wong, W. & Pellegrino, S. *Wrinkled membranes Part I: Experiments*. *Journal of Mechanics of Materials and Structures - J MECH MATER STRUCT* **1**, (2006).

[116] Ciarletta, P., Destrade, M. & Gower, A. L. Shear instability in skin tissue. *Q. J. Mech. Appl. Math.* **66**, 273–288 (2013).

[117] Destrade, M., Gilchrist, M. D., Motherway, J. A. & Murphy, J. G. Bimodular rubber buckles early in bending. *Mech. Mater.* **42**, 469–476 (2010).

[118] Destrade, M., Ní Annaidh, A. & Coman, C. D. Bending instabilities of soft biological tissues. *Int. J. Solids Struct.* **46**, 4322–4330 (2009).

[119] BIOT, M. A. Surface instability of rubber in compression. *Appl. Sci. Res. Sect. A* **12**, 168–182 (1963).

[120] A., B. M. & Crisp, B. E. Interfacial instability in finite elasticity under initial stress. *Proc. R. Soc. London. Ser. A. Math. Phys. Sci.* **273**, 340–344 (1963).

[121] Jiang, H. *et al.* Finite deformation mechanics in buckled thin films on compliant supports. *Proc. Natl. Acad. Sci.* **104**, 15607 LP-15612 (2007).

[122] Song, J. *et al.* Buckling of a stiff thin film on a compliant substrate in large deformation. *Int. J. Solids Struct.* **45**, 3107–3121 (2008).

[123] Li, B., Huang, S.-Q. & Feng, X.-Q. Buckling and postbuckling of a compressed thin film bonded on a soft elastic layer: a three-dimensional analysis. *Arch. Appl. Mech.* **80**, 175 (2009).

[124] Trujillo, V., Kim, J. & Hayward, R. C. Creasing instability of surface-attached hydrogels. *Soft Matter* **4**, 564–569 (2008).

[125] Gent, A. N. & Cho, I. S. Surface Instabilities in Compressed or Bent Rubber Blocks. *Rubber Chem. Technol.* **72**, 253–262 (1999).

[126] Hong, W., Zhao, X. & Suo, Z. Formation of creases on the surfaces of elastomers and gels. *Appl. Phys. Lett.* **95**, 111901 (2009).

[127] Wang, Q. & Zhao, X. Phase Diagrams of Instabilities in Compressed Film-Substrate Systems. *J. Appl. Mech.* **81**, 510041–5100410 (2014).

[128] Ghatak, A. & Das, A. L. Kink Instability of a Highly Deformable Elastic Cylinder. *Phys. Rev. Lett.* **99**, 76101 (2007).

[129] Mora, S., Abkarian, M., Tabuteau, H. & Pomeau, Y. Surface instability of soft solids under strain. *Soft Matter* **7**, 10612–10619 (2011).

[130] Xu, B., Chen, D. & Hayward, R. C. Mechanically Gated Electrical Switches by

Creasing of Patterned Metal/Elastomer Bilayer Films. *Adv. Mater.* **26**, 4381–4385 (2014).

[131] Tanaka, T. Kinetics of phase transition in polymer gels. *Phys. A Stat. Mech. its Appl.* **140**, 261–268 (1986).

[132] Pandey, A. & Holmes, D. P. Swelling-induced deformations: a materials-defined transition from macroscale to microscale deformations. *Soft Matter* **9**, 5524–5528 (2013).

[133] Weiss, F. *et al.* Creases and wrinkles on the surface of a swollen gel. *J. Appl. Phys.* **114**, 73507 (2013).

[134] Zalachas, N., Cai, S., Suo, Z. & Lapusta, Y. Crease in a ring of a pH-sensitive hydrogel swelling under constraint. *Int. J. Solids Struct.* **50**, 920–927 (2013).

[135] Kim, J. Morphological analysis of crease patterns formed on surface-attached hydrogel with a gradient in thickness. *J. Appl. Polym. Sci.* **131**, (2014).

[136] Tanaka, T. *et al.* Mechanical instability of gels at the phase transition. *Nature* **325**, 796 (1987).

[137] Yoon, J., Kim, J. & Hayward, R. C. Nucleation, growth, and hysteresis of surface creases on swelled polymer gels. *Soft Matter* **6**, 5807–5816 (2010).

[138] Guvendiren, M., Burdick, J. A. & Yang, S. Solvent induced transition from wrinkles to creases in thin film gels with depth-wise crosslinking gradients. *Soft Matter* **6**, 5795–5801 (2010).

[139] Ortiz, O., Vidyasagar, A., Wang, J. & Toomey, R. Surface Instabilities in Ultrathin, Cross-Linked Poly(N-isopropylacrylamide) Coatings. *Langmuir* **26**, 17489–17494 (2010).

[140] Dervaux, J., Couder, Y., Guedeau-Boudeville, M.-A. & Ben Amar, M. Shape Transition in Artificial Tumors: From Smooth Buckles to Singular Creases. *Phys. Rev. Lett.* **107**, 18103 (2011).

[141] Dervaux, J. & Amar, M. Ben. Mechanical Instabilities of Gels. *Annu. Rev. Condens. Matter Phys.* **3**, 311–332 (2012).

[142] Arifuzzaman, M., Wu, Z. L., Kurokawa, T., Kakugo, A. & Gong, J. P. Swelling-induced long-range ordered structure formation in polyelectrolyte hydrogel. *Soft Matter* **8**, 8060–8066 (2012).

[143] Barros, W., de Azevedo, E. N. & Engelsberg, M. Surface pattern formation in a swelling gel. *Soft Matter* **8**, 8511–8516 (2012).

[144] Wang, Q., Zhang, L. & Zhao, X. Creasing to Cratering Instability in Polymers under Ultrahigh Electric Fields. *Phys. Rev. Lett.* **106**, 118301 (2011).

[145] Wang, Q., Niu, X., Pei, Q., Dickey, M. D. & Zhao, X. Electromechanical instabilities of thermoplastics: Theory and in situ observation. *Appl. Phys. Lett.* **101**, 141911 (2012).

[146] Wang, Q. & Zhao, X. Creasing-wrinkling transition in elastomer films under electric fields. *Phys. Rev. E* **88**, 42403 (2013).

[147] Park, H. S., Wang, Q., Zhao, X. & Klein, P. A. Electromechanical instability on dielectric polymer surface: Modeling and experiment. *Comput. Methods Appl. Mech. Eng.* **260**, 40–49 (2013).

[148] Xu, B. & Hayward, R. C. Low-Voltage Switching of Crease Patterns on Hydrogel Surfaces. *Adv. Mater.* **25**, 5555–5559 (2013).

[149] Wang, Q., Robinson, D. & Zhao, X. On-demand hierarchical patterning with electric fields. *Appl. Phys. Lett.* **104**, 231605 (2014).

[150] Yoon, J., Bian, P., Kim, J., McCarthy, T. J. & Hayward, R. C. Local Switching of Chemical Patterns through Light-Triggered Unfolding of Creased Hydrogel Surfaces. *Angew. Chemie Int. Ed.* **51**, 7146–7149 (2012).

[151] Mazen, D., Teng, Z., Ruike, Z., Huajian, G. & Kyung-Suk, K. Ruga mechanics of creasing: from instantaneous to setback creases. *Proc. R. Soc. A Math. Phys. Eng. Sci.* **469**, 20120753 (2013).

[152] Mazen, D. & Kyung-Suk, K. Ruga-formation instabilities of a graded stiffness boundary layer in a neo-Hookean solid. *Proc. R. Soc. A Math. Phys. Eng. Sci.* **470**, 20140218 (2014).

[153] Hohlfeld, E. *Creasing, point-bifurcations, and the spontaneous breakdown of scale-invariance*. (2008).

[154] Hohlfeld, E. & Mahadevan, L. Scale and Nature of Sulcification Patterns. *Phys. Rev. Lett.* **109**, 25701 (2012).

[155] Hohlfeld, E. Coexistence of Scale-Invariant States in Incompressible Elastomers. *Phys. Rev. Lett.* **111**, 185701 (2013).

[156] Gabriel, P., Fukahori, Y., Thomas, A. G. & Busfield, J. J. C. FEA MODELING OF SCHALLAMACH WAVES. *Rubber Chem. Technol.* **83**, 358–367 (2010).

[157] Shivapooja, P. *et al.* Bioinspired Surfaces with Dynamic Topography for Active Control of Biofouling. *Adv. Mater.* **25**, 1430–1434 (2013).

[158] Chan, E. P., Karp, J. M. & Langer, R. S. A 'Self-Pinning' Adhesive Based on Responsive Surface Wrinkles. *J. Polym. Sci. B. Polym. Phys.* **49**, 40–44 (2011).

[159] Saha, K. *et al.* Surface creasing instability of soft polyacrylamide cell culture substrates. *Biophys. J.* **99**, L94–L96 (2010).

[160] Jeong-Yun, S., Shuman, X., Myoung-Woon, M., Hwan, O. K. & Kyung-Suk, K. Folding wrinkles of a thin stiff layer on a soft substrate. *Proc. R. Soc. A Math. Phys. Eng. Sci.* **468**, 932–953 (2012).

[161] Pocivavsek, L. *et al.* Geometric tools for complex interfaces: from lung surfactant to the mussel byssus. *Soft Matter* **5**, 1963–1968 (2009).

[162] Brau, F., Damman, P., Diamant, H. & Witten, T. A. Wrinkle to fold transition: influence of the substrate response. *Soft Matter* **9**, 8177–8186 (2013).

[163] Ebata, Y., Croll, A. B. & Crosby, A. J. Wrinkling and strain localizations in polymer thin films. *Soft Matter* **8**, 9086–9091 (2012).

[164] Audoly, B. Localized buckling of a floating elastica. *Phys. Rev. E* **84**, 11605 (2011).

[165] Croll, A. *Pattern Driven Stress Localization in Thin Diblock Copolymer Films*. *Macromolecules* **45**, (2012).

[166] Holmes, D. P. & Crosby, A. J. Draping Films: A Wrinkle to Fold Transition. *Phys. Rev. Lett.* **105**, 38303 (2010).

[167] Leahy, B. D. *et al.* Geometric Stability and Elastic Response of a Supported

Nanoparticle Film. *Phys. Rev. Lett.* **105**, 58301 (2010).

[168] Reis, P. M., Corson, F., Boudaoud, A. & Roman, B. Localization through Surface Folding in Solid Foams under Compression. *Phys. Rev. Lett.* **103**, 45501 (2009).

[169] Zhao, R., Zhang, T., Diab, M., Gao, H. & Kim, K.-S. The primary bilayer ruga-phase diagram I: Localizations in ruga evolution. *Extrem. Mech. Lett.* **4**, 76–82 (2015).

[170] Cao, C., Chan, H. F., Zang, J., Leong, K. W. & Zhao, X. Harnessing Localized Ridges for High-Aspect-Ratio Hierarchical Patterns with Dynamic Tunability and Multifunctionality. *Adv. Mater.* **26**, 1763–1770 (2014).

[171] Zang, J., Zhao, X., Cao, Y. & Hutchinson, J. W. Localized ridge wrinkling of stiff films on compliant substrates. *J. Mech. Phys. Solids* **60**, 1265–1279 (2012).

[172] Takei, A., Jin, L., Hutchinson, J. W. & Fujita, H. Ridge Localizations and Networks in Thin Films Compressed by the Incremental Release of a Large Equi-biaxial Pre-stretch in the Substrate. *Adv. Mater.* **26**, 4061–4067 (2014).

[173] Yanping, C. & W., H. J. From wrinkles to creases in elastomers: the instability and imperfection-sensitivity of wrinkling. *Proc. R. Soc. A Math. Phys. Eng. Sci.* **468**, 94–115 (2012).

[174] Cassie, A. B. D. & Baxter, S. Wettability of porous surfaces. *Trans. Faraday Soc.* **40**, 546–551 (1944).

[175] Liu, C., Ju, J., Zheng, Y. & Jiang, L. Asymmetric ratchet effect for directional transport of fog drops on static and dynamic butterfly wings. *ACS Nano* **8**, 1321–1329 (2014).

[176] Liu, Y., Wang, J. & Zhang, X. Accurate determination of the vapor-liquid-solid contact line tension and the viability of Young equation. *Sci. Rep.* **3**, 1–6 (2013).

[177] Wenzel, R. N. Resistance of solid surfaces to wetting by water. *Ind. Eng. Chem.* **28**, 988–994 (1936).

[178] Gao, L. & Mccarthy, T. J. Contact Angle Hysteresis Explained. 6234–6237 (2006). doi:10.1021/la060254j

[179] Kota, A. K., Mabry, J. M. & Tuteja, A. Superoleophobic surfaces: design criteria and recent studies. *Surf. Innov.* **1**, 71–83 (2013).

[180] Bae, W. G. *et al.* 25th anniversary article: Scalable multiscale patterned structures inspired by nature: The role of hierarchy. *Adv. Mater.* **26**, 675–699 (2014).

[181] Hatton, B. D. & Aizenberg, J. Writing on superhydrophobic nanopost arrays: Topographic design for bottom-up assembly. *Nano Lett.* **12**, 4551–4557 (2012).

[182] Kusumaatmaja, H., Vrancken, R. J., Bastiaansen, C. W. M. & Yeomans, J. M. Anisotropic Drop Morphologies on Corrugated Surfaces. *Langmuir* **24**, 7299–7308 (2008).

[183] Zhang, F. & Low, H. Y. Anisotropic Wettability on Imprinted Hierarchical Structures. *Langmuir* **23**, 7793–7798 (2007).

[184] Yao, X. *et al.* Adaptive fluid-infused porous films with tunable transparency and wettability. *Nat. Mater.* **12**, 529 (2013).

[185] Nakajima, A. Design of hydrophobic surfaces for liquid droplet control. *Npg Asia Mater.* **3**, 49 (2011).

[186] Smith, J. D. *et al.* Droplet mobility on lubricant-impregnated surfaces. *Soft Matter* **9**, 1772–1780 (2013).

[187] Biot, M. A. *Mechanics of incremental deformation*. (Wiley, 1965).

[188] Rahmawan, Y., Moon, M.-W., Kim, K.-S., Lee, K.-R. & Suh, K.-Y. Wrinkled, Dual-Scale Structures of Diamond-Like Carbon (DLC) for Superhydrophobicity. *Langmuir* **26**, 484–491 (2010).

[189] Tallinen, T., Biggins, J. S. & Mahadevan, L. Surface Sulci in Squeezed Soft Solids. *Phys. Rev. Lett.* **110**, 24302 (2013).

[190] Mariotti, G., Pruss, S. B., Perron, J. T. & Bosak, T. Microbial shaping of sedimentary wrinkle structures. *Nat. Geosci.* **7**, 736 (2014).

[191] Liu, Z. *et al.* Ultrathin high-temperature oxidation-resistant coatings of hexagonal boron nitride. *Nat. Commun.* **4**, 2541 (2013).

[192] Gibbs, J. W. *Scientific Papers*. (Dover, 1991).

[193] Ogden, R. W. *Non-Linear Elastic Deformations*. (Courier Corporation, 2013).

[194] Bhavikatti, S. S. *Finite Element Analysis*. (New Age International, 2005).

[195] Kim, J., Hanna, J. A., Byun, M., Santangelo, C. D. & Hayward, R. C. Designing Responsive Buckled Surfaces by Halftone Gel Lithography. *Science (80-.).* **335**, 1201 LP-1205 (2012).

[196] Jeon, S.-J., Hauser, A. W. & Hayward, R. C. Shape-Morphing Materials from Stimuli-Responsive Hydrogel Hybrids. *Acc. Chem. Res.* **50**, 161–169 (2017).

[197] Liu, Y., Boyles, J. K., Genzer, J. & Dickey, M. D. Self-folding of polymer sheets using local light absorption. *Soft Matter* **8**, 1764–1769 (2012).

[198] Stuart, M. A. C. *et al.* Emerging applications of stimuli-responsive polymer materials. *Nat. Mater.* **9**, 101 (2010).

[199] Xu, B. B., Liu, Q., Suo, Z. & Hayward, R. C. Reversible Electrochemically Triggered Delamination Blistering of Hydrogel Films on Micropatterned Electrodes. *Adv. Funct. Mater.* **26**, 3218–3225 (2016).

[200] Holmes, D. P., Tavakol, B., Froehlicher, G. & Stone, H. A. Control and manipulation of microfluidic flow via elastic deformations. *Soft Matter* **9**, 7049–7053 (2013).

[201] Ohzono, T. & Monobe, H. Morphological Transformation of a Liquid Micropattern on Dynamically Tunable Microwrinkles. *Langmuir* **26**, 6127–6132 (2010).

[202] Park, S., Huh, Y. S., Craighead, H. G. & Erickson, D. A method for nanofluidic device prototyping using elastomeric collapse. *Proc. Natl. Acad. Sci.* **106**, 15549 LP-15554 (2009).

[203] Görrn, P., Lehnhardt, M., Kowalsky, W., Riedl, T. & Wagner, S. Elastically Tunable Self-Organized Organic Lasers. *Adv. Mater.* **23**, 869–872 (2011).

[204] Lee, E. *et al.* Tilted Pillars on Wrinkled Elastomers as a Reversibly Tunable Optical Window. *Adv. Mater.* **26**, 4127–4133 (2014).

[205] Zeng, S. *et al.* Bio-inspired sensitive and reversible mechanochromisms via

strain-dependent cracks and folds. *Nat. Commun.* **7**, 11802 (2016).

[206] Huang, X., Sun, Y. & Soh, S. Stimuli-Responsive Surfaces for Tunable and Reversible Control of Wettability. *Adv. Mater.* **27**, 4062–4068 (2015).

[207] Arifuzzaman, M. *et al.* Geometric and Edge Effects on Swelling-Induced Ordered Structure Formation in Polyelectrolyte Hydrogels. *Macromolecules* **46**, 9083–9090 (2013).

[208] Li, Q. *et al.* Patterning Poly(dimethylsiloxane) Microspheres via Combination of Oxygen Plasma Exposure and Solvent Treatment. *J. Phys. Chem. B* **119**, 13450–13461 (2015).

[209] Rodríguez-Hernández, J. Wrinkled interfaces: Taking advantage of surface instabilities to pattern polymer surfaces. *Prog. Polym. Sci.* **42**, 1–41 (2015).

[210] Auguste, A., Jin, L., Suo, Z. & Hayward, R. C. Post-wrinkle bifurcations in elastic bilayers with modest contrast in modulus. *Extrem. Mech. Lett.* **11**, 30–36 (2017).

[211] Tallinen, T. & Biggins, J. S. Mechanics of invagination and folding: Hybridized instabilities when one soft tissue grows on another. *Phys. Rev. E* **92**, 22720 (2015).

[212] Huck, W. T. S. *et al.* Ordering of Spontaneously Formed Buckles on Planar Surfaces. *Langmuir* **16**, 3497–3501 (2000).

[213] Wang, Q. & Zhao, X. A three-dimensional phase diagram of growth-induced surface instabilities. *Sci. Rep.* **5**, 8887 (2015).

[214] Wang, Q. & Zhao, X. Beyond wrinkles: Multimodal surface instabilities for multifunctional patterning. *MRS Bull.* **41**, 115–122 (2016).

[215] Stoop, N., Lagrange, R., Terwagne, D., Reis, P. M. & Dunkel, J. Curvature-induced symmetry breaking determines elastic surface patterns. *Nat. Mater.* **14**, 337 (2015).

[216] Paulsen, J. D. *et al.* Curvature-induced stiffness and the spatial variation of wavelength in wrinkled sheets. *Proc. Natl. Acad. Sci.* **113**, 1144 LP-1149 (2016).

[217] Jiménez, F. L., Stoop, N., Lagrange, R., Dunkel, J. & Reis, P. M. Curvature-Controlled Defect Localization in Elastic Surface Crystals. *Phys. Rev. Lett.* **116**, 104301 (2016).

[218] Howard G. Allen. *Analysis and Design of Structural Sandwich Panels*. (Pergamon, 1969).

[219] Bailey, R. W. & Fidler, R. Stress analysis of plates and shells containing patterns of reinforced holes. *Nucl. Eng. Des.* **3**, 41–53 (1966).

[220] Mark L. Kachanov, B. Shafiro, I. T. *Handbook of Elasticity Solutions*. (Springer Netherlands, 2003).

[221] Faustini, M. *et al.* Dynamic Shaping of Femtoliter Dew Droplets. *ACS Nano* **12**, 3243–3252 (2018).

[222] Song, Y. *et al.* structured graphene surface for fog collection and. 3813–3822 (2018). doi:10.1039/c7nr07728a

[223] Vanangamudi, A., Dumée, L. F., Ligneris, E. Des, Duke, M. & Yang, X. Thermo-responsive nanofibrous composite membranes for efficient self-cleaning of

protein foulants. *J. Memb. Sci.* **574**, 309–317 (2019).

[224] Sabbah, A., Youssef, A. & Damman, P. Superhydrophobic Surfaces Created by Elastic Instability of PDMS. *Appl. Sci.* **6**, 152 (2016).

[225] Esfahani, M. R. *et al.* A novel gold nanocomposite membrane with enhanced permeation, rejection and self-cleaning ability. *J. Memb. Sci.* **573**, 309–319 (2019).

[226] Haapanen, J. *et al.* On the limit of superhydrophobicity: defining the minimum amount of TiO2 nanoparticle coating. *Mater. Res. Express* **6**, 35004 (2018).

[227] Lee, K.-M., Park, H., Kim, J. & Chun, D.-M. Fabrication of a superhydrophobic surface using a fused deposition modeling (FDM) 3D printer with poly lactic acid (PLA) filament and dip coating with silica nanoparticles. *Appl. Surf. Sci.* **467–468**, 979–991 (2019).

[228] Quéré, D. Wetting and Roughness. *Annu. Rev. Mater. Res.* **38**, 71–99 (2008).

[229] Pocivavsek, L. *et al.* Topography-driven surface renewal. **14**, 948–953 (2018).

[230] Ghosh, U. U., Nair, S., Das, A., Mukherjee, R. & DasGupta, S. Replicating and resolving wetting and adhesion characteristics of a Rose petal. *Colloids Surfaces A Physicochem. Eng. Asp.* **561**, 9–17 (2019).

[231] Choi, C.-H., Lee, H. & Weitz, D. A. Rapid Patterning of PDMS Microfluidic Device Wettability Using Syringe-Vacuum-Induced Segmented Flow in Nonplanar Geometry. *ACS Appl. Mater. Interfaces* **10**, 3170–3174 (2018).

[232] Yang, Y. *et al.* Inorganic Surface Coating with Fast Wetting–Dewetting Transitions for Liquid Manipulations. *ACS Appl. Mater. Interfaces* **10**, 19182–19188 (2018).

[233] Estellé, P., Cabaleiro, D., Żyła, G., Lugo, L. & Murshed, S. M. S. Current trends in surface tension and wetting behavior of nanofluids. *Renew. Sustain. Energy Rev.* **94**, 931–944 (2018).

[234] Yang, C., Wu, L. & Li, G. Magnetically Responsive Superhydrophobic Surface: In Situ Reversible Switching of Water Droplet Wettability and Adhesion for Droplet Manipulation. *ACS Appl. Mater. Interfaces* **10**, 20150–20158 (2018).

[235] Coux, M., Clanet, C. & Quéré, D. Soft, elastic, water-repellent materials. *Appl. Phys. Lett.* **110**, (2017).

[236] Rhee, D., Lee, W. K. & Odom, T. W. Crack-Free, Soft Wrinkles Enable Switchable Anisotropic Wetting. *Angew. Chemie - Int. Ed.* **56**, 6523–6527 (2017).

[237] Adera, S., Raj, R., Enright, R. & Wang, E. N. Non-wetting droplets on hot superhydrophilic surfaces. *Nat. Commun.* **4**, 1–7 (2013).

[238] Storozhenko, M., Umanskyi, O., Krasovskyy, V., Antonov, M. & Terentjev, O. Wetting and interfacial behaviour in the TiB2-NiCrBSiC system. *J. Alloys Compd.* **778**, 15–22 (2019).

[239] Raj, R., Adera, S., Enright, R. & Wang, E. N. three-dimensional droplet shape control. *Nat. Commun.* **5**, 1–8 (2014).

[240] Salem, T. K., Budaklı, M., Şahan, O. & Arık, M. An experimental and analytical study on the influence of superhydrophobic micro-textured surfaces on liquid wetting phenomena. *Colloids Surfaces A Physicochem. Eng. Asp.* **555**, 191–

200 (2018).

[241] Chatterjee, S., Pal Singh, K. & Bhattacharjee, S. Wetting hysteresis of atomically heterogeneous systems created by low energy inert gas ion irradiation on metal surfaces: Liquid thin film coverage in the receding mode and surface interaction energies. *Appl. Surf. Sci.* **470**, 773–782 (2019).

[242] Tian, Y. L. *et al.* Journal of Colloid and Interface Science Fabrication of bio-inspired nitinol alloy surface with tunable anisotropic wetting and high adhesive ability. *J. Colloid Interface Sci.* **527**, 328–338 (2018).

[243] Koşak Söz, Ç., Trosien, S. & Biesalski, M. Superhydrophobic Hybrid Paper Sheets with Janus-Type Wettability. *ACS Appl. Mater. Interfaces* **10**, 37478–37488 (2018).

[244] Han, H. *et al.* Single-Droplet Multiplex Bioassay on a Robust and Stretchable Extreme Wetting Substrate through Vacuum-Based Droplet Manipulation. *ACS Nano* **12**, 932–941 (2018).

[245] Malvadkar, N. A., Hancock, M. J., Sekeroglu, K., Dressick, W. J. & Demirel, M. C. An engineered anisotropic nanofilm with unidirectional wetting properties. *Nat. Mater.* **9**, 1023 (2010).

[246] Wang, P., Bian, R., Meng, Q., Liu, H. & Jiang, L. Bioinspired Dynamic Wetting on Multiple Fibers. *Adv. Mater.* **29**, 1703042 (2017).

[247] Ge, P. *et al.* Smart Anisotropic Wetting Surfaces with Reversed pH-Responsive Wetting Directions. **28**, 1802001 (2018).

[248] Cheng, Z. *et al.* Superhydrophobic Shape Memory Polymer Arrays with Switchable Isotropic / Anisotropic Wetting. **1705002**, 1–11 (2018).

[249] Park, J. K. & Kim, S. Droplet manipulation on a structured shape memory polymer surface. *Lab Chip* **17**, 1793–1801 (2017).

[250] Giordano, M. C. & de Mongeot, F. B. Anisotropic Nanoscale Wrinkling in Solid-State Substrates. *Adv. Mater.* **30**, 1801840 (2018).

[251] Zeng, S. *et al.* Moisture-Responsive Wrinkling Surfaces with Tunable Dynamics. *Adv. Mater.* **29**, 1700828 (2017).

[252] Lin, G., Zhang, Q., Lv, C., Tang, Y. & Yin, J. Small degree of anisotropic wetting on self-similar hierarchical wrinkled surfaces. *Soft Matter* **14**, 1517–1529 (2018).

[253] Chang, T.-H. *et al.* Controlled Crumpling of Two-Dimensional Titanium Carbide (MXene) for Highly Stretchable, Bendable, Efficient Supercapacitors. *ACS Nano* **12**, 8048–8059 (2018).

[254] Xie, J. *et al.* Synergism of Self-Wrinkling and Ultrasonic Cleaning to Fabricate Hierarchically Patterned Conducting Films. *Adv. Mater. Interfaces* **5**, 1800905 (2018).

[255] Lee, W.-K. *et al.* Monolithic Polymer Nanoridges with Programmable Wetting Transitions. *Adv. Mater.* **30**, 1706657 (2018).

[256] Peppou-Chapman, S. & Neto, C. Mapping Depletion of Lubricant Films on Antibiofouling Wrinkled Slippery Surfaces. *ACS Appl. Mater. Interfaces* **10**, 33669–33677 (2018).

[257] Shao, Z., Zhao, Y., Zhang, W., Cao, Y. & Feng, X. Soft Matter Curvature induced

hierarchical wrinkling patterns in soft bilayers. 7977–7982 (2016). doi:10.1039/c6sm01088a

[258] Lu, H., Liu, Y., Xu, B. Bin, Hui, D. & Fu, Y. Q. Spontaneous biaxial pattern generation and autonomous wetting switching on the surface of gold/shape memory polystyrene bilayer. *Compos. Part B Eng.* **122**, 9–15 (2017).

[259] Wang, D. *et al.* Spatially configuring wrinkle pattern and multiscale surface evolution with structural confinement. *Adv. Funct. Mater.* **28**, 1–9 (2018).

[260] Xia, D. & Brueck, S. R. J. Strongly Anisotropic Wetting on One-Dimensional Nanopatterned Surfaces. *Nano Lett.* **8**, 2819–2824 (2008).

[261] Xia, D., He, X., Jiang, Y.-B., Lopez, G. P. & Brueck, S. R. J. Tailoring Anisotropic Wetting Properties on Submicrometer-Scale Periodic Grooved Surfaces. *Langmuir* **26**, 2700–2706 (2010).

[262] McDonald, J. C. & Whitesides, G. M. Poly(dimethylsiloxane) as a Material for Fabricating Microfluidic Devices. *Acc. Chem. Res.* **35**, 491–499 (2002).

[263] Xia, Y. & Whitesides, G. M. Soft Lithography. *Angew. Chemie Int. Ed.* **37**, 550–575 (1998).

[264] Ng, J. M. K., Gitlin, I., Stroock, A. D. & Whitesides, G. M. Components for integrated poly(dimethylsiloxane) microfluidic systems. *Electrophoresis* **23**, 3461–3473 (2002).

[265] Mata, A., Boehm, C., Fleischman, A. J., Muschler, G. & Roy, S. Growth of connective tissue progenitor cells on microtextured polydimethylsiloxane surfaces. *J. Biomed. Mater. Res.* **62**, 499–506 (2002).

[266] Jo, B.-., Lerberghe, L. M. Van, Motsegood, K. M. & Beebe, D. J. Three-dimensional micro-channel fabrication in polydimethylsiloxane (PDMS) elastomer. *J. Microelectromechanical Syst.* **9**, 76–81 (2000).

[267] Unger, M. A., Chou, H.-P., Thorsen, T., Scherer, A. & Quake, S. R. Monolithic Microfabricated Valves and Pumps by Multilayer Soft Lithography. *Science (80-.).* **288**, 113 LP-116 (2000).

[268] Im, S. H. & Huang, R. Evolution of Wrinkles in Elastic-Viscoelastic Bilayer Thin Films. *J. Appl. Mech.* **72**, 955–961 (2005).

[269] Peter Kohnke. *ANSYS Theory Reference*. (SAS IP, Inc., 1999).

[270] S., R. R. & Keightley, R. E. Large elastic deformations of isotropic materials VI. Further results in the theory of torsion, shear and flexure. *Philos. Trans. R. Soc. London. Ser. A, Math. Phys. Sci.* **242**, 173–195 (1949).

[271] Woo, C.-S., Kim, W.-D. & Kwon, J.-D. A study on the material properties and fatigue life prediction of natural rubber component. *Mater. Sci. Eng. A* **483–484**, 376–381 (2008).

[272] Gent, A. N. *Engineering with Rubber*. (Carl Hanser Verlag GmbH & Co. KG, 2012).

[273] *Abaqus 6.10 Analysis User's Manual Volume III: Materials*. (Dassault Systemes, 2010).

Appendix

Recent publications and related award certifications are presented in this section. Please see next pages for detail.

polymers

MDPI

Article

Spatially Engraving Morphological Structure on a Polymeric Surface by Ion Beam Milling

Ansu Sun [1], Ding Wang [1], Honghao Zhou [1], Yifan Li [1], Chris Connor [1], Jie Kong [2,*], Jining Sun [3,*] and Ben Bin Xu [1,*]

[1] Mechanical and Construction Engineering, Faculty of Engineering and Environment, Northumbria University, Newcastle upon Tyne NE1 8ST, UK
[2] MOE Key Laboratory of Materials Physics and Chemistry in Extraordinary Conditions, Shaanxi Key Laboratory of Macromolecular Science and Technology, School of Science, Northwestern Polytechnic University, Xi'an 710072, China
[3] School of Engineering and Physical Sciences, Heriot-Watt University, Edinburgh EH14 4AS, UK
* Correspondence: kongjie@nwpu.edu.cn (J.K.); jining.sun@hw.ac.uk (J.S.); ben.xu@northumbria.ac.uk (B.B.X.)

Received: 6 May 2019; Accepted: 17 July 2019; Published: 23 July 2019

Abstract: Polymer surface patterning and modification at the micro/nano scale has been discovered with great impact in applications such as microfluidics and biomedical technologies. We propose a highly efficient fabricating strategy, to achieve a functional polymer surface, which has control over the surface roughness. The key development in this fabrication method is the polymer positive diffusion effect (PDE) for an ion-bombarded polymeric hybrid surface through focused ion beam (FIB) technology. The PDE is theoretically explored by introducing a positive diffusion term into the classic theory. The conductivity-induced PDE constant is discussed as functions of substrates conductivity, ion energy and flux. The theoretical results agree well with the experiential results on the conductivity-induced PDE, and thus yield good control over roughness and patterning milling depth on the fabricated surface. Moreover, we demonstrate a controllable surface wettability in hydrophobic and superhydrophobic surfaces (contact angles (CA) range from 108.3° to 150.8°) with different CA hysteresis values ranging from 31.4° to 8.3°.

Keywords: ion beam milling; topographic surface; wetting; contact angle hysteresis

1. Introduction

Surface patterning and modification at micro-/nano-scales have been of great importance in creating functional surfaces for a wide range of applications, such as water repelling and self-cleaning [1–4], antifouling [5], anti-icing [6], adhesion control, and drag reduction technologies [7,8]. To create surfaces with desired roughness and topography, some techniques have been commonly used, such as lithography-based plasma etching and deposition, coating on top of patterned substrates, and/or soft-lithography pattern transferring, and, more recently, creating stimuli-responsive surface cracking, wrinkling [9–13] and other deformations on smart material surfaces [14–16].

The focused ion beam (FIB) technique has proven its efficiency in manufacturing semiconductors, metals and metal oxides, with its unique capability for rapid prototyping and high precision [17,18]. The fundamental mechanism of FIB is that highly energetic ions driven by an electrical field knock atoms off the material surface by electro-collision and the recoil action between the ion and target material surface (Figure 1). For ion-milled surfaces, the morphological evolution can cause kinetic roughness, which has attracted increasing research interest in recent decades [19–21]. However, limited attempts have been reported on the topic of FIB processing on polymeric substrates, since the charging effect from the insulated polymer matrix significantly reduces manufacturing precision,

and the understanding of the morphological evolution for an ion-milled polymer surface remains yet to be fully explored [22–25]. Compared to other surface morphology modification techniques, the FIB method has great potential for scalable patterning with both roughness level and geometry size ranging from a few nanometers to 10 μm.

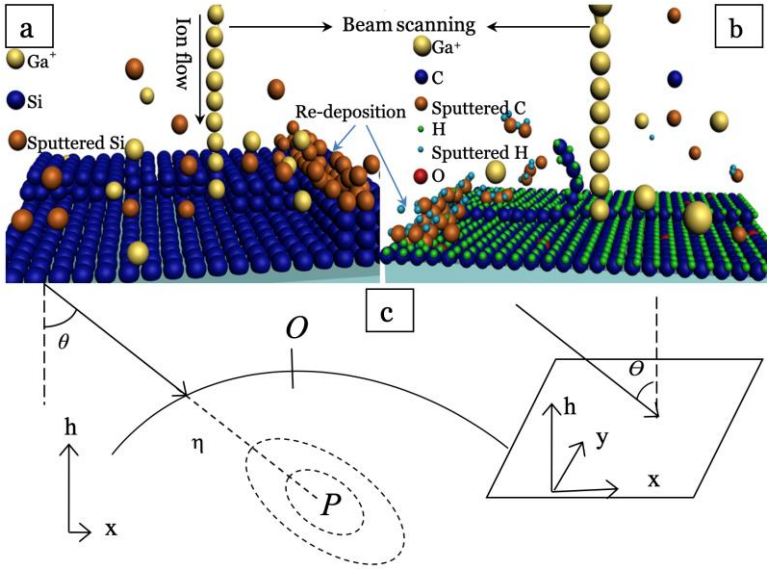

Figure 1. Schematics of focused ion beam (FIB) milling on (**a**) silicon and (**b**) conductive polymeric hybrid surface. (**c**) Following a straight trajectory (solid line), the ion penetrates an average distance α inside the solid (dashed line) and completely releases its kinetic energy at P. The dotted equal energy contours indicate the energy decreasing area around point P. The energy released at point P contributes to erosion at O. The inset shows the laboratory coordinate frame: the ion beam forms an angle θ with the normal to the average surface orientation, z, and the in-plane direction x is chosen along the projection of the ion beam.

2. Theoretical Background

As shown in Figure 1, ion bombardment is commonly considered as atomic processes taking place inside the bombarded material within a finite penetration depth. The ions pass through a distance α before they completely release their kinetic energy with a spatial distribution inside the target substrates. An ion releasing its energy at point P in the solid contributes energy to the surface point O that may induce the atoms in O to break their bonds and leave the surface or diffuse along it. The pattern formation by ion beam sputtering has been previously understood as the interplay between the unstable dependence of the sputtering yield on surface curvature and stabilizing surface relaxation mechanisms [26,27]. The most successful model to predict surface evolution under ion sputtering was the Bradley and Harper (BH) equation [28]. BH theory describes the ripple formation by discussing the surface topography $h(x, y, t)$, measured from an initial smooth configuration in the (x, y) plane. However, it could not explain the surface roughening well [29–31]. Therefore, Makeev, Barabási and Cuerno [32] refined the noisy Kuramoto–Sivashinsky (KS) equation [33,34] based on the Sigmund theory of sputter erosion [35], where the surface was bombarded by ions, and included the Kardar–Parisi–Zhang (KPZ) nonlinear term in the BH equation. Cuerno et al [26,36,37] further developed an effective evolution equation:

$$\frac{\partial h}{\partial t} = -v\nabla^2 h + \lambda_1(\nabla h)^2 - \lambda_2\nabla^2(\nabla h)^2 - K\nabla^4 h \quad (1)$$

where v, λ_1 and λ_2 are the average coefficients determined by the experimental parameters such as ion flux, ion energy, etc. For an amorphous solid in equilibrium with its vapor, $K\nabla^4 h$ (known as

the MBE equation) [38] has been studied and obtained [39,40]. Equation (1) was originally used to describe dynamic scaling on the surface under the thermal surface diffusion; here, the conditional surface diffusion factor, K, can be decomposed with conductivity-induced PDE constant, D^c [39,41]:

$$K = \frac{D^c \beta \Omega^2 M_{con}}{k_b T} \exp\left(\frac{-\Delta E}{k_b T}\right) \quad (2)$$

where β is the surface free energy per unit, Ω represents the atomic volume, M_{con} denotes the number density of conductive particles, k_b is the Boltzmann constant, T is the absolute temperature, and ΔE is the activation energy for surface diffusion. The value of D^c could be determined by the evolved Nernst–Einstein equation [42,43]:

$$D^c \equiv \frac{\sigma_{dc} k_b T}{e^2 M_{con}} \quad (3)$$

Here σ_{dc} represents the DC conductivity of sample and e is the elementary charge. To simplify the discussion, the symmetric case ($\delta = u$, which are the distribution distances in directions parallel and perpendicular along the beam) was applied to the current model, and the incident angle θ is zero. The linear wavelength instability could be calculated as in Ref. [34]:

$$l_i = 2\pi\left(\frac{2K}{v}\right)^{1/2} \quad (4)$$

which correlates to ion flux and matrix conductivity, and where i refers to the direction (x or y). Given a small incidence angle $= -(F\alpha)/2\delta$, where $F \equiv \left(\epsilon Jp/\sqrt{2\pi}\right)\exp\left(-\frac{\alpha^2}{2\delta^2}\right)$ [44,45], Equation (1) could describe the surface roughening caused by PDE, after considering the conductivity induced ion diffusion by Equations (2) and (3). The J means the average ion flux, ϵ denotes the total energy carried by the ion and p is a proportionality constant between power deposition and rate of erosion.

The surface roughness evolution could be predicted from the following equation [26]:

$$\tau = v\lambda_2/(K\lambda_1) \quad (5)$$

Equation (5) has been applied under different experimental conditions [46,47].

We have previously demonstrated carbon-based polymer composites with exciting properties induced by enhanced electrical conductivity [48,49]. In this project, conductive polymer composites will be used to overcome the challenge from the dielectric surface charging effect during the FIB process. A new concept of conductivity-induced PDE is proposed to understand ion impacting a conductive polymer surface and to predict the surface evolution during FIB. The ion-bombarded surface topographic features with conductivity-induced PDE are theoretically predicted using Monte Carlo simulation, and also experimentally assessed. Comparative studies of FIB-induced surface patterning and morphological evolution are carried out. The emerging application of fabricated surfaces is explored with surface wetting controls. We expect that the findings in this work will advance the current understanding of FIB fabrication on polymer surfaces.

3. Experimental Methods

Conductive polymer nanocomposites such as polystyrene–carbon nano-particles (CNPs) were used to create the conductive polymer surfaces [50–53]. The styrene-based precursor (PS, Veriflex®, CRG Co. Ltd., Miamisburg, OH, US) [50,51] and the CNPs (VULCAN® XC72R, CABOT, Boston, MA, US), were ultrasonically agitated in a three-neck flask for 2 h at 1000 rpm [54]. Then the curing agent (Luperox ATC50, Sigma-Aldrich, St. Louis, MI, US) was added, and the mixture stirred for 45 min. Polystyrene–carbon nano-particles composite (CNP/PS) films with a thickness of 200 μm were made by casting the mixture into a PTFE mold and baking in a vacuum oven at 75 °C for 36 h.

Electrical conductivity was measured using an I-V testing set-up and thermo-electrical testing was performed through a Schlumberger Solartron 1250 Frequency Response Analyser from 20 to 100 °C in an isolated chamber with an ambiance of air.

A dual-beam FIB instrument (FEI, Quanta3D FEG, Thermo Fisher Scientific, Waltham, MA, US) equipped with liquid gallium ion source (Ga+, 30 KeV) and Scanning electron microscopy (SEM) was used. The topographic surface was assessed with an atom force microscopy (AFM, Triboscope, Bruker, Coventry, UK). Sputter yield was calculated through Monte Carlo simulation (TRIDYN, binary collision approximation ion irradiation simulation) [55,56], which simulates the ion irradiation of amorphous targets in the binary collision approximation. It allows for a dynamic rearrangement of the local composition of the target material [57]. Therefore, effects in high-fluence implantation, ion mixing, and preferential sputtering caused by atomic collision processes can be concluded [58]. Considering the current macromolecular-based hybrid system, an enthalpy of sublimation value (6.2 eV) was set in the simulation by consulting the chemically covalent bond energies and atom composition.

4. Results and Discussion

Figure 2a illustrates the conductive hybrids, based on the SEM fracture surface morphologies for 2 vol. % CNP/PS. The background SEM showed that the CNPs were distributed uniformly throughout the textured polymer matrix. The electrical current (imaginary) flowed through the conductive hybrid while the threshold network was generated. Figure 2b presents the DC conductivity results with little variations as a function of CNP concentrations at room temperature. When CNP concentrations (φ_{CNP}) increased from 0.5 to 2 vol.%, the conductivity dramatically increased from 1×10^{-8} to 100 S/m, and this increment slowed down when the CNP concentration exceeded 2 vol. %. The conductivity for $\varphi_{CNP} > 2$ vol. % was sufficient to enter the general semiconductor region.

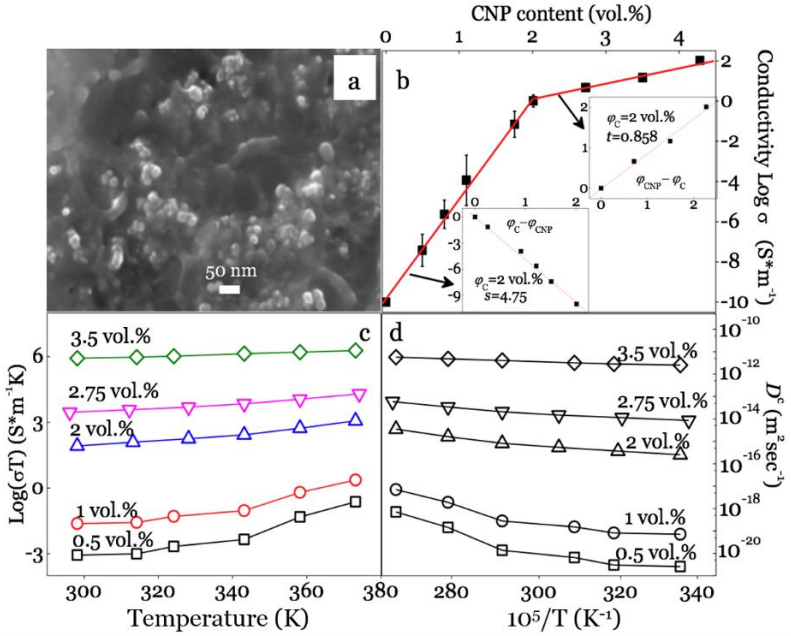

Figure 2. (**a**) Scanning electron microscopy (SEM) observation of the conductive surface for 2 vol. % CNP/PS; (**b**) DC conductivity results as a function of CNP content and the inset linear fitting curves needed for determining the threshold value; (**c**) DC conductivity for composites with dependency on temperature and CNP concentration; (**d**) calculated conductivity diffusion coefficients as a function of temperature.

Such a percolation network has been well understood as a polymer-based inorganic (σ_1)–organic (σ_2, $\sigma_2 << \sigma_1$) conducting system, or resistors and capacitors [59–61]. At a lower CNP concentration, conduction is mainly dominated by hopping conduction among the nanofillers, thus appearing closer

to the insulator [59,61]. They became conductors when the filler concentration increased to a critical value, i.e., the percolation threshold (φ_c), which formed the electron bridge within the substrate by the filler state [62]. To determine φ_c, the conductivity σ was fitted based on the power laws [59,63]:

$$\sigma(\varphi_{CNP}) \propto (\varphi_c - \varphi_{CNP})^{-s} \text{ when } \varphi CNP < \varphi_c \quad (6)$$

$$\sigma(\varphi_{CNP}) \propto (\varphi_{CNP} - \varphi_c)^{t} \text{ when } \varphi CNP > \varphi_c \quad (7)$$

where t and s are the critical exponents in the conducting and insulating regions. The linear-fitting results clearly defined the threshold network with φ_c = 2 vol. %, t = 0.858, and s = 4.75 (the inset in Figure 2b). Previous reports [64,65] noted that a higher critical value ($t > 2$) in a polymer/CNP system will reduce the conductive efficiency, whereas, a good conductive efficiency (t = 0.858) was achieved due to the uniform nanofiller distribution by the adopted techniques.

The conductivity–temperature relationship is shown in Figure 2c, where the measured conductivity gradually increased with the rising temperature, which enhanced the hopping conductivity in composites [66]. The sample conductivity for 2 vol. % CNP/PS approached the percolation limit of an insulator-dominating state, and further rises in temperature significantly increased the conductivity through the enhanced hopping. When the CNP content was above φ_c, the CNP particles/clusters were more likely to link with each other, forming a continuously distributed CNP network in the matrix. Figure 2d summarizes the calculated conductivity diffusion coefficients with dependency on temperature. For the composites that hadn't formed the threshold network, the diffusion coefficients were low, and the value was located in the ion diffusion range inside of the insulated solid (<10^{-18} m^2/sec) [67]. With the CNP content increased, the PDE constant significantly increased from 10^{-21} to 10^{-11}. It should be noticed that the diffusion constant for an ion-liquid system is 10^{-11}–10^{-9} m^2/sec [67]. This conductive network generation by adding CNP enhanced the overall ion diffusion capability dramatically. From the information in Figure 2c,d, the thermal effect on sample conductivity, or D^c, which caused a changing factor of 10–100, is negligible when comparing the large improvement by increasing conductivity.

Since all coefficients in Equation (1) are determined by ion flux and K, the coefficient K can be calculated with D^c (in Figure 2d) by Equations (2) and (3). We next investigate the influence from material with a fixed ion flux $\phi = 1.2 \times 10^9$ ions/(μm^2/sec). With the Monte Carlo algorithm it could be obtained that v = 187 nm^2/min, λ_1 = 78.4 nm/min, and λ_2 = 4373.2 nm^3/min. The simulated roughness τ is displayed in Figure 3a–c, compared with the experimental AFM plots. The quantitative agreement in the order of magnitude between the experimental and the theoretical results was found for predicting the surface evolution trend, and the surface roughness decreased constantly with the CNP content increases. The experimental values were only half of the theoretical values for 1 vol. % and 2 vol. % CNP/PS composites. For 3.5 vol. % CNP/PS, the magnitude of the experimental result agreed well with theory, which could be attributed to the metallic type surface morphological evolution occurring during ion milling on the samples with high conductivity. Furthermore, the asymptotic morphologies revealed the increasing l_i values as well as the reduction of τ with the target conductivity increases, implying a higher self-smoothing effect and a thermal relaxation mechanism led to a less defined pattern order for the hybrids. The discrepancy between the experimental data and theoretical prediction can be explained by ignoring the rapid temperature rises during ion sputter, which induces a thermal diffusion.

The milling depth values are plotted as a function of ion flux in Figure 3d–f; the grey areas represent the overall removal depth, including the targeted milling depth (500 nm), and the calculated roughness, while the up-edge indicates the accumulating value of roughness and targeted removal depth. As predicted, the self-smoothing conductive-induced PDE was found as shown in each figure. Both the experimental and numerical morphologies presented a low surface roughness associated with low ion flux values, contrary to the much higher roughness values under higher ion flux. This could be derived from the flux related parameters in Equation (5), v, λ_1 and λ_2, which change significantly with

applying higher ion flux. Moreover, the experimental average removal depth was reduced at high ion flux for all samples; this could be due to the inaccurate numerical calculation at high roughness. Figure 3d–f shows the roughness reduced with increased conductivity both in experimental and numerical results, proving that the pattern characteristics are dominated by the sample conductivity. Figure 3a–c also reflects that the roughness peak at high conductivity values is broader when the sample was bombarded at the same flux values. It should be noted that the ion flux employed in this work is 10–1000 times higher than those have been reported [26,36,68]; the thermally activated surface diffusion effect could not be ignored when the target's temperature increases, which causes the self-smoothing effect on the milled surface as well as conductivity-induced PDE does.

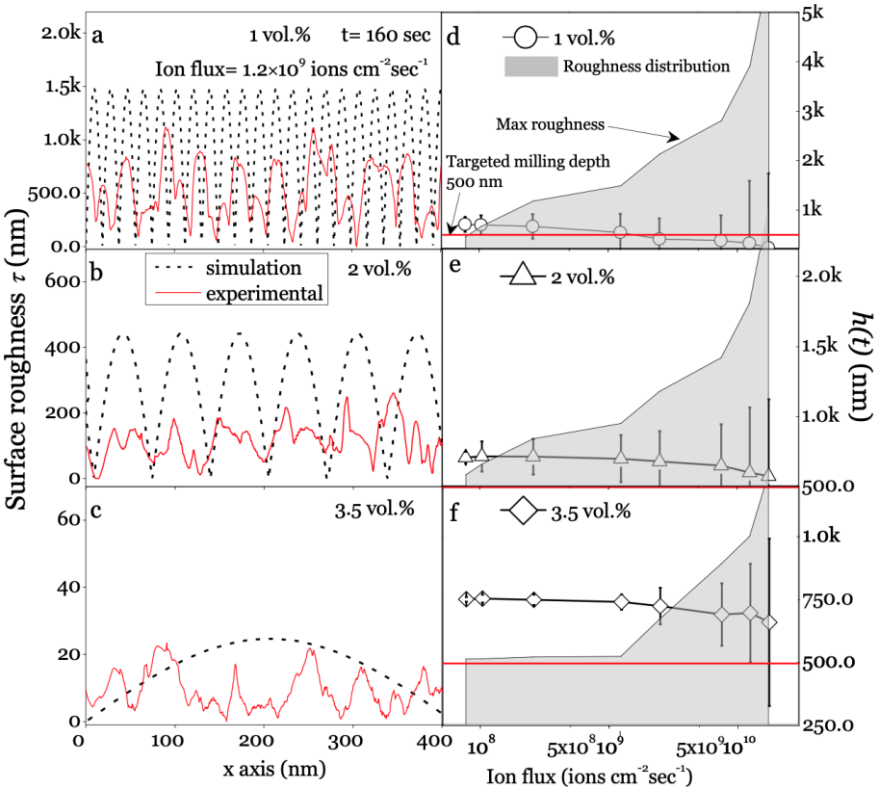

Figure 3. (**a**–**c**) Experimental atom force microscopy (AFM) profiles on a milled surface and numerical longitudinal plots for different composites (milling time = 160 sec); (**d**–**f**) Time evolving milling efficiency (removal depth, h(t)) with surface roughness (error bar); the gray area represents the roughness with targeted removal depth of 500 nm.

The experimental topographic information is summarized in Figure 4 with SEM images, AFM profiles and statistical analysis for AFM data. The deteriorating trends are presented with dependencies on ion flux and sample conductivity; the SEM observation illustrates that higher ion flux creates more surface roughness, probably combined with the re-deposition [69]. The milling precision was improved with sample conductivity increases, which could be identified from the evolving morphology in the SEM images under different ion flux; simultaneously, the AFM contour plots agree with this improvement well, with showing concentrated milled depth. The contour plots also reflect that the highest roughness appears for 1 vol. % CNP/PS, which indicates milling accuracy was lowered with low conductivity. The statistical analysis from AFM suggests wide distributed milling depths for the 1 vol. % sample especially under the high ion flux (1.25×10^{10} and 1.75×10^{10} ions/(μm^2/sec)). Meanwhile, a concentrated distribution for 3.5 vol. % CNP/PS was observed under the low ion flux, which represented high uniformity for the milling depth. Figure 4 also reveals that the actual average milling depths were around 700 nm for most conditions with considerable errors, which some distance from the target removal depth of 500 nm. The possible reason could be the thermal induced polymer

chain broken during the high energy ion sputter process, which could be understood as the thermal induced positive effect. Although improved milling precision was achieved for 2 vol. % and 3.5 vol. % CNP/PS, the actual milling depth decreases for 1 vol.% CNP/PS when ion flux increased. This could be attributed to the calculation uncertainty caused by the ultimate roughness, as previously mentioned, the residual surface charge and the re-deposition caused by molecular chain breaking [70]. Additionally, the Monte Carlo codes in this work considered the effects in high-fluence implantation, ion mixing and preferential sputtering caused by atomic collision processes, and proved a positive correspondence between ion milling efficiency and sample conductivity. However, it did not take account of the thermal induce surface diffusion, which has been previously proved with the stabilization effect on an milled surface [26,44,71].

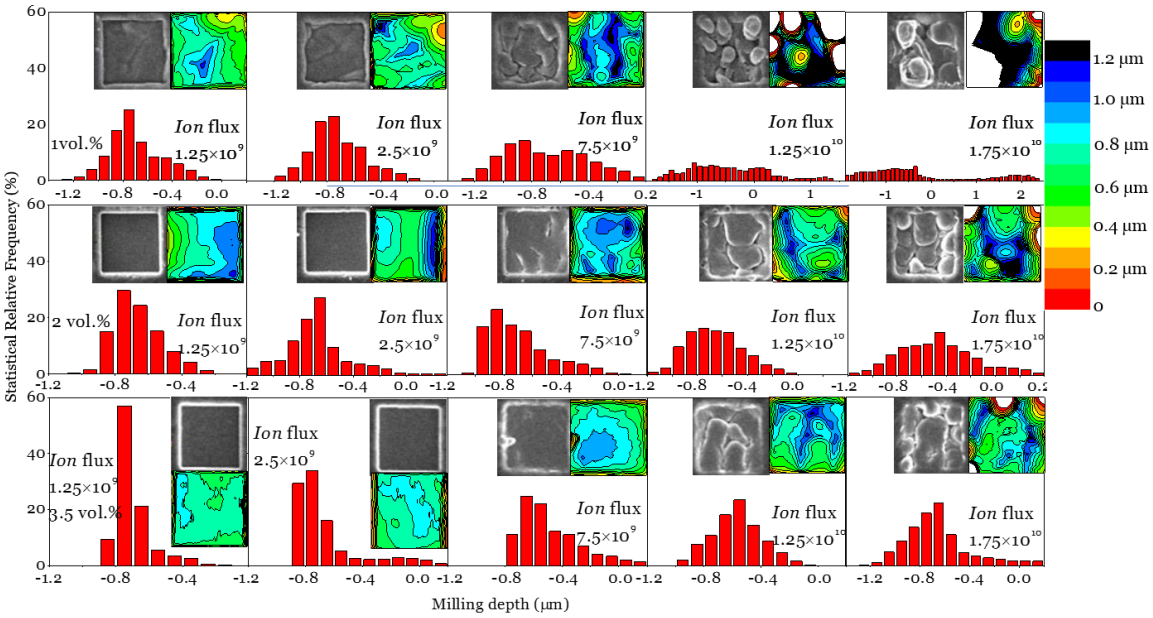

Figure 4. Statistical depth analysis for the milled patterns (5 × 5 μm^2, milling time = 160 s) based on AFM results (inset, contour plots) under different ion flux, combined with the SEM images (inset).

5. Application Demonstration

The CNP/PS polymer matrix surfaces were FIB ion milled into different micro-roughness regions (2 × 2 mm^2 areas pre-patterned with 20 × 20 μm^2 square pattern arrays) with milling depths ranging from 0.5 to 1.2 μm, and R_a (arithmetic mean roughness) values ranging from 700 to 4800 nm (0.7 to 4.8 μm). Different patterns are demonstrated in Figure 5a, from line array to dedicated probe shape. The processing efficiency and the precision are significantly increased. We next selected the dot array pattern (Figure S1) for the surface wetting testing. A self-assembly monolayer (SAM) of Trichloro(1H,1H,2H,2H-perfluorooctyl)silane (FOTS, Sigma-Aldrich, St. Louis, MI, US), was applied from the vapor phase at room temperature (~20 °C) for 30 min to facilitate a conformal hydrophobic layer over the CNP/PS topologies.

To set a benchmark, the static contact angle (CA) of 2 μL of deionized (DI) water on a smooth FOTS surface was measured to be 107°. Figure 5b shows that on the modified CNP/PS surface, the CA ranges from 108.3° to 150.8° (Figure 5c). Dynamic CA measurements (advancing and receding) were also taken, with different CAH (Figure 5d) values ranging from 31.4° to 8.3°. These values shown in Figure 5c,d were close to Wenzel state prediction at lower roughness (<3.5 μm), and closer to the Cassie–Baxter state at higher roughness [13] with CA = 150.8° and CAH = 8.3°, which conforms to the superhydrophobic surfaces (SHS) criteria of CA > 150° and CAH < 10°.

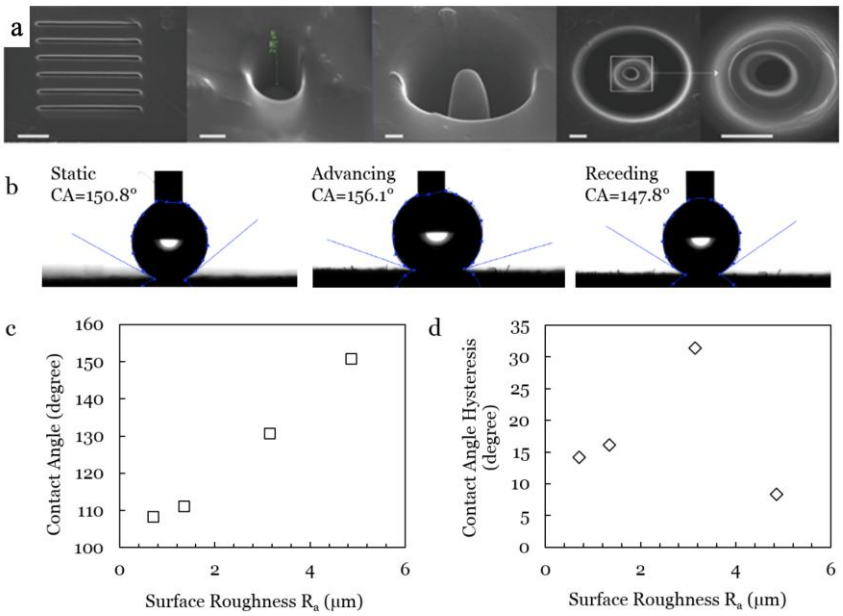

Figure 5. (**a**) FIB engineered nanostructures, from left to right, lines pattern, nano-hole, nano-probe, nano-tunnel; the scale bar is 500 nm. Static contact angle (CA) and contact angle hysteresis (CAH = advancing CA - receding CA) characterization on patterned CNP/PS polymer with FOTS layer. (**b**) CA and CAH values of a DI water droplet on superhydrophobic surface (Ra = 4.8 μm). Relationships between (**c**) CA and surface roughness, and (**d**) CAH and surface roughness.

6. Conclusions

Good structure property relationships were revealed with the homogeneous dispersing state of CNPs in a PS matrix from SEM observation, measured conductivity and the stable electrical–temperature performance. The assessment of ion milled surfaces indicated that milling accuracy and surface roughness are highly dependent on the sample's conductivity. A good agreement between experimental results and the theoretical prediction was achieved in describing the surface's evolving trend, including the general analytical conditions for the coarsening process to occur and the roughness of the surface with different ion flux and material conductivity. Resulting micro-roughness patterns were coated with hydrophobic monolayer FOTS and demonstrated surface wettability control, resulting in hydrophobic and superhydrophobic surfaces (CA ranging from 108.3° to 150.8°) with different CA hysteresis values ranging from 31.4° to 8.3°.

It must be noted that the ion bombardment on a macromolecular surface is far more complicated than a silicon surface. In future work it would thus be interesting to investigate ion sputtering on conductive polymer (composites) surfaces with conductivity and thermal-induced PDEs, and more substrate-related factors, such as molecular chain movements and polymer degradation.

Supplementary Materials: The following are available online at http://www.mdpi.com/2073-4360/11/7/1229/s1, Figure S1: FIB milled nano hole array for surface wetting control.

Author Contributions: Conceptualization, B.X., J.S., Y.L. and J.K.; methodology, A.S., D.W. and H.Z.; formal analysis, A.S., D.W., H.Z., Y.L. and C.C.; writing—original draft preparation, all authors; writing—review and editing, B.X., J.S., Y.L. and J.K.; project administration, B.X., J.S., Y.L. and J.K.; funding acquisition, B.X.

Funding: This research was funded by EPSRC (Grant Nos. EP/N007921/1 and EP/L026899/1).

Acknowledgments: The authors would like to thank Everbeing who donated the probing system used in this work, and MEMSstar, Ltd., for providing the SAM coating facility. Data associated with this paper are available via Northumbria Research Data Management scheme.

Conflicts of Interest: The authors declare no conflict of interest.

References

1. Simpson, J.T.; Hunter, S.R.; Aytug, T. Superhydrophobic materials and coatings: A review. *Rep. Prog. Phys.* **2015**, *78*, 086501. [CrossRef] [PubMed]
2. Yilgör, E.; Söz, C.K.; Yilgör, I. Wetting behavior of superhydrophobic poly(methyl methacrylate). *Prog. Org. Coat.* **2018**, *125*, 530–536. [CrossRef]
3. Bhushan, B.; Jung, Y.C. Natural and biomimetic artificial surfaces for superhydrophobicity, self-cleaning, low adhesion, and drag reduction. *Prog. Mater. Sci.* **2011**, *56*, 1–108. [CrossRef]
4. Wang, S.; Liu, K.; Yao, X.; Jiang, L. Bioinspired Surfaces with Superwettability: New Insight on Theory, Design, and Applications. *Chem. Rev.* **2015**, *115*, 8230–8293. [CrossRef]
5. Kochkodan, V.; Hilal, N. A comprehensive review on surface modified polymer membranes for biofouling mitigation. *Desalination* **2015**, *356*, 187–207. [CrossRef]
6. Kreder, M.J.; Alvarenga, J.; Kim, P.; Aizenberg, J. Design of anti-icing surfaces: Smooth, textured or slippery? *Nat. Rev. Mater.* **2016**, *1*, 15003. [CrossRef]
7. Zhang, C.; McAdams, D.A.; Grunlan, J.C. Nano/Micro-Manufacturing of Bioinspired Materials: A Review of Methods to Mimic Natural Structures. *Adv. Mater.* **2016**, *28*, 6292–6321. [CrossRef]
8. Zhang, P.; Lin, L.; Zang, D.; Guo, X.; Liu, M. Designing Bioinspired Anti-Biofouling Surfaces based on a Superwettability Strategy. *Small* **2017**, *13*, 1503334. [CrossRef]
9. Wang, D.; Cheewaruangroj, N.; Li, Y.; McHale, G.; Jiang, Y.; Wood, D.; Biggins, J.S.; Xu, B.B. Spatially configuring wrinkle pattern and multiscale surface evolution with structural confinement. *Adv. Funct. Mater.* **2018**, *28*, 1704228. [CrossRef]
10. Huang, X.; Sun, Y.; Soh, S. Stimuli-Responsive Surfaces for Tunable and Reversible Control of Wettability. *Adv. Mater.* **2015**, *27*, 4062–4068. [CrossRef]
11. Rhee, D.; Lee, W.K.; Odom, T.W. Crack-Free, Soft Wrinkles Enable Switchable Anisotropic Wetting. *Angew. Chem. Int. Ed.* **2017**, *56*, 6523–6527. [CrossRef] [PubMed]
12. Lu, H.; Liu, Y.; Xu, B.; Hui, D.; Fu, Y.Q. Spontaneous biaxial pattern generation and autonomous wetting switching on the surface of gold/shape memory polystyrene bilayer. *Compos. Part B Eng.* **2017**, *122*, 9–15. [CrossRef]
13. Liu, Y.; Genzer, J.; Dickey, M.D. "2D or not 2D": Shape-programming polymer sheets. *Prog. Polym. Sci.* **2016**, *52*, 79–106. [CrossRef]
14. Xu, B.; Huang, W.; Pei, Y.; Chen, Z.; Kraft, A.; Reuben, R.; De Hosson, J.; Fu, Y. Mechanical properties of attapulgite clay reinforced polyurethane shape-memory nanocomposites. *Eur. Polym. J.* **2009**, *45*, 1904–1911. [CrossRef]
15. Moon, M.W.; Lee, S.H.; Sun, J.Y.; Oh, K.H.; Vaziri, A.; Hutchinson, J.W. Wrinkled hard skins on polymers created by focused ion beam. *Proc. Natl. Acad. Sci. USA* **2007**, *104*, 1130–1133. [CrossRef]
16. Xu, B.; Fu, Y.Q.; Huang, W.M.; Pei, Y.T.; Chen, Z.G.; De Hosson, J.T.; Kraft, A.; Reuben, R.L. Thermal-Mechanical Properties of Polyurethane-Clay Shape Memory Polymer Nanocomposites. *Polymers* **2010**, *2*, 31–39. [CrossRef]
17. Giannuzzi, L.A.; Utlaut, M. A review of Ga+ FIB/SIMS. *Surf. Interface Anal.* **2011**, *43*, 475. [CrossRef]
18. Roediger, P.; Wanzenboeck, H.D.; Waid, S.; Hochleitner, G.; Bertagnolli, E. Focused-ion-beam-inflicted surface amorphization and gallium implantation—New insights and removal by focused-electron-beam-induced etching. *Nanotechnology* **2011**, *22*, 235302. [CrossRef]
19. Völlner, J.; Ziberi, B.; Frost, F.; Rauschenbach, B. Topography evolution mechanism on fused silica during low-energy ion beam sputtering. *J. Appl. Phys.* **2011**, *109*, 43501.
20. Oehrlein, G.S.; Phaneuf, R.J.; Graves, D.B. Plasma-polymer interactions: A review of progress in understanding polymer resist mask durability during plasma etching for nanoscale fabrication. *J. Vac. Sci. Technol. B* **2011**, *29*, 10801. [CrossRef]
21. Cahill, D.G. Morphological instabilities in thin-film growth and etching. *J. Vac. Sci. Technol. A* **2003**, *21*, S110–S116. [CrossRef]
22. Brostow, W.; Gorman, B.P.; Olea-Mejia, O. Focused ion beam milling and scanning electron microscopy characterization of polymer+ metal hybrids. *Mater. Lett.* **2007**, *61*, 1333. [CrossRef]
23. Brunner, S.; Gasser, P.; Simmler, H.; Wakili, K.G. Investigation of multilayered aluminium-coated polymer laminates by focused ion beam (FIB) etching. *Surf. Coat. Technol.* **2006**, *200*, 5908. [CrossRef]

24. Pialat, E.; Trigaud, T.; Bernical, V.; Moliton, J.P. Milling of polymeric photonic crystals by focused ion beam. *Mater. Sci. Eng. C* **2005**, *25*, 618. [CrossRef]
25. Mulders, J.; De Winter, D.; Duinkerken, W.; De Winter, M. Measurements and calculations of FIB milling yield of bulk metals. *Microelectron. Eng.* **2007**, *84*, 1540–1543. [CrossRef]
26. Muñoz-Garcia, J.; Gago, R.; Vazquez, L.; Sánchez-García, J.A.; Cuerno, R. Observation and Modeling of Interrupted Pattern Coarsening: Surface Nanostructuring by Ion Erosion. *Phys. Rev. Lett.* **2010**, *104*, 026101. [CrossRef]
27. Muñoz-Garcia, J.; Castro, M.; Cuerno, R. Nonlinear Ripple Dynamics on Amorphous Surfaces Patterned by Ion Beam Sputtering. *Phys. Rev. Lett.* **2006**, *96*, 086101. [CrossRef] [PubMed]
28. Bradley, R.M. Theory of ripple topography induced by ion bombardment. *J. Vac. Sci. Technol. A* **1988**, *6*, 2390–2395. [CrossRef]
29. Eklund, E.A.; Bruinsma, R.; Rudnick, J.; Williams, R.S. Submicron-Scale Surface Roughening Induced by Ion Bombardment. *Phys. Rev. Lett.* **1991**, *67*, 1759. [CrossRef]
30. Mitsui, T.; Stein, D.; Kim, Y.R.; Hoogerheide, D.; Golovchenko, J.A. Nanoscale Volcanoes: Accretion of Matter at Ion-Sculpted Nanopores. *Phys. Rev. Lett.* **2006**, *96*, 036102. [CrossRef]
31. Rodríguez-Laguna, J.; Santalla, S.N.; Cuerno, R. Intrinsic geometry approach to surface kinetic roughening. *J. Stat. Mech. Theory Exp.* **2011**, *2011*, 05032. [CrossRef]
32. Kardar, M.; Parisi, G.; Zhang, Y.C. Dynamic Scaling of Growing Interfaces. *Phys. Rev. Lett.* **1986**, *56*, 889–892. [CrossRef] [PubMed]
33. Makeev, M.A.; Barabási, A.L. Effect of surface roughness on the secondary ion yield in ion sputtering. *Appl. Phys. Lett.* **1998**, *73*, 2209–2211. [CrossRef]
34. Cuerno, R.; Barabasi, A.L. Dynamic Scaling of Ion-Sputtered Surfaces. *Phys. Rev. Lett.* **1995**, *74*, 4746–4749. [CrossRef] [PubMed]
35. Sigmund, P. Theory of Sputtering. I. Sputtering Yield of Amorphous and Polycrystalline Targets. *Phys. Rev.* **1969**, *184*, 383–416. [CrossRef]
36. Castro, M.; Cuerno, R.; Vazquez, L.; Gago, R. Self-Organized Ordering of Nanostructures Produced by Ion-Beam Sputtering. *Phys. Rev. Lett.* **2005**, *94*, 016102. [CrossRef] [PubMed]
37. Muñoz-Garcia, J.; Cuerno, R.; Castro, M. Coupling of morphology to surface transport in ion-beam-irradiated surfaces: Normal incidence and rotating targets. *J. Phys. Condens. Matter* **2009**, *21*, 224020. [CrossRef]
38. Walmann, T.; Malthe-Sørenssen, A.; Feder, J.; Jøssang, T.; Hardy, H.H.; Meakin, P. Scaling Relations for the Lengths and Widths of Fractures. *Phys. Rev. Lett.* **1996**, *77*, 5393–5396. [CrossRef]
39. Mullins, W.W. Theory of thermal grooving. *J. Appl. Phys.* **1957**, *28*, 333. [CrossRef]
40. Herring, C. Effect of Change of Scale on Sintering Phenomena. *J. Appl. Phys.* **1950**, *21*, 301–303. [CrossRef]
41. Mullins, J.F.; Lettieri, M.F. Chemosurgery of facial wrinkles. *Tex. State J. Med.* **1963**, *59*, 488. [PubMed]
42. Jain, H.; Mundy, J. Analysis of ac conductivity of glasses by a power law relationship. *J. Non-Cryst. Solids* **1987**, *91*, 315–323. [CrossRef]
43. Voss, S.; Imre, Á.W.; Mehrer, H. Mixed-alkali effect in Na–Rb borate glasses: A tracer diffusion and electrical conductivity study. *Phys. Chem. Chem. Phys.* **2004**, *6*, 3669–3675. [CrossRef]
44. Makeev, M.A.; Cuerno, R.; Barabási, A.L. Morphology of ion-sputtered surfaces. *Nuclear Instrum. Methods Phys. Res. Sect. B Beam Interact. Mater. Atoms* **2002**, *197*, 185. [CrossRef]
45. Makeev, M.A.; Barabási, A.L. Secondary ion yield changes on rippled interfaces. *Appl. Phys. Lett.* **1998**, *72*, 906–908. [CrossRef]
46. Muñoz-García, J.; Cuerno, R.; Castro, M. Short-range stationary patterns and long-range disorder in an evolution equation for one-dimensional interfaces. *Phys. Rev. E* **2006**, *74*, 050103. [CrossRef]
47. Kim, J.H.; Ha, N.B.; Kim, J.S.; Joe, M.; Lee, K.R.; Cuerno, R. One-dimensional pattern of Au nanodots by ion-beam sputtering: Formation and mechanism. *Nanotechnology* **2011**, *22*, 285301. [CrossRef]
48. Lu, H.; Wang, X.; Yao, Y.; Gou, J.; Hui, D.; Xu, B.; Fu, Y. Synergistic effect of siloxane modified aluminum nanopowders and carbon fiber on electrothermal efficiency of polymeric shape memory nanocomposite. *Compos. Part B Eng.* **2015**, *80*, 1–6. [CrossRef]
49. Dai, X.; Du, Y.; Yang, J.; Wang, D.; Gu, J.; Li, Y.; Wang, S.; Xu, B.B.; Kong, J. Recoverable and self-healing electromagnetic wave absorbing nanocomposites. *Compos. Sci. Technol.* **2019**, *174*, 27–32. [CrossRef]
50. Hood, P.J.; Havens, D.E. Structural and optical applications for shape memory polymers (SMP. Polymer Patches). U.S. Patent US6986855B1, 24 1 2002.

51. Hood, P.J.; Garrigan, S.; Auffinger, F. Method of Making and Using Shape Memory. U.S. Patent US8808479B2, 15 12 2006.
52. Xu, B.; Zhang, L.; Pei, Y.T.; Luom, J.K.; Tao, S.W.; de Hosson, J.T.M.; Fu, Y.Q. Electro-responsive polystyrene shape memory polymer nanocomposites. *Nanosci. Nanotechnol. Lett.* **2012**, *4*, 814–820. [CrossRef]
53. Lei, M.; Xu, B.; Pei, Y.; Lu, H.; Fu, Y.Q. Micro-mechanics of nanostructured carbon/shape memory polymer hybrid thin film. *Soft Matter* **2016**, *12*, 106–114. [CrossRef] [PubMed]
54. Xu, B.; Fu, Y.Q.; Ahmad, M.; Luo, J.K.; Huang, W.M.; Kraft, A.; Reuben, R.; Pei, Y.T.; Chen, Z.G.; De Hosson, J.T.M. Thermo-mechanical properties of polystyrene-based shape memory nanocomposites. *J. Mater. Chem.* **2010**, *20*, 3442–3448. [CrossRef]
55. Barna, A.; Kotis, L.; Labar, J.L.; Osvath, Z.; Toth, A.L.; Menyhard, M.; Zalar, A.; Panjan, P. Producing metastable nanophase with sharp interface by means of focused ion beam irradiation. *J. Appl. Phys.* **2007**, *102*, 044305. [CrossRef]
56. Roush, M.; Andreadis, T.; Davarya, F.; Goktepe, O. Dynamic simulation of changes in near-surface composition during ion bombardment. *Appl. Surf. Sci.* **1982**, *11*, 235–242. [CrossRef]
57. Möller, W.; Eckstein, W.; Biersack, J. Tridyn-binary collision simulation of atomic collisions and dynamic composition changes in solids. *Comput. Phys. Commun.* **1988**, *51*, 355–368. [CrossRef]
58. Sun, J.; Luo, X.; Ritchie, J.M.; Chang, W.; Wang, W. An investigation of redeposition effect for deterministic fabrication of nanodots by focused ion beam. *Precis. Eng.* **2012**, *36*, 31. [CrossRef]
59. Dang, Z.M.; Lin, Y.H.; Nan, C.W. Novel ferroelectric polymer composites with high dielectric constants. *Adv. Mater.* **2003**, *15*, 1625. [CrossRef]
60. Pecharroman, C.; Esteban-Betegon, F.; Bartolome, J.F.; Lopez-Esteban, S.; Moya, J.S. New Percolative BaTiO3–Ni Composites with a High and Frequency-Independent Dielectric Constant. *Adv. Mater.* **2001**, *13*, 1541. [CrossRef]
61. Pötschke, P.; Dudkin, S.M.; Alig, I. Dielectric spectroscopy on melt processed polycarbonate—Multiwalled carbon nanotube composites. *Polymer* **2003**, *44*, 5023–5030. [CrossRef]
62. Regev, O.; ElKati, P.N.B.; Loos, J.; Koning, C.E. Preparation of Conductive Nanotube–Polymer Composites Using Latex Technology. *Adv. Mater.* **2004**, *16*, 284. [CrossRef]
63. Dang, Z.M.; Wang, L.; Yin, Y.; Zhang, Q.; Lei, Q.Q. Giant dielectric permittivities in functionalized carbon-nanotube/electroactive-polymer nanocomposites. *Adv. Mater.* **2007**, *19*, 852. [CrossRef]
64. Kolb, M.; Botet, R.; Jullien, R. Scaling of Kinetically Growing Clusters. *Phys. Rev. Lett.* **1983**, *51*, 1123–1126. [CrossRef]
65. Karásek, L.; Meissner, B.; Asai, S.; Sumita, M. Percolation Concept: Polymer-Filler Gel Formation, Electrical Conductivity and Dynamic Electrical Properties of Carbon-Black-Filled Rubbers. *Polym. J.* **1996**, *28*, 121–126. [CrossRef]
66. Jonscher, A.K. New interpretation of dielectric loss peaks. *Nature* **1975**, *256*, 566–568. [CrossRef]
67. Mehrer, H. (Ed.) *Series in Solid-State Sciences*; Springer: Berlin, Germany, 2007; p. 221.
68. Nicoli, M.; Cuerno, R.; Castro, M. Unstable Nonlocal Interface Dynamics. *Phys. Rev. Lett.* **2009**, *102*, 256102. [CrossRef] [PubMed]
69. Ishitani, T.; Ohnishi, T.; Madokoro, Y.; Kawanami, Y. Focused-ion-beam "cutter" and "attacher" for micromachining and device transplantation. *J. Vac. Sci. Technol. B* **1991**, *9*, 2633. [CrossRef]
70. Roy, X.; Sarazin, P.; Favis, B.D. Ultraporous nanosheath materials by layer-by-layer deposition onto co-continuous polymer-blend templates. *Adv. Mater.* **2006**, *18*, 1015. [CrossRef]
71. Cuerno, R.; Vazquez, L.; Gago, R.; Castro, M. Surface nanopatterns induced by ion-beam sputtering. *J. Phys. Condens. Matter* **2009**, *21*, 220301. [CrossRef]

ACS APPLIED MATERIALS & INTERFACES

Research Article

Cite This: ACS Appl. Mater. Interfaces 2019, 11, 17706−17713

www.acsami.org

Poly(dimethylsilylene)diacetylene-Guided ZIF-Based Heterostructures for Full Ku-Band Electromagnetic Wave Absorption

Peng Miao,[†] Kaiyang Cheng,[‡] Hongqiang Li,[‡] Junwei Gu,[†] Kaijie Chen,[†] Steven Wang,[§] Ding Wang,[∥] Terence X. Liu,[∥] Ben B. Xu,*[,∥] and Jie Kong*[,†]

[†]MOE Key Laboratory of Materials Physics and Chemistry in Extraordinary Conditions, Shaanxi Key Laboratory of Macromolecular Science and Technology, School of Science, Northwestern Polytechnical University, Xi'an 710072, P. R. China

[‡]MOE Key Laboratory of Advanced Micro-Structure Materials, School of Physics Science and Engineering, Tongji University, Shanghai 200092, P.R. China

[§]School of Chemical Engineering and Advanced Materials, Newcastle University, Newcastle Upon Tyne NE1 7RU, U.K.

[∥]Mechanical and Construction Engineering, Faculty of Engineering and Environment, Northumbria University, Newcastle upon Tyne NE1 8ST, U.K.

Supporting Information

ABSTRACT: Zeolitic imidazolate frameworks (ZIFs), a group of metal−organic frameworks (MOFs), hold promise as building blocks in electromagnetic (EM) wave absorbing/shielding materials and devices. In this contribution, we proposed a facile strategy to synthesize three-dimensional ZIF-67-based hierarchical heterostructures through coordinated reaction of a preceramic component, poly(dimethylsilylene)diacetylene (PDSDA) with ZIF-67, followed by carbonizing the PDSDA-wrapped ZIF at high temperature. The introduction of PDSDA leads to controllable generation of a surface network containing branched carbon nanotubes and regional distributed graphitic carbons, in addition to the nanostructures with a well-defined size and porous surface made by cobalt nanoparticles. The surface structures can be tailored through variations in pyrolysis temperatures, therefore enabling a simple and robust route to facilitate a suitable structural surface. The heterostructure of the ZIF nanocomplex allows the existence of dielectric loss and magnetic loss, therefore yielding a significant improvement on EM wave absorption with a minimum reflection coefficient (RC_{min}) of −50.9 dB at 17.0 GHz at a thickness of 1.9 mm and an effective absorption bandwidth (EAB) covering the full Ku-band (12.0−18.0 GHz).

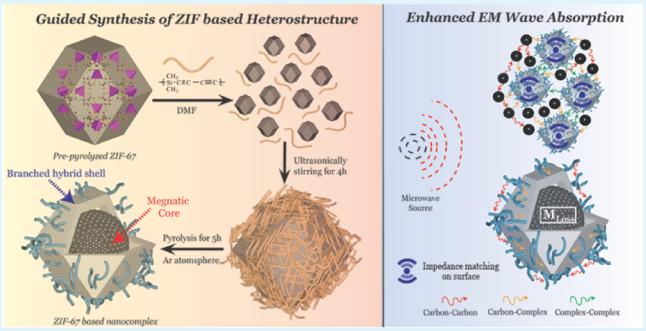

KEYWORDS: *zeolitic imidazolate frameworks, electromagnetic wave absorbing, nanocomplex, heterostructure, coordination reaction*

INTRODUCTION

Metal−organic frameworks (MOFs) have attracted significant interest in the last few decades from various fields such as absorbent materials for gas separation, energy storage, luminescence materials, and biosensors.[1−5] The high designability on functionalities for MOFs can be facilitated via changing the precursors and/or synthetic conditions,[6,7] as well as post-synthesis modifications (extended annealing, etc.).[8−10] Recently, a subgroup of MOFs, zeolitic imidazolate framework (ZIF), has gained significant interest because of its high porosity,[11,12] excellent mechanical stability,[13] tunable surface properties,[14,15] and exceptional chemical and thermal stabilities.[11,16] ZIFs also offer excellent configurability on structures by substituting the metal centre with other ions,[5,17,18] such as Cu^{2+}, Ni^{2+}, and Cd^{2+}, yielding zeolite-like structures,[19,20] which is desired for electromagnetic (EM) wave absorption/shielding.[21−30] The ultra-wide band absorption in specific bands such as Ku-band (12−18 GHz) and X-band (8.2−12.4 GHz) for EM wave absorbing materials is always important for their application in wireless communication, satellite communication, and medical and aerospace fields.[31,32]

Thus far, the ZIF faces challenges to achieve a high real permittivity (ε') and poor impedance matching after pyrolysis, which lead to a strong reflectivity of EM waves on the surface and poor performance of EM wave absorption. One potential solution is to construct a structural surface using low dielectric materials to "trap" the EM wave on the surface. The concept remains yet to be achieved because of the challenges in facilitating nanostructures during multi-step synthesis and the withholding of the synthesized structure during pyrolysis at high temperatures during the post-synthesis treatment. Ceramic materials with a lower complex permittivity can

Received: March 4, 2019
Accepted: April 23, 2019
Published: April 23, 2019

DOI: 10.1021/acsami.9b03944
ACS Appl. Mater. Interfaces 2019, 11, 17706−17713

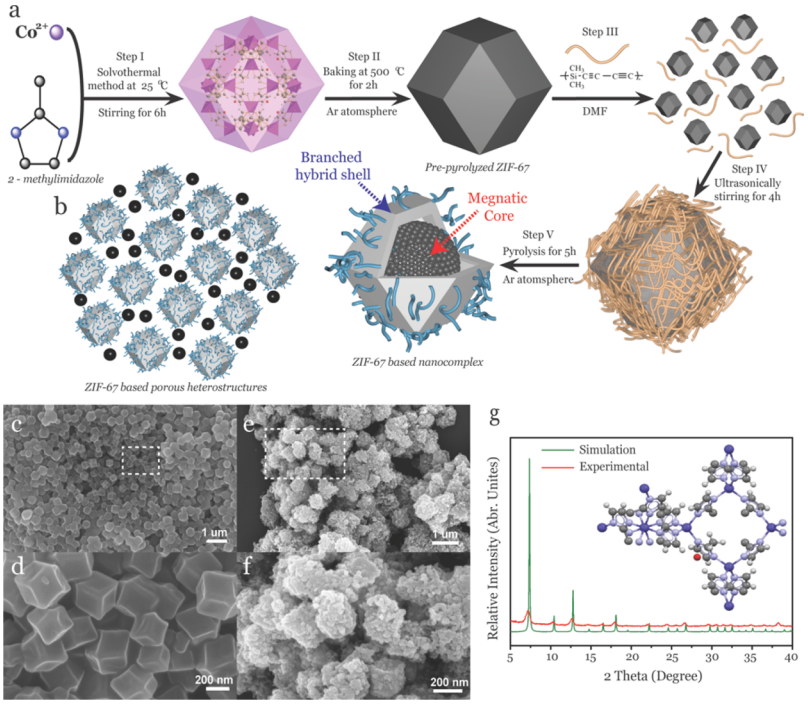

Figure 1. Schematic illustration of the fabrication route toward the ZIF-67-based heterostructure nanocomplex (a,b), SEM images of ZIF-67 (c) after step II in (a) with magnified observation (d) in the selected area, the morphology of the ZIF-67-based heterostructure nanocomplex with magnified observation in the selected area (e,f), and theoretical and experimental XRD results for the ZIF-67 crystal (g).

essentially bridge the gap and provide good EM wave absorption properties.[33−35] A dedicated heterostructure from ceramics can be achieved by introducing the polymeric ceramic precursors into the multi-stage synthesis, resulting in controllable generation of the surface structure after pyrolysis. However, this route has been less considered in ZIF-based nanomaterials.

Here, we proposed a facile strategy to synthesize a ZIF-67-based nanocomplex with hierarchical structures by initializing a coordination reaction between poly(dimethylsilylene)-diacetylenes (PDSDA), a polymeric ceramic precursor with a lower complex permittivity with cobalt in ZIF-67.[36,37] After pyrolysis, we successfully prepared a nanocomplex consisting of multi-lengthscale interfaces between core−shell structures with a porous low dielectric external shell (formed by PDSDA), a high permittivity magnetic core (formed by ZIF-67), carbon nanotubes (formed by amorphous carbon locally catalyzed by cobalt) on the surface, and amorphous carbons. We demonstrate enhanced EM wave absorption with a minimum reflection coefficient (RC_{min}) of −50.9 dB at 17.0 GHz with a sample thickness of 1.9 mm and an effective absorption bandwidth (EAB) covering the full Ku-band (12.0−18.0 GHz) with a designable heterostructure.

EXPERIMENTAL SECTION

Materials. Dichlorodimethylsilane (98%), trichloroethylene (>98%), hexachloro-1, 3-butadiene (97%), *n*-butyllithium (1.6 M solution in hexanes), and *N*,*N*-dimethylformamide (DMF) were purchased from Alfa Aesar, China (Tianjin, China). Cobalt nitrate hexahydrate (99.99% metals basis) was bought from Macklin Co. (Shanghai, China), and 2-methylimidazole (99%) was purchased from TCI Co. (Shanghai, China). All other reagents were used as received.

Synthesis of PDSDA. The synthesis of PDSDA was conducted using the standard Schlenk technique.[38,39] 0.14 mol (42.51 g) *n*-butyllithium was dissolved in 60 mL tetrahydrofuran at −78 °C in an acetone/dry ice bath under an argon atmosphere. Then, 0.035 mol (9.456 g) hexachloro-1,3-butadiene was added through an argon-purged syringe. Subsequently, 0.035 mol dichlorodimethylsilane (4.578 g) was dropped into the flask at −78 °C. After stirring at room temperature for 12 h, chlorotrimethylsilane (2 mL) was added. Then the mixture was dissolved in toluene to filter out lithium chloride. The polymer was precipitated in methanol and dried in a vacuum environment. Finally, the alkyne-containing PDSDA was obtained.

Syntheses of ZIF-67 and Pre-Pyrolyzed ZIF-67. ZIF-67 was synthesized according to refs.[40,42] 1.5 mmol cobalt nitrate in 12 mL deionized water and 67 mmol dimethylimidazole in 80 mL deionized water were mixed and stirred vigorously for 6 h. After stirring for 24 h, the purple precipitates were collected by centrifugating three times using methanol as the eluent. Finally, the as-prepared ZIF-67 was a purple solid. The ZIF-67 was pyrolyzed at 500 °C for 2 h (heating rate 5 K/min under argon) in a tube furnace to prepare pre-pyrolyzed ZIF-67 (P-ZIF-67). 0.02 g of PDSDA and 0.1 g of pre-pyrolyzed ZIF-67 were mixed in DMF at room temperature under ultrasonication for 4 h to fulfill the coordinated reaction to get P-ZIF-67 wrapped with PDSDA.

Preparation of the ZIF-67-Based Nanocomplex. The P-ZIF-67 wrapped with PDSDA was pyrolyzed at various temperatures (500, 600, 700, and 800 °C) under an argon atmosphere in a tube furnace (GSL-1700X, Kejing New Mater. Ltd., Hefei, China). The obtained Co/Si/C/N nanocomplex was named Co/Si/C/N-500, Co/Si/C/N-600, Co/Si/C/N-700, and Co/Si/C/N-800, according to the pyrolyzed temperature.

Characterization. Fourier transform infrared spectroscopy (FT-IR) measurement was performed on a FT-IR spectrometer (DSOR 27, Bruck, Germany). Thermogravimetric analysis and mass spectrometry analysis were conducted on a simultaneous thermal device (449C Jupiter, Netzsch, Gerätebau GmbH, Selb, Germany) coupled with a quadrupole mass spectrometer. The flow of argon is 40 mL/min and the heating rate is 10 K/min. The crystal structure was analyzed by using a X-ray diffractometer (XRD) (Rigaku D/Max-2550VB+/PC) with Cu Kα irradiation (λ = 1.54178 Å, 40.0 kV, 40.0 mA). Scanning electron microscopy (SEM) (Hitachi-S-4800) and

DOI: 10.1021/acsami.9b03944
ACS Appl. Mater. Interfaces 2019, 11, 17706−17713

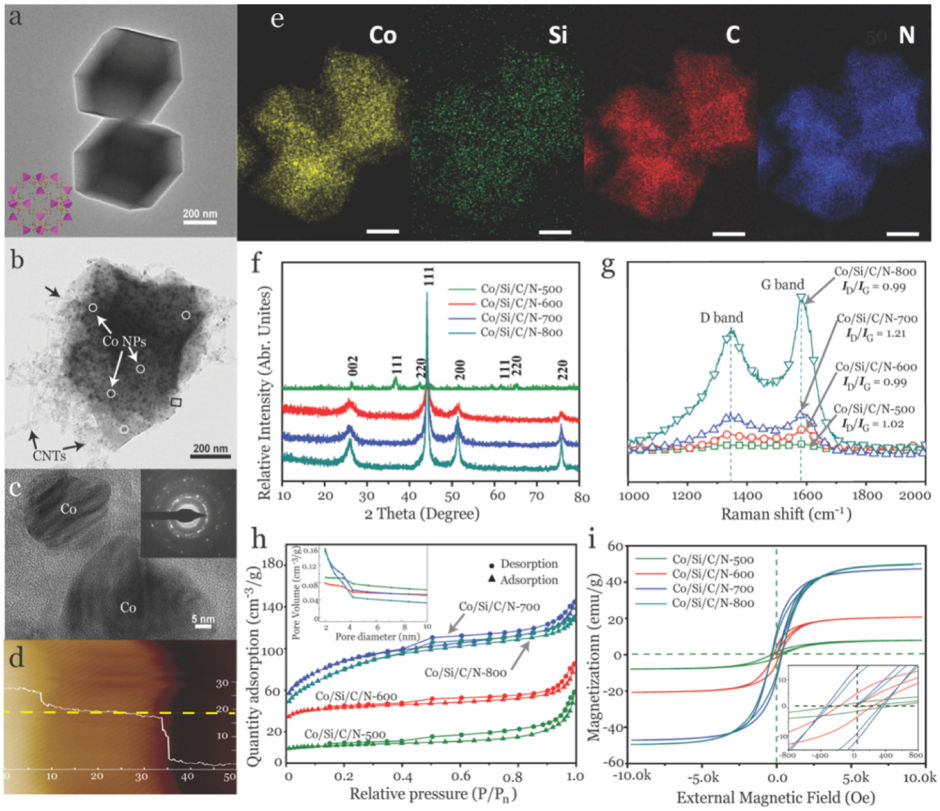

Figure 2. The TEM images of pre-pyrolyzed ZIF-67 crystals collected after step II (a) and ZIF-67-based heterostructure nanocomplex after step V (b), with magnified observation of Co nanoparticles and the selected area electron diffraction (SAED) image (inset) in (c), the AFM profile (d) of the selected area in (b), the EDS mapping (Co, Si, C, N) (e) of the nanocomplex in (b), XRD (f) and Raman results (g) for the nanocomplex at different temperatures, N_2 adsorption and pore size distribution plots (h), and hysteresis loop and coercivity (inset) of the nanocomplex (i).

transmission electron microscopy (TEM) (FEI Talos-F200X) were used to observe the morphology and elemental distribution of samples. The Raman spectrum (inVia, Renishaw, USA) was equipped with a 514 nm Ar laser excitation device. A Micromeritics Tristar 3020 (Micromeritics Co.) nitrogen adsorption instrument was used to measure the specific surface and pore size distribution (Brunauer–Emmett–Teller, BJH model). The magnetic hysteresis loop was measured using a vibrating sample magnetometer (Lake Shore VSM 7307) at 298.15 K.

EM Wave Absorption Measurement. The complex permittivity and complex permeability of the Co/Si/C/N heterostructure nanocomplex were measured using a vector network analyzer (MS4644A, Anritsu) in the frequency range of 2–18 GHz. The milled Co/Si/C/N samples were dispersed in a paraffin matrix with 30% mass fraction to form coaxial rings with an inner diameter of 3.04 mm and an outer diameter of 7.0 mm. On the basis of the generalized transmission line theory and metal backplane model,[43,44] the reflection coefficient (RC) can be calculated using the relative complex permittivity according to the following equation:[45]

$$\mathrm{RC} = 20 \log_{10} \left| \frac{Z_{\mathrm{in}} - 1}{Z_{\mathrm{in}} + 1} \right| \tag{1}$$

$$Z_{\mathrm{in}} = \sqrt{\frac{\mu_{\mathrm{r}}}{\varepsilon_{\mathrm{r}}}} \tanh\left[j \frac{2\pi f d}{c} \sqrt{\mu_{\mathrm{r}} \varepsilon_{\mathrm{r}}} \right] \tag{2}$$

where Z_{in}, ε_{r}, and μ_{r} are the normalized input impedance, permittivity, and permeability of the materials, respectively. f, d and c represent the frequency, thickness (m), and velocity of the EM wave in vacuum, respectively.

RESULTS AND DISCUSSION

The synthesis route of the ZIF-67-based heterostructure nanocomplex is schematically illustrated in Figure 1a, where the ZIF-67 is prepared from cobalt nitrate and 2-methylimidazole (step I).[40,41,43] The pre-pyrolyzed ZIF-67 (step II) represents a basic polyhedral geometry with 80% yield as shown in the Supporting Information (Figure S1) with a number of cobalt atoms. In step III and step IV, the PDSDA was wrapped on ZIFs to fulfill the low complex permittivity and high ceramic yield (Figure S1) in the final nanocomplex. The complete disappearance of the alkenyl peak at 2100 cm^{-1} in FT-IR (Figure S2) suggests that the coordination reaction successfully occurs between the transitional metal ions (Co^{2+}) with the alkenyl groups in PDSDA.[39] After pyrolysis at high temperatures (500 °C or above) under an Ar atmosphere (step V), we successfully obtained the ZIF-67-based heterostructure nanocomplex (Figure 1b), which is assumed to have a core–shell structure (Figure 1a) with a low dielectric shell (formed by PDSDA) and high real permittivity (ε'), magnetic core (formed by ZIF-67), and branched carbon nanotubes on the surface as metal Co could indorse graphitic carbon to form carbon nanotubes and amorphous carbons.[46–48] The samples are labeled Co/Si/C/N-500, Co/Si/C/N-600, Co/Si/C/N-700, and Co/Si/C/N-800, where the digital number refers to the pyrolysis temperature.

The morphology and structure of pre-pyrolyzed ZIF-67 and its derived nanocomplex were evaluated by SEM (Figure 1c–f), where we observed a typical rhombic dodecahedron morphology for pre-pyrolyzed ZIF-67 (Figure 1c–d) in a size distribution of 300–400 nm.[49,50] After initializing the

DOI: 10.1021/acsami.9b03944
ACS Appl. Mater. Interfaces 2019, 11, 17706–17713

coordinated reaction with PDSDA on the ZIF surface and pyrolyzing at high temperature, we obtained a highly mesoporous surface on the ZIF-based nanocomplex (Figure 1e,f). The powder X-ray diffraction (XRD) result for pre-pyrolyzed ZIF-67 (Figure 1g) suggests a sodalite topology of $(Co(mIM)_2)$ in good agreement with the theoretical crystal structure. Overall, the good preservation in the dodecahedron shape was presented after pyrolyzing at high temperatures.[51,52]

By thermally pyrolyzing in an inert atmosphere, the organic ligands in the ZIF-67 crystal (Figure 2a) can be carbonized, and metal ions will be reduced to form a hybrid metal/carbon structure.[53,54] By characterizing the pyrolyzed ZIF-based nanocomplex using TEM, we found (i) clear boundaries as being defined by the original ZIF (Figure 2b) covered by (ii) highly branched carbon nanotubes (CNTs, typically ca. 10 nm in diameter and ca. a few micrometers in length), and (iii) a mesoporous surface where metallic cobalt particles (Figure 2c) were formed. After the decomposition and carbonization, most of the cobalt deposited outside of the carbon matrix to form a porous shell. The corresponding SAED pattern (inset, Figure 2c) confirms that the polycrystallinity phase occur for the pyrolyzed ZIF-67. The organic ligands in PDSDA were catalyzed by cobalt to generate CNTs on the surface, as well as graphene skirts regionally located at the edge of the nanocomplex (Figure 2d).

From the EDS mapping in Figure 2e, we find a uniform distribution of C (red), Si (green), and N (blue) with the same profile of pre-pyrolyzed ZIF (labelled by Co), which proves the homogeneity coverage of the branched CNTs on the ZIF nanocomplex. We next assess the elemental and valence states of the ZIF-67-based nanocomplex at 700 °C using XPS (Figure S3a). The high-resolution C 1s spectrum (from 282 to 292 eV, Figure S3b) reveals four types of carbon bonds corresponding to C−C (284.6 eV), C−N (285.4 eV), C−O (286.5 eV), and O−C═O (289.2 eV).[39,55−57] The Co 2p spectrum (from 773 to 789 eV for Co $2p_{3/2}$ and from 790 to 809 eV for Co $2p_{1/2}$, Figure S3c) agrees well with four signature peaks, that is, Co (779.0 eV), Co trivalent (783.6 eV), and bivalent (794.5 and 800 eV). The divalent cobalt is oxidized to trivalent cobalt when exposed to air.[58] The N 1s spectrum (from 395 to 405 eV, Figure S3d) deconvolutes into pyridinium-N at 398.5 eV, pyrrole nitrogen at 400.3 eV, graphitic nitrogen at 401.3 eV, and nitric oxide at 404.5 eV.[59] The Si 2p spectrum (from 98 to 106 eV, Figure S3e) indicates the coexistence of three deconvoluted peaks of SiC (100.8 eV), SiO_xC_y (102.5 eV), and SiO_2 (103.4 eV).[60] Combined with the thermogravimetric analysis (TGA) curve (green) in Figure S1, the PDSDA seems only partially degraded at 700 and 800 °C, indicating that a transition layer can be formed.

We next investigated the temperature-dependent phase composition and morphology changes of the synthesized nanocomplex by analyzing the powder XRD results (Figure 2f). Weak diffraction peaks are found for the Co/Si/C/N-500 at the CoN(111) and (220) crystal face at $2\theta = 36.9°$ and $2\theta = 61.7°$ (JCPDS#83-0831) and Co_2N(111) and (200) crystal face at $2\theta = 42.5°$ and $2\theta = 65.3°$ (JCPDS#72-1368), respectively. However, no obvious characteristic peaks of CoN are shown for Co/Si/C/N-600, Co/Si/C/N-700, and Co/Si/C/N-800, indicating the collapse of the CoN structure at 600 °C. The diffraction peaks at $2\theta = 44.5°$, $2\theta = 51.5°$, and $2\theta = 76.0°$ are assigned to the (111), (200), and (220) crystal face of cubic Co crystals. The enhanced peak for graphitic carbons is observed when the pyrolysis temperature increases. The grain sizes for graphitic carbons and cubic Co are calculated using the Debye−Scherrer equation.[50,61]

$$D = \frac{K\lambda}{\beta \cos\theta} \tag{3}$$

where $K = 0.90$, $\lambda = 0.154$ nm, θ is the diffraction angle, and β is the full width at half maxima of the most intense peak. The calculated grain sizes of cubic cobalt atoms in Co/Si/C/N-600, Co/Si/C/N-700, and Co/Si/C/N-800 are 15.3, 16.4, and 20.7 nm, respectively, and the dendritic structure gradually grows on the surface of the ZIF-67-based nanocomplex when the temperature increases to 600 °C and above (Figure S4).

Raman spectra are used to understand the morphological distribution of carbons in the pyrolyzed nanocomplex (Figure 2g). With the increase of pyrolysis temperature, the I_D/I_G of the integrated intensity changes to represent the degree of disorder. Compared to Co/Si/C/N-600/800, the I_D/I_G of Co/Si/C/N-700 is higher, indicating a higher lattice disorder in sp^2-hybridized carbon atoms and/or deposition of amorphous carbon. The black spot (cobalt nanoparticles, Figure 2b) is distributed around the dendritic polyhedron and causes hysteresis. Meanwhile, the branching dendrite extends free space and offers more contact surface, thus improving the impedance matching. The results of XRD in Figure 2f indicate clear polycrystalline phases, for example, (111), (200), and (220), for the metallic cobalt, which agree well with TEM and SAED results as shown in Figure 2c.

We then analyzed the porosity of the nanocomplex by plotting N_2 adsorption desorption curves using the BJH calculation method (Figure 2h). All samples present a typical type IV adsorption hysteresis characteristic loop at the nominal pressure (p/p_0) of 0.15−1.0 and 0.40−1.0.[62,63] The rapid increase of the N_2 adsorption curve near the nominal pressure of 0.95 is attributed to the capillary condensation, revealing the presence of large pores in a sample with a size distribution from 1.5 to 4.0 nm (see Table S2). For the ZIF67 crystals, the specific surface area is up to 2055.4 m^2/g. Because of the introduction of PDSDA with a high ceramic yield on surfaces, the specific surface area and pore size of the ZIF-based nanocomplex rapidly decreased when pyrolysis temperature increases. The small specific surface area of Co/Si/C/N-500 indicates the incomplete formation of a porous structure at low temperature. The Co/Si/C/N-700 shows a high specific surface area of 319.2 m^2/g, whilst we discover a decrease in the porosity for Co/Si/C/N-800, likely to occur once the skeleton structures collapse and/or partially damage at high temperature.

For EM wave absorption application, the general guideline suggests that more than 90% of the incident EM wave will be absorbed when the value of RC reaches −10 dB or less, which is considered as a key criterion to determine EAB. By plotting the RC data for the Co/Si/C/N porous complex at a frequency range of 2−18 GHz (Figure 3a), an RC_{min} value of −50.9 dB is found for Co/Si/C/N-700 with an EAB of 5.72 GHz, which covers almost the whole Ku-band (12−18 GHz). This excellent EM wave absorption property is enabled by the multi-length scale heterostructure formed after introducing PDSDA into ZIF-67, where the pyrolyzed material without PDSDA presents an opposite performance (Figure S5). It should also be noted that the complex presents a strong magnetic effect after pyrolysis (inset, Figure 3a), as part of the unique feature of ZIF-67. The thickness-dependent peak shift can be given by the following equation[63]

DOI: 10.1021/acsami.9b03944
ACS Appl. Mater. Interfaces 2019, 11, 17706−17713

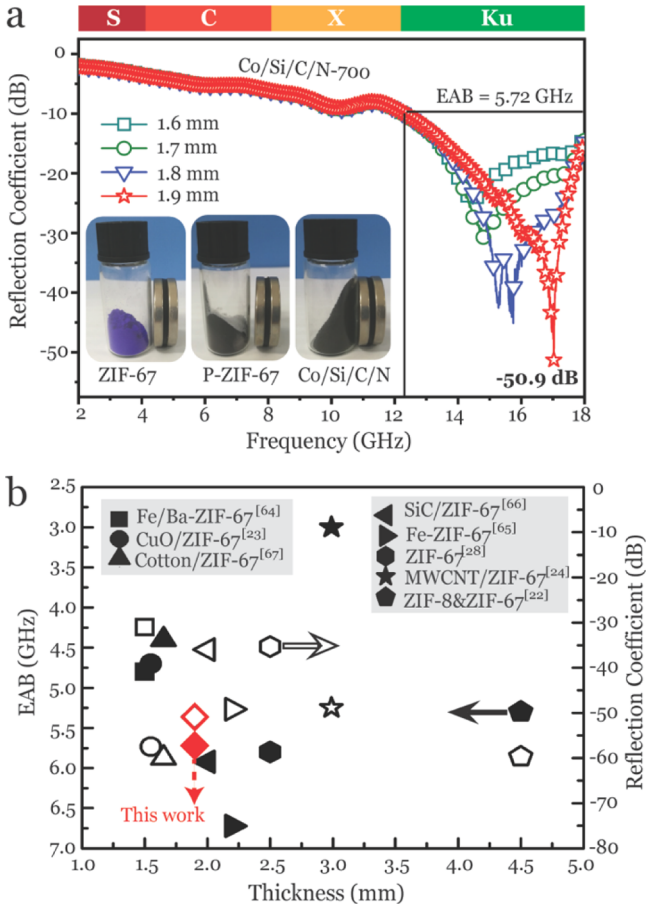

Figure 3. Reflection coefficient of Co/Si/C/N-700 at various thicknesses and demonstration of coercivity for ZIF-67, P-ZIF-67, and Co/Si/C/N-700 under magnetic field (a), and comparison of the EM wave absorption properties of the ZIF-67-based nanocomplex with other reported values (b), where the solid symbol and hollow symbol refer to EAB and RC_{min}, respectively.

$$t_m = \frac{\lambda}{4\sqrt{|\varepsilon_r \mu_r|}} = \frac{c}{4f_m\sqrt{\varepsilon_r \mu_r}} \quad (4)$$

where t_m and f_m are the thickness and frequency of the peak dip, and λ and c represent the wavelength of the EM wave and the light velocity in a vacuum, respectively. The Co/Si/C/N-700 presents the best EAB and RC_{min} performance among the rest of the samples (Figure S6), indicating that the optimized heterostructure is achieved at 700 °C. The ZIF-67-based complex in this research also presents advantage when comparing to the other reports (Figure 3b).

In transition-metal/ZIF-67 complex systems, that is Zn/ZIF-67,[22] CuO/ZIF-67,[23] and Fe/Ba-ZIF-67,[64] the Co/Si/C/N-700 with a RC_{min} value of −50.9 dB and an EAB of 5.72 GHz shows the best EAB and RC_{min}. Even though Fe/ZIF-67 shows an EAB of 6.72 GHz and a RC_{min} of −49.2 dB when the mass fraction in the paraffin matrix is as high as 40%,[65] the thickness and density are also much higher than those of the Co/Si/C/N nanocomplex. When it comes to silicon or carbon/ZIF-67 systems, for example, MWCNT/ZIF-67,[24] SiC/ZIF-67,[66] and cotton/Ba-ZIF-67,[67] our Co/Si/C/N nanocomplex also possesses superior absorption in the whole Ku-band (12.0−18.0 GHz), which has not been reported elsewhere in silicon or carbon/ZIF-67 systems.

The EM wave absorption performance is determined by complex permittivity and permeability. The real part (ε') of permittivity and the imaginary part (ε'') are related to polarization and dielectric loss ability, respectively. From the viewpoint of impedance matching, the low ε' and high ε'' are favorable to the enhanced EM wave absorption, that is, low reflection coefficient. As shown in Figure S7, the Z value of Co/Si/C/N-700 with a thickness of 1.9 mm is in the range of 0.8−1.0 in the Ku-band, implying good impedance matching performance and excellent EM wave absorption. The attenuation constant α of the Co/Si/C/N nanocomplex calculated through eq 5 can access the dissipation effect for the EM wave. The strong attenuation capability gradually increased in the high frequency range as shown in Figure S7. Meanwhile, the best impedance matching as well as large attenuation ability of Co/Si/C/N-700 endows strong broadband absorbing performance.[52]

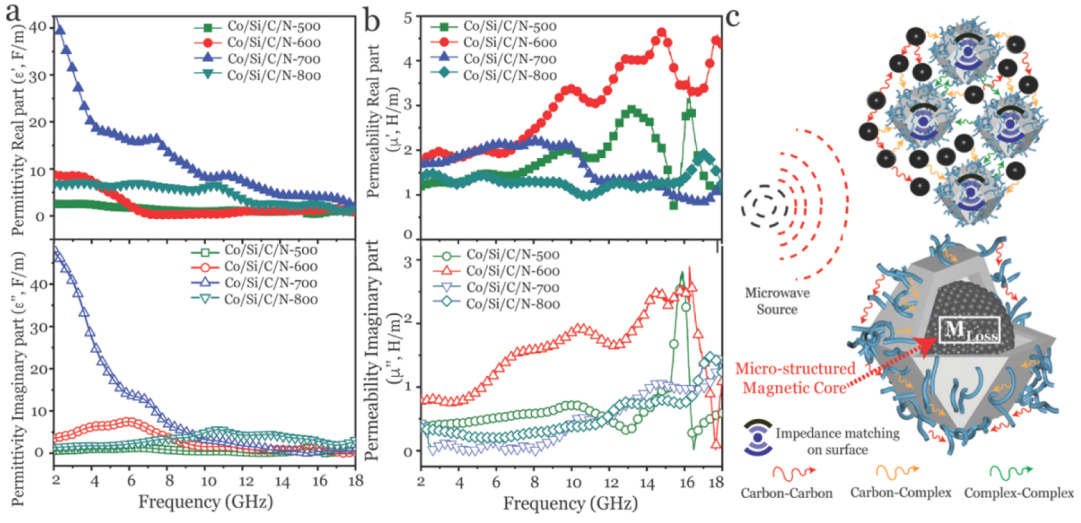

Figure 4. Complex permittivity plots (a) and permeability plots (b) for the Co/Si/C/N nanocomplex, and the illustration of hypothesized interfacial-driven EM wave attenuation for the Co/Si/C/N nanocomplex (c).

DOI: 10.1021/acsami.9b03944
ACS Appl. Mater. Interfaces 2019, 11, 17706−17713

$$\alpha = \frac{\sqrt{2}\pi f}{c} \times \sqrt{(\mu''\varepsilon'' - \mu'\varepsilon') + \sqrt{(\mu'\varepsilon'' + \mu''\varepsilon')^2 + (\mu''\varepsilon'' - \mu'\eta')^2}} \quad (5)$$

Furthermore, in Figure 4a, the values of the real part (ε') and imaginary part (ε'') in 2−18 GHz for all samples are presented. For Co/Si/C/N-700, the ε' value is in the range of 10−42 in 2−10 GHz. With the increase of the frequency, the ε' gradually decreased to about 5. At the same time, the ε'' (from 0.8 to 47) of Co/Si/C/N-700 is lower than that of other samples. Thus, Co/Si/C/N-700 shows the low reflection coefficient and wide EAB in the Ku-band. The magnetic permeability of the Co/Si/C/N nanocomplex is also sensitive to the frequency. As shown in Figure 4b, the real part (μ') and imaginary part (μ'') increased in 2−18 GHz for Co/Si/C/N-500, Co/Si/C/N-600, and Co/Si/C/N-800, while the μ' decreased after 10 GHz for Co/Si/C/N-700. The μ'' of Co/Si/C/N-700 is higher than that of Co/Si/C/N-500 and Co/Si/C/N-800 in 10−18 GHz. Overall, from the contribution of both dielectric loss and magnetic loss, the Co/Si/C/N-700 shows excellent EM absorption among all the nanocomplexes.

As well known, the attenuation of the EM wave is the consequence caused by the combined effects from dielectric loss and magnetic loss. Dielectric tangent loss ($\tan \delta_\varepsilon = e''/\varepsilon'$) and magnetic tangent loss ($\tan \delta_\mu = \mu''/\mu'$) are calculated to assess the EM dissipation factors. Figure S8 shows the value of EM loss with the Co/Si/C/N nanocomplex. It is obvious that the $\tan \delta_\varepsilon$ value of Co/Si/C/N-700 decreases as the frequency increases, whereas the $\tan \delta_\mu$ value shows an opposite trend. To well understand the effect of magnetic loss on the EM wave attenuation, we plot the hysteresis loop of the Co/Si/C/N porous complex in Figure 2i. The ZIF-67 and P-ZIF-67 only show a linear paramagnetic response. However, the Co/Si/C/N nanocomplex shows a strong ferromagnetic response with a gradually rising saturation magnetization (M_s) (7.9, 20.6, 47.3, and 50.1 emu/g) when the pyrolysis temperature increases. Because the absolute values of susceptibility are less than 1 ($|\chi| < 1$, Table S2), the paramagnetic response of the Co/Si/C/N nanocomplex can be judged. The magnetization is attributed to the CoN and Co_2N nanocrystals in the nanocomplex. Because the Co/Si/C/N-700 possesses the highest remanence (M_r) of 13.2 emu/g and coercivity (H_c) of 350 Oe in comparison to other three samples (44−277 Oe), it can dissipate the EM wave into heat to attenuate at a high frequency.[68]

Based on the analyses mentioned above, the illustration of hypothesized interfacial-driven EM wave attenuation for the Co/Si/C/N nanocomplex is presented in Figure 4c. The heterostructured Co/Si/C/N nanocomplex consisting of a low dielectric layer, porous structure, and regular distribution of magnetic cobalt particles provides multiple interfaces to enable unique impedance matching and EM loss. The low dielectric layer like dendrites and porous structures can allow the EM wave to enter the polyhedron and convert into heat and atomic vibration. The conductive network formed by amorphous carbon and cobalt particles can maximize the interfacial polarization loss. Ferromagnetism of the cobalt particle and transmission of the low dielectric layer to a high dielectric core allow more EM wave absorption rather than reflection, thus enhancing the formation of a magnetic eddy current.[69,70] The combining effect from multi-lengthscale structures among the interfaces contribute to outstanding EM wave absorption properties together.

CONCLUSIONS

A facile strategy was developed to achieve a ZIF-67-based heterostructured nanocomplex by introducing a surface coordinated reaction between PDSDA and ZIF-67. The involvement of PDSDA allows the ZIF host to undergo significant surface morphological transformations by carbonizing the organic ligand during the pyrolysis. The nanocomplex possesses a hierarchical heterostructure consisting of an MOF defined by the original ZIF particles, nano-structured surface made by branched CNTs and a regionally distributed graphene skirt, and a mesoporous surface based on Co particles. After further exploring the structure-functionality relationship of the nanocomplex, unique EM wave absorption for the synthesized nanocomplex is demonstrated, by achieving a RC_{min} value of −50.9 dB and a EAB of 5.72 GHz at a thin thickness of 1.9 mm that almost covers the whole Ku-band (12.0−18.0 GHz). We expect that this study of the structural design of the ZIF-based nanocomplex will open up a new window for developing high-performance EM wave absorbing materials in future.

ASSOCIATED CONTENT

Supporting Information

The Supporting Information is available free of charge on the ACS Publications website at DOI: 10.1021/acsami.9b03944.

TGA-mass curves of polymers, XPS spectra, and reflection coefficient of ceramics (PDF)

AUTHOR INFORMATION

Corresponding Authors

*E-mail: ben.xu@northumbria.ac.uk (B.X.).
*E-mail: kongjie@nwpu.edu.cn (J.K.).

ORCID

Ben B. Xu: 0000-0002-6747-2016
Jie Kong: 0000-0002-9405-3204

Notes

The authors declare no competing financial interest.

ACKNOWLEDGMENTS

This work was financially supported by the National Natural Science Foundation of China (21875190), the Natural Science Basic Research Plan in Shaanxi Province of China (2018JC-008, Distinguished Young Scholar), the Shaanxi Province Key Research and Development Plan for Industry Innovation Chain (Cluster) (2018ZDCXL-GY-09-07), the Analytical and Testing Center of NPU, and the Engineering and Physical Sciences Research Council (EPSRC) grants-EP/N007921 and EP/N032861/1.

REFERENCES

(1) Han, L.; Yu, X.-Y.; Lou, X. W. D. Formation of Prussian-Blue-Analog Nanocages via a Direct Etching Method and their Conversion into Ni-Co-Mixed Oxide for Enhanced Oxygen Evolution. *Adv. Mater.* **2016**, *28*, 4601−4605.

(2) Li, J.-R.; Kuppler, R. J.; Zhou, H.-C. Selective Gas Adsorption and Separation in Metal-Organic Frameworks. *Chem. Soc. Rev.* **2009**, *38*, 1477−1504.

(3) Zhang, W.; Lu, G.; Cui, C.; Liu, Y.; Li, S.; Yan, W.; Xing, C.; Chi, Y. R.; Yang, Y.; Huo, F. A Family of Metal-Organic Frameworks

DOI: 10.1021/acsami.9b03944
ACS Appl. Mater. Interfaces 2019, 11, 17706−17713

Exhibiting Size-Selective Catalysis with Encapsulated Noble-Metal Nanoparticles. *Adv. Mater.* **2014**, *26*, 4056−4060.
(4) Wu, H. B.; Lou, X. W. Metal-Organic Frameworks and Their Derived Materials for Electrochemical Energy Storage and Conversion: Promises and Challenges. *Sci. Adv.* **2017**, *3*, No. eaap9252.
(5) Saha, S.; Das, G.; Thote, J.; Banerjee, R. Photocatalytic Metal-Organic Framework from CdS Quantum Dot Incubated Luminescent Metallohydrogel. *J. Am. Chem. Soc.* **2014**, *136*, 14845−14851.
(6) Yoon, S. M.; Park, J. H.; Grzybowski, B. A. Large-Area, Freestanding MOF Films of Planar, Curvilinear, or Micropatterned Topographies. *Angew. Chem., Int. Ed.* **2017**, *56*, 127−132.
(7) Zhang, Z.; Chen, Y.; Xu, X.; Zhang, J.; Xiang, G.; He, W.; Wang, X. Well-defined Metal-Organic Framework Hollow Nanocages. *Angew. Chem., Int. Ed.* **2014**, *53*, 429−433.
(8) Zhuang, X.; Gehrig, D.; Forler, N.; Liang, H.; Wagner, M.; Hansen, M. R.; Laquai, F.; Zhang, F.; Feng, X. Conjugated Microporous Polymers with Dimensionality-controlled Heterostructures for Green Energy Devices. *Adv. Mater.* **2015**, *27*, 3789−3796.
(9) Kim, M.; Cahill, J. F.; Fei, H.; Prather, K. A.; Cohen, S. M. Postsynthetic Ligand and Cation Exchange in Robust Metal-Organic Frameworks. *J. Am. Chem. Soc.* **2012**, *134*, 18082−18088.
(10) Kaneti, Y. V.; Dutta, S.; Hossain, M. S. A.; Shiddiky, M. J. A.; Tung, K.-L.; Shieh, F.-K.; Tsung, C.-K.; Wu, K. C.-W.; Yamauchi, Y. Strategies for Improving the Functionality of Zeolitic Imidazolate Frameworks: Tailoring Nanoarchitectures for Functional Applications. *Adv. Mater.* **2017**, *29*, 1700213−1700244.
(11) Phan, A.; Doonan, C. J.; Uribe-Romo, F. J.; Knobler, C. B.; O'Keeffe, M.; Yaghi, O. M. Synthesis, Structure, and Carbon Dioxide Capture Properties of Zeolitic Imidazolate Frameworks. *Acc. Chem. Res.* **2010**, *43*, 58−67.
(12) Banerjee, R.; Phan, A.; Wang, B.; Knobler, C.; Furukawa, H.; O'Keeffe, M.; Yaghi, O. M. High-throughput Synthesis of Zeolitic Imidazolate Frameworks and Application to CO_2Capture. *Science* **2008**, *319*, 939−943.
(13) Tan, J. C.; Bennett, T. D.; Cheetham, A. K. Chemical structure, network topology, and porosity effects on the mechanical properties of Zeolitic Imidazolate Frameworks. *Proc. Natl. Acad. Sci. U.S.A.* **2010**, *107*, 9938−9943.
(14) Aromí, G.; Barrios, L. A.; Roubeau, O.; Gamez, P. Triazoles and tetrazoles: Prime ligands to generate remarkable coordination materials. *Coord. Chem. Rev.* **2011**, *255*, 485−546.
(15) Morris, W.; Doonan, C. J.; Furukawa, H.; Banerjee, R.; Yaghi, O. M. Crystals as Molecules: Postsynthesis Covalent Functionalization of Zeolitic Imidazolate Frameworks. *J. Am. Chem. Soc.* **2008**, *130*, 12626−12627.
(16) Wang, B.; Côté, A. P.; Furukawa, H.; O'Keeffe, M.; Yaghi, O. M. Colossal Cages in Zeolitic Imidazolate Frameworks as Selective Carbon Dioxide Reservoirs. *Nature* **2008**, *453*, 207−211.
(17) Liu, S.; Xiang, Z.; Hu, Z.; Zheng, X.; Cao, D. Zeolitic Imidazolate Framework-8 as a Luminescent Material for the Sensing of Metal Ions and Small Molecules. *J. Mater. Chem.* **2011**, *21*, 6649−6653.
(18) Peralta, D.; Chaplais, G.; Simon-Masseron, A.; Barthelet, K.; Chizallet, C.; Quoineaud, A.-A.; Pirngruber, G. D. Comparison of the Behavior of Metal-Organic Frameworks and Zeolites for Hydrocarbon Separations. *J. Am. Chem. Soc.* **2012**, *134*, 8115−8126.
(19) Lewis, D. W.; Ruiz-Salvador, A. R.; Gómez, A.; Rodriguez-Albelo, L. M.; Coudert, F.-X.; Slater, B.; Cheetham, A. K.; Mellot-Draznieks, C. Zeolitic Imidazole Frameworks: Structural and Energetics Trends Compared with Their Zeolite Analogues. *CrystEngComm* **2009**, *11*, 2272−2276.
(20) Karagiaridi, O.; Bury, W.; Sarjeant, A. A.; Stern, C. L.; Farha, O. K.; Hupp, J. T. Synthesis and Characterization of Isostructural Cadmium Zeolitic Imidazolate Frameworks via Solvent-assisted Linker Exchange. *Chem. Sci.* **2012**, *3*, 3256−3260.
(21) Shahzad, F.; Alhabeb, M.; Hatter, C. B.; Anasori, B.; Man Hong, S.; Koo, C. M.; Gogotsi, Y. Electromagnetic Interference Shielding with 2D Transition Metal Carbides (MXenes). *Science* **2016**, *353*, 1137−1140.
(22) Feng, W.; Wang, Y.; Chen, J.; Li, B.; Guo, L.; Ouyang, J.; Jia, D.; Zhou, Y. Metal Organic Framework-Derived CoZn Alloy/N-doped Porous Carbon Nanocomposites: Tunable Surface Area and Electromagnetic Wave Absorption Properties. *J. Mater. Chem. C* **2018**, *6*, 10−18.
(23) Ma, J.; Zhang, X.; Liu, W.; Ji, G. Direct Synthesis of MOF-Derived Nanoporous CuO/Carbon Composites for High Impedance Matching and Advanced Microwave Absorption. *J. Mater. Chem. C* **2016**, *4*, 11419−11426.
(24) Yin, Y.; Liu, X.; Wei, X.; Li, Y.; Nie, X.; Yu, R.; Shui, J. Magnetically Aligned Co-C/MWCNTs Composite Derived from MWCNT-Interconnected Zeolitic Imidazolate Frameworks for a Lightweight and Highly Efficient Electromagnetic Wave Absorber. *ACS Appl. Mater. Interfaces* **2017**, *9*, 30850−30861.
(25) Yin, Y.; Liu, X.; Wei, X.; Yu, R.; Shui, J. Porous CNTs/Co Composite Derived from Zeolitic Imidazolate Framework: A Lightweight, Ultrathin, and Highly Efficient Electromagnetic Wave Absorber. *ACS Appl. Mater. Interfaces* **2016**, *8*, 34686−34698.
(26) Lv, H.; Yang, Z.; Wang, P. L.; Ji, G.; Song, J.; Zheng, L.; Zeng, H.; Xu, Z. J. A Voltage-Boosting Strategy Enabling a Low-Frequency, Flexible Electromagnetic Wave Absorption Device. *Adv. Mater.* **2018**, *30*, 1706343−1706351.
(27) Lu, S.; Meng, Y.; Wang, H.; Wang, F.; Yuan, J.; Chen, H.; Dai, Y.; Chen, J. Great Enhancement of Electromagnetic Wave Absorption of MWCNTs@Carbonaceous CoO Composites Derived from MWCNTs-Interconnected Zeolitic Imidazole Framework. *Appl. Surf. Sci.* **2019**, *481*, 99−107.
(28) Wang, K.; Chen, Y.; Tian, R.; Li, H.; Zhou, Y.; Duan, H.; Liu, H. Porous Co-C Core-Shell Nanocomposites Derived from Co-MOF-74 with Enhanced Electromagnetic Wave Absorption Performance. *ACS Appl. Mater. Interfaces* **2018**, *10*, 11333−11342.
(29) Lv, H.; Yang, Z.; Ong, S. J. H.; Wei, C.; Liao, H.; Xi, S.; Du, Y.; Ji, G.; Xu, Z. J. A Flexible Microwave Shield with Tunable Frequency-Transmission and Electromagnetic Compatibility. *Adv. Funct. Mater.* **2019**, *29*, 1900163.
(30) Luo, C.; Tang, Y.; Jiao, T.; Kong, J. High-Temperature Stable and Metal-Free Electromagnetic Wave-Absorbing SiBCN Ceramics Derived from Carbon-Rich Hyperbranched Polyborosilazanes. *ACS Appl. Mater. Interfaces* **2018**, *10*, 28051−28061.
(31) Yin, X.; Kong, L.; Zhang, L.; Cheng, L.; Travitzky, N.; Greil, P. Electromagnetic Properties of Si−C−N Based Ceramics and Composites. *Int. Mater. Rev.* **2014**, *59*, 326−355.
(32) Dai, X.; Du, Y.; Yang, J.; Wang, D.; Gu, J.; Li, Y.; Wang, S.; Xu, B. B.; Kong, J. Recoverable and Self-healing Electromagnetic Wave Absorbing Nanocomposites. *Compos. Sci. Technol.* **2019**, *174*, 27−32.
(33) Luo, C.; Jiao, T.; Gu, J.; Tang, Y.; Kong, J. Graphene Shield by SiBCN Ceramic: A Promising High-Temperature Electromagnetic Wave-Absorbing Material with Oxidation Resistance. *ACS Appl. Mater. Interfaces* **2018**, *10*, 39307−39318.
(34) Luo, C.; Jiao, T.; Tang, Y. S.; Kong, J. Excellent Electromagnetic Wave Absorption of Iron-Containing SiBCN Ceramics at 1158K High-Temperature. *Adv. Eng. Mater.* **2018**, *20*, 1701168.
(35) Song, Y.; He, L.; Zhang, X.; Liu, F.; Tian, N.; Tang, Y.; Kong, J. Highly Efficient Electromagnetic Wave Absorbing Metal-Free and Carbon-Rich Ceramics Derived from Hyperbranched Polycarbosilazanes. *J. Phys. Chem. C* **2017**, *121*, 24774−24785.
(36) West, R.; David, L. D.; Djurovich, P. I.; Stearley, K. L.; Srinivasan, K. S. V.; Yu, H. Phenylmethylpolysilanes: formable silane copolymers with potential semiconducting properties. *J. Am. Chem. Soc.* **1981**, *103*, 7352−7354.
(37) Kong, J.; Schmalz, T.; Motz, G.; Müller, A. H. E. Magnetoceramic Nanocrystals from the Bulk Pyrolysis of Novel Hyperbranched Polyferrocenyl(boro)carbosilanes. *J. Mater. Chem. C* **2013**, *1*, 1507−1514.
(38) Corriu, R. J. P.; Guerin, C.; Henner, B.; Jean, A.; Garnier, F.; Yassar, A.; Kuhlmann, T. Organosilicon polymers: synthesis of poly[(silanylene)diethynylene]s with conducting properties. *Chem. Mater.* **1990**, *2*, 351−352.

DOI: 10.1021/acsami.9b03944
ACS Appl. Mater. Interfaces 2019, 11, 17706−17713

(39) Luo, C.; Duan, W.; Yin, X.; Kong, J. Microwave-Absorbing Polymer-Derived Ceramics from Cobalt-Coordinated Poly-(dimethylsilylene)diacetylenes. *J. Phys. Chem. C* **2016**, *120*, 18721−18732.
(40) Wu, R.; Xue, Y.; Liu, B.; Zhou, K.; Wei, J.; Chan, S. H. Cobalt Diselenide Nanoparticles Embedded within Porous Carbon Polyhedra as Advanced Electrocatalyst for Oxygen Reduction Reaction. *J. Power Sources* **2016**, *330*, 132−139.
(41) Torad, N. L.; Hu, M.; Ishihara, S.; Sukegawa, H.; Belik, A. A.; Imura, M.; Ariga, K.; Sakka, Y.; Yamauchi, Y. Direct Synthesis of MOF-Derived Nanoporous Carbon with Magnetic Co Nanoparticles toward Efficient Water Treatment. *Small* **2014**, *10*, 2096−2107.
(42) Jiang, Z.; Li, Z.; Qin, Z.; Sun, H.; Jiao, X.; Chen, D. LDH Nanocages Synthesized with MOF Templates and Their High Performance as Supercapacitors. *Nanoscale* **2013**, *5*, 11770−11775.
(43) Lerf, A.; He, H.; Forster, M.; Klinowski, J. Structure of Graphite Oxide Revisited‖. *J. Phys. Chem. B* **1998**, *102*, 4477−4482.
(44) Miles, P. A.; Westphal, W. B.; Von Hippel, A. Dielectric Spectroscopy of Ferromagnetic Semiconductors. *Rev. Mod. Phys.* **1957**, *29*, 279−307.
(45) You, B.; Jiang, N.; Sheng, M.; Drisdell, W. S.; Yano, J.; Sun, Y. Bimetal-Organic Framework Self-Adjusted Synthesis of Support-Free Nonprecious Electrocatalysts for Efficient Oxygen Reduction. *ACS Catal.* **2015**, *5*, 7068−7076.
(46) Wu, R.; Wang, D. P.; Rui, X.; Liu, B.; Zhou, K.; Law, A. W. K.; Yan, Q.; Wei, J.; Chen, Z. In-situ Formation of Hollow Hybrids Composed of Cobalt Sulfides Embedded within Porous Carbon Polyhedra/carbon Nanotubes for High-performance Lithium-ion Batteries. *Adv. Mater.* **2015**, *27*, 3038−3044.
(47) Tang, J.; Salunkhe, R. R.; Liu, J.; Torad, N. L.; Imura, M.; Furukawa, S.; Yamauchi, Y. Thermal Conversion of Core-Shell Metal-Organic Frameworks: A New Method for Selectively Functionalized Nanoporous Hybrid Carbon. *J. Am. Chem. Soc.* **2015**, *137*, 1572−1580.
(48) Xia, W.; Zhu, J.; Guo, W.; An, L.; Xia, D.; Zou, R. Well-defined carbon polyhedrons prepared from nano metal-organic frameworks for oxygen reduction. *J. Mater. Chem. A* **2014**, *2*, 11606−11613.
(49) Bhat, I.; Husain, S.; Khan, W.; Patil, S. I. Effect of Zn Doping on Structural, Magnetic and Dielectric Properties of La-FeO_3Synthesized through Sol-gel Auto-combustion Process. *Mater. Res. Bull.* **2013**, *48*, 4506−4512.
(50) Jacobs, B. W.; Houk, R. J. T.; Anstey, M. R.; House, S. D.; Robertson, I. M.; Talin, A. A.; Allendorf, M. D. Ordered metal nanostructureself-assembly using metal-organic frameworks as templates. *Chem. Sci.* **2011**, *2*, 411−416.
(51) Lu, S.; Meng, Y.; Wang, H.; Wang, F.; Yuan, J.; Chen, H.; Dai, Y.; Chen, J. Great Enhancement of Electromagnetic Wave Absorption of Mwcnts@Carbonaceous CoO Composites Derived from Mwcnts-Interconnected Zeolitic Imidazole Framework. *Appl. Surf. Sci.* **2019**, *481*, 99−107.
(52) Fang, J.; Liu, T.; Chen, Z.; Wang, Y.; Wei, W.; Yue, X.; Jiang, Z. A Wormhole-Like Porous Carbon/Magnetic Particles Composite as an Efficient Broadband Electromagnetic Wave Absorber. *Nanoscale* **2016**, *8*, 8899−8909.
(53) Chen, Y.-Z.; Wang, C.; Wu, Z.-Y.; Xiong, Y.; Xu, Q.; Yu, S.-H.; Jiang, H.-L. From Bimetallic Metal-Organic Framework to Porous Carbon: High Surface Area and Multicomponent Active Dopants for Excellent Electrocatalysis. *Adv. Mater.* **2015**, *27*, 5010−5016.
(54) Salunkhe, R. R.; Tang, J.; Kamachi, Y.; Nakato, T.; Kim, J. H.; Yamauchi, Y. Asymmetric Supercapacitors Using 3D Nanoporous Carbon and Cobalt Oxide Electrodes Synthesized from a Single Metal-Organic Framework. *ACS Nano* **2015**, *9*, 6288−6296.
(55) Zhao, W.; Kong, J.; Liu, H.; Zhuang, Q.; Gu, J.; Guo, Z. Ultra-high Thermally Conductive and Rapid Heat Responsive Poly-(benzobisoxazole) Nanocomposites with Self-Aligned Graphene. *Nanoscale* **2016**, *8*, 19984−19993.
(56) Bhadra, B. N.; Song, J. Y.; Khan, N. A.; Jhung, S. H. TiO_2-Containing Carbon Derived from a Metal-Organic Framework Composite: A Highly Active Catalyst for Oxidative Desulfurization. *ACS Appl. Mater. Interfaces* **2017**, *9*, 31192−31202.
(57) Zhao, W.; Tang, Y.; Xi, J.; Kong, J. Functionalized Graphene Sheets with Poly(ionic liquid)s and High Adsorption Capacity of Anionic Dyes. *Appl. Surf. Sci.* **2015**, *326*, 276−284.
(58) Chen, H.; Wang, M. Q.; Yu, Y.; Liu, H.; Lu, S.-Y.; Bao, S.-J.; Xu, M. Assembling Hollow Cobalt Sulfide Nanocages Array on Graphene-like Manganese Dioxide Nanosheets for Superior Electrochemical Capacitors. *ACS Appl. Mater. Interfaces* **2017**, *9*, 35040−35047.
(59) Song, Z.; Liu, W.; Cheng, N.; Norouzi Banis, M.; Li, X.; Sun, Q.; Xiao, B.; Liu, Y.; Lushington, A.; Li, R.; Liu, L.; Sun, X. Origin of the High Oxygen Reduction Reaction of Nitrogen and Sulfur co-doped MOF-derived Nanocarbon Electrocatalysts. *Mater. Horiz.* **2017**, *4*, 900−907.
(60) Wang, B.; Wang, Y.; Lei, Y.; Wu, N.; Gou, Y.; Han, C. Tailoring of Porous Structure in Macro-Meso-Microporous SiC Ultrathin FiberviaElectrospinning Combined with Polymer-Derived Ceramics Route. *Mater. Manuf. Processes* **2015**, *31*, 1357−1365.
(61) Ashiq, M. N.; Qureshi, R. B.; Malana, M. A.; Ehsan, M. F. Fabrication, Structural, Dielectric and Magnetic Properties of Tantalum and Potassium Doped M-type Strontium Calcium Hexaferrites. *J. Alloys Compd.* **2015**, *651*, 266−272.
(62) Xia, W.; Zou, R.; An, L.; Xia, D.; Guo, S. A Metal−organic Framework Route to in situ Encapsulation of Co@Co_3O_4@C Core@Bishell Nanoparticles into a Highly Ordered Porous Carbon Matrix for Oxygen Reduction. *Energy Environ. Sci.* **2015**, *8*, 568−576.
(63) Li, G.; Wang, L.; Li, W.; Ding, R.; Xu, Y. $CoFe_2O_4$ and/or Co_3Fe_7Loaded Porous Activated Carbon Balls as a Lightweight Microwave Absorbent. *Phys. Chem. Chem. Phys.* **2014**, *16*, 12385−12392.
(64) Wang, L.; Guan, Y.; Qiu, X.; Zhu, H.; Pan, S.; Yu, M.; Zhang, Q. Efficient Ferrite/Co/Porous Carbon Microwave Absorbing Material based on Ferrite@Metal-Organic Framework. *Chem. Eng. J.* **2017**, *326*, 945−955.
(65) Quan, B.; Liang, X.; Ji, G.; Ma, J.; Ouyang, P.; Gong, H.; Xu, G.; Du, Y. Strong Electromagnetic Wave Response Derived from the Construction of Dielectric/Magnetic Media Heterostructure and Multiple Interfaces. *ACS Appl. Mater. Interfaces* **2017**, *9*, 9964−9974.
(66) Zhang, K.; Wu, F.; Xie, A.; Sun, M.; Dong, W. In Situ Stringing of Metal Organic Frameworks by SiC Nanowires for High-Performance Electromagnetic Radiation Elimination. *ACS Appl. Mater. Interfaces* **2017**, *9*, 33041−33048.
(67) Zhao, H.; Cheng, Y.; Ma, J.; Zhang, Y.; Ji, G.; Du, Y. Sustainable Route from Biomass Cotton to Construct Lightweight and High-Performance Microwave Absorber. *Chem. Eng. J.* **2018**, *339*, 432−441.
(68) Ohkoshi, S.-I.; Kuroki, S.; Sakurai, S.; Matsumoto, K.; Sato, K.; Sasaki, S. A Millimeter-Wave Absorber Based on Gallium-Substituted ε-Iron Oxide Nanomagnets. *Angew. Chem., Int. Ed.* **2007**, *46*, 8392−8395.
(69) Cao, M.-S.; Yang, J.; Song, W.-L.; Zhang, D.-Q.; Wen, B.; Jin, H.-B.; Hou, Z.-L.; Yuan, J. Ferroferric Oxide/Multiwalled Carbon Nanotube vs Polyaniline/Ferroferric Oxide/Multiwalled Carbon Nanotube Multiheterostructures for Highly Effective Microwave Absorption. *ACS Appl. Mater. Interfaces* **2012**, *4*, 6948−6955.
(70) Fang, J.; Liu, T.; Chen, Z.; Wang, Y.; Wei, W.; Yue, X.; Jiang, Z. A Wormhole-Like Porous Carbon/Magnetic Particles Composite as an Efficient Broadband Electromagnetic Wave Absorber. *Nanoscale* **2016**, *8*, 8899−8909.

DOI: 10.1021/acsami.9b03944
ACS Appl. Mater. Interfaces 2019, 11, 17706−17713

Composites Science and Technology 174 (2019) 27–32

Contents lists available at ScienceDirect

Composites Science and Technology

journal homepage: www.elsevier.com/locate/compscitech

Recoverable and self-healing electromagnetic wave absorbing nanocomposites

Xingyi Dai[a], Yuzhang Du[a], Jiye Yang[a], Ding Wang[b], Junwei Gu[a], Yifan Li[b], Steven Wang[c], Ben B. Xu[b,**], Jie Kong[a,*]

[a] MOE Key Laboratory of Materials Physics and Chemistry in Extraordinary Conditions, Shaanxi Key Laboratory of Macromolecular Science and Technology, School of Science, Northwestern Polytechnical University, Xi'an, 710072, PR China
[b] Mechanical and Construction Engineering, Faculty of Engineering and Environment, Northumbria University, Newcastle upon Tyne, NE1 8ST, UK
[c] School of Chemical Engineering and Advanced Materials, Newcastle University, Newcastle Upon Tyne, Tyne and Wear, NE1 7RU, UK

ARTICLE INFO

Keywords:
Self-healing
Reprocessing
Recycling
Electromagnetic wave absorption
Dynamic covalent bonds

ABSTRACT

Recent advancements in electronics engineering require materials with the resiliency and sustainability to extend their life time. With this regard, we presented a sustainable multi-functional nanocomposites strategy by introducing dynamic imine bonds based polyazomethine (PAM) as molecular interconnects and Fe_3O_4-loaded multiwalled carbon nanotubes as electromagnetic (EM) wave absorbing units. Driven by the reversible dynamic imine bonds, our materials show robust spontaneous self-healing with excellent healing efficiencies of 95% for PAM and 90% for nanocomposite, and an accelerated recovery under a moderate mechanical stimulus. By adding Fe_3O_4-loaded multiwalled carbon nanotubes, the hybrids show excellent EM wave absorbing properties with 50% increment on minimum reflection coefficient (−40.6 dB) than the reported value. We demonstrate a full degradability by decomposing a nanocomposite sheet of 100 mg in an acidic solution within 90 min at room temperature. The nanofillers and monomers after degradation can be re-used to synthesis nanocomposites. The testing results for recoverable nanocomposites show a good retention on mechanical property. This novel strategy may shed a light on the downstream applications in EM wave absorbing devices and smart structures with great potential to accelerate circular economy.

1. Introduction

Electromagnetic (EM) interference and pollution have been seen as threats to public health and environment, caused by the ubiquitously use of cell phones, motors, computers, remote sensors, radars, etc. [1,2] One of the essential solutions is to innovate and apply high performance EM wave absorbing materials in products, which has attracted considerable interests in last few years [3–5]. In comparison to other conventional materials (metals, ceramics and carbons), polymeric nanocomposites offer great advantages due to their flexibility, easy processing, light-weight, low cost, etc. [6–8] However, intrinsic characteristics from polymeric materials still bottle-necked the advancement where mechanical failures (cracking and fracture) can be easily found within structures/devices during operation [9–12]. The disposal of failed products arises even more concerns relevant to the environmental sustainability. Therefore, a circular material strategy that can provide resiliency, i.e. self-recovery and sustainability (recyclability), would be highly desirable for next generation EM wave absorbing devices [13–15].

Self-healing property, fulfilled by the reversibility of macromolecular systems, has been studied extensively under noncovalent (physical) interactions, *i.e.* the inherent long-chain entanglements [16], metal-ligand coordination [17], host-guest interactions [18,19], ionic interactions [20], electrostatic interactions [21], π-π stacking [22], and hydrogen bonds [23]. Self-healing can be obtained by generating reversible chemical covalent bonds in the materials network [24–27], those chemical interactions include acylhydrazone bonds [28–30], disulfide bonds [31,32], boronic ester linkages [33], diarylbibenzofuranone links [34], thiuram disulfide units [35], Diels-Alder reactions [36], and imine bonds (−CH═N−) [37–40].

Notably, Bao and co-workers synthesised a polydimethylsiloxane (PDMS) elastomer with spontaneous self-healing function by forming supramolecular dynamic interactions with coordination complexes [41]. Recently, Yu et al. developed a PDMS elastomer with self-healing

* Corresponding author.
** Corresponding author.
E-mail addresses: ben.xu@northumbria.ac.uk (B.B. Xu), kongjie@nwpu.edu.cn (J. Kong).

https://doi.org/10.1016/j.compscitech.2019.02.018
Received 11 December 2018; Received in revised form 13 February 2019; Accepted 17 February 2019
Available online 19 February 2019
0266-3538/

property by incorporating imine bond, and demonstrated conceptual applications in flexible interconnector and chemical sensor [42]. Zhang et al. designed a kind of electromagnetic shielding materials with easy-processing and self-healing capacity under external force and magnetic force [43]. Wang et al. also reported an EM wave absorption coating with self-healing property, a less ideal minimum reflection coefficient was reported as −27.2 dB with a thickness of 4 mm [44]. Nevertheless, polymeric nanocomposites based EM absorbing materials with sustainable features has been under exploited, partially due to the high viscosity and irreversible physical interactions brought by the nanofillers.

In this work, we propose a synthesis strategy to achieve EM wave absorbing nanocomposites by using dynamic imine bonds-based polyazomethine (PAM) as macromolecular interconnects and Fe_3O_4-loaded multiwalled carbon nanotubes (Fe_3O_4@MWCNTs) as EM wave absorbing units. The nanocomposite presents a unique spontaneous self-healing, and an outstanding reprocessability that can be reformed under a low compressive stress at room temperature. We demonstrate a good sustainability for our composites by instantly degrading the polymer network in an acidic solution, from where the nanofillers and monomers can be collected and reused, therefore lead to an improved environmental impact by using this facile materials strategy.

2. Experimental section

2.1. Materials

Trimethylolethane (98.0%, TCI), *p*-toluenesulfonylchioride (99.0%, TCI), 4-dimethylaminopyridine (DMAP, 99.0%, Aladdin), 4-hydroxy benzaldehyde (99.0%, Aladdin), potassium carbonate (99.0%, Aladdin), poly(propylene glycol)bis(2-aminopropyl ether) (PEA, M_n = 2000Da, Aladdin), iron(II) chloride tetrahydrate ($FeCl_2{\cdot}4H_2O$, 99.0%, Aladdin), iron chloride hexahydrate ($FeCl_3{\cdot}6H_2O$, 99.0%, Aladdin). Multi-walled carbon nanotubes (MWCNTs, average diameter of 20–40 nm, length of 10–30 μm, purity > 90%) were purchased from Chengdu Org. Chem. Co. Ltd. All other reagents were utilized as received unless otherwise specified.

2.2. Two steps synthesis of 1, 1, 1-tris[(4-formylphenoxy)methyl]ethane

The first step is to synthesis tris[(4-tolylsulfonyl)methyl]ethane. As shown in Supporting Information (Fig. S1), trimethylolethane (2.45 g, 20 mmol) and a catalytic amount of DMAP were dissolved in 30 mL pyridine, then the mixture was cooled to 0 °C in an ice bath. Later, we added *p*-toluenesulfonylchioride (13.34 g, 70 mmol) in 20 mL pyridine drop by drop into above mixture. The mixture was then removed from the ice-water bath and the reaction was kept going for 12 h at room temperature. When the reaction was completed, the mixture was diluted with 100 mL dichloromethane, and then washed with 200 mL 1 M HCl solution, 200 mL water and dried. The solvent was evaporated and a white crystalline solid was obtained by crystallization (9.8 g, yield: 84.1%). ^{1}H NMR (400 MHz, $CDCl_3$, δ): 7.72 (d, 6H, ArH), 7.38 (d, 6H, ArH), 3.79 (s, 6H, −CH2-), 2.49 (s, 9H, −CH3), 0.92 (s, 3H, −CH3).

The second step began with mixing tris[(4-tolylsulfonyl)methyl] ethane (5.83 g, 10 mmol), 4-hydroxy benzaldehyde (4.98 g, 40 mmol) and potassium carbonate (5.58 g, 40 mmol) in 30 mL anhydrous *N, N*-dimethylformamide (DMF) under nitrogen atmosphere, and the mixture was heated at 150 °C under reflux for 12 h. Then, the mixture was extracted into 100 mL dichloromethane and washed with 200 mL water, 100 mL saturated brine and dried over anhydrous $MgSO_4$. The solvent was evaporated and the crude product was achieved after purification (3.2 g, yield: 74.1%). ^{1}H NMR (400 MHz, $CDCl_3$, δ): 9.91 (s 3H, −CHO), 7.87 (d, 6H, ArH), 7.05 (d, 6H, ArH), 4.22 (s, 6H, −CH2-), 1.41 (s, 3H, −CH3).

2.3. Preparations of polyazomethine (PAM) and Fe_3O_4@MWCNTs/PAM nanocomposites

For PAM sample preparation, poly(propylene glycol)bis(2-aminopropyl ether) (PEA, 200 mg, 0.1 mmol) was dissolved in 0.5 mL anhydrous *N, N*-dimethylformamide (DMF), followed by adding tris[(4-formylphenoxy)methyl]ethane (31 mg, 0.0667 mmol). After uniformly mixing the solution, glacial acetic acid (AcOH, 2.5 μL) was added. The mixture was then slowly transferred to the Teflon moulds and sealed at room temperature for 12 h. The prepared PAM was dried at 35 °C in the open air for 24 h, to allow the chemical cross-linking to complete within the materials. Fe_3O_4 decorated multi-walled carbon nanotubes (Fe_3O_4@MWCNTs) were prepared as presented in Fig. S2. For Fe_3O_4@MWCNTs/PAM nanocomposites, certain amount of synthesised Fe_3O_4@MWCNTs nanofillers were added and ultra-sonicated for 30 min when mixing PEA and tris[(4-formylphenoxy)methyl]ethane in DMF. The rest processes were the same to that for PAM.

2.4. Characterization

^{1}H NMR analyses were recorded by a Bruker Avance 400 spectrometer (Bruker BioSpin, Switzerland) at 25 °C with deuterated chloroform ($CDCl_3$) as the solvent. Chemical shifts are referenced to tetramethylsilane (TMS). The uniaxial tensile tests were carried out following the requirements in ISO37-4, using an Instron 3342 universal tester at a crosshead speed of 20 mm min^{-1}. At least four specimens for each healing time and repeated repair were tested to obtain the average values of the tensile strength, fracture strain, as well as standard deviation. Optical observations were performed under an upright microscope (Olympus IX73). The surface microstructures were assessed *via* a field emission scanning electron microscope (FE-SEM, SU-8010, Hitachi) operated at an accelerating voltage of 1.0 kV. The surface profiles were performed with a Dektak XT (Bruker) with a line scanning rate of 0.05 mm per second. Other analyses, such as Fourier transform infrared spectroscopy, Powder X-ray diffraction, X-ray photoelectron spectroscopy are presented in Supporting Information.

2.5. Microwave absorption measurements and analysis

The relative complex permittivity and permeability were measured on rectangular specimens (22.8 mm × 10.2 mm × 2.0 mm) by a vector network analyzer (VNA, MS4644A, Anritsu, Japan) using waveguide method in the frequency range of 8.2–12.4 GHz. On the basis of the metal backplane model, the reflection coefficient (RC) can be calculated from the measured relative complex permittivity and permeability according to the transmission line theory by the following equations:

$$RC = 20\log_{10}\left|\frac{Z_{in}-1}{Z_{in}+1}\right| \tag{1}$$

$$Z_{in} = \sqrt{\frac{\mu_r}{\varepsilon_r}}\tanh\left[j\frac{2\pi fd}{c}\sqrt{\mu_r\varepsilon_r}\right] \tag{2}$$

where Z_{in} stands the normalized input impedance, μ_r and ε_r are, respectively, the relative complex permeability and permittivity, and f represents the frequency of the microwaves, d is the thickness of tested materials, and c is the light velocity in vacuum [45,46].

3. Results and discussion

The reversible dynamic imine bond enabled self-healing process is illustrated in Fig. 1a. The key molecular interconnect is the dynamic A_2-B_3 imine bonds based cross-linked PAM network, where A_2 and B_3 represent poly(propylene glycol)bis(2-aminopropyl ether) and 1, 1, 1-tris[(4-formylphenoxy)methyl]ethane, respectively. The formation of dynamic imine bond (−CH═N−) can be traced from the ^{1}H NMR results (Fig. S3) with a signature peak signalling at 8.24 ppm. This also agrees

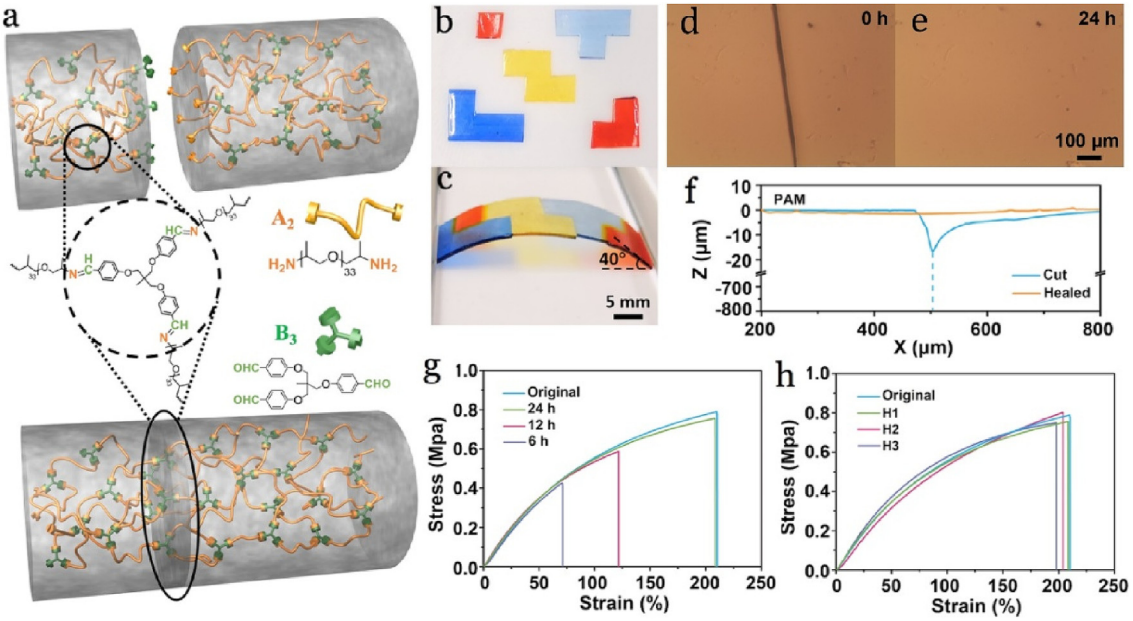

Fig. 1. (a) Illustration of self-healing effect driven by coupling the dynamic imine bonds at fractured surface, with the chemical structure drawings for A_2 and B_3 monomers. Splicing of a collection of (b)PAM '*Tetris*' tiles *via* self-healing and (c) uniaxially compressing the spliced sheet to buckle. Optical microscopic images of PAM (d) before and (e) after self-healing. (f) Surface profiles for pure PAM before and after self-healing. Tensile testing results for PAM (g) at different healing time and (h) after healing for one, two, three cycles (H1, H2, H3).

well with the FT-IR data (Fig. S4), where a new absorption peak for −CH═N− bond was found at 1640 cm^{-1}.

To assess the self-healing performance enabled by the dynamicimine bonds, pure PAM tiles with shapes as '*Tetris*' elements (Fig. 1b) are prepared and assembled into a rectangular sheet at free-standing state, then left to heal in an open air at 25 °C. Interestingly, the '*Tetris*' tiles spontaneously splice together into one single sheet after 24 h, without applying any external stimuli. We subsequently perform a quick assessment for the spliced sheet under a uniaxial compression, the flat sheet transforms into a buckling state (Fig. 1c), and it also can be stretched (Movie S1), which indicates a good homogeneity for the healed sample. Optical microscopic observations were used to record the spontaneous self-healing on the surface of pure PAM. A nearly full restoration of surface can be observed (Fig. 1d) after a healing process for 24 h (Fig. 1e). The surface profiles in Fig. 1f describe the out of plane morphological changes for specimens (0.8 mm in thickness) during self-healing. The dash line represents the true cut profiles that can't be reflected due to the instrumental limit from the probe. After self-healing, the surface is reinstated with negligible residual depths of less than 2 μm.

Supplementary video related to this article can be found at https://doi.org/10.1016/j.compscitech.2019.02.018.

We next study the self-healing property quantitatively by measuring the uniaxial tensile stress-strain relationship as a function of healing time at 25 °C (Fig. 1g). For the as-fabricated sample (or original sample), the results suggest a Young's modulus (E_{pure}) of ~0.76 ± 0.08 MPa, a breaking strain of 215% and peak strength of 0.79 MPa for pure PAM. The healing efficiency is defined as η_s/η_o, where η_s is the fracture strain for current sample, and η_o is the fracture strain for original sample. The healing efficiency results indicate a clear dependency on the healing time, the elongations reach ~100% of that for the original PAM sample after healing for 24 h. It was found that the specimens healed for 6 h and 12 h broke at the incision, while the specimen healed for 24 h did not break at the contacted surface under the tensile testing. This observation further confirmed that the mechanical properties of PAM can be completely restored after a certain period of self-repair and PAM has excellent self-repairing characteristics. Cyclic tensile test was performed to verify the robustness of this self-healing effect, where sample was cut into two parts from the middle and performed the spontaneous self-healing for 24 h for each cycle. The stress-strain curves in Fig. 1h indicate robust self-healing performances for both of pure PAM by showing a η_s/η_o of 95% for PAM after three cycles (H3). The reversible nature of dynamic imine bonds plays a key role in this remarkable self-healing function. The 'mobile' ends between scratched surfaces, $-NH_2$ groups and −CH═O groups, spontaneously couple to form −CH═N− bonds when the surfaces physically contact, therefore led to a self-healing functionality [47–49].

To explore the EM absorbing application for this unique PAM materials, Fe_3O_4@MWCNTs/PAM nanocomposites was fabricated, as illustrated in (Fig. 2a). In addition, refining the compatibility between the fillers and polymer matrix is the key issue to improve the absorption performance of composites. By modifying the CNTs with Fe_3O_4, the aggregation of CNTs could be avoided due to the presence of Fe_3O_4 magnetic nanoparticles on its surface, which effectively decreased the Van Der Waals' interactions between CNTs, meanwhile the intrinsic aggregation of Fe_3O_4 magnetic nanoparticles will be prevented since the existence of CNTs.Thus, Fe_3O_4@MWCNTs nanocomposites could uniformly disperse in the polymer matrix for the synergy between Fe_3O_4 and CNTs. By taking advantage of coupling the imine bonds on the surface, we even weld pure PAM and nanocomposite samples together (Fig. 2b) and demonstrate a good elasticity for the welded sample under stretching (Fig. S7 and Movie S2) and bending. A brief test to verify the bonding strength after the formation of dynamic imine bonds between surfaces of pure PAM and nanocomposite with 15 wt% Fe_3O_4@MWCNTs films (1 mm in thickness, 0.2 g in weight for each film, Fig. 2c), the alien films bond so tight that the bilayer can hold a shear load of 200 g, five hundred folds of the weight for bilayer film.

Supplementary video related to this article can be found at https://doi.org/10.1016/j.compscitech.2019.02.018.

In tensile testing section, the data from 15 wt% Fe_3O_4@MWCNTs/PAM nanocomposite is selected. For the as-fabricated samples (or original samples), the results suggest a Young's modulus (E_{comp}) of ~2.25 ± 0.22 MPa, a breaking strain of 192% and peak strength of 3.07 MPa for the nanocomposites with 15 wt% Fe_3O_4@MWCNTs. As noticed, the enhancement in Young's module, E_{comp}/E_{pure} ~3, shows a considerable gap to the calculated value (E_{comp}/E_{pure} ~ 62) based on

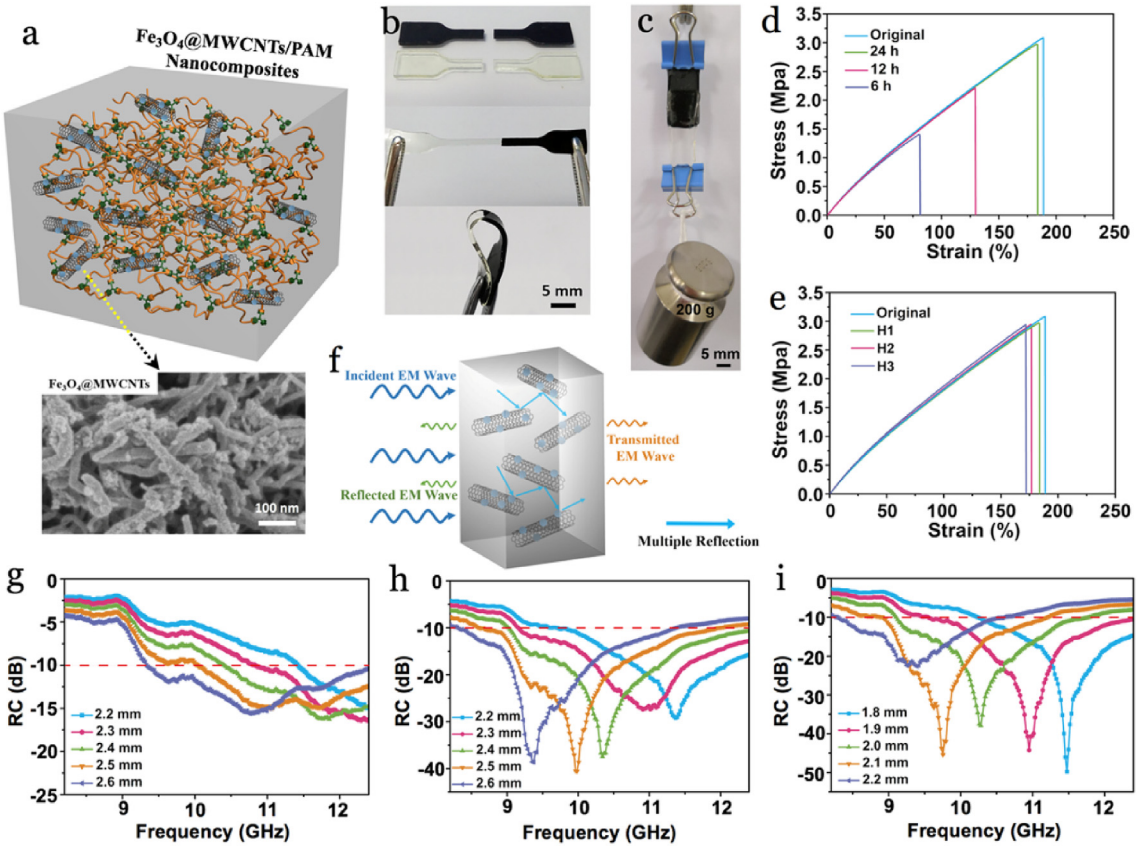

Fig. 2. (a) Illustration of the structure for Fe_3O_4@MWCNTs/PAM nanocomposites with an inset SEM image for the Fe_3O_4@MWCNTs nanoparticles. Self-healing enabled (b) welding of cut dumbbell samples and (c) tough bonding of films (1 mm in thickness) between the PAM and 15 wt% Fe_3O_4@MWCNTs/PAM. Tensile testing results for 15 wt% Fe_3O_4@MWCNTs/PAM nanocomposite (d) at different healing time and (e) after healing for one, two, three cycles (H1, H2, H3). (f) Schematic of EM wave absorption mechanism in nanocomposite. Reflection coefficient (RC) results for Fe_3O_4@MWCNTs/PAM nanocomposite in 8.2–12.4 GHz with nanofiller's concentrations of (g) 10 wt%, (h) 15 wt%, and (i) 20 wt%.

Halpin and Tsai's equations [50,51], because of the decreasing of physical interaction area after coating Fe_3O_4 particles on the surface of MWCNT. Similar to Pure PAM sample, a high healing efficiency, $\eta_s/\eta_o \sim$ 98%, was shown (Fig. 2d) for nanocomposites sample with 15 wt% Fe_3O_4@MWCNTs after healing for 24 h. Further cyclic test results indicate robust self-healing performances for the same nanocomposite with aη_s/η_o of 90% after three cycles (H3).

The EM wave absorbing property of materials, mainly determined by the Fe_3O_4@MWCNTs nanoparticles in matrix, are generally associated with their electromagnetic parameters, *i.e.* relative complex permittivity ($\varepsilon_r = \varepsilon' - j\varepsilon''$) and relative complex permeability ($\mu_r = \mu' - j\mu''$), where the real parts (ε' and μ') represent the storage ability of EM wave and imaginary parts (ε'' and μ'') are related to dissipation of EM wave [52]. Recent theoretical development on the EM wave absorption also proposed a hypothesis that an enhancement of absorption (Fig. 2f) can be achieved by creating a multiple reflection state within the materials when uniformly distributing nanoparticles in matrix [53,54].

When measuring the complex permittivity and permeability for the nanocomposites (Fig. S5), we found that both ε' and ε'' values significantly increased in X-band (8.2–12.4 GHz) as the concentration of Fe_3O_4@MWCNTs increases. A high value of μ'', strong dielectric loss and magnetic loss properties were achieved for the composite with 15 wt% nanofillers (Figs. S5c and S5f). By calculating the reflection coefficient (RC) *via* the transmission line theory (Equs. (1) and (2)), the nanocomposite with 15 wt% Fe_3O_4@MWCNTs hold the strongest EM wave absorptions with a minimum RC to −40.6 dB at 10.0 GHz (Fig. 2g–i), 150% of the value in the previous report [44]. The effective absorption bandwidth is much higher (3.4 GHz) to cover 81% X-band. This significant enhancement could be attributed to the minimal reflection on the PAM surface (low $\varepsilon' \sim 3$) benefited from good impedance matching. And the Fe_3O_4@MWCNTs attenuates the EM waves with the complementary effect between dielectric loss and magnetic loss over a wide range of frequency. The strong dielectric loss is attributed to electron polarization relaxation and interfacial polarizations between Fe_3O_4 and MWCNTs, and between MWCNTs and PAM matrix. The Fe_3O_4 nanoparticles make a contribution to the magnetic loss, which is mainly induced by the natural resonance and eddy current loss. It should be noted that the uniformly distribution of Fe_3O_4@MWCNTs can lead to multiple reflections of EM wave, thus further strengthen EM wave absorption performance for the nanocomposite [55,56].

The dynamic imine bonds also offer a unique reprocessability to our materials with a moderate mechanical compression. To demonstrate this feature, coloured pure PAM pieces (dimensional size less than 1 cm×1 cm, 1 mm in thickness, see inset in Fig. 3a) are cut and put into a mould. After being compressed under 5 MPa for 3 h at 25 °C, all pieces re-united into one single sheet. To further understand this mechano-reformation process, we performed time dependent reformation experiments with different compression stresses (up to 10 MPa). Surprisingly, it only took 1 h to achieve a full reformation when applying 10 MPa. The reformation for 15% Fe_3O_4@MWCNTs nanocomposites took slightly longer (Fig. 3b) than Pure PAM at the same compression stress. The tensile results for reformed samples (Fig. 3c and d) suggest a good retention of mechanical property for both pure PAM and nanocomposites with 15 wt% Fe_3O_4@MWCNTs, after the fourth reprocessing cycle (R4).

In addition to the good self-healing and mechano-reformation capabilities, the dynamic bond also enables an outstanding recyclability,

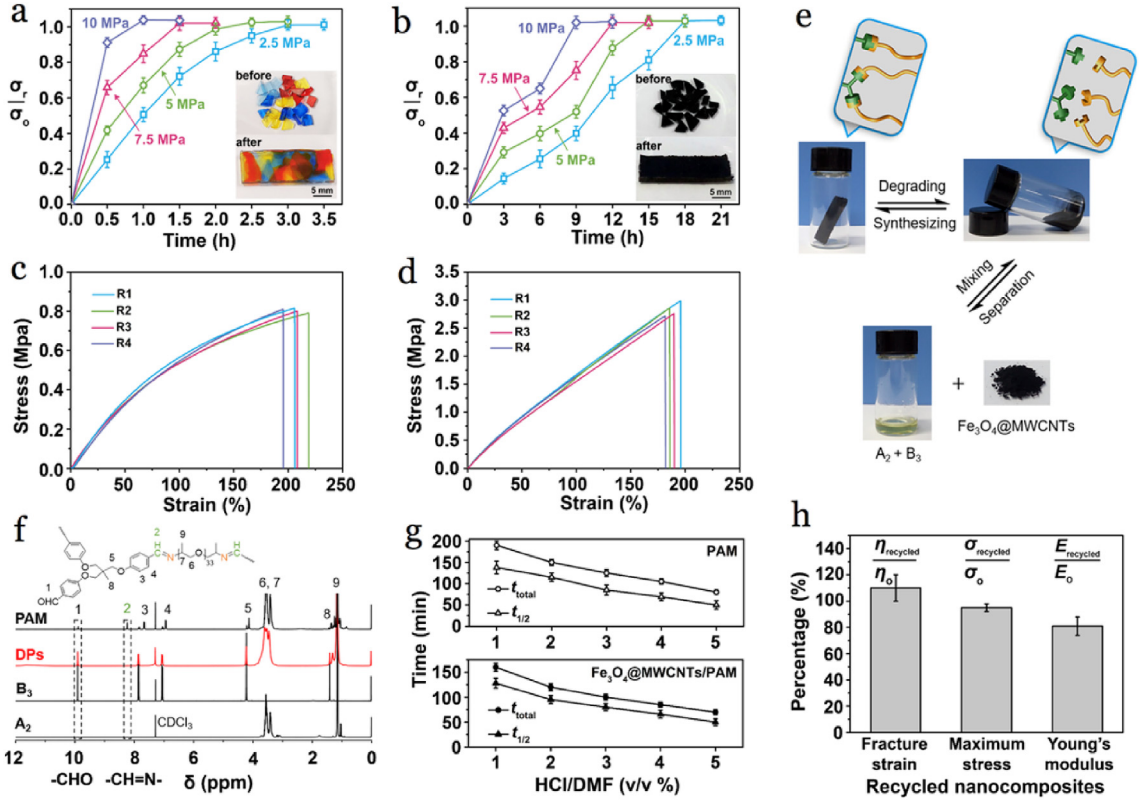

Fig. 3. The accelerated reformation processes for (a) PAM and (b) 15 wt% Fe_3O_4@MWCNTs/PAM nanocomposite at various compressive stresses, the scale bar is 5 mm. The tensile testing results after cyclic reformation at 5 MPa for (c) pure PAM for 3 h and (d) 15 wt% Fe_3O_4@MWCNTs/PAM nanocomposite for 15 h. (e) The sustainable roadmap of Fe_3O_4@MWCNTs/PAM nanocomposites. (f) ^{1}H NMR results for the solution after degradation. (g) Degradation efficiency tests for pure PAM and 15 wt% Fe_3O_4@MWCNTs/PAM nanocomposites. (h) Mechanical analysis results for the re-synthesised composite sample and the original sample.

where the organic network of composite can be fully decomposed by decoupling the −CH═N− bonds in an acidic solution (Fig. 3e), such as glacial acetic acid, hydrochloric acid and trifluoroacetic acid. At a solution of HCl/DMF (2 v/v %), purePAM film (~100 mg, Fig. S6) can be instantly degraded within 2.5 h, rather than swelling in pure DMF. The ^{1}H NMR data for the post-degradation solution for PAM (Fig. 3f), reveals a complete degradation of PAM network, the imine proton peak for −CH═N− at 8.24 ppm disappears and the characteristic signal of end aldehyde groups at 9.86 ppm becomes stronger than that of PAM.

We further study the degradation efficiency by measuring the weight loss as a function of the acid concentration. The t_{total} (time for degrading all polymeric phase in sample, Fig. 3g) for nanocomposite with 15 wt% Fe_3O_4@MWCNTs takes about 80% of the t_{total} for pure PAM at the same acid concentration. The kinetics data indicates that the $t_{1/2}$ (time for degrading 50 wt% polymer in sample) takes ~ 70% of t_{total} for pure PAM and ~80% of t_{total} for nanocomposite with 15 wt% Fe_3O_4@MWCNTs, due to the decreased physical contact area as a result of the volumetric blocking by the nanofillers. When increasing the acid concentration to 5 v/v%, the degradation reaches an instant level by showing a $t_{1/2}$ less than 50 min for pure PAM and a $t_{1/2}$ less than 60 min for nanocomposite with 15 wt% Fe_3O_4@MWCNTs. After full decomposition, we re-synthesised the nanocomposite from the recycled components. After assessing the mechanical property, we found that the recycled nanocomposite (Fig. 3h) maintains a similar fracture strain, maximum stress and shows a slightly low young's modules ($E_{recycled}/E_o$ ~ 80%), comparing to the original samples.

4. Conclusion

In summary, we propose a dynamic imine bond enable resilient and circular materials strategy with potentials in EM wave absorbing application. The synthesised materials show unique self-healing feature and robust reprocessing capability driven by the dynamic imine bonds based molecular interconnects. By adding Fe_3O_4@MWCNTs, excellent EM wave absorbing property was achieved with 50% of enhancement on the EM wave absorption. Moreover, a highly efficient recyclability is demonstrated by instantly dissolving PAM based materials in an acidic solution within 1.5 h, by de-coupling the molecular interconnects. After separation, the nanofillers and monomers can be reused, therefore lead to a good environmental sustainability. We expect this molecular interconnect enabled sustainable nanocomposites technology to find applications in the fields of flexible electronics, micro-devices and smart structures.

Acknowledgements

This work was financially supported by the National Natural Science Foundation of China through grants (21875190, 21374089), Shaanxi Natural Science Funds for Distinguished Young Scholars (2018JC-008) and the Engineering and Physical Sciences Research Council (EPSRC) grant from UK -EP/N007921/1 and EP/N032861/1.

Appendix A. Supplementary data

Supplementary data to this article can be found online at https://doi.org/10.1016/j.compscitech.2019.02.018.

References

[1] A.P. Singh, M. Mishra, P. Sambyal, B.K. Gupta, B.P. Singh, A. Chandra, S.K. Dhawan, Encapsulation of γ-Fe_2O_3 decorated reduced graphene oxide in polyaniline core-shell tubes as an exceptional tracker for electromagnetic environmental pollution, J. Mater. Chem. A 2 (2014) 3581–3593.

[2] S. Xiao, H. Mei, D. Han, K.G. Dassios, L. Cheng, Ultralight lamellar amorphous carbon foam nanostructured by SiC nanowires for tunable electromagnetic wave absorption, Carbon 122 (2017) 718–725.

[3] C. Luo, W. Duan, X. Yin, J. Kong, Microwave-absorbing polymer-derived ceramics from cobalt-coordinated poly(dimethylsilyiene)diacetylenes, J. Phys. Chem. C 120 (2016) 18721–18732.

[4] N. Yousefi, X. Sun, X. Lin, X. Shen, J. Jia, B. Zhang, B. Tang, M. Chan, J. Kim, Highly aligned graphene/polymer nanocomposites with excellent dielectric properties for high-performance electromagnetic interference shielding, Adv. Mater. 26 (2014) 5480–5487.

[5] F. Shahzad, M. Alhabeb, C.B. Hatter, B. Anasori, S.M. Hong, C.M. Koo, Y. Gogotsi, Electromagnetic interference shielding with 2D transition metal carbides (MXenes), Science 353 (2016) 1137–1140.

[6] Z. Chen, C. Xu, C. Ma, W. Ren, H. Cheng, Lightweight and flexible graphene foam composites for high-performance electromagnetic interference shielding, Adv. Mater. 25 (2013) 1296–1300.

[7] H. Lv, Y. Guo, Z. Yang, Y. Cheng, L.P. Wang, B. Zhang, Y. Zhao, Z.J. Xu, G. Ji, A brief introduction to the fabrication and synthesis of graphene based composites for the realization of electromagnetic absorbing materials, J. Mater. Chem. C 5 (2017) 491–512.

[8] I. Arief, S. Biswas, S. Bose, FeCo-anchored reduced graphene oxide framework-based soft composites containing carbon nanotubes as highly efficient microwave absorbers with excellent heat dissipation ability, ACS Appl. Mater. Interfaces 9 (2017) 19202–19214.

[9] T. Huynh, P. Sonar, H. Haick, Advanced materials for use in soft self-healing devices, Adv. Mater. 29 (2017) 1604973.

[10] Z. Zou, C. Zhu, Y. Li, X. Lei, W. Zhang, J. Xiao, Rehealable, fully recyclable, and malleable electronic skin enabled by dynamic covalent thermoset nanocomposite, Sci. Adv. 4 (2018) eaaq0508.

[11] W. Yang, B. Shao, T. Liu, Y. Zhang, R. Huang, F. Chen, Q. Fu, Robust and mechanically and electrically self-healing hydrogel for efficient electromagnetic interference shielding, ACS Appl. Mater. Interfaces 10 (2018) 8245–8257.

[12] D.Y. Wu, S. Meure, D. Solomon, Self-healing polymeric materials: a review of recent developments, Prog. Polym. Sci. 33 (2008) 479–522.

[13] H. Lv, Z. Yang, P.L. Wang, G. Ji, J. Song, L. Zheng, H. Zeng, Z. Xu, A voltage-boosting strategy enabling a low-frequency, flexible electromagnetic wave absorption device, Adv. Mater. 30 (2018) 1706343.

[14] C. Luo, T. Jiao, Y. Tang, J. Kong, Excellent electromagnetic wave absorption of iron-containing SiBCN ceramics at 1158 K high-temperature, Adv. Eng. Mater. 20 (2018) 1701168.

[15] X. Gao, J. Li, Y. Gao, S. Guo, H. Wu, R. Chen, Microwave absorbing properties of alternating multilayer composites consisting of poly(vinyl chloride) and multi-walled carbon nanotube filled poly(vinyl chloride) layers, Compos. Sci. Technol. 130 (2016) 10–19.

[16] B.J. Blaiszik, S.L.B. Kramer, S.C. Olugebefola, J.S. Moore, N.R. Sottos, S.R. White, Self-healing polymers and composites, Annu. Rev. Mater. Res. 40 (2010) 179–211.

[17] G. Weng, S. Thanneeru, J. He, Dynamic coordination of Eu-iminodiacetate to control fluorochromic response of polymer hydrogels to multistimuli, Adv. Mater. 30 (2018) 1706526.

[18] M. Nakahata, Y. Takashima, H. Yamaguchi, A. Harada, Redox-responsive self-healing materials formed from host-guest polymers, Nat. Commun. 2 (2011) 511.

[19] K. Miyamae, M. Nakahata, Y. Takashima, A. Harada, Self-healing, expansion-contraction, and shape-memory properties of a preorganized supramolecular hydrogel through host-guest interactions, Angew. Chem. Int. Ed. 54 (2015) 8984–8987.

[20] A. Das, A. Sallat, F. Boehme, M. Suckow, D. Basu, S. Wiessner, K.W. Stoeckelhuber, B. Voit, G. Heinrich, Ionic modification turns commercial rubber into a self-healing material, ACS Appl. Mater. Interfaces 7 (2015) 20623–20630.

[21] T.L. Sun, T. Kurokawa, S. Kuroda, A. Bin Ihsan, T. Akasaki, K. Sato, M.A. Haque, T. Nakajima, J.P. Gong, Physical hydrogels composed of polyampholytes demonstrate high toughness and viscoelasticity, Nat. Mater. 12 (2013) 932–937.

[22] J. Fox, J.J. Wie, B.W. Greenland, S. Burattini, W. Hayes, H.M. Colquhoun, M.E. Mackay, S.J. Rowan, High-strength, healable, supramolecular polymer nanocomposites, J. Am. Chem. Soc. 134 (2012) 5362–5368.

[23] Y. Chen, A.M. Kushner, G.A. Williams, Z. Guan, Multiphase design of autonomic self-healing thermoplastic elastomers, Nat. Chem. 4 (2012) 467–472.

[24] S.J. Rowan, S.J. Cantrill, G. Cousins, J. Sanders, J.F. Stoddart, Dynamic covalent chemistry, Angew. Chem. Int. Ed. 41 (2002) 898–952.

[25] R.J. Wojtecki, M.A. Meador, S.J. Rowan, Using the dynamic bond to access macroscopically responsive structurally dynamic polymers, Nat. Mater. 10 (2011) 14–27.

[26] Z. Wei, J.H. Yang, J. Zhou, F. Xu, M. Zrinyi, P.H. Dussault, Y. Osada, Y.M. Chen, Self-healing gels based on constitutional dynamic chemistry and their potential applications, Chem. Soc. Rev. 43 (2014) 8114–8131.

[27] N. Roy, B. Bruchmann, J.-M. Lehn, Dynamers: dynamic polymers as self-healing materials, Chem. Soc. Rev. 44 (2015) 3786–3807.

[28] G. Deng, C. Tang, F. Li, H. Jiang, Y. Chen, Covalent cross-linked polymer gels with reversible sol-gel transition and self-healing properties, Macromolecules 43 (2010) 1191–1194.

[29] X. Yang, G. Liu, L. Peng, J. Guo, L. Tao, J. Yuan, C. Chang, Y. Wei, L. Zhang, Highly efficient self-healable and dual responsive cellulose-based hydrogels for controlled release and 3D cell culture, Adv. Funct. Mater. 27 (2017) 1703174.

[30] P. Wang, G. Deng, L. Zhou, Z. Li, Y. Chen, Ultra stretchable, self-healable hydrogels based on dynamic covalent bonding and triblock copolymer micellization, ACS Macro Lett. 6 (2017) 881–886.

[31] A. Rekondo, R. Martin, A. Ruiz De Luzuriaga, G. Cabanero, H.J. Grande, I. Odriozola, Catalyst-free room-temperature self-healing elastomers based on aromatic disulfide metathesis, Mater. Horiz. 1 (2014) 237–240.

[32] S.-M. Kim, S.-H. Jeon, S.-A. Shin, S. Park, J. Jegal, S.Y. Hwang, D.X. Oh, J. Park, Superior toughness and fast self-healing at room temperature engineered by transparent elastomers, Adv. Mater. 30 (2018) 1705145.

[33] O.R. Cromwell, J. Chung, Z. Guan, Malleable and self-healing covalent polymer networks through tunable dynamic boronic ester bonds, J. Am. Chem. Soc. 137 (2015) 6492–6495.

[34] K. Imato, M. Nishihara, T. Kanehara, Y. Amamoto, A. Takahara, H. Otsuka, Self-healing of chemical gels cross-linked by diarylbibenzofuranone-based trigger-free dynamic covalent bonds at room temperature, Angew. Chem. Int. Ed. 51 (2012) 1138–1142.

[35] Y. Amamoto, H. Otsuka, A. Takahara, K. Matyjaszewski, Self-healing of covalently cross-linked polymers by reshuffling thiuram disulfide moieties in air under visible light, Adv. Mater. 24 (2012) 3975–3980.

[36] K.K. Oehlenschlaeger, J.O. Mueller, J. Brandt, S. Hilf, A. Lederer, M. Wilhelm, R. Graf, M.L. Coote, F.G. Schmidt, C. Barner-Kowollik, Adaptable hetero Diels-Alder networks for fast self-healing under mild conditions, Adv. Mater. 26 (2014) 3561–3566.

[37] M.E. Belowich, J.F. Stoddart, Dynamic imine chemistry, Chem. Soc. Rev. 41 (2012) 2003–2024.

[38] B. Yan, J. Huang, L. Han, L. Gong, L. Li, J.N. Israelachvili, H. Zeng, Duplicating dynamic strain-stiffening behavior and nanomechanics of biological tissues in a synthetic self-healing flexible network hydrogel, ACS Nano 11 (2017) 11074–11081.

[39] J. Ahner, M. Micheel, R. Geitner, M. Schmitt, J. Popp, B. Dietzek, M.D. Hager, Self-healing functional polymers: optical property recovery of conjugated polymer films by uncatalyzed imine metathesis, Macromolecules 50 (2017) 3790–3796.

[40] Y. Liu, Z. Tang, Y. Chen, S. Wu, B. Guo, Programming dynamic imine bond into elastomer/graphene composite toward mechanically strong, malleable, and multi-stimuli responsive vitrimer, Compos. Sci. Technol. 168 (2018) 214–223.

[41] X. Yan, Z. Liu, Q. Zhang, J. Lopez, H. Wang, H. Wu, S. Niu, H. Yan, S. Wang, T. Lei, J. Li, D. Qi, P. Huang, J. Huang, Y. Zhang, Y. Wang, G. Li, J.B.H. Tok, X. Chen, Z. Bao, Quadruple H-bonding cross-linked supramolecular polymeric materials as substrates for stretchable, anti tearing, and self-healable thin film electrodes, J. Am. Chem. Soc. 140 (2018) 5280–5289.

[42] B. Zhang, P. Zhang, H. Zhang, C. Yan, Z. Zheng, B. Wu, Y. Yu, A transparent, highly stretchable, autonomous self-healing poly(dimethyl siloxane) elastomer, Macromol. Rapid Commun. 38 (2017) 1700110.

[43] H. Zhang, H. Han, X. Xu, Dynamic and regional constructive electromagnetic protecting materials made by MWNT/Fe_3O_4/poly pyrrole doped vitrimers, Compos. Sci. Technol. 158 (2018) 61–66.

[44] Y. Wang, M. Pan, X. Liang, B. Li, S. Zhang, Electromagnetic wave absorption coating material with self-healing properties, Macromol. Rapid Commun. 38 (2017) 1700447.

[45] C. Luo, T. Jiao, J. Gu, Y. Tang, J. Kong, Graphene shieled by SiBCN ceramic: a promising high temperature electromagnetic wave-absorbing material with oxidation resistance, ACS Appl. Mater. Interfaces 10 (2018) 39307–39318.

[46] C. Luo, Y. Tang, T. Jiao, J. Kong, High-temperature stable and metal-free electromagnetic wave-absorbing SiBCN ceramics derived from carbon-rich hyperbranched polyborosilazanes, ACS Appl. Mater. Interfaces 10 (2018) 28051–28061.

[47] Y. Yang, X. Ding, M.W. Urban, Chemical and physical aspects of self-healing materials, Prog. Polym. Sci. 49 (2015) 34–59.

[48] K. Imato, A. Takahara, H. Otsuka, Self-healing of a cross-linked polymer with dynamic covalent linkages at mild temperature and evaluation at macroscopic and molecular levels, Macromolecules 48 (2015) 5632–5639.

[49] A. Chao, J. Negulescu, D. Zhang, Dynamic covalent polymer networks based on degenerative imine bond exchange: tuning the malleability and self-healing properties by solvent, Macromolecules 49 (2016) 6277–6284.

[50] J.C. Halpin, Stiffness and expansion estimates for oriented short fiber composites, J. Compos. Mater. 3 (1969) 732–734.

[51] J.C. Affdl, J.L. Kardos, The Halpin-Tsai equations: a review, Polym. Eng. Sci. 16 (1976) 344–352.

[52] L. Wang, X. Jia, Y. Li, F. Yang, L. Zhang, L. Liu, X. Ren, H. Yang, Synthesis and microwave absorption property of flexible magnetic film based on graphene oxide/carbon nanotubes and Fe_3O_4 nanoparticles, J. Mater. Chem. A 2 (2014) 14940–14946.

[53] Y. Sun, J. Xu, W. Qiao, X. Xu, W. Zhang, K. Zhang, X. Zhang, X. Chen, W. Zhong, Y. Du, Constructing two-, zero-, and one-dimensional integrated nanostructures: an effective strategy for high microwave absorption performance, ACS Appl. Mater. Interfaces 8 (2016) 31878–31886.

[54] N. Zhou, Q. An, Z. Xiao, S. Zhai, Z. Shi, Rational design of superior microwave shielding composites employing synergy of encapsulating character of alginate hydrogels and task-specific components (Ni NPs, Fe_3O_4/CNTs), ACS Sustain. Chem. Eng. 5 (2017) 5394–5407.

[55] N. Li, G. Huang, Y. Li, H. Xiao, Q. Feng, N. Hu, S. Fu, Enhanced microwave absorption performance of coated carbon nanotubes by optimizing the Fe_3O_4 nanocoating structure, ACS Appl. Mater. Interfaces 9 (2017) 2973–2983.

[56] S.P. Pawar, M. Gandi, C. Saraf, S. Bose, Exceptional microwave absorption in soft polymeric nanocomposites facilitated by engineered nanostructures, J. Mater. Chem. C 4 (2016) 4954–4966.

Nanotechnology and Precision Engineering 2 (2019) 8–14

Contents lists available at ScienceDirect

Nanotechnology and Precision Engineering

journal homepage: http://www.keaipublishing.com/en/journals/nanotechnology-and-precision-engineering/

Enhancement of surface wettability via micro- and nanostructures by single point diamond turning

Nicolás Cabezudo [a], Jining Sun [a,*], Behnam Andi [a], Fei Ding [b], Ding Wang [c], Wenlong Chang [b], Xichun Luo [b], Ben B. Xu [c]

[a] School of Engineering and Physical Sciences, Heriot-Watt University, Edinburgh, UK
[b] Centre for Precision Manufacturing, DMEM, University of Strathclyde, Glasgow, UK
[c] Faculty of Engineering and Environment, Northumbria University, Newcastle upon Tyne, UK

ARTICLE INFO

Keywords:
Contact angle
Wettability
Single-point diamond turning
Structured surface
Hydrophobicity

ABSTRACT

Studies on surface wettability have received tremendous interest due to their potential applications in research and industrial processes. One of the strategies to tune surface wettability is modifying surface topography at micro- and nanoscales. In this research, periodic micro- and nanostructures were patterned on several polymer surfaces by ultra-precision single point diamond turning to investigate the relationships between surface topographies at the micro- and nanoscales and their surface wettability. This research revealed that single-point diamond turning could be used to enhance the wettability of a variety of polymers, including polyvinyl chloride (PVC), polyethylene 1000 (PE1000), polypropylene copolymer (PP) and polytetrafluoroethylene (PFTE), which cannot be processed by conventional semiconductor-based manufacturing processes. Materials exhibiting common wettability properties ($\theta \approx 90°$) changed to exhibit "superhydrophobic" behavior ($\theta > 150°$). Compared with the size of the structures, the aspect ratio of the void space between micro- and nanostructures has a strong impact on surface wettability.

1. Background

Surface behavior plays a key role in many physical or chemical properties such as wettability,[1] optical properties,[2] thermal emissivity,[3] corrosion,[4] and other biological and chemical processes.[5–8] Wettability is the tendency of one fluid to spread on or adhere to a solid surface. Wettability can be measured by the contact angle, which is conventionally measured through the liquid, where a liquid–vapor interface meets a solid surface. Different theories have been proposed to explain wetting phenomena.[9] Young defined the wettability for ideal surfaces as in Eq. (1).

$$\cos(\Theta_{ideal}) = \frac{\Upsilon_{sv} + \Upsilon_{sl}}{\Upsilon_{lv}} \quad (1)$$

where θ_{ideal} is the ideal contact angle, γ_{lv} is the surface tension of the liquid/vapor interface, γ_{sl} is the surface tension of the solid/liquid interface, and γ_{sv} represents the surface tension of the solid/vapor interface. Depending on the value of the contact angle, surfaces can be classified into four groups: superhydrophobic (θ>150°), hydrophobic (90°<θ< 150°), hydrophilic (10°<θ<90°), and superhydrophilic (θ<10°).[10]

The wettability can also be researched by the advancing contact angle (θ_a), receding contact angle (θ_r), and hysteresis angle (θ_H). The advancing contact angle is a measure of the liquid–solid cohesion, whereas the receding contact angle is a measure of liquid–solid adhesion. Contact angle hysteresis can arise from molecular interactions between the liquid and solid or from surface anomalies, such as roughness or heterogeneities.[11] It is defined as the difference between the value of the angle of advance and the value of the receding contact angle (Eq. (2)).

$$\theta_H = \theta_A - \theta_r \quad (2)$$

Surface energy and topography are the main factors affecting wettability. Wettability has been widely researched as a function of surface texture, material's chemistry, and processing conditions.[12]

Surface topography can be altered modifying roughness.[13,14] The presence of features on surfaces can lead to large values of hysteresis where substantial forces may be required to initiate drop movement.[15] For very rough surfaces, drops can be suspended atop patterns, leaving air between them.[16] This suspension enables to have substrates with superhydrophobic behavior where drops can roll easily on them behaving as self-cleaning surfaces.

* Corresponding author.
E-mail address: Jining.Sun@hw.ac.uk (J. Sun).

https://doi.org/10.1016/j.npe.2019.03.008

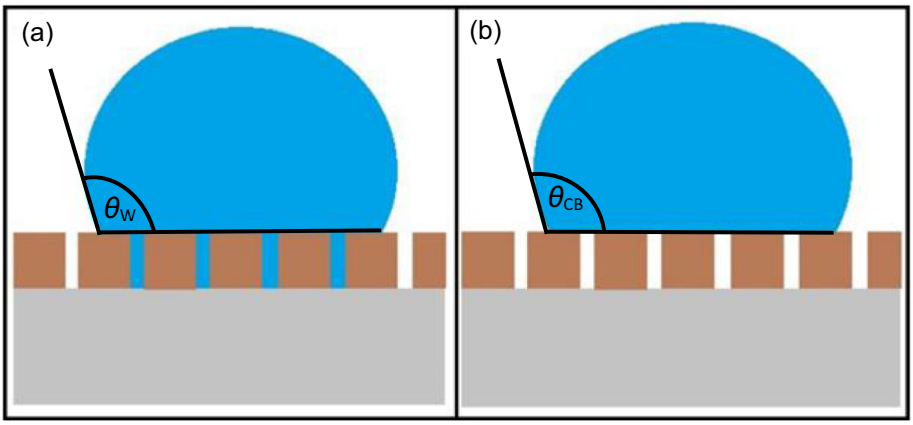

Fig. 1. Sketches of a liquid droplet in (a) the Wenzel state with an apparent contact angle θ_W and (b) the Cassie–Baxter state with an apparent contact angle θ_{CB}.

Wenzel and Cassie–Baxter created models for explaining wettability in real surfaces that exhibit some degree of roughness or are chemically heterogeneous. The Wenzel model supposes that a liquid can penetrate in the pores of the surface, and contact is homogeneous. Wenzel's equation is shown in Eq. (3):

$$\cos(\theta_W) = r \bullet \cos\theta_{ideal} \tag{3}$$

where θ_{ideal} is the contact angle in an ideal surface that cannot be practically obtained. θ_W is the contact angle in a real surface, and r is the Wenzel roughness factor. The factor r tries to explain that the roughness enhances the wettability properties of the smooth surfaces.

The Cassie–Baxter model describes heterogeneous wetting contact between the droplet and surface due to air entrapment. According to this theory, there is an area fraction where the liquid and solid are in contact and another area fraction where the liquid and gas stay in contact. The Cassie–Baxter model is defined in Eq. (4).

$$\cos(\theta_{CB}) = f_1 \bullet \cos\theta_1 + f_2 \bullet \cos\theta_2 \tag{4}$$

where θ_{CB} is the contact angle in a real surface, θ_1 and θ_2 are the contact angles of the two surfaces that are in contact (liquid–vapor and liquid–solid), and f_1 and f_2 are the apparent area fractions of surface components. Sketches of the Wenzel and Cassie–Baxter model are shown in Fig. 1.

The contact angle is generally expected to obey the Wenzel model on substrates with moderate roughness, and it follows Cassie–Baxter behavior on highly rough surfaces. On hydrophobic surfaces ($\theta \approx 100°$) of moderate roughness ($r_s \approx 2$), both Wenzel and Cassie–Baxter states can co-exist. Some researchers believe the wettability models are limited because they use contour area rather than the contact line.[17]

Superhydrophobic examples are found in lotus leaves[18] and certain insects and birds[19] where superhydrophobicity is achieved by surface textures consisting of micro- and nano-scale hierarchical structures. On the basis of these principles, two main strategies are developed for the preparation of superhydrophobic surfaces. One strategy consists of the deposition of hydrophobic materials that can be applied as coating layers such as poly(dimethylsiloxane) (PDMS)[20] or fluorinated silane compounds.[21] This strategy is associated with certain disadvantages such as cost, long procedure, and problems with substrate biocompatibility. The other strategy consists of machining of patterns on the surfaces by photolithography and electron beam lithography.[22] Photolithography has the disadvantage of limited choices in photoresist and substrate. Electron beam lithography presents the disadvantage of being a slow and expensive manufacturing technique that cannot be applied at a large scale.

Single point diamond turning (SPDT) is a versatile and highly controllable technique for manufacturing micro- and nanostructured surfaces with high accuracy. Compared with lithography technologies, SPDT can be used to machine a wide range of materials including polymers, metals, and ceramics, with high throughput at very large scales. This technique is based on turning with diamond as the cutting tool to mechanically remove materials with a precision in several nanometers

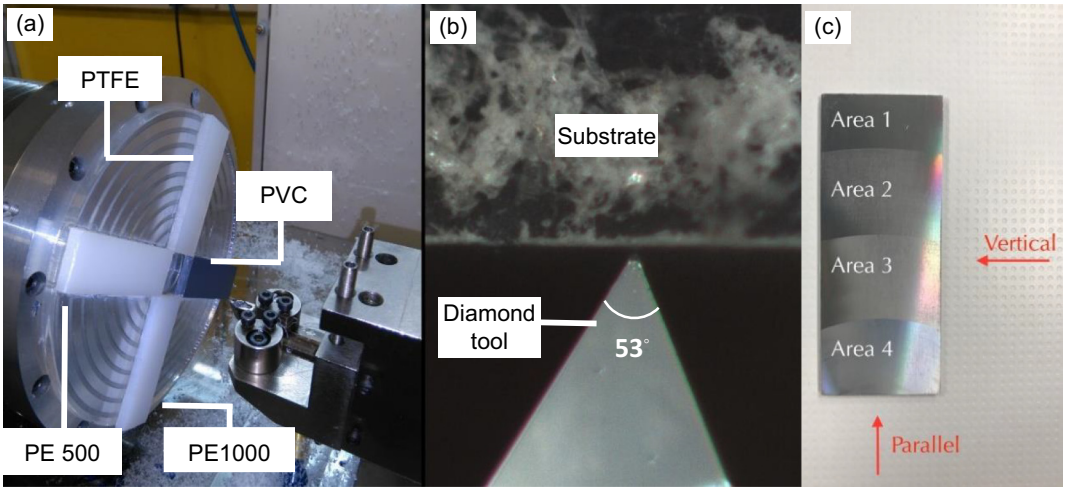

Fig. 2. Overall manufacturing process: (a) experimental setup of diamond turning process; (b) microscope image of the diamond cutting process; (c) an aluminum sample with four different structures in 4 μm (Area 1), 2 μm (Area 2), 1 μm (Area 3), and 500 nm (Area 4).

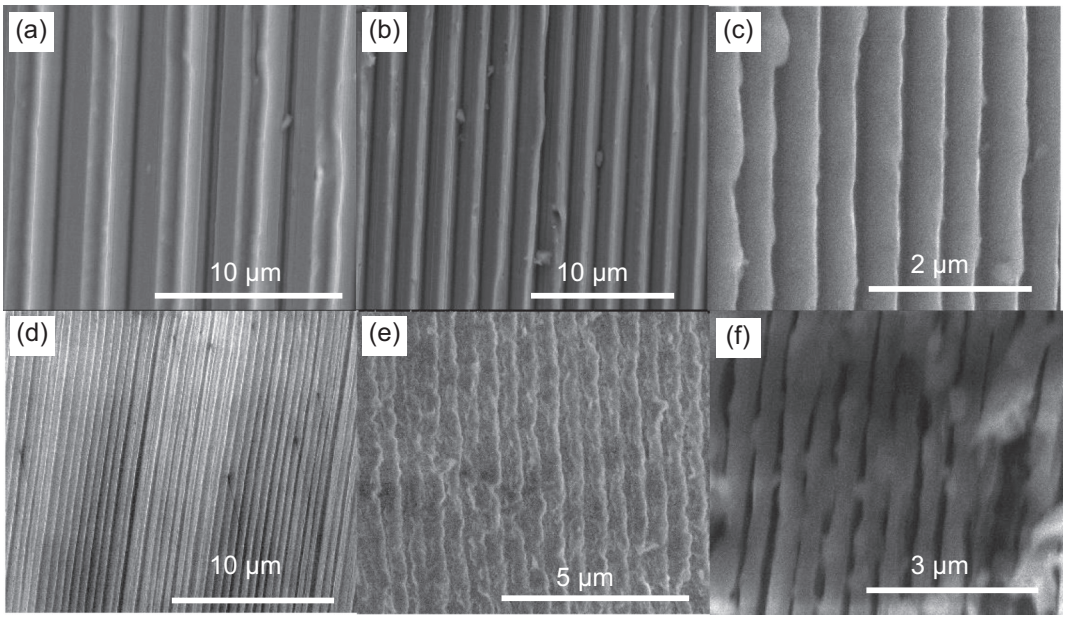

Fig. 3. SEM images of micro and nanostructures on different materials: (a) 4 μm gratings on aluminum; (b) 2 μm gratings on aluminum; (c) 0.5 μm gratings on aluminum; (d) 0.5 μm gratings on PE1000; (e) 0.5 μm gratings on PTFE; and (f) 0.5 μm gratings on PVC.

on a wide variety of materials. SPDT is affected by process and material factors. The material factors include material swelling and recovery, grain boundaries, material spring back, and minimum undeformed chip thickness.[23]

Through manufacturing of micro- and nanostructures on a variety of materials by SPDT, this research aimed to investigate how surface topographies affect wettability in hydrophobic and hydrophilic regimes. For this reason, micro- and nanostructures on the surfaces of several materials, including aluminum, polyvinyl chloride (PVC), polyethylene, polypropylene copolymer, PFTE and polypropylene copolymer (PP), with feature dimensions from 500 nm to several micrometers, were employed. The surface of the different patterned areas and the wettability of these materials were characterized and analyzed. Finally, the values of contact angles obtained for the different patterned and flat surfaces were compared, and the patterns' height was found to affect the wettability for these materials.

2. Experimental procedures

Through a customized five axis ultra-precision machine, micro- and nanogratings (500 nm, 1 μm, 2 μm, and 4 μm) were machined on materials including aluminum, PVC, polyethylene 1000 (PE 1000), polyethylene 500 (PE 500), polypropylene copolymer (PP), and PFTE. Under a spindle speed of 1000 rpm, feed rates of 4 mm/min, 2 mm/min, 1 mm/min, and 0.5 mm/min were employed to achieve 4 μm, 2 μm, 1 μm, and 0.5 μm per revolution. A sharp point diamond tool with

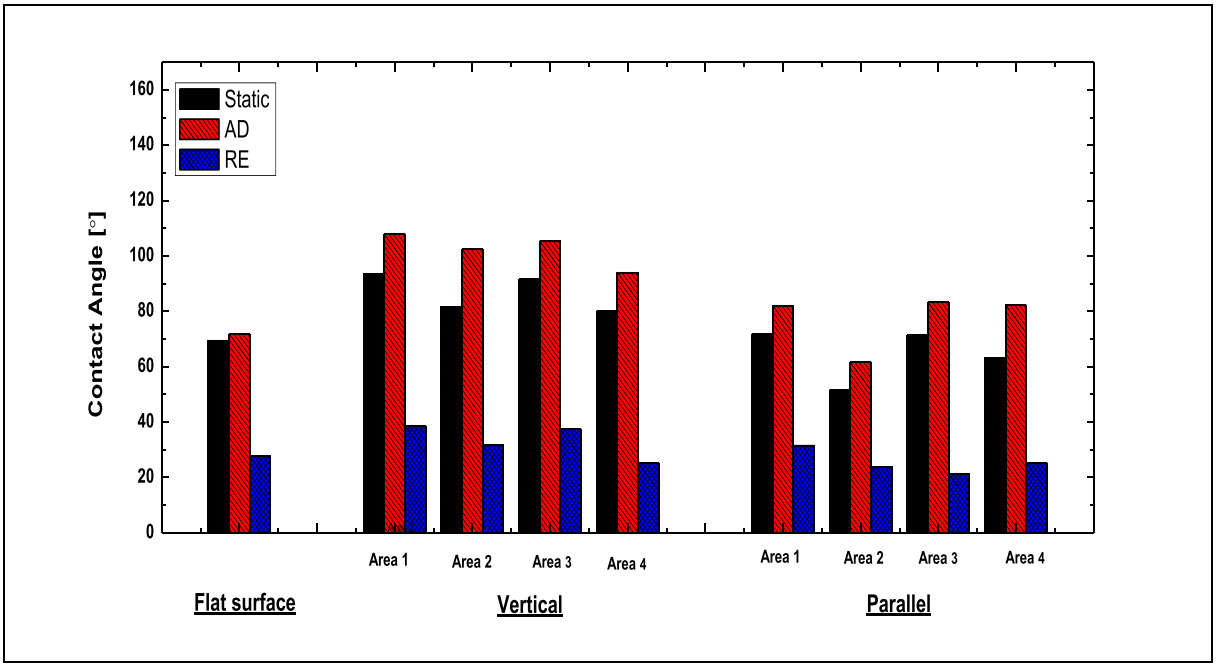

Fig. 4. Contact angle measurements for aluminum.

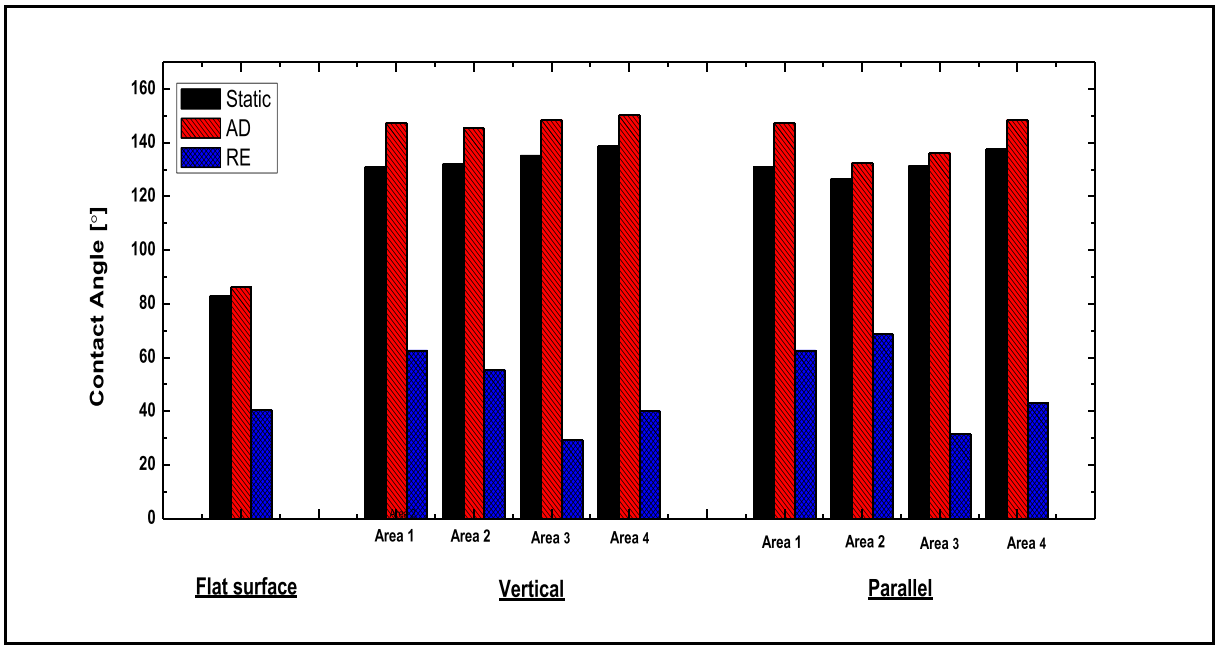

Fig. 5. Contact angle measurements for PVC.

an inclined angle of 53° was used. The size of the structures was controlled by changing the cutting depth. The 53° inclined angle ensured that the width of the gratings was the same as the cutting depth. Mineral spirit mist was used as coolant during the cutting process. To ensure the consistency of the cutting process, all substrates (75 mm × 25 mm) were mounted circularly around the center of the headstock (Fig. 2(a)). An optical microscope image of the diamond cutting process is shown in Fig. 2(b). On each substrate, gratings in dimensions of 4 μm, 2 μm, 1 μm, and 0.5 μm were cut within the ribbon areas 1–4 (Fig. 2(c)). The fabrication results were measured by scanning electron microscopy (SEM; FEI Quanta 3D FEG). To avoid contaminating the surfaces, all samples were uncoated and measured under low vacuum SEM mode (120 Pa).

The wettability of the surfaces was characterized by measuring the contact angles (Krüss Drop Shape Analyzer – DSA30) at different areas of each sample, along vertical and parallel directions (Fig. 2(c)). To reduce error in measurement, five water droplets (2 μL each) were randomly placed in each area. For each droplet, apparent contact angles including static contact angle, advancing contact angle, and receding contact angle were measured, and the average value was considered the measurement result.

3. Results and discussion

SEM images of the micro and nanostructures from 4 μm to 500 nm on different substrates are shown in Fig. 3. Under the same cutting depth, the actual surface topography of the gratings on metal and plastic surfaces slightly differed due to the different elastic recovery rates after material removal.

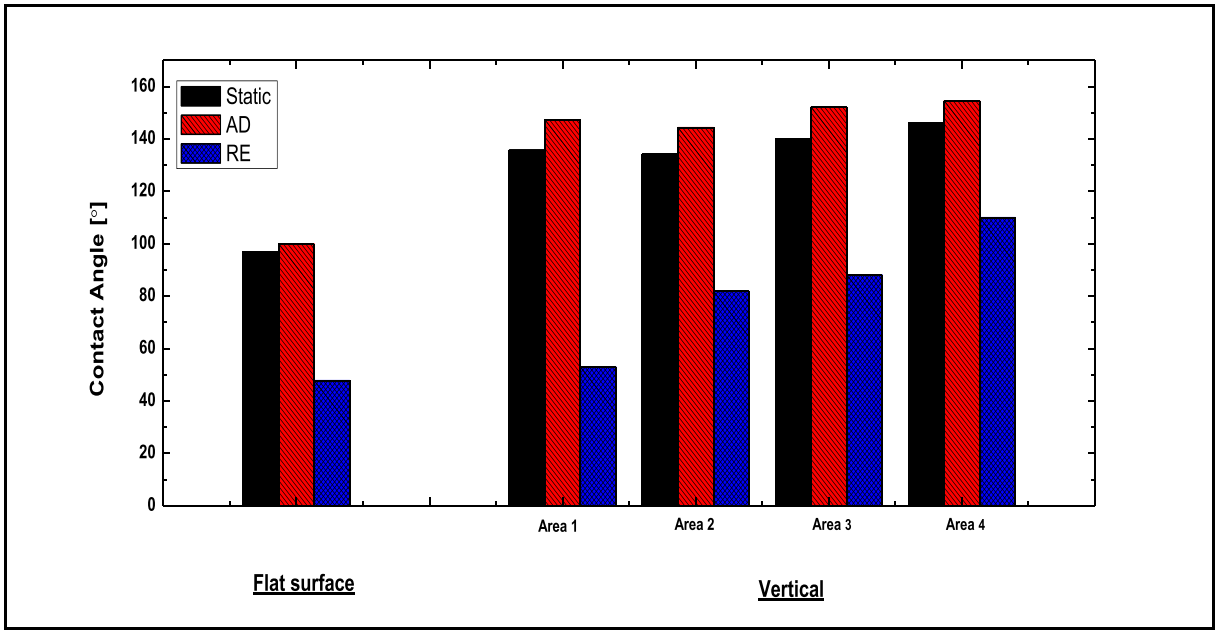

Fig. 6. Contact angle measurements for PE 1000.

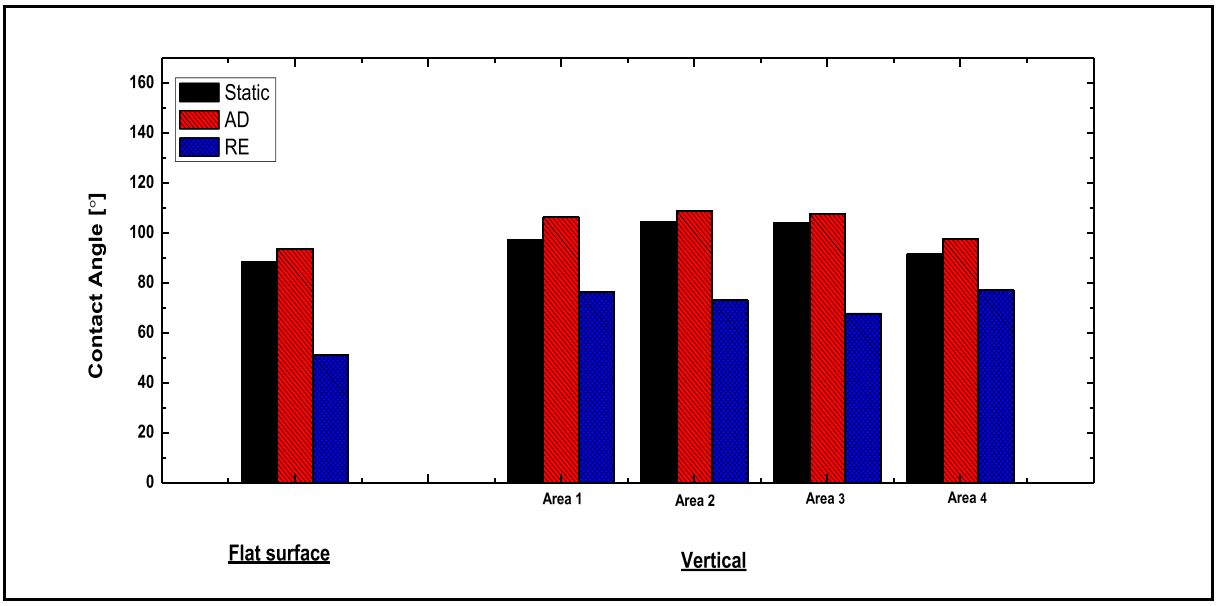

Fig. 7. Contact angle measurements for PE 500.

For each material, contact angles on flat surface and structured surfaces (areas 1–4) were measured. The measurement results for contact angles are shown in Figs. 4–9. For aluminum and PVC, all contact angles were measured along both vertical and parallel directions (Fig. 2(c)). The measurement results for these two materials are illustrated in Figs.4 and 5.

For each material, the roughness factor (R_f) and packing parameter (p) were calculated. The packing parameter is the fraction of the structured surface area over the total area of the substrate. The roughness factor was estimated theoretically given that the patterns adopt a square shape and considering the height, width, and distance. For the different patterned areas, the distance between patterns was constant, so the pitch distance did not influence the roughness factor. The width of the patterns showed small variations in the different materials due to the different elastic behavior of the materials during the machining process, resulting in minimal changes in the roughness factor. Therefore, the roughness factor would depend mainly on the height of the patterns. Considering that the height of the pattern ranged from 4 μm to 500 nm, the roughness factor was expected to decrease from Area 1 (pattern height of 4 μm) to Area 4 (pattern height of 500 nm). The roughness factors and packing parameters for different materials are shown in Table 1.

Given the existence of micro and nanostructures, in areas 1 and 3, the wettability of aluminum changed from hydrophilic ($\theta = 69.4°$) to hydrophobic (up to 93.6°). This result contradicts the Wenzel model defined in Eq. (3). The Wenzel model predicts that an increase in the surface roughness for hydrophilic materials can enhance their hydrophobicity behavior and exhibit small apparent contact angles. Thus, air bubbles successfully trapped by these structures possibly affect the wetting behavior of aluminum substrates, and the droplet follows a composite state. If the droplet is in the composite state, the apparent contact angle should be calculated using Cassie and Baxter's model

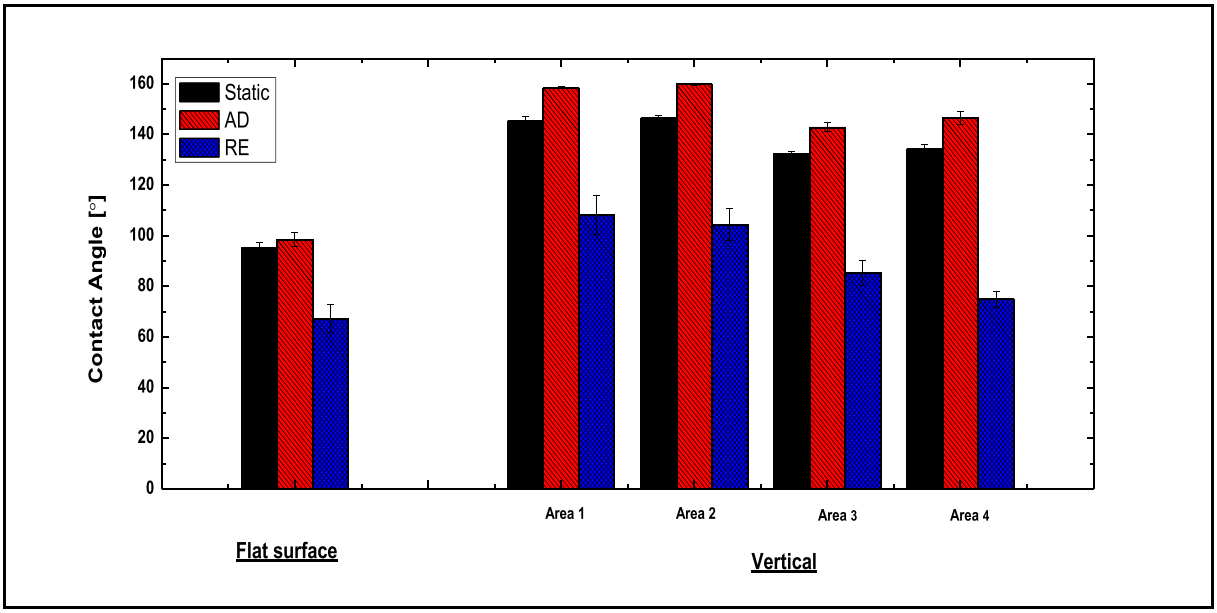

Fig. 8. Contact angle measurements for PP.

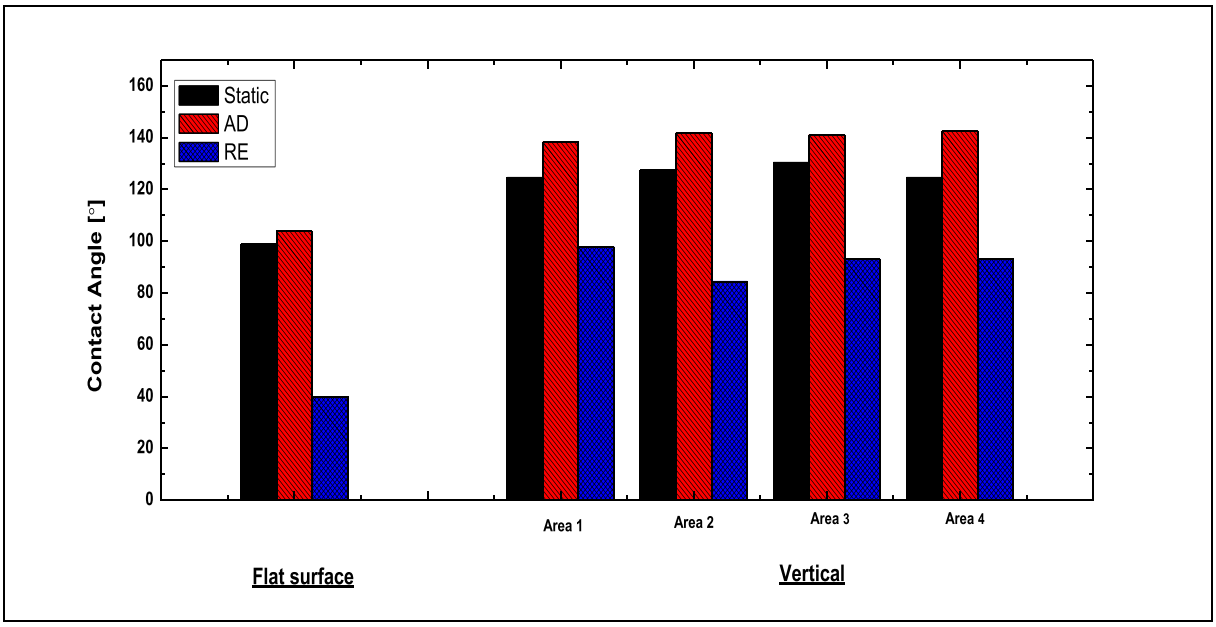

Fig. 9. Contact angle measurements for PTFE.

defined by Eq. (4). Zu et al. performed a theoretical analysis on substrates patterned by square patterns following the Cassie–Baxter model. This model predicts that the area fraction of the solid–liquid interface, *f*, is only dependent on the pattern width and pitch distance. This model predicts that the apparent contact angle should decrease with the increase in pattern height for flat substrates with $\theta < 90°$.[24] This model cannot explain the experimental results. These results can be explained by taking into account the phenomenon of passivation where aluminum forms a thin surface layer of aluminum oxide upon contact with oxygen in the atmosphere through oxidation, which is enhanced at high temperatures. This layer creates porosity on the surface of the structures. The formation of this oxidized structure can resemble anodized aluminum. The surface of passivated aluminum transitions from slightly hydrophilic to moderately hydrophobic up to film thicknesses of about 6 μm.[25]

PVC, PE 1000, PP, and PTFE exhibited a great change in their wettability behavior ($\Delta\theta > 50°$) when micro- and nanostructures were introduced to the surfaces, shifting from non-extraordinary wettability behavior ($\theta \approx 90°$) to superhydrophobic behavior ($\theta > 150°$). All four areas with structures ranging from 500 nm to 4 μm showed similar contact angles. The Wenzel model predicts that patterned materials with intrinsic contact angles $\theta > 90°$ demonstrate an enhancement in their hydrophobic behavior when the roughness factor is increased. According to Nosonovsky et al., the change in contact angle in the Wenzel model depends on the different geometric parameters of the surface structure such as width and height of the pillars, distance between pillars, patterns shape, and pattern packing.[26] This model explains that the aspect ratio and packing parameter of the structures have an outstanding effect on the variation in the contact angle on surfaces with patterned structures. In the different patterned areas, the pattern height decreased from 4 μm to 500 nm, whereas the width of the patterns showed small variations in the different materials due to the different elastic behavior of the materials during the machining process. The aspect ratio was in the range of 1–5 for the different manufactured areas. In the different patterned surfaces, p oscillated between 0.5 and 0.9. According to this theoretical analysis, an increase in the aspect ratio for materials with intrinsic contact angles $\theta > 90°$ could extensively enhance the hydrophobicity of the materials.

With the patterned surfaces, the hydrophobicity of PE 500 only slightly increased ($\Delta\theta \approx 10°–15°$). According to theoretical analysis, the Cassie–Baxter model indicates that the height of the pillars does not influence the wettability of the materials.[24] This phenomenon is quite unique especially when compared with PE 1000, which has very similar wettability on flat surfaces. This effect can also be explained by their different surface topography. PE 1000 offers higher wear resistance and impact strength than PE 500. Therefore, under the same cutting parameters, PE1000 is more difficult to remove than PE 500. As shown in Fig. 10, the gaps between each patterns (1 μm) on PE 1000 (Fig. 10(a)) were smaller than those on PE 500 (Fig. 10(b)), leading to a void space with high aspect ratio, which facilitated air trapping and resulted in a high contact angle. Thus, for hydrophobic surfaces ($\theta \approx 100°$) of moderate roughness ($R_s \approx 2$), both wettability models can co-exist, and the droplet may stay in a state of metastable equilibrium.[24]

The contact angle hysteresis of each material is also studied. Theoretical analysis of other researchers demonstrated that contact angle hysteresis depends on the width/pitch ratio of the structures, as well as the density of the pillars.[27,28] Among the tested materials, aluminum, PE 500, PP, and PTFE did not show a measurable change in contact angle hysteresis with the different patterns, whereas PE 1000 exhibited an enhancement in contact angle hysteresis with an increased the roughness factor. By contrast, PVC showed a reduction in contact angle hysteresis when the roughness factor increased. Our observation revealed a relationship between contact angle hysteresis and the size of the surface structures. Recent research demonstrated that contact angle hysteresis is strongly correlated with the projected area fraction for fully wetting space (f_w).[29] For all the polymer materials used in this work, f_w varied from 0 to 1, depending on the structures and surface finish. Although the same size of structures was achieved on different materials, the surface finish differed (Fig. 3). Such a difference caused the unpredictable behavior of contact angle hysteresis on different materials. Other studies indicated that contact angle hysteresis is affected by the height of the patterns, pitch distance,[30] and shape of patterns.[31,32] The main

Table 1
Roughness factor and packing parameter estimation for the different materials.

Material	R_f	*p*
Aluminum	3.8–4.79	0.84–0.90
PVC	3.9–5.08	0.55–0.96
PE 1000	3.83–4.56	0.76–0.79
PE 500	3.01–4.07	0.54–0.73
PTFE	1.08–2.86	0.76–0.80
PP	2.62–4.12	0.70–0.76

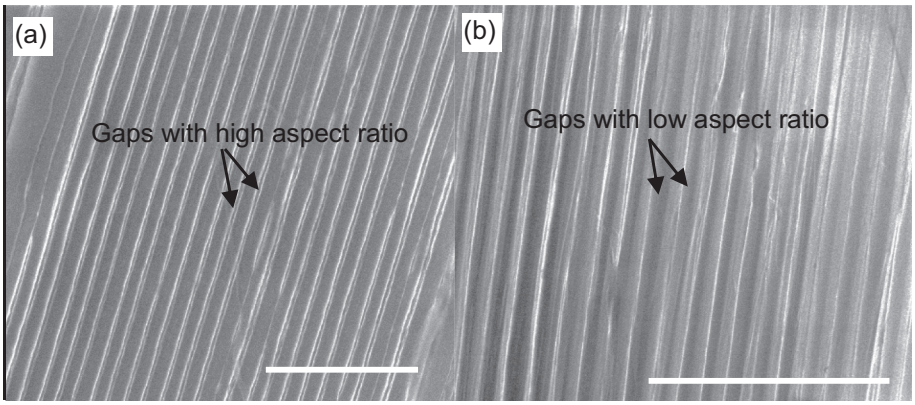

Fig. 10. SEM images of 1 μm gratings on PE 1000 (a) and PE 500 (b) (scale bar is 10 μm).

finding in the literature is that sharp patterns lead to a remarkable enhancement in contact angle hysteresis.[33] Further research should focus on controlling surface finish and the shape of structures for an in-depth study of contact angle hysteresis.

4. Conclusions

By using SPDT, this research demonstrated the changes in surface wettability through micro- and nanostructures on materials that cannot be processed by conventional lithography-based technologies. Results revealed that the wettability of polymers such as PVC, PE 1000, PP, and PTFE can be greatly enhanced ($\Delta\theta \approx 50°$). Meanwhile, aluminum and PE 500 exhibit a moderate change in their wettability properties ($\Delta\theta \approx 10°$) when features are manufactured on their surfaces. From 500 nm to 4 μm, the correlation between the sizes of the structures and surface wettability is not strong. In such a scale, the aspect ratio of void structures plays an important role in surface wettability. For the same material, void space with high aspect ratio can trap air easily, resulting in a high contact angle. In addition, the experimental results can be well explained through the introduction of the roughness factor and the packing parameter, which indicates that surfaces with different wettabilities can be tuned through these parameters and then fabricated by SPDT.

Acknowledgment

The authors gratefully acknowledge the financial support from Heriot-Watt University (Edinburgh) and the Engineering and Physical Sciences Research Council (EP/K018345/1) for this study.

References

1. De Gennes PG. Wetting: statics and dynamics. Rev Mod Phys 1985;57(3):827-63.
2. DeAro JA, Weston KD, Buratto SK, Lemmer U. Mesoscale optical properties of conjugated polymers probed by near-field scanning optical microscopy. Chem Phys Lett 1997;277:532-8.
3. Wang L, Xu G, Liu C, Hou H, Tan S. Surface-modified CeO_2 coating with excellent thermal shock resistance performance and low infrared emissivity at high-temperature. Surf Coat Technol 2019;357:559-66.
4. Manam NS, Harun WSW, Shri DNA, et al. Study of corrosion in biocompatible metals for implants: a review. J Alloys Compd 2017;701:698-715.
5. Garrett TR, Bhakoo M, Zhanga Z. Bacterial adhesion and biofilms on surfaces. Prog Nat Sci 2008;18(9):1049-56.
6. Anselme K, Ponche A, Bigerelle M. Relative influence of surface topography and surface chemistry on cell response to bone implant materials. Part 2: biological aspects. SAGE Journals 2010;224(12):1487-507.
7. Lundqvist M, Stigler J, Elia G, Lynch I, Cedervall T, Dawson KA. Nanoparticle size and surface properties determine the protein corona with possible implications for biological impacts. Proc Natl Acad Sci U S A 2008;105(38):14265-70.
8. Albanese A, Tang PS, Chan WCW. The effect of nanoparticle size, shape, and surface chemistry on biological systems. Annu Rev Biomed Eng 2012;14:1-16.
9. Loeb GI, Schrader ME. *Modern Approaches to Wettability: Theory and Applications.* Springer Science. 1992.
10. Mittal KL. *Advances in contact angle, wettability and adhesion.* Wiley. 2018.
11. Extrand CW. *Encyclopedia of surface and colloid science.* Marcel Dekker. 2002:2414.
12. Miwa M. Effects of the surface roughness on sliding angles of water droplets on superhydrophobic surfaces. Langmuir 2000;16(13):5754-60.
13. Wenzel RN. Resistance of solid surfaces to wetting by water. Ind Eng Chem 1936;28(8):988-94.
14. Cassie ABD, Baxter S. Wettability of porous surfaces. Trans Faraday Soc 1944;40:546-51.
15. Bartell FE, Shepard JWJ. Surface roughness as related tohysteresis of contact angles. II. The systems paraffin–3 molar calcium chloride solution–air and paraffin–glycerol–air. Phys Chem 1953;57:455-8.
16. Johnson Jr RE, Dettre RH, Jhonson JR. Contact angle measurements on rough surfaces. Advances in Chemistry 1964;43(8):136-44.
17. Gao LC, McCarthy TJ. *How Wenzel and Cassie were wrong.* ,23 Langmuir. 2007:3762-5.
18. Quéré D. Rough ideas on wetting. Physica A: Statistical Mechanics and its Applications 2002;313(1–2):32-46.
19. Barthlott W, Neinhuis C. Purity of the sacred lotus, or escape from contamination in biological surfaces. Planta 1997;202:1-8.
20. Khorasani MT, Mirzadeh H, Kermani Z. Wettability of porous polydimethylsiloxane surface: morphology study. Appl Surf Sci 2005;242(3):339-45.
21. Song XY, Zhai J, Wang YL, Jiang L. Fabrication of superhydrophobic surfaces by self-assembly and their water-adhesion properties. J Phys Chem B 2005;109:4048-52.
22. Lasagni FA. *Fabrication and characterization in the micro-nano range new trends for two and three dimensional structures.* Springer. 2011.
23. Sohn A, Lamonds L, Garrard K. Modelling of vibration in single-point diamond turning. Proceedings of the ASPE, American Society for Precision Engineering, 21st Annual Meeting; 2006.
24. Zu Q, Yan Y, Li J, Han Z. Wetting behaviours of a single droplet on biomimetic micro structured surfaces. Journal of Bionic Engineering 2010;7:191-8.
25. Buijnsters J. Surface wettability of macroporous anodized aluminum oxide. ACS Appl Mater Interfaces 2013;5(8):3224-33.
26. Nosonovsky M, Bhushan B. Roughness-induced superhydrophobicity: a way to design non-adhesive surfaces. J Physics Condensed Matter 2008;20, 225009.
27. Hejazi V, Nosonovsky M. Contact angle hysteresis in multiphase systems. Colloid Polym Sci 2013;291:329-38.
28. Shia Z, Zhan X. Contact angle hysteresis analysis on superhydrophobic surface based on the design of channel and pillar models. Mater Des 2017;131:323-33.
29. Cheng K, Naccarato B, Kim KJ, Kumar A. Theoretical consideration of contact angle hysteresis using surface-energy-minimization methods. Int J Heat Mass Transf 2016;102:154-61.
30. Forsberg P. Contact line pinning on microstructured surfaces for liquids in the Wenzel state. Langmuir 2010;26(2):860-5.
31. Eick JD, Good R, Neumann A. Thermodynamics of contact angles. II. Rough solid surfaces. J Colloid Interfacial Sci 1975;53:235-8.
32. Huh C, Mason S. Effects of surface roughness on wetting (theoretical). J Colloid Interfacial Sci 1977;60:11-38.
33. Joanny JF, Gennes PG. A model for contact angle hysteresis. J Chem Phys 1984;81:552.

ADVANCED FUNCTIONAL MATERIALS
www.afm-journal.de

Spatially Configuring Wrinkle Pattern and Multiscale Surface Evolution with Structural Confinement

Ding Wang, Nontawit Cheewaruangroj, Yifan Li, Glen McHale, Yinzhu Jiang, David Wood, John Simeon Biggins, and Ben Bin Xu**

Surface elastic instabilities, such as wrinkling and creasing, can enable a convenient strategy to impart reversible patterned topography to a surface. Here the classic system of a stiff layer on a soft substrate is focused, which famously produces parallel harmonic wrinkles at modest uniaxial compression that period-double repeatedly at higher compressions and ultimately evolve into deep folds and creases. By introducing micrometer-scale planar Bravais lattice holes to spatially pattern the substrate, these instabilities are guided into a wide variety of different patterns, including wrinkling in parallel bands and star shape bands, and radically reduce the threshold compression. The experimental patterns and thresholds are enabled to understand by considering a simple plane-strain model for the patterned substrate-deformation, decorated by wrinkling on the stiff surface layer. The experiments also show localized wrinkle-crease transitions at modest compression, yielding a hierarchical surface with different generations of instability mixed together. By varying the geometrical inputs, control over the stepwise evolution of surface morphologies is demonstrated. These results demonstrate considerable control over both the patterns and threshold of the surface elastic instabilities, and have relevance to many emerging applications of morphing surfaces, including in wearable/flexible electronics, biomedical systems, and optical devices.

1. Introduction

Elastic instabilities such as wrinkles, creases and folds, are usually considered as unwanted when they appear in engineering structures, as they can precipitate fracture and failure. Recently, scientists have significantly advanced our understanding of the mechanics of elastic instabilities,[1–7] opening the possibility of transforming these unwanted phenomena into tools for producing useful shape changes in response to a range of external stimuli.[8–13] The latter perspective has enabled engineering opportunities with self-adaptive/autonomous structures in low dimensions and has implications in many different contexts such as micro-/nanofluidics,[14–16] flexible electronics,[17,18] adhesion,[19,20] organic solar cells,[21] tunable optics,[22–24] wettability,[25–27] and promising methods for surface patterning.[1,28–31] While our scientific/technical understanding has advanced, there remains much to be explored about the control of instability morphology, and in particular how to configure instabilities, such as wrinkling and creasing, to desired patterns with selective distribution covering the surface and bespoke thresholds for the formation and evolution of instabilities.

When compressing a bilayer elastomer system with a stiff skin layer, the formation of surface wrinkles releases in-plane compression of the stiff layer, as bending is energetically more favorable than compression. With further compression, the wrinkles experience further bifurcations, including period-doubling and quadrupling,[5,32] and finally develop into deep folds/creases.[33–35] These wrinkling and postwinkling behaviors have been well understood by considering the intrinsic material properties of a bilayer (module mismatch, Poisson's ratio, etc.), structural variables (thickness) and the prestrains imposed on the system. However, thus far, such compressive instabilities have been studied in nonpatterned surface systems, where both wrinkling and further bifurcations occur as global events,

D. Wang, Dr. Y. Li, Prof. G. McHale, Dr. B. B. Xu
Smart Materials and Surfaces Laboratory
Faculty of Engineering and Environment
Northumbria University
Newcastle upon Tyne NE1 8ST, UK
E-mail: ben.xu@northumbria.ac.uk
Dr. J. S. Biggins
Engineering Department
Cambridge University
Trumpington St, Cambridge CB2 1PZ, UK
E-mail: jsb56@cam.ac.uk
The ORCID identification number(s) for the author(s) of this article can be found under https://doi.org/10.1002/adfm.201704228.

DOI: 10.1002/adfm.201704228

N. Cheewaruangroj
Cavendish Laboratory
Cambridge University
19 JJ Thomson Avenue, Cambridge CB3 0HE, UK
Dr. Y. Jiang
State Key Laboratory of Silicon Materials
Laboratory of Advanced Materials and Applications for Batteries of Zhejiang Province
School of Materials Science and Engineering
Zhejiang University
Hangzhou, Zhejiang 310027, P. R. China
Prof. D. Wood
Department of Engineering
Durham University
Durham DH1 3LE, UK

spanning the entire surface at once. Notably, Huck et al. investigated the spontaneous formation of patterns of aligned buckles on a flat gold/polydimethylsiloxane (PDMS) bilayer with placed confinement.[36] Kim et al. studied the morphological transitions on the surface of a bilayer under a biaxial compressive stress and revealed a mechanism to controllably generate a 2D wrinkle/fold pattern on the entire film surface.[3] Wang and Zhao have summarized the instability bifurcations on flat surfaces and generated a phase diagram by considering the geometrical variations and module mismatches.[37,38] Recent work has also studied bilayer instabilities on surfaces with curvature,[39–42] where wrinkling is still a global event, but where the pattern and threshold are influenced by the curvature. Here we investigate whether we can induce wrinkling and further bifurcations in patterned subregions of a bilayer by explicitly patterning the surface, thus paving the way for bespoke instability morphologies at bespoke thresholds.

Such controllable formation and development of instabilities in targeted regions are highly desirable for engineering applications such as strain sensing structures, actuating units in wearable devices, healthcare devices, bio-fluidic devices, etc. In this paper, we demonstrate a simple strategy to generate 2D harmonic surface wrinkle patterns and control transitions thresholds on the surface of an elastic bilayer under uniaxial compressive stress, by employing structural confinement (a Bravais lattice of holes) to regulate the in-plane stress map on a surface. The regions adjoining the Bravais lattice holes nucleate harmonic wrinkle networks at small compressive strains due to confinement. At higher compression, the wrinkle-crease transition is initialized at selected areas with strain energy localization guided by the curved geometrical boundary from the edge of Bravais lattice holes, which then finally develop into a global creasing. The dynamics of the formation of planar wrinkle patterns and localized wrinkle-crease transition are studied, and we illustrate a distinct stepwise instability pattern evolution toward a hierarchical surface. We also combine experiments with numerical simulations to track the in-plane stress state and study the generation of harmonic morphology under the confinement.

2. Results and Discussion

The Bravais lattice template was prepared by lithographically fabricating SU-8 pillars on a silicon wafer (**Figure 1**a). The Bravais pattern was then transferred to a soft substrate by coating the template with a thin (125 μm) layer of softer PDMS (shear modulus ≈0.1 MPa), which was then cured on a substantially prestretched elastic "mounting" base layer (thickness ≈3 mm, shear modulus ≈0.35 MPa). After curing, the PDMS structure was released from the template, aided by a salinization treatment applied to the template to reduce surface adhesion. Under compression, patterned surfaces composed of polygonal shapes, i.e., triangles, squares, etc., can yield strain energy concentrations and localized bulk deformations around their corners, making it difficult to reach the energy threshold to trigger the surface instability. Therefore, we used patterned surfaces with circular (hole) shapes to avoid strain energy localization and also expected that the curvatures can be used to regulate the formation of instabilities. Two different Bravais lattices (Figure 1b–e), square and centered square, were employed with varied geometrical aspect ratios, hole diameter (Φ), hole distance (D), hole depth (h), to establish a range of patterned soft surfaces. Finally, oxygen plasma treatment was used to create a thin stiff layer on the patterned soft substrate (Figure 1f) prior to the compression.

Upon subsequent release of the mounting layer from a prestretched length L_0 to a length L, the patterned PDMS layer is under compression, which we characterize by the nominal (far-field) uniaxial compressive strain $\varepsilon = L_0/L - 1$. The oxygen plasma effect was examined on a surface with pattern features of D = 160 μm, Φ = 80 μm, h = 20 μm. For surfaces without plasma treatment, the holes slowly closed as the compressive strain increased, but no surface wrinkling was observed (Movie S1, Supporting Information). In contrast, on the plasma treated surface (Movie S2, Supporting Information), we observed a series of patterned surface instabilities as compression increased, starting with wrinkles formed at $\varepsilon \approx 0.04$, then in-plane wrinkling bifurcation (period doubling) at $\varepsilon \approx 0.08$, followed by the nucleation of creasing (wrinkling-creasing transition) at $\varepsilon \approx 0.1$, and global creasing at $\varepsilon \approx 0.3$, and finally the closure of lattice holes at $\varepsilon \approx 0.55$.

The morphological development of the surfaces was characterized under reflected light optical microscopy to study the dynamic surface evolution with different lattice arrays. A series of observations were made at the same strain sequence to reveal surface states at the same deformation level. For the pattern with a square lattice (Figure 1g), the in-plane wrinkle pattern appears to be lateral straight stripes and does not change much with different aspect ratios (Figure S1, Supporting Information). For the pattern with centered square lattice, the case is more interesting and we see three types of in-plane wrinkling patterns formed at small compressive stress with a high sensitivity to the aspect ratios of lattice we applied. For $D/\Phi = 1$, an in-plane curved stripes pattern is developed with a strong dependency on the local curvature determined by the lattice hole and aspect ratio of lattice array (Figure 1h). Straight wrinkle stripes pattern is evident when $D/\Phi = 2$ (Figure 1i), which is similar to the surface patterned with square lattice. However, an in-plane 'star' wrinkle pattern is generated for $D/\Phi = 4$ (Figure 1j), the wrinkle morphology shows a 2D periodic distribution around each hole with a "star" shape, implying a diagonal strain energy localization.

At higher compression, all patterned surfaces develop morphological evolutions showing a wrinkle-crease transition, the surface creases nucleate at the edge of lattice hole perpendicular to the compression direction at $\varepsilon \approx 0.06$–0.013. The creases progress as the compression increases, and fully cover the surface at $\varepsilon \approx 0.3$. Among these morphological transitions, an interesting phenomenon is discovered that a single crease can be generated on the surface with centered square lattice holes (D = 80 μm, Φ = 20 μm, h = 20 μm). This has great potential to enable new types of surface actuator with targeted compression effects within the scale of a few micrometers. It should also be noted that the critical strains for initializing the transition ($\varepsilon \approx 0.06$–0.013) are much lower than the typical critical strain value of $\varepsilon_{crease} \approx 0.35$–$0.55$.[2,7] The reason is that the nominal strain level we used as a control parameter does not well reflect the strain

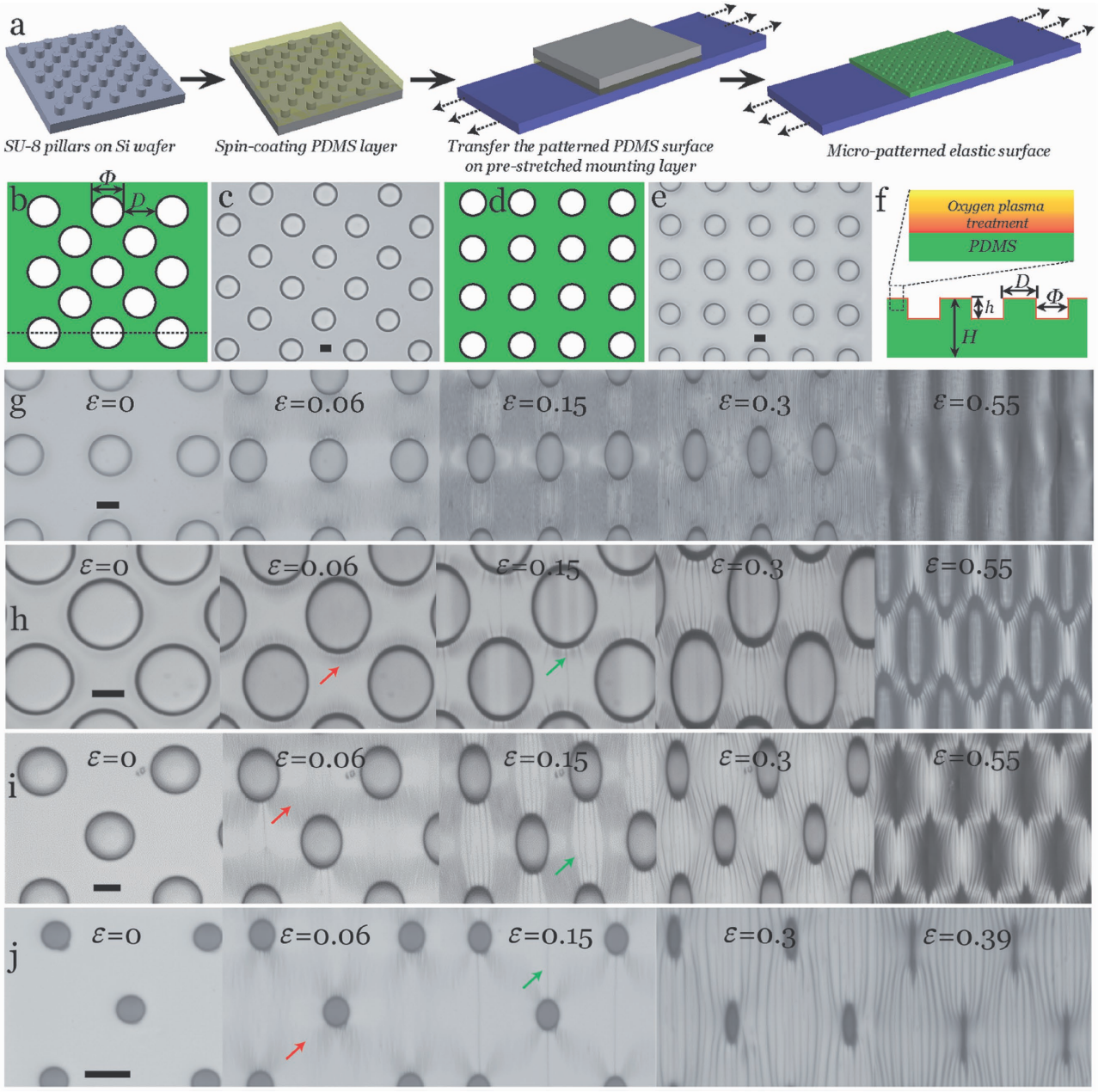

Figure 1. Illustration of design and fabrication process of structural confinements and guided formation of surface morphologies under compression. a) The structural surface was fabricated by spin-coating a thin PDMS precursor layer on a lithographically made template (SU-8 pillars array on a silicon wafer), then transferring and curing the thin PDMS layer (≈125 µm) onto the top of a pre-stretched mounting elastomer layer with thickness ≈3 mm. Two in-plane arrays with varied aspect ratios are designed, b) illustration and c) optical microscopy for centered square lattice array, d) illustration, and e) optical microscopy for square lattice array. f) The microfabricated surface was treated with oxygen plasma to achieve a stiff skin layer (≈50 nm). g) The observation of surface morphology changes on square lattice array patterned surface at different compression levels. h–j) The observation of surface morphology changes on a centered lattice array patterned surface at the same compression sequences in (g) with different aspect ratios. The wrinkle patterns are marked with red arrows and creases are marked with green arrows. All images in this figure have been formatted with the same scale bar of 20 µm.

localization on the structural confined surface. The strain energy localization at a curved boundary near a hole edge for a patterned surface could be several folds of that on a nonpatterned surface. We will discuss these features in more detail later in this report.

To understand the instability patterns (**Figure 2**a–c) and thresholds observed above, we conducted a numerical analysis by calculating the pattern of deformation under the imposed global compressive strain for lattice patterned surfaces (Figure 2d). Deformation around a single hole and square/centered square arrays of holes has been previously studied within linear elasticity,[43,44] and generally produce stress concentrations near the holes. To generalize these results to our

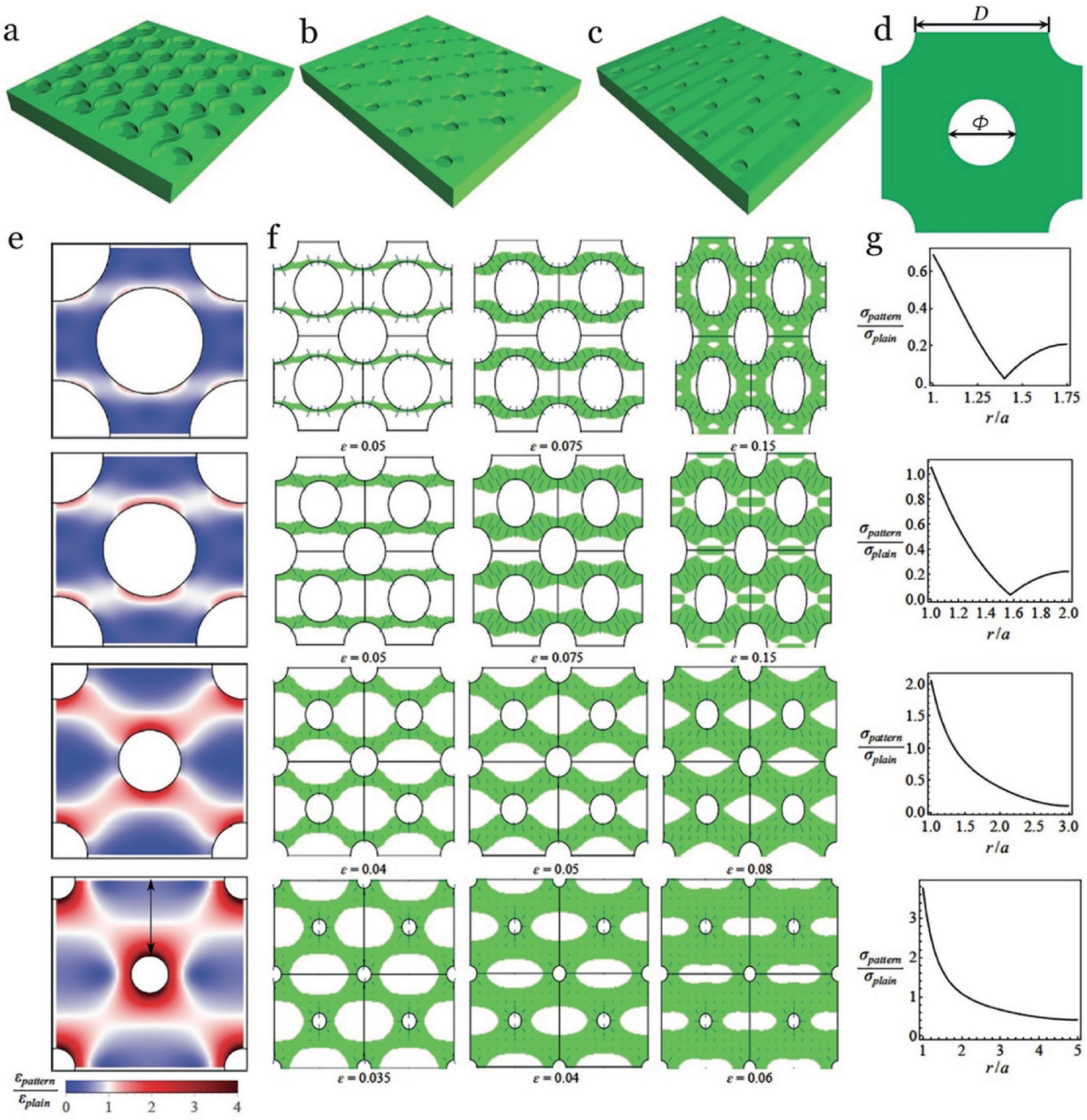

Figure 2. Analytical approach of the generated harmonic winkle patterns. Three harmonic patterns are generated as a) curved ribbon, b) star shape, c) straight belt. d) A representative unit area is chosen for numerical analysis. e) Compression of the patterned substrate relative to the compression of the nonpatterned substrate. Blue and red indicate the less and more compressive areas. f) Evolution of wrinkling region as a function of applied strain in the deformed bilayer system with patterned holes. Green areas are the wrinkling regions. Lines indicate the direction along which the wrinkles will grow while their lengths are the relative distance from the wrinkling threshold. g) Compressive stress in the stiff layer in the patterned bilayer system relative to the nonpatterned system values at different position from the rim of the hole of radius a (maximum stress) to the edge of the unit cell (see arrow in (e) bottom). All plotted with $D/\Phi = 0.75$, 1, 2, and 4.

lattices, we modeled the patterned substrate as a linear-elastic 2D plane-strain system consisting of an infinite incompressible elastic material containing the appropriate infinite lattice of holes. As seen in Figure 2e, we consider a square unit cell of the resulting system (centered square patterned surface), and used Mathematica finite elements to solve the plane strain field in response to an imposed compressive strain, $\varepsilon_{\text{plain}}$, in the x direction and, as measured in experiments, a sympathetic extension of 0.3 $\varepsilon_{\text{plain}}$ in the y direction, and with stress free boundary conditions at the edges of the holes.

In Figure 2f, we plot the local maximum compressive strain in our solutions, $\varepsilon_{\text{pattern}}$, as a fraction of $\varepsilon_{\text{plain}}$, for several

different aspect ratios of lattice. We see that the compressive strain is strongly localized around the holes. In centered square lattices with smaller holes, there are also clearly star-shaped patterns of increased compression running between the holes. We show the same plots for a simple square lattice in Figure S2 (Supporting Information), showing compression concentration in lateral straight stripes through the holes at all aspect ratios of pattern.

We next calculate the wrinkling pattern on the stiff plasma-treated skin that decorates this base-state deformation. To do this, we first calculate the compressive stress σ_c in the thin film, assuming it has a Poisson ratio of $\nu_f = 0.3$ directly follows the deformation in the soft substrate. The value of this compressive stress, as a fraction of the compressive stress that would be observed in a nonpatented system, is plotted for each lattice in Figure 2g, as a function of distance from the center of the central hole, along the line shown in the bottom figure of Figure 2e. For a centered square lattice patterned surface, we see that the compressive stress is strongly enhanced at the edge of hole, particularly in lattices with small holes, explaining why wrinkling occurs earlier in patterned systems. To predict wrinkling patterns, we apply the standard result for wrinkling on a substrate, which is that wrinkling will occur if $\sigma_c > \frac{1}{4}\left(3\frac{\overline{E}_s}{\overline{E}_f}\right)^{2/3}\overline{E}_f$, where $\overline{E}_f$ and $\overline{E}_s$ refer to the plane-strain elastic modulus for the oxidized stiff layer and PDMS substrate, respectively, which are related to the Young's moduli, E, by $\overline{E} = E/(1-\nu^2)$, where ν is the Poisson ratio. Taking the physically reasonable modulus ratio $\overline{E}_f/\overline{E}_s = 100$, we plot, in Figure 2f, how the predicted wrinkle regions grow as the global compression is increased. We see, in accordance with experiment, that moving from large holes to small holes does indeed change the wrinkling pattern from wavy lines, to straight lines, to stars, and that the patterns with smaller holes wrinkle at smaller global compressions, because the compressive stress is more concentrated around the hole.

After plasma treatment for 10 seconds, the surface modulus measurement (Figure S3, Supporting Information) obtained by AFM indentation suggests the plane-strain elastic modulus mismatch between the film and the substrate is about $\overline{E}_f/\overline{E}_s \approx 25$. Accordingly, the critical strain for wrinkling from linear stability analysis[45–48] is $\varepsilon_w = 0.25(3\overline{E}_s/\overline{E}_f)^{2/3} = 0.061$, which agrees well with our result of $\varepsilon \approx 0.068 \pm 0.008$ for a nonpatterned surface (Figure S4, Supporting Information). However, it does not agree with the case of a lattice patterned surface, in which wrinkle patterns are already present at $\varepsilon = 0.06$, indicating that wrinkling occurs at a lower threshold strain as a result of strain energy localization near the lattice holes. Furthermore, according to the report from Kim et al., as compression is increased in systems with $\overline{E}_f/\overline{E}_s \approx 25$, wrinkles are expected to period double then evolve into creases. We expect patterning to also reduce the thresholds for these further bifurcations, but they cannot be effectively identified under reflective optical microscopy.

To unveil more details, we used AFM to track the surface morphology changes as the compressive strain was gradually increased, focusing on the region of stress concentration "above" a hole as indicated by the dashed box in **Figure 3**a. For the centered square patterned surface with aspect ratio of D = 80 μm, Φ = 40 μm, h = 43 μm, we found the onset of wrinkling starts at a small compressive strain of ε = 0.02 (Figure 3b–c) and progress to cover the region by $\varepsilon = 0.11$. The initial wavelength (λ_0) is predicted to be $\lambda_0 = (2\pi h_f)(\overline{E}_f/3\overline{E}_s)^{1/3}$, or 700 nm for an oxidized layer thickness of h_f = 55 nm, which is in reasonable agreement with the measured value of ≈850 nm. The progressive wrinkling over this range of strain presumably reflects the influence of the energy boundaries resulting from the local curvature. We also find the creases start to nucleate at $\varepsilon = 0.11$, and start to grow at $\varepsilon = 0.15$, then fully cover the region at $\varepsilon = 0.25$. A hierarchical surface is formed at $\varepsilon = 0.55$, where we can see the periodic surface under the reflective optical microscopy in Figure 3d.

There is clearly a curvature guided formation of wrinkle at $\varepsilon = 0.02$ with nonuniform amplitude distribution which reveals the state of energy concentration, where the hole edge perpendicular to the compression axis scores the highest (Figure 3c). The period doubling pattern can be observed at $\varepsilon = 0.15$ with every second wrinkle growing in amplitude while its neighbors shrink. The strain value for this bifurcation is also smaller than the reported strain value ≈0.17.[5] From $\varepsilon = 0.15$, further compression does not noticeably influence the in-plane morphology, since the AFM result cannot reflect the out of plane deformation toward the substrate, i.e., self-contact area of the crease. Therefore, we add the cross-sectional scanning data of the film from laser-scanning confocal fluorescence microscopy (LSCM, Figure 3e) to reveal the out of plane morphological development for the selected area (Figure 3f). At a strain of ε = 0.15 (Figure 3c), the LSCM data shows a shallow crease depth (self-contact area) within 100 nm, where it is considered as the onset of the crease. Similar with the wrinkling, this second bifurcation is found to be highly sensitive to the presence of local planar curvature (Figure S5, Supporting Information). At higher compressive strains, the crease depth develops under higher compressive strains and extends to all scanned areas.

We next consider the lattice pattern effects on post wrinkling bifurcations occurring at a higher strain level. It should be noted that the crease nucleates but it does not grow across the regime adjoining the lattice holes (Figure S6, Supporting Information) for $D/\Phi \leq 1$. We expect this may arise due to the viscoelastic nature of the substrate, and/or the influence of large curvature. A brief classification of the transitions based on the crease number initiated is summarized in **Figure 4**a–c for the lattice patterned surface with aspect ratio $D/\Phi > 1$. There are two transition types (single crease and multiple creases) for the stripe pattern, and the formation of creasing is revealed in Figure 4d. The "star" type wrinkle pattern seems more likely to generate a single crease when being further compressed.

We next plot the normalized wrinkle amplitude (A/λ_0) as a function of the nominal applied strain on a nonpatterned surface (Figure 4e) and a Bravais lattice patterned surface (Figure 4f, D = 80 μm, Φ = 40 μm, h = 43 μm). In each case, beyond wrinkling onset, two additional instabilities/bifurcations are seen, corresponding to period doubling and then crease formation. However, both the onset of wrinkling and the further bifurcations occur at considerably lower global strains in the patterned system: the critical wrinkle strain for the

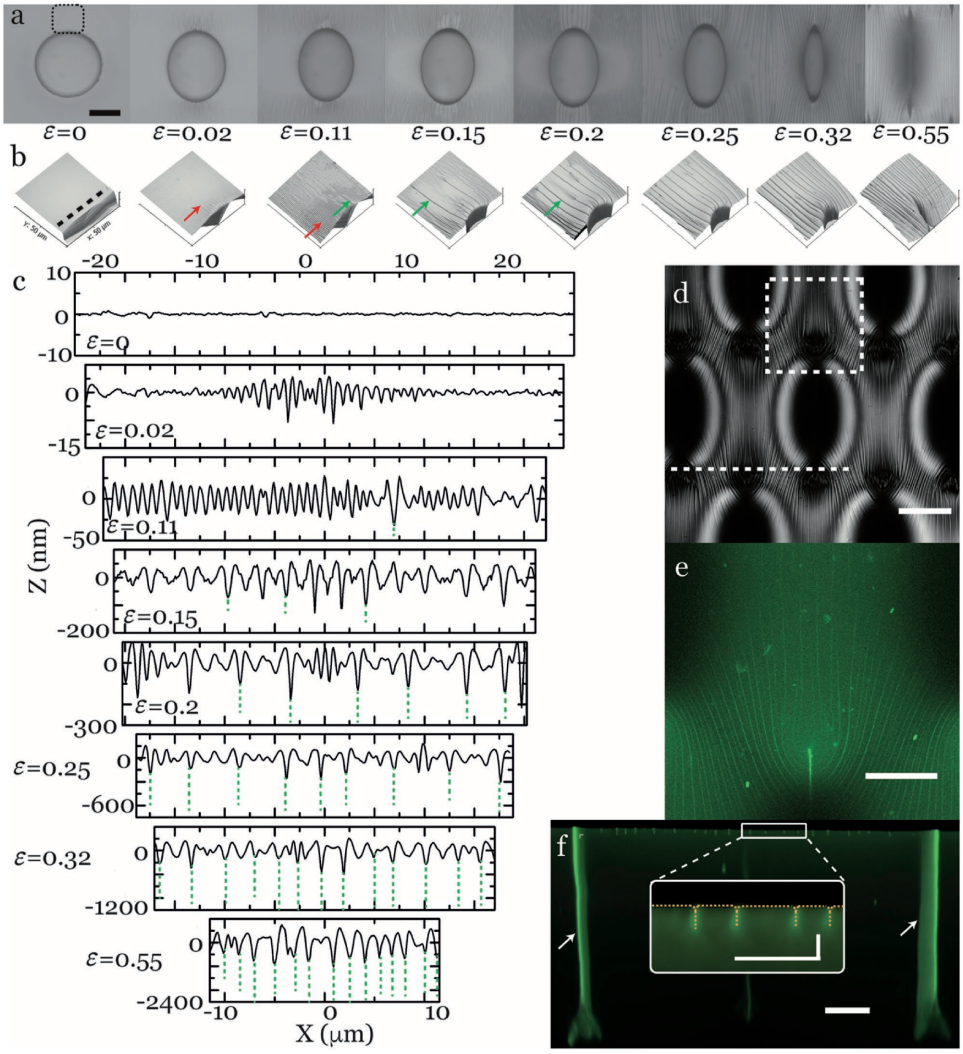

Figure 3. Characterization of the instabilities on the single hole and their evolutions under the uniaxial compression. a) Top view observations and b) AFM profiling of the selected area in (a) for surface morphology changes under the uniaxial compression for a unit area (centered square lattice array) with in-plane aspect ratio of D = 80 μm, Φ = 40 μm, h = 43 μm. c) The surface morphology development is plotted with the dependency on compression strain, the surface starts to initialize localized wrinkles on ε = 0.02, then develops into periodic doubling at ε = 0.15, the surface starts to form creases locally at ε = 0.2, where the sharp self-contacts within the PDMS (green dashed lines) are detected by LSCM, and finally the creasing develops globally. d) The reflective image shows a surface hierarchy formed when the hole reached the "off" state at a compression deformation of 0.55. Laser confocal scanning reveals e) the in-plane distribution of creases and f) the out of plane morphology developed into the PDMS substrate for the selected area in (d), the arrows show the high intensity fluorescence signal due to the closure of neighboring holes. The scale bar for the inset figure in (f) is 3 μm. The other scale bars are 40 μm.

patterned surface of ≈0.02 is less than one third of that in the flat surface ($\varepsilon \approx 0.068$), the critical strain for periodic doubling in the patterned surface is ≈0.06, whereas it is ≈0.18 in flat surface, and for the final bifurcation, the wrinkle-crease transition, the critical strain needed is ≈0.08 in the patterned surface, which is less than half of that for the flat surface ($\varepsilon \approx 0.22$). We can understand this threshold reduction effect by considering the stress concentration in our analytic calculations for systems with $D/\Phi = 2$ (seen in Figure 2g), which exhibit a two-fold stress concentration at the edge of the hole relative to the nonpatterned system, and hence predicts two-fold reduction in the various thresholds. The discrepancy between this calculation and the observed three-fold reduction is probably due to our analytic plane-strain approximation not capturing the full 3D structure of the actual deformation field.

It is important to understand quantitatively how these instabilities develop in the presence of the curved boundary from the edge of lattice holes. Thus, we plot the normalized strains for the onset of each instability as a function of the radius of lattice hole for $D/\Phi = 2$. As seen in Figure 4g, the critical strains are clearly separated in different ranges, while the planar curvature decided by the radius of the holes influence the strains significantly. The overall strains are reduced as a result of the strain localization guided by the curved boundary, and it seems the strains for each instability are likely to collapse, which agrees well with the reported value by Kim that the doubling bifurcations are

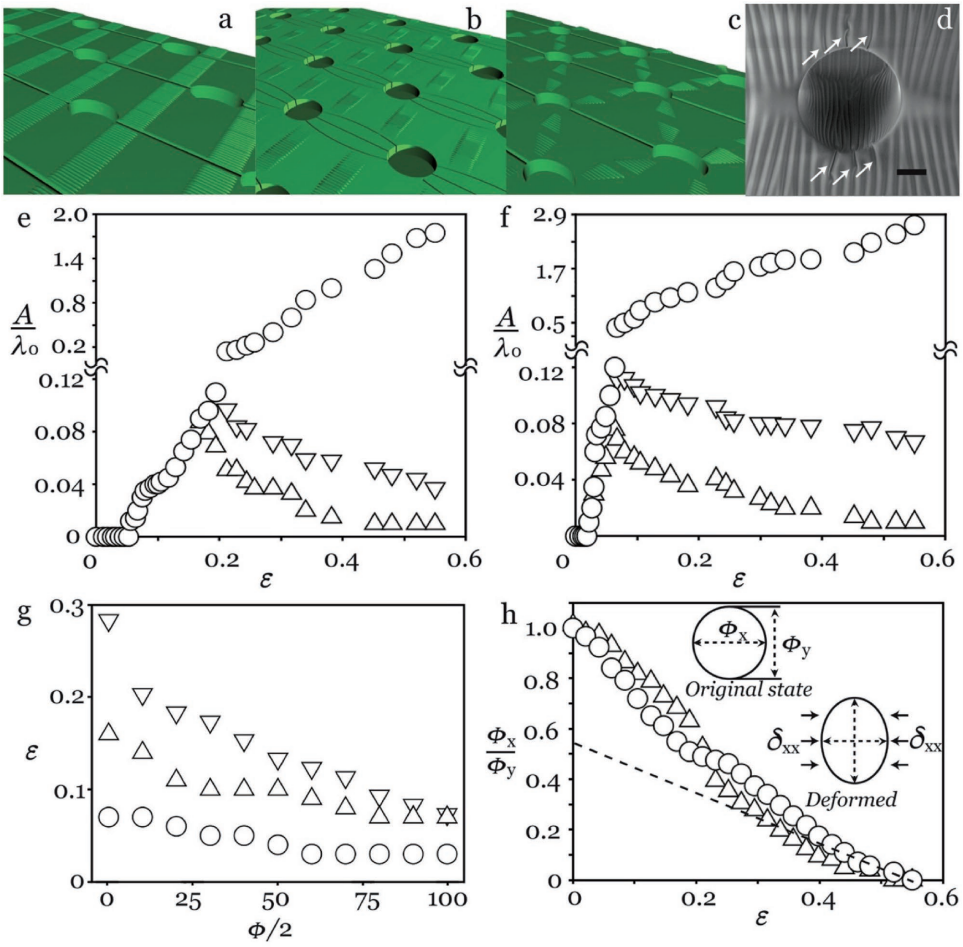

Figure 4. The evolution of surface morphology at higher compression, from wrinkling to creasing. Schematic illustrations of the transition from wrinkling to creasing for different harmonic patterns, a) straight belt, b) star shape, and c) curved ribbon. d) SEM image reveals the transition moment from wrinkling to creasing with the captured initialization of creases. The normalized amplitudes of surface features A/λ_0 reveal two postwrinkling bifurcations with increasing strain for e) homogeneous PDMS surface and f) patterned PDMS surface (centered lattice) with in-plane aspect ratio of D = 80 μm, Φ = 40 μm, h = 43 μm. Normalized amplitudes changes along with two bifurcations and represented with first order (○), second order (△), and third order (▽). g) The critical strains for initiating wrinkle (○), periodic doubling (△), creasing (▽) for the centered square array with different diameter. h) The compression (△) and recovery (○) curves show the hysteresis and nonlinearity on the deformation of a single hole under uniaxial compression.

likely to be mixed with creasing with the $\overline{E}_f/\overline{E}_s$ value in the range of 14–47.[34,35] A key advantage of the elastic instability enabled technology is that, as an elastic process, it should yield a low degree of hysteresis. We then investigate the hysteresis of the lattice patterned surface with labeling the lateral dimension change in the hole (Figure 4f). The results suggest a robust transformation, which indicates that the viscoelastic relaxation of the soft PDMS layer used here is less important.

3. Conclusion

In this report, we present an approach to generate periodic planar wrinkle 2D patterns and controllable instability evolution toward a hierarchical surface by preplacing Bravais lattice patterns on the surface as in-plane structural confinements. The bilayer system shows kinetic bistabilities at certain well-defined strain values initializing the wrinkles and further elastic bifurcations at the designated areas/locations which are closely related to the geometries of the confinements. The formation of lateral wrinkle patterns has been studied with the dependencies on the geometrical variables of in-plane confinements and the results are in good agreement with the predictions from numerical analysis. At higher compression, we also reveal a targeted formation of wrinkle-to-crease transition as result of the reorganization of surface strain field. We anticipate this localized formation of surface instabilities, and the demonstration of bistability over a substantial range of strains will open new opportunities for applications of elastic instabilities on responsive surfaces for future lab on chip devices, by enabling delicate responses to mechanical inputs as selectively sensing or actuating structures.

4. Experimental Section

Microengineeringand Surface Treatment of Pattern Template: Structural patterned templates of SU-8 microcylinders on silicon wafer were

obtained through a standard photolithographic fabrication technique. Templates with different lattice arrays (square and centered square) and varied aspect ratios were prepared. A SAM of trichloro(1H,1H,2H,2H-perfluorooctyl)silane (Sigma-Aldrich), was applied from the vapor phase at 20 °C for 30 min to facilitate subsequent release of the PDMS film.

Fabrication of Structural Confined Elastic Bilayer: The mounting layer was made from a commercial available elastomer product (Elite Double 22, shear modulus ≈ 0.35 MPa) from Zhermack Ltd. After mixing the vinylpolysiloxane base with a curing agent with a weight ratio of 1:1 for 1 min, the mixture was cured in the petri dish at 20 °C for 6 h. The cured elastomeric film was ≈3 mm in thickness, and a stripe of ≈6 mm × 20 mm was cut and prestretched to 400% of its original length on a uniaxial mechanical strain stage. The soft PDMS layer with thickness of 125 µm (Sylgard 184, Dow Corning, 30:1 for elastomer base:crosslinker) was prepared by spin-coating the degassed mixture on a SU-8 patterned silicon wafer (≈1 cm^2) at 1000 rpm for 120 s, followed by curing at 70 °C for 1 h. An adhesive PDMS layer with the same composition of 30:1 was spin-coated on this cured layer at 3000 rpm for 120 s, to bond to the mounting layer. After transferring the adhesive coated soft PDMS layer to the mounting layer, the assembly was baked at 70 °C for 8 h to cure the adhesive layer. Prior to characterization, the bilayer was treated with oxygen plasma (HPT-100, Henniker) under a working power of 100 W, with a mixed gas atmosphere of oxygen/nitrogen ratio ≈ 0.2.

Characterization: The bilayer was progressed to measurement as soon as the oxygen plasma treatment was completed. Incremental deformation in nominal strain of ≈0.004 were applied to the sample by releasing the mounting layer prestretch by a fixed amount at regular intervals and situated for 15 min in room temperature. Sample surfaces were observed in situ using an upright optical microscope (Nikon LV-100) in brightfield reflection mode. For the laser scanning confocal microscopic imaging (Nikon A1R), the top layer was labeled by adding a small amount of fluorescent monomer (0.1 mg fluorescein-*o*-acrylate per 1 g PDMS). Scanning electron microscopy (MIRA3, TESCAN) was used to observe the surface structure. The surface topographic features were assessed with an atom force microscopy (D3100, Veeco).

Numerical Analysis: The numerical analysis used a finite element package in Mathematica to solve the 2D plane strain linear elasticity problem for the deformation in the patterned soft substrate. A repeatable 2D unit cell was first defined with the geometry corresponding to the experiment and, as seen in Figure S7 (Supporting Information), the domain by a fine mesh consisting of around 4000 triangles was described.

A plain-strain deformation was then assumed, described by the 2D displacement field $(u(x,y)\hat{x}+v(x,y)\hat{y})$ so the plane strain stress tensor is

$$\sigma=\frac{E}{(1+\nu)}\begin{pmatrix}\frac{(1-\nu)u_{,x}+\nu v_{,y}}{(1-2\nu)} & \frac{u_{,y}+v_{,x}}{2}\\ \frac{u_{,y}+v_{,x}}{2} & \frac{\nu u_{,x}+(1-\nu)v_{,y}}{(1-2\nu)}\end{pmatrix} \quad (1)$$

where E is the Young's modulus, ν is the Poisson's ratio, and the comma-notation denotes partial derivatives. The Mathematica finite element package was then used to solve $\nabla\cdot\sigma=0$ in the meshed domain, subject to the boundary conditions that $\sigma\cdot\hat{n}=0$ on the hole edges, and that the straight edges of the cell move with the macroscopic strain of the underlying substrate ($-\varepsilon$ in the x-direction and 0.3ε in the y-direction) as seen in Figure S7 (Supporting Information).

After solving for the displacement fields (Figure 2e), the stress on the film could be evaluated from the stress tensor above. To determine whether the region is unstable toward wrinkling, the stress tensor was diagonalized to find its maximum compressive stress (Figure 2g). By comparing this compressive stress with the theoretical critical value, the wrinkling region could be identified (Figure 2f), while the wrinkle direction (the short lines in Figure 2f) was perpendicular to the principal direction of the maximum compressive stress.

Supporting Information

Supporting Information is available from the Wiley Online Library or from the author.

Acknowledgements

The work was supported by the Engineering and Physical Sciences Research Council (EPSRC) grant-EP/N007921/1 and Royal Society research grant-RG150662. B.B.X. and D.W. would thank Reece Innovation for the studentship support and Dr. Gary Wells for the useful discussions.

Conflict of Interest

The authors declare no conflict of interest.

Keywords

Bravais lattice, elastic instabilities, micropatterns, morphological bifurcations, wrinkling

Received: July 26, 2017
Revised: September 6, 2017
Published online: November 7, 2017

[1] N. Bowden, S. Brittain, A. G. Evans, J. W. Hutchinson, G. M. Whitesides, *Nature* **1998**, *393*, 146.
[2] D. Chen, J. Yoon, D. Chandra, A. J. Crosby, R. C. Hayward, *J. Polym. Sci., Part B: Polym. Phys.* **2014**, *52*, 1441.
[3] P. Kim, M. Abkarian, H. A. Stone, *Nat. Mater.* **2011**, *10*, 952.
[4] E. Hohlfeld, L. Mahadevan, *Phys. Rev. Lett.* **2011**, *106*, 105702.
[5] F. Brau, H. Vandeparre, A. Sabbah, C. Poulard, A. Boudaoud, P. Damman, *Nat. Phys.* **2011**, *7*, 56.
[6] T. Tallinen, J. Y. Chung, J. S. Biggins, L. Mahadevan, *Proc. Natl. Acad. Sci. USA* **2014**, *111*, 12667.
[7] D. Chen, S. Cai, Z. Suo, R. C. Hayward, *Phys. Rev. Lett.* **2012**, *109*, 038001.
[8] B. Xu, R. C. Hayward, *Adv. Mater.* **2013**, *25*, 5555.
[9] J. Kim, J. A. Hanna, M. Byun, C. D. Santangelo, R. C. Hayward, *Science* **2012**, *335*, 1201.
[10] S.-J. Jeon, A. W. Hauser, R. C. Hayward, *Acc. Chem. Res.* **2017**, *50*, 161.
[11] Y. Liu, J. K. Boyles, J. Genzer, M. D. Dickey, *Soft Matter* **2012**, *8*, 1764.
[12] M. A. C. Stuart, W. T. S. Huck, J. Genzer, M. Muller, C. Ober, M. Stamm, G. B. Sukhorukov, I. Szleifer, V. V. Tsukruk, M. Urban, F. Winnik, S. Zauscher, I. Luzinov, S. Minko, *Nat. Mater.* **2010**, *9*, 101.
[13] B. B. Xu, Q. Liu, Z. Suo, R. C. Hayward, *Adv. Funct. Mater.* **2016**, *26*, 3218.
[14] D. P. Holmes, B. Tavakol, G. Froehlicher, H. A. Stone, *Soft Matter* **2013**, *9*, 7049.
[15] T. Ohzono, H. Monobe, *Langmuir* **2010**, *26*, 6127.
[16] S.-m. Park, Y. S. Huh, H. G. Craighead, D. Erickson, *Proc. Natl. Acad. Sci. USA* **2009**, *106*, 15549.
[17] B. Xu, D. Chen, R. C. Hayward, *Adv. Mater.* **2014**, *26*, 4381.
[18] J. A. Rogers, T. Someya, Y. Huang, *Science* **2010**, *327*, 1603.
[19] P.-C. Lin, S. Vajpayee, A. Jagota, C.-Y. Hui, S. Yang, *Soft Matter* **2008**, *4*, 1830.
[20] E. P. Chan, E. J. Smith, R. C. Hayward, A. J. Crosby, *Adv. Mater.* **2008**, *20*, 711.
[21] J. B. Kim, P. Kim, N. C. Pegard, S. J. Oh, C. R. Kagan, J. W. Fleischer, H. A. Stone, Y. L. Loo, *Nat. Photonics* **2012**, *6*, 327.

[22] P. Görrn, M. Lehnhardt, W. Kowalsky, T. Riedl, S. Wagner, *Adv. Mater.* **2011**, *23*, 869.
[23] E. Lee, M. Zhang, Y. Cho, Y. Cui, J. Van der Spiegel, N. Engheta, S. Yang, *Adv. Mater.* **2014**, *26*, 4127.
[24] S. S. Zeng, D. Y. Zhang, W. H. Huang, Z. F. Wang, S. G. Freire, X. Y. Yu, A. T. Smith, E. Y. Huang, H. Nguon, L. Sun, *Nat. Commun.* **2016**, *7*, 11802.
[25] K. Khare, J. Zhou, S. Yang, *Langmuir* **2009**, *25*, 12794.
[26] S. G. Lee, D. Y. Lee, H. S. Lim, D. H. Lee, S. Lee, K. Cho, *Adv. Mater.* **2010**, *22*, 5013.
[27] X. Huang, Y. Sun, S. Soh, *Adv. Mater.* **2015**, *27*, 4062.
[28] J. Kim, J. Yoon, R. C. Hayward, *Nat. Mater.* **2010**, *9*, 159.
[29] M. Arifuzzaman, Z. L. Wu, R. Takahashi, T. Kurokawa, T. Nakajima, J. P. Gong, *Macromolecules* **2013**, *46*, 9083.
[30] Q. Li, X. Han, J. Hou, J. Yin, S. Jiang, C. Lu, *J. Phys. Chem. B* **2015**, *119*, 13450.
[31] J. Rodríguez-Hernández, *Prog. Polym. Sci.* **2015**, *42*, 1.
[32] A. Auguste, L. Jin, Z. Suo, R. C. Hayward, *Extreme Mech. Lett.* **2017**, *11*, 30.
[33] T. Tallinen, J. S. Biggins, *Phys. Rev. E* **2015**, *92*, 022720.
[34] M. Diab, T. Zhang, R. Zhao, H. Gao, K.-S. Kim, *Proc. R. Soc. A* **2013**, *469*, 20120753.
[35] R. Zhao, T. Zhang, M. Diab, H. Gao, K.-S. Kim, *Extreme Mech. Lett.* **2015**, *4*, 76.
[36] W. T. S. Huck, N. Bowden, P. Onck, T. Pardoen, J. W. Hutchinson, G. M. Whitesides, *Langmuir* **2000**, *16*, 3497.
[37] Q. Wang, X. Zhao, *Sci. Rep.* **2015**, *5*, 8887.
[38] Q. Wang, X. Zhao, *MRS Bull.* **2016**, *41*, 115.
[39] D. Breid, A. J. Crosby, *Soft Matter* **2013**, *9*, 3624.
[40] N. Stoop, R. Lagrange, D. Terwagne, P. M. Reis, J. Dunkel, *Nat. Mater.* **2015**, *14*, 337.
[41] J. D. Paulsen, E. Hohlfeld, H. King, J. Huang, Z. Qiu, T. P. Russell, N. Menon, D. Vella, B. Davidovitch, *Proc. Natl. Acad. Sci. USA* **2016**, *113*, 1144.
[42] F. L. Jiḿenez, N. Stoop, R. Lagrange, J. Dunkel, P. M. Reis, *Phys. Rev. Lett.* **2016**, *116*,104301.
[43] Y. Cao, J. W. Hutchinson, *J. Appl. Mech.* **2012**, *79*, 031019.
[44] H. G. Allen, *Analysis and Design of Structural Sandwich Panels*, Pergamon, Oxford **1969**.
[45] J. Genzer, J. Groenewold, *Soft Matter* **2006**, *2*, 310.
[46] R. W. Bailey, R. Fidler, *Nucl. Eng. Des.* **1966**, *3*, 41.
[47] M. L. Kachanov, B. Shafiro, I. Tsukrov, *Handbook of Elasticity Solutions*, Springer, Netherlands **2003**.
[48] H. Jiang, D.-Y. Khang, J. Song, Y. Sun, Y. Huang, J. A. Rogers, *Proc. Natl. Acad. Sci. USA* **2007**, *104*, 15607.

Responsive Hydrogels Based Lens Structure with Configurable Focal Length for Intraocular Lens (IOLs) Application

*Yifan Li, Ding Wang, Jack Richardson, Ben Bin Xu**

Summary: Stimuli-responsive hydrogel has attracted wide interests in bio-applications, especially in bio-optical systems that need tuning and adjustment of their optical performances. In this paper, we have investigated the materials and structural designs for the potential intraocular Lens (IOLs) design by studying swelling induced morphology changes and subsequently optical properties of ionic responsive Poly (Acrylamide-*co*-sodium acrylate) hydrogel. The equilibrium swelling ratio and swelling kinetics of gel were measured under both free standing and confined conditions. The Poly (Acrylamide-*co*-sodium acrylate) hydrogel has shown reversible swelling response to the ion concentration. Autonomous focusing of the gel lens was demonstrated under the certain ionic stimulus. Initial optical results have been presented with designable stimuli-responsive focal length shifting under structural confinement.

Keywords: hydrogel; intraocular Lens; ionic; stimuli-responsive

Introduction

One of the recent research interests in intraocular lens (IOLs) technology is to achieve variable focal lengths by using suitable materials and novel designs. The most common solution is to either directly fabricate the lens and its components onto curved surfaces by moulding, or geometrically reshape a planar system.[1–4] By far, all reported IOLs designs are of fixed focal length, the technical challenge remains to be addressed under the term of developing gel lens with adjustable focal length in an autonomous and reversible manner. From the perspective of customer experiences, the IOLs with self-regulating focal length could offer convenient care solutions to perspective patients by providing vision tolerance to avoid over-sight or/and over-intensity after surgery.[2]

By applying various external stimuli such as temperature, pH, electric and magnetic fields, and chemical triggers, hydrogel can undergo reversible deformation to change its size and shape.[4–11] Stimuli-responsive hydrogels have been developed into various sensor and actuator applications include bio-medical sensors, artificial muscle actuators, scaffolds for tissue engineering, active surfaces and drug delivery systems.[12–15] The swelling and de-swelling of the polymer network was firstly discovered as a result from reversible titration of weakly ionised polyelectrolyte gels.[3] Given a proper boundary condition, curvilinear layouts could be generated on the surface of gel during swelling. Such stimuli induced geometrical change will result in strong nonplanar imaging capability and autonomous control.[16–18] Recent study by Dong and co-workers[19] presented a hydrogel based adaptive liquid lens, where the water-oil interfaces were

Smart Materials and Surfaces Lab, Faculty of Engineering and Environment, Northumbria University, Newcastle upon Tyne NE1 8ST, UK
E-mail: ben.xu@northumbria.ac.uk

pinned and deformed by actuating ring-shaped hydrogel structures by changing temperature and pH, mimicking the mechanism of a human eye. The utilisation of responsive materials could simplify the lens design without degrading the field of view, focal area, illumination uniformity, or image quality.[20]

In this article, we introduce a conceptual design to confine the circular gel structure on the rim with a 3D printed holder. The purpose is to configure the curvature of gel lens in a coordinated manner under the ionic stimulus, to achieve variable focal length autonomously. When swelling occurs under the given confinement, the original thickness of fabricated curved lens changes in an elastic and reversible way that allow us to control the curvature of the lens. This actuation is defined precisely by the nature of the polyelectrolyte gel in this work and the kinetic is studied. The investigation of the focal length change suggests that the fabricated gel lens covers the whole range of the human eyes. The conceptual gel lens in this study could be an active substrate to integrate with other elements for advanced eye prosthetic device development.

Results and Discussion

The gel lens structure was designed to be confined by a 3D printed holder with hollowed structure for the swelling tests (Figure 1a–d). Stimuli responsive poly-(acrylamide-*co*-sodium acrylate) (PAAM-*co*-NaAc) hydrogels (Figure 1e) has been used. As the copolymer gel can response to both ionic and thermal stimuli,[21] the degree of swelling and morphology change of the thin gel layer under certain confinement can be varied through changes to either the ionic strength of the phosphate buffered saline (PBS) solution (ionic strength = 150 mM) or temperature. The conceptual gel lens design has used a circular shape with a diameter of 13.8 mm, and varied thicknesses. The prototyping of gel lens consisted of three steps (Figure 1f). Firstly, the self–designed micro-mould was assembled. Secondly, the reaction-moulding of the gel was performed. And finally, the cover slip was removed to release the lens. The lens was designed with different aspect ratios by controlling the initial height from 250 μm to 2 mm, with a fixed projection diameter of 13.8 mm.

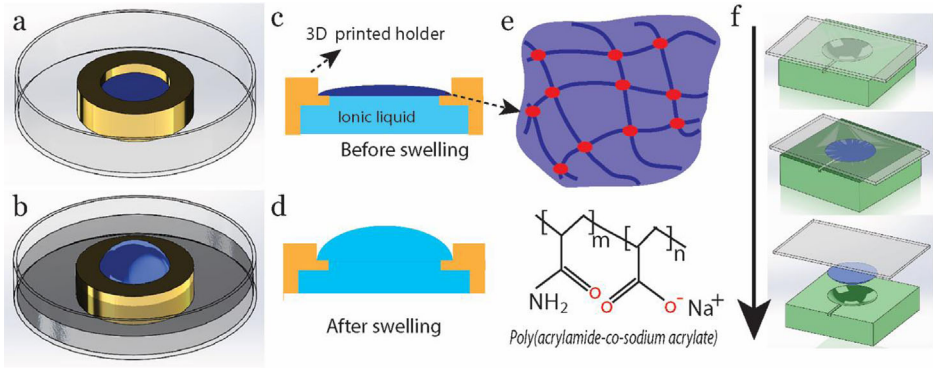

Figure 1.
Experimental design of an ion-concentration controlled swelling hydrogel adaptive lens. The stimuli hydrogel is placed on a 3D printed holder to give a ring confinement during the swelling. (a) The pre-swelling set, (b) the Lens effect after swelling. The cross section views of pre-swelling state (c), and post swelling state (d). (e) The illustration of gel network and chemical composition for the PAAm-*co*-NaAc in our study. (f) From top to bottom, the gelation process in a micro-mould consisting of a 3D printed mould and a cover slip.

The gel swelling test was performed in PBS solutions at room temperature (20 °C) with three different confining conditions, free standing (bulk, Figure 2a), side confinement (Figure 2b), and rim confinement (Figure 2c). As illustrated in Figure 2d, the conceptual lens design with rim confinement could present a focal length change when the nonlinear morphology changes occur as a result of the ionic swelling. The swelling results are compared in Figure 2e, the rim confinement swelling presents the significant deformation with a $H/h \sim 2.42$, while the free standing swelling achieve the equilibrium state at a $H/h \sim 1.56$ for one dimension, and a $H/h \sim 2.06$ for side confinement. Under the rim confinement, the lens structure could achieve higher deformation from the central axial, yielding a significant curvature changes during the swelling process.

The next step was to build a multi-point laser marking based focal length measurement system (Figure 3a) to characterize the focal length changes for the gel based lens structure under ionic swelling. By setting the dimensional variables of the system and controlling the position of the laser input, we will receive the laser mark in the paper receiver. As shown in Figure 3b, the distance from lens to paper receiver can be set by controlling the Z-stage, where I_c is the position when the laser gets through the centroid of the gel lens and the I_e is the laser gets through the edge, we will have focal length $\sim Dl/(D\text{-}d)$. For each measurement, one I_c and at least three I_e need to be measured. Resulted sample marks of the I_c and I_e are shown in Figure 3c and d. As a dynamical process, we used the ionic strength in buffer solution to control the swell ratio (H/h), the calculated focal lengths are shown in Figure 3e. When the swelling started, the focal length was start drop into measurable range at ~26 mm, then keep dropping when the lens was further swollen. The focal length reached a practical range of ~15 when the H/h is 1.7, and remained relatively stable within this range. We noted a wide distribution of the data during the high swelling state, this was caused by the data processing when the Numerical Aperture (NA) was applied to compensate the deflection, while the actual incident angle was hard to capture during the dynamic swelling. The experimental set will be further improved with laser confocal system to identify the laser incident angle. In all, the responsive gel based lens supported by the rim confinement have demonstrated variable-focus ability and can autonomously respond to ionic stimuli.

This responsive hydrogel-based lens is easy to fabricate and its stimuli-responsive nature offers a highly adaptable property, which could be used as substrate to be integrated with other elements such as circuits and sensor for prosthetic application. Moreover, the mechanical

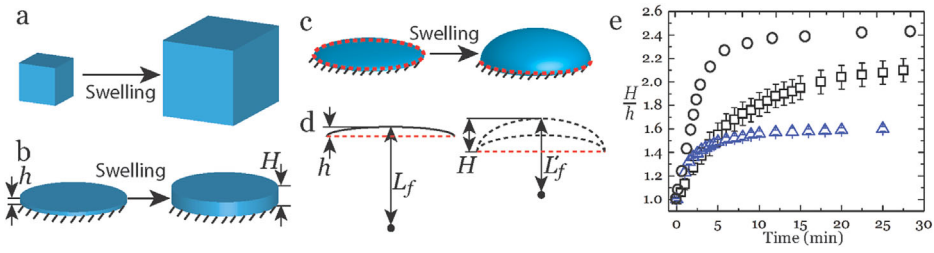

Figure 2.
Schematic and measurement of the morphology change under different swelling state, (a) free standing, (b) one side confinement, (c) ring confinement for PAAm-*co*-NaAc gel lens, (d) the parameters to describe the morphology change of the lens, the original height h, the original Focal Length L_f, the height after swelling H, and the Focal Length after swelling L'_f. (e) The swelling kinetics of the gel under different confining state, free standing (Δ), side confinement (□), and ring confinement in this study (O).

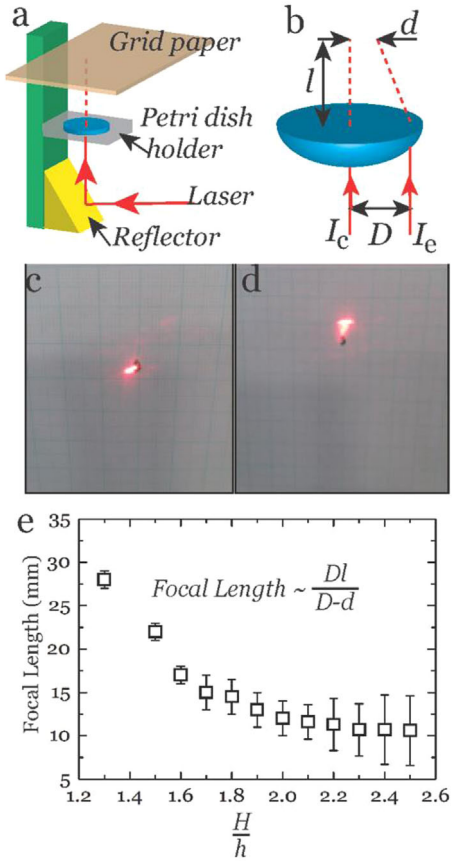

Figure 3.
(a) The experimental set to determine the focal length for the lens during the ionic swelling by laser marking. (b) Dimensional parameters for calculation of the focal length. Sample laser targeting for (c) I_c and (d) I_e. (e) Calculated focal length with different swelling ratio for the PAAm-*co*-NaAc gel lens.

confinement has realised a wide range of focal length change, which could significantly improve the vision quality by achieving a wide field of view. However, there are still some work need be done to understand the mechanics of the geometrical curvature change under rim confinement, and the calculation correction of focal length changes at high swelling level.

Conclusion

We have developed a novel IOLs technique with ionic responsive gel under specific confinement. The ionic swelling induced morphological transformation enabled a wide range of focal length changes ($\infty \rightarrow 10$ mm). This technology also enables simple and cost effective fabrication as well as reasonable fast response times (in the a few minutes). The responsive gel based lens has a highly adaptive property and could autonomously respond to changes of ionic strength in the environment and provide visible output signals. It could also be used as substrate to integrated other elements to generate novel opto-electronic systems for prosthetic applications.

Experimental Section

3D Printing Micro Mold and Device Assembly

The lens mold was printed via Objet 24 desktop system with photo cured acrylic based material. The mold design employed standard contact lens parameters, and was completed in Solidwork software before being loaded into a Strasys® Objet24 system for printing. The printed parts were cleaned and rinsed with isopropanol (IPA), before being annealed on a hot plate at 100 °C for 15 min. The assembly of gelation chamber was constructed by the printed mold and a glass cover slip.

Gelation and Lens Fabrication

The Poly (Acrylamide-*co*-sodium acrylate) hydrogel was synthesized with 825 mM acrylamide, 115 mM sodium acrylate, 4.5 mM *N*,*N*′-methylenebis(acrylamide), 5 mM of Flourescein *o*-acrylate (for swelling test only), 0.3 μL of *N*,*N*,*N*′,*N*′-tetramethylethylenediamine and 1.0 μL of a 10 wt% aqueous ammonium persulfate solution. Gelation was completed within 20 min in the assembled chamber. After removing the coverslip, the gel lens can be obtained and then put into a phosphate buffer saline solution (Sigma-Aldrich) prepared with a total ionic strength of 150 mM.

Gel Swelling Study and Focal Length Measurement with Laser Marking

The swelling testing was carried out via direct optical observation of the fluorescence dyed gel products. For the free standing mode, the gel was cut into cube with varied original dimensions of 2.5 mm, 5 mm and 7.5 mm. For the side confined and rim confinement swelling tests, the gel sheets used the same diameter of 13.8 mm, and the sheets with varied thickness of 250 μm, 500 μm and 750 μm respectively. The lens sheet has a thickness gradient similar with spherical cap. Gels were allowed to equilibrate for 2 h in the PBS solution with certain ionic strength and the gel was imaged using either a Zeiss® Axiovert 200 inverted optical microscope (2.5×, 5× and 10× objectives) or a Zeiss® LSM 510 META laser scanning confocal fluorescence microscope, where a HeNe laser (wavelength 520 nm) was used to excite the fluorescence fluorophore (detection filter: 480 nm). The focal length characterization was carried via a multi points laser marking and calculated the focal length. The low energy HeNe laser (power ~4 mW, wavelength ~633 nm) was adopted in this measurement to prevent any possible degradations of the gel. The final focal length calculation was correct with the Numerical Aperture (NA), to compensate the deflection between then liquid/air interface.

Acknowledgements: The work was supported by the Engineering and Physical Sciences Research Council (EPSRC) grant EP/N007921/1 and Royal Society Research Grant-RG150662. The authors also acknowledge fundings from the EU-COST MP1106 network, Royal society of Chemistry and British Council.

[1] O. Findl, W. Buehl, R. Menapace, S. Sacu, M. Georgopoulos, G. Rainer, *Ophthalmology* **2005**, *112*, 2004.
[2] M. A. Farbowitz, N. A. Zabriskie, A. S. Crandall, R. J. Olson, K. M. Miller, *J. Cataract. Refract. Surg.* **2000**, *26*, 1339.
[3] R. Chiarelli, and D. De Rossi, in: *Ionic Interactions in Natural and Synthetic Macromolecules*, A. Ciferri, A. Perico, Eds., Wiley, Hoboken **2012**, p. 581.
[4] D. Schmaljohann, *Adv. Drug Deliv. Rev.* **2006**, *58*, 1655.
[5] B. Xu, R. C. Hayward, *Adv. Mater.* **2013**, *25*, 5555.
[6] B. Xu, Q. H. Liu, Z. G. Suo, R. C. Hayward, *Adv. Func. Mater.* **2016**, *26*, 3218.
[7] G. Grassi, R. Farra, P. Caliceti, G. Guarnieri, S. Salmaso, M. Carenza, M. Grassi, *Am. J. Drug Deliv.* **2005**, *3*, 239.
[8] K. Sawahata, M. Hara, H. Yasunaga, Y. Osada, *J. Controlled Release* **1990**, *14*, 253.
[9] R. Yoshida, K. Sakai, T. Okano, Y. Sakurai, *Adv. Drug Deliv. Rev.* **1993**, *11*, 85.
[10] J. Dolbow, E. Fried, H. D. Jia, *J. Mech. Phys. Solids* **2004**, *52*, 51.
[11] H. L. Lim, Y. Hwang, M. Kar, S. Varghese, *Biomater. Sci.* **2014**, *2*, 603.
[12] A. Richter, G. Paschew, S. Klatt, J. Lienig, K. Arndt, H. P. Adler, *Sensors* **2008**, *8*, 561.
[13] Y. Qiu, K. Park, *Adv. Drug Deliv. Rev.* **2012**, *64*, 49.
[14] I. M. El-Sherbiny, M. H. Yacoub, *Global Cardiol. Sci. Practice* **2013**, *3*, 38.
[15] S. H. Lee, T. H. Kim, M. D. Lima, r. H. Baughman, S. J. Kim, *Nanoscale* **2016**, *8*, 3248.
[16] R. Dinyari, S. B. Rim, K. Huang, P. B. Catrysse, P. Peumans, *Appl. Phys. Lett.* **2008**, *92*, 091114.
[17] P. J. Hung, K. Jeong, G. L. Liu, L. P. Lee, *Appl. Phys. Lett.* **2003**, *85*, 6051.
[18] S. B. Rim, P. B. Catrysse, R. Dinyari, K. Huang, P. Peumans, *Opt. Express* **2008**, *16*, 4965.
[19] L. Dong, A. K. Agarwal, D. J. Beebe, H. R. Jiang, *Nature* **2006**, *442*, 551.
[20] H. C. Ko, M. P. Stoykovich, J. Song, V. Malyarchuk, W. M. Choi, C. J. Yu, J. B. 3rd Geddes, J. Xiao, S. Wang, Y. Huang, J. A. Rogers, *Nature* **2008**, *454*, 748.
[21] V. Trujillo, J. Kim, R. C. Hayward, *Soft Matter* **2008**, *4*, 564.

Eureka moment for Northumbria's 'smart' researchers

Two Northumbria researchers working in smart surfaces have won a prize in the Eureka and Discovery category of the Engineering and Physical Sciences Research Council's (EPSRC) annual photography competition.

Senior lecturer Dr Ben Bin Xu and PhD student Ding Wang's prize-winning photograph is a visually striking image of a thin elastic material, which has been heavily compressed during their research. The pair are members of the Smart Materials and Surfaces Lab with the faculty of Engineering and Environment at Northumbria. Their current research, funded by a £97k grant from the EPSRC, is focused on the micro-mechanics of soft materials such as gels and silicone elastomers and how these can be used in future engineering applications.

Dr Xu, a senior lecturer in Mechanical and Construction Engineering at Northumbria said: "While the wrinkling, buckling and folding of the surfaces of thin films, such as aging skin or the crumpling of a thin film device, are traditionally seen as faults, this wrinkling can actually be used to improve multifunctional chip devices for use in biology, tissue engineering and chemical engineering. This photo, captured by Ding Wang during our research, is a wonderful visual representation of the work we are carrying out. For the image to be recognised in this very prestigious national competition is a fantastic achievement."

The EPSRC's Science Photography Competition is now in its fourth year and is open to all EPSRC-funded researchers. This year the competition attracted more than 100 entries across five categories – Eureka and Discovery, Equipment and Facilities, People and Skills, Innovation, and Weird and Wonderful.

Competition judge Dr Helen Czerski said: "Scientists and engineers are often so busy focusing on the technical details of their research that they can be blind to what everyone else sees first: the aesthetics of their work. Science is a part of our culture, and it can contribute in many different ways. This competition is a wonderful reminder of the emotional and artistic aspects of science, and it's great that EPSRC researchers have found this richness in their own work."

The EPSRC is the main funding agency for engineering and physical sciences research and invests £800 million a year in research and postgraduate training, building the knowledge and skills base needed to address the scientific and technological challenges facing the nation. Northumbria offers a range of fascinating courses in the field of Mathematics, Physics and Electrical Engineering, with a number of research groups at the University driving breakthroughs and discoveries in these disciplines.

DISCOVER MORE

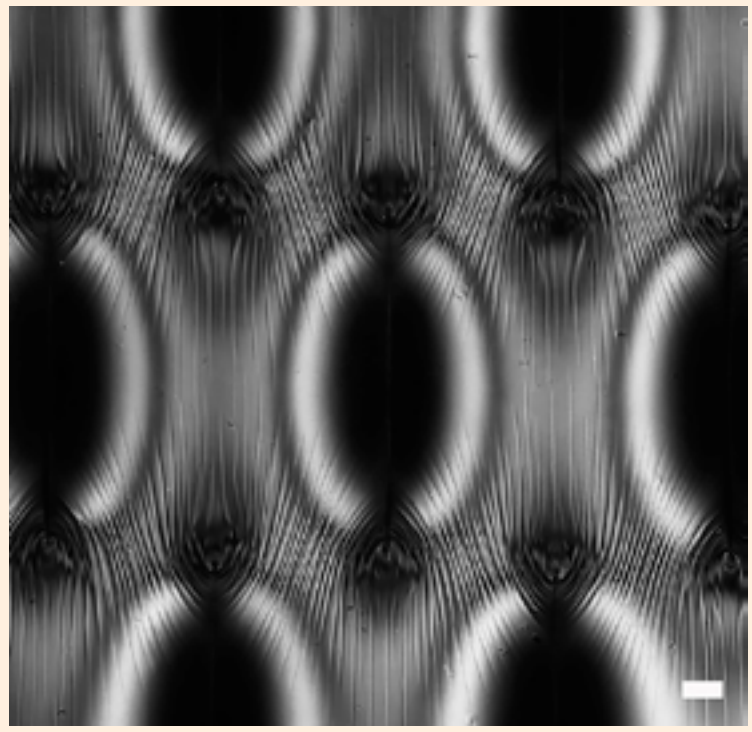

Not all wrinkles are unwanted, by Senior Lecturer Dr Ben Bin Xu and PhD student Ding Wang.

United Nations asks Northumbria professor to help address global problem

Eliminating the practice of Female Genital Mutilation (FGM) is a step closer thanks to the expertise of a Northumbria academic.

Professor Ngianga-Bakwin Kandala

A world-leading biostatistics expert, Professor Ngianga-Bakwin Kandala was invited to a prestigious United Nations (UN) conference in April to discuss his analysis of the complex social, cultural and environmental reasons why FGM occurs. His work in statistical analysis and modelling will help policy makers understand the causes of FGM and design solutions, which could help eradicate this global problem. Using data provided by National Statistics Offices, charities and NGOs to identity FGM hotspots, Professor Kandala focused his analysis on Kenya in the first instance and presented these findings at this year's joint UNFPA-UNICEF Female Genital Mutilation/Cutting (FGM/C): Accelerate Change conference.

Professor Kandala, who is based in Northumbria's Mathematics, Physics and Electrical Engineering department, said: "The Bayesian method of analysing data allows us to take all the complex social, cultural and environmental factors into account to produce a far more accurate and multi-dimension view of the situation and how it is changing over time.

"We can then present these findings in a way which allows policy makers to understand the problem and design bespoke solutions for individual countries or communities.

"This is the first time data in relation to FGM has been analysed using this method and on this scale and I was delighted to be asked by the UN to present my findings at the Accelerate Change conference."

Professor Kandala has spent the last 15 years working with organisations such as the World Health Organisation, children's charity UNICEF and the UK's Department for International Development (DFID) to map global health and disease in developing countries using statistical analysis. In recent years, he has played a major role in helping establish a group to train biostatisticians in Africa.

Alongside his work in developing countries, Professor Kandala is also interested in studying the relationship between air pollution and health in developed countries, including the UK, in the future. This would include studying links between Mono-nitrogen Oxide, sulphur dioxide, particulate matter, benzene, heart failure, hospital admissions and mortality and mapping health trends in relation to air pollution.

The United Nations.

Speaking about Professor Kandala's invite to the UN, Professor Glen McHale, Pro Vice-Chancellor (Engineering & Environment), said: "The work Professor Kandala is carrying out is of global importance and is an excellent example of the type of internationally significant and ground-breaking research being carried out by our academics here at Northumbria."

DISCOVER MORE

www.northumbria.ac.uk/maths

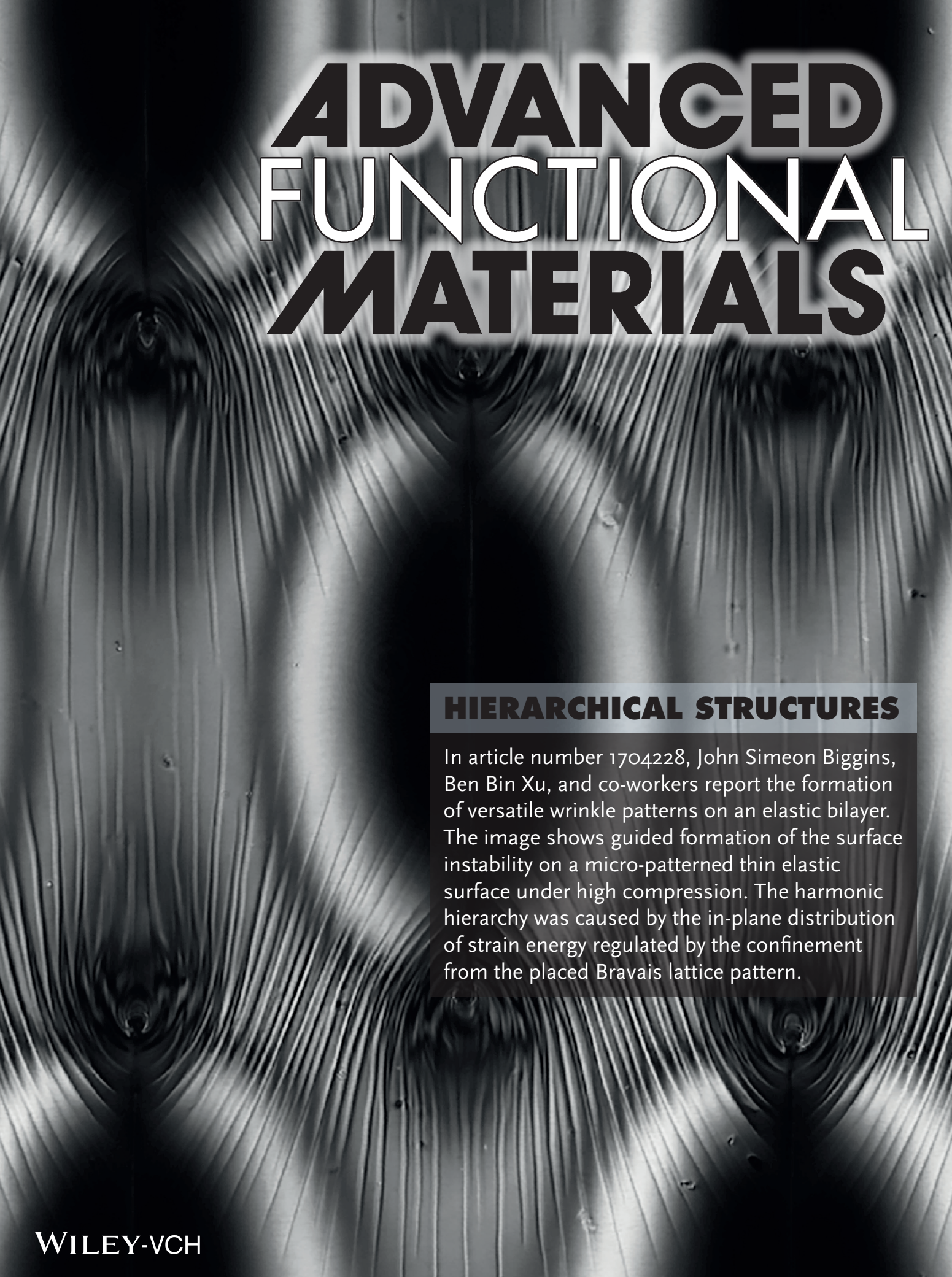

ADVANCED FUNCTIONAL MATERIALS

HIERARCHICAL STRUCTURES

In article number 1704228, John Simeon Biggins, Ben Bin Xu, and co-workers report the formation of versatile wrinkle patterns on an elastic bilayer. The image shows guided formation of the surface instability on a micro-patterned thin elastic surface under high compression. The harmonic hierarchy was caused by the in-plane distribution of strain energy regulated by the confinement from the placed Bravais lattice pattern.

WILEY-VCH

SCI
where science meets business

This is to certify that on 7 September 2018

Ding Wang

was awarded the

Joint First Prize
Poster Presentation

for

Excellence in Chemical Research

at the 25th Annual SCI-CSCST Conference
of the SCI Chinese UK Group and
the Chinese Society of Chemical Science & Technology in the UK

Weiping Wu
Chair, SCI Chinese UK Group

Sharon Todd
Executive Director, SCI

Society of Chemical Industry
International Headquarters, 14/15 Belgrave Square, London, SW1X 8PS, UK
T: +44 (0)20 7598 1500 F: +44 (0)20 7598 1545 www.soci.org

SCI
where science meets business

This is to certify that

Ding Wang

was awarded the

Joint Third Prize

Oral Presentation

for

Excellence in Chemical Research

at the 2017 24th Joint Annual Conference
of the SCI Chinese UK Group and
the Chinese Society of Chemical Science & Technology in the UK

Weiping Wu
Chairman, SCI Chinese UK Group

Sharon Todd
SCI Executive Director

Society of Chemical Industry
14/15 Belgrave Square, London, SW1X 8PS UK
T: +44 (0)20 7598 1500 www.soci.org

SYNOPSYS®

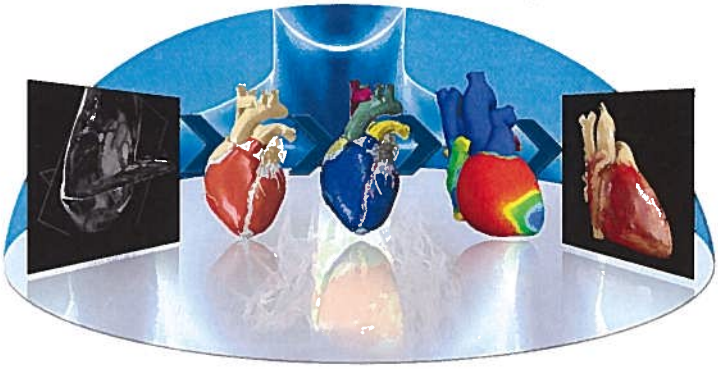

This is to certify that

Ding Wang

has attended a 1-day Workshop on

Advanced Biomedical Modeling: From Image to Simulation

held at
Synopsys NE Limited
Reading, Berkshire

20th October 2016

Trainer *Celia Butler*

SSA

3DS SIMULIA